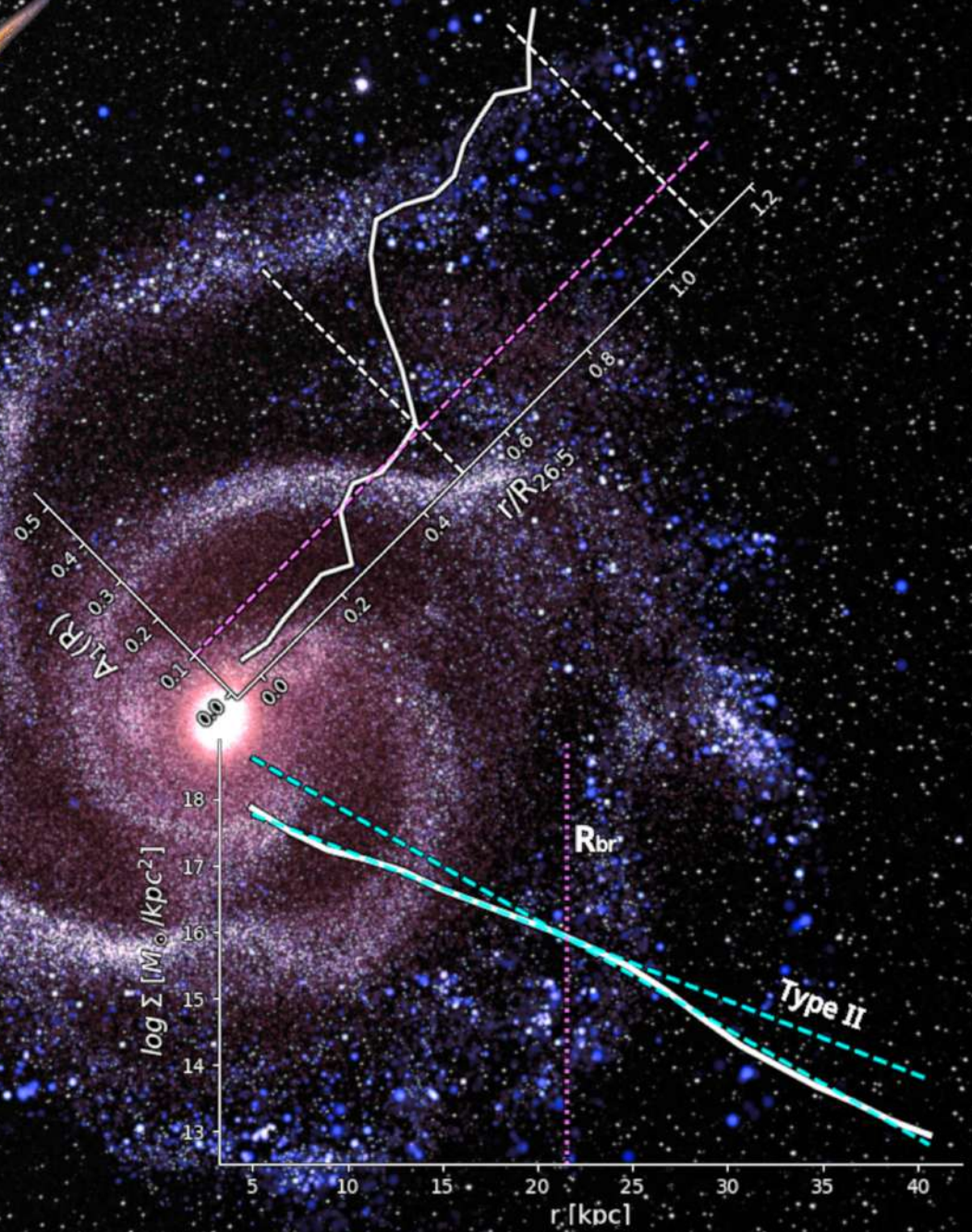


# Disk Galaxies in a Cosmological Context: Linking stellar distributions, morphological perturbations and the dark matter halo



Silvio Varela Lavín

**Disk Galaxies in a Cosmological Context:  
Linking stellar distributions, morphological  
perturbations and the dark matter halo**

Silvio Varela Lavín



**UNIVERSIDAD  
DE LA SERENA**  
CHILE

**Doctoral Thesis**

To fulfill the requirements for the degree of  
Doctorate in Astronomy  
at Universidad de La Serena under the supervision of  
Prof. Dr. Facundo Ariel Gómez (Astronomy, Universidad de La Serena)  
Prof. Dra. Patricia Beatriz Tissera (Astronomy, Pontificia Universidad Católica de Chile)

**Silvio Varela Lavin**

April 5, 2024

**Cover Image:** The center and lower left galaxies are RGB composites of galaxies ID477328 and ID562742 from the TNG50-1 simulation of the IllustrisTNG project. The top galaxy is the edge-on galaxy NGC 4565. The top plot corresponds to the radial distribution of the  $m = 1$  amplitude of the

Fourier modes,  $A_1$ , described in Chapter 4. The lower plot is the stellar surface mass density, accompanied by a piecewise double exponential fit, described in Chapter 3. Both plots correspond to actual measurements of the center galaxy ID477328.

**Credit:** The center and bottom left galaxies were made using Py-SPHViewer Benitez-Llambay (2015), the galaxy on the top is NGC 4565 from ESO. The image was built using the GIMP<sup>1</sup> program.

---

<sup>1</sup><https://www.gimp.org>

# Contents

Page

<b>1</b>	<b>Introduction</b>	<b>5</b>
1.1	Formation and evolution of galaxies . . . . .	5
1.2	Spiral galaxies . . . . .	10
1.3	The matter distribution of disk galaxies . . . . .	10
1.3.1	Bulge and bar . . . . .	10
1.3.2	Disc . . . . .	11
1.3.3	Halo . . . . .	13
1.4	Perturbations in disk galaxies . . . . .	16
1.5	This thesis . . . . .	22
<b>2</b>	<b>Numerical models of cosmological galaxies</b>	<b>24</b>
2.1	The role of cosmological simulations and some definitions . . . . .	24
2.2	EAGLE simulations. . . . .	25
2.3	IllustrisTNG project . . . . .	28
2.4	Auriga project . . . . .	31
2.5	Resolution and numerical heating . . . . .	33
2.5.1	EAGLE project . . . . .	34
2.5.2	IllustrisTNG project . . . . .	38
2.5.3	Auriga project . . . . .	39
<b>3</b>	<b>Exploring the outskirts of the EAGLE disc galaxies</b>	<b>44</b>
3.1	Introduction . . . . .	45
3.2	Simulated galaxies . . . . .	46
3.2.1	The simulated galaxy sample . . . . .	47
3.2.2	Break-Finder (BF) algorithm . . . . .	49
3.3	Analysis . . . . .	49
3.3.1	Stellar surface density profiles . . . . .	49
3.3.2	Age profiles . . . . .	51
3.3.3	The angular momentum content . . . . .	53
3.3.4	Distributions of $R_{\min}$ , $R_{\max}$ and $R_{\text{br}}$ . . . . .	57
3.3.5	Statistical analysis of $\Sigma$ and the age profiles . . . . .	59
3.3.6	Distribution of the mono-age stellar populations . . . . .	59
3.3.7	Statistical analysis of the star formation activity . . . . .	61

---

3.3.8	Statistical analysis of the median vertical height profiles . . . . .	63
3.4	discussion and Conclusions . . . . .	65
<b>4</b>	<b>Lopsided Galaxies in a cosmological context: a new galaxy-halo connection</b>	<b>68</b>
4.1	Introduction . . . . .	69
4.2	Simulations . . . . .	71
4.2.1	The IllustrisTNG project . . . . .	71
4.2.2	Selection criteria . . . . .	73
4.3	Methods . . . . .	73
4.3.1	Characteristic scales . . . . .	73
4.3.2	Quantification of $m = 1$ asymmetries . . . . .	74
4.3.3	Estimating the asymmetries in DM haloes and stellar component . . . . .	77
4.4	Results . . . . .	78
4.4.1	General disc morphological properties . . . . .	78
4.4.2	Structural properties of lopsided galaxies . . . . .	79
4.4.3	The role of the central mass distribution . . . . .	79
4.4.4	Evolution of lopsided galaxies . . . . .	81
4.4.5	Main driving agents . . . . .	85
4.5	Conclusions and discussion . . . . .	92
<b>5</b>	<b>The effects of the DM overdensity wakes on disk galaxies</b>	<b>96</b>
5.1	Introduction . . . . .	97
5.2	Basis-Function Expansions . . . . .	98
5.3	Simulation data . . . . .	100
5.4	Analysis and results . . . . .	100
5.4.1	Spherical density model . . . . .	100
5.4.2	Building basis functions . . . . .	101
5.4.3	Density field reconstruction . . . . .	103
5.4.4	Potential field reconstruction . . . . .	105
5.4.5	Stability of the basis reconstruction over time . . . . .	106
5.5	Discussion and Future work . . . . .	109
<b>6</b>	<b>Summary</b>	<b>111</b>
	Acknowledgements . . . . .	116
6.0.1	Financial acknowledgments . . . . .	116
6.0.2	Personal acknowledgments . . . . .	116
	<b>Bibliography</b>	<b>118</b>

# Chapter 1

## Introduction

This thesis is focused on the detailed analysis of the galactic stellar component of late type galaxies to characterize their evolution as well as their connection with their inner dark matter distribution. By analyzing the stellar distribution and populations within simulated disk galaxies, we aim to explore crucial aspects of the physical processes that shape their evolution and formation. The analysis in this thesis, based on state-of-the-art cosmological simulations, allows us to explore the coupling between the baryons and the dark matter, and to characterize its impact on the galaxies dynamical structure, morphology and stellar distribution. To accomplish this, we use different suites of cosmological hydrodynamical simulations, focusing on a carefully selected sample of disk-dominated galaxies and Milky Way-like masses.

### 1.1 Formation and evolution of galaxies

The study of galaxy formation and evolution is one of the most fascinating and complex topics in astronomy, with new questions and challenges constantly arising. Prior to the formation of the first structures and galaxies, the Universe was in its early epoch, characterized by a remarkable event known as the "Big Bang". The Standard Cosmological Model describes this epoch, as well as other key events such as primordial nucleosynthesis and recombination. It also provides a fundamental framework for understanding the history and structure of our universe. The currently accepted version of this model is the Lambda Cold Dark Matter ( $\Lambda$ CDM) model (Peebles, 1980).

The  $\Lambda$ CDM model describes the density distribution of the Universe using three cosmological components: dark energy, dark matter, and baryonic matter. Dark energy ( $\Omega_\Lambda$ ) constitutes the fraction of the total energy of the Universe, modelled as a repulsive force and linked to its accelerated expansion. Dark matter ( $\Omega_c$ ) accounts for the density of cold dark matter, interacting with baryonic matter through gravitational effects, which manifest in the formation of very large-scale as well as small-scales structures. Baryonic matter, represented by  $\Omega_b$ , denotes the fraction of the total mass of the Universe potentially composed of observable matter, containing particles that can interact with photons. Considering a spatially flat Universe ( $\Omega = 1$ ), the sum of these cosmological parameters is approximately 1 (i.e.,  $\Omega_\Lambda + \Omega_c + \Omega_b \approx 1$ ). This indicates that dark energy, cold dark matter, and baryonic matter jointly constitute the contributors to the Universe's total energy density in distinct proportions.

The  $\Lambda$ CDM model considered a rather successful model in cosmology, serves as a well defined framework for describing various cosmological phenomena. An essential key to understanding the distribution of

matter and energy in the early Universe is the Cosmic Microwave Background (CMB) (Penzias & Wilson, 1965; Boggess et al., 1992; Louis et al., 2017; Planck Collaboration et al., 2014, 2016, 2020). This radiation has allowed us to measure the power spectrum of the primordial fluctuations, and thus to constrain the parameters associated with the cosmological model. Moreover, the  $\Lambda$ CDM model successfully predicts the formation of the large-scale structure of galaxies, where the presence of cold dark matter plays a significant role in shaping clusters of galaxies, galaxies, filaments, and voids (Peebles, 1980). Through the Big Bang nucleosynthesis model also makes predictions about the abundances of hydrogen, helium, and lithium that can be compared with astronomical observations obtained from stellar evolution models and galaxy formation models (Peebles, 1966; Wagoner, 1973; Coc & Vangioni, 2017). The large number of observational evidence and theoretical analysis highlights the robustness and comprehensiveness of the  $\Lambda$ CDM model in explaining various cosmological phenomena.

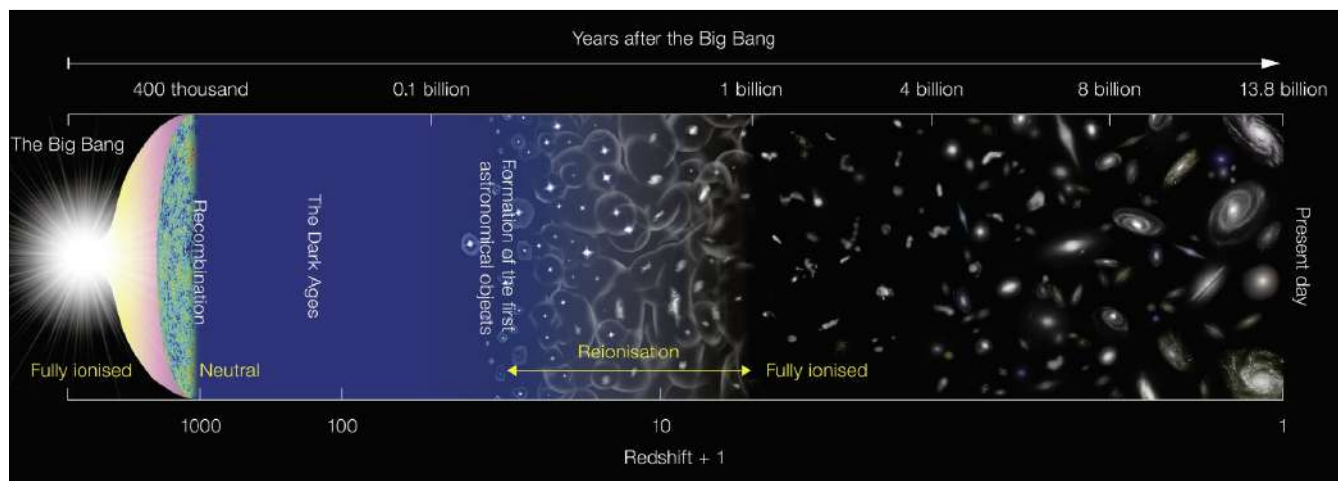


Figure 1.1.1: This illustrative image depicts the evolutionary timeline of the Universe since the momentous event of the Big Bang. The early Universe, primarily composed of searing hot plasma, underwent an exponential expansion phase termed inflation. As this expansion unfolded, the Universe gradually cooled, leading to the decoupling of photons from baryons. This significant event resulted in the formation of the Cosmic Microwave Background (CMB), a snapshot of the Universe’s earliest state. The cosmic journey continued as the Universe expanded and cooled further, allowing gravity to sculpt the emergence of the first cosmic structures, including filaments and clusters. The seeds of the first galaxies and stars took root and formed. Over time, the Universe evolved through an intricate dance of mergers and interactions among galaxies. Within individual galaxies, stars matured, culminating in dramatic supernova explosions, which enriched the galaxies with heavier elements. Credit: ESO

According to this paradigm, the basic timeline of the Universe can be described as follows (see Fig. 1.1.1). During its first  $10^{-43}$  seconds, referred to as the Planck epoch (Barrow, 1983), the universe was a hot ( $10^{28}$  K), dense soup of energy in which the fundamental forces (electromagnetic, strong and weak nuclear) were unified except for the gravitational force. Subsequently, in the first  $10^{-32}$  seconds after the Big Bang, the Universe underwent a rapid expansion phase known as inflation (Guth, 1981).

During inflation, the Universe expanded exponentially by a factor of at least  $10^{26}$ , smoothing out any irregularities and setting the stage for the formation of galaxies and other cosmic structures.

Following the inflationary epoch, the Universe continued to expand, albeit at a slower rate, known as the radiation-dominated era. In this era, nucleosynthesis was primordial, where there was a dense plasma of photons, electrons and protons. The Universe reached temperatures between  $10^9$  to  $10^{12}$  K and the formation of atoms was not possible, as the photons were in Thomson scattering equilibrium between protons and electrons. As the Universe expanded and cooled, the plasma eventually condensed into atoms in an event known as recombination. This milestone occurred when the Universe was approximately 380,000 years old and resulted in the release of a burst of photons, now observed as the cosmic microwave background (CMB) radiation (Penzias & Wilson, 1965). The CMB serves as a snapshot of the Universe when it was just 380,000 years old and is highly uniform across the sky, in agreement with the predictions of the inflation epoch. However, it also contains small perturbations, which are believed to have been the seeds for the formation of galaxies and other cosmic structures.

The subsequent stages of the Universe involved further expansion and cooling, leading to the clumping of matter and the formation of galaxies, clusters of galaxies, and other structures. This ongoing expansion and cooling process have persisted to the present day, yielding an estimated age of approximately 13.8 Gyr for the Universe Planck Collaboration et al. (2020). Within this cosmic timeline, the small perturbations present in the CMB were amplified by the force of gravity, particularly influenced by the contribution of dark matter. As a result, baryonic matter collapsed gravitationally within these dark matter halos, eventually forming the first stars, galaxies, and clusters of galaxies. This gravitational collapse of matter from the initial CMB perturbations has given rise to the filamentary structure known as the cosmic web, which is a prominent feature of the Universe. Observations of galaxies and quasars in large galaxy surveys have provided valuable insights into the existence and physical properties of this cosmic web (Fontanelli, 1984; Fairall, 1995; Takeuchi et al., 1999).

The gravitational interactions between galaxies and halos are fundamental factors in the  $\Lambda$ CDM model, playing a crucial role in the evolution and formation of galaxies. These interactions lead to the hierarchical growth of DM halos, ranging from small groups to massive clusters (see Fig 1.1.2). According to this hierarchical model, early galaxies frequently merged with others of similar mass. As the Universe expanded and cooled over time, such mergers became less common, and interactions with galaxies of different masses became more significant.

The hierarchical model of structure formation serves as a framework for understanding the origins and evolution of galaxies, supported by observational evidence and cosmological simulations (Conselice et al., 2003; Giocoli et al., 2010; Rodriguez-Gomez et al., 2015). And, as we will see later in this Thesis, perturbations of galaxies DM halos, induced by such gravitational interactions, can play a very relevant role on determining their present day dynamics, structure and overall evolution. Indeed, the galaxies within their DM halos exhibit a variety of shapes, sizes, colors, and kinematics, leading astronomers to develop different methods to classify them (Hubble, 1926; de Vaucouleurs, 1959; Zhu et al., 2018). The most commonly used system for galaxy classification is the Hubble tuning fork diagram, which was introduced by Edwin Hubble in 1926 (Fig. 1.1.3). This classification has allowed astronomer to categorized galaxies according to four main types: ellipticals, spirals, lenticulars, and irregulars, each displaying distinctive morphological features. Elliptical galaxies, characterized by the absence of visible spiral structures, tend to have an approximately elliptical shape, may be intrinsically oblate, prolate or triaxial, depending on their symmetries, also tend to have a redder color compared to spiral galax-

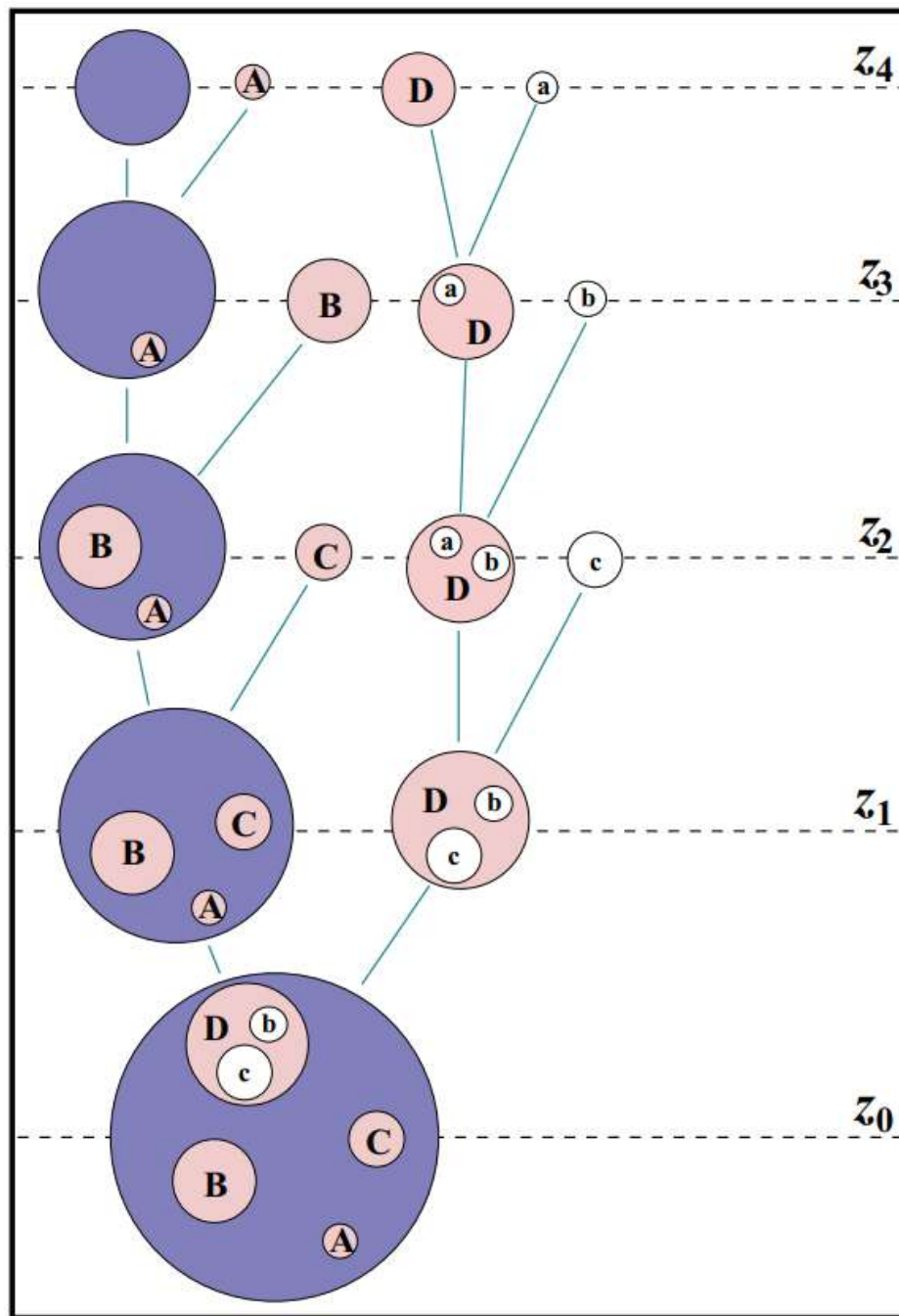


Figure 1.1.2: Diagram illustrating the progression of a dark matter halo's merger tree through distinct time intervals. The prominently shaded halos on the left symbolize the development of the central halo progenitor, incorporating 'satellite' halos denoted as A, B, C, and D, thus initiating a set of subhalos. Satellite system D has also undergone its own acquisition of satellite halos (a, b, and c) prior to being assimilated by the primary host halo. Among these, those that persist (b and c) contribute to the formation of a secondary population of subhalos. Credit: Giocoli et al. (2010)

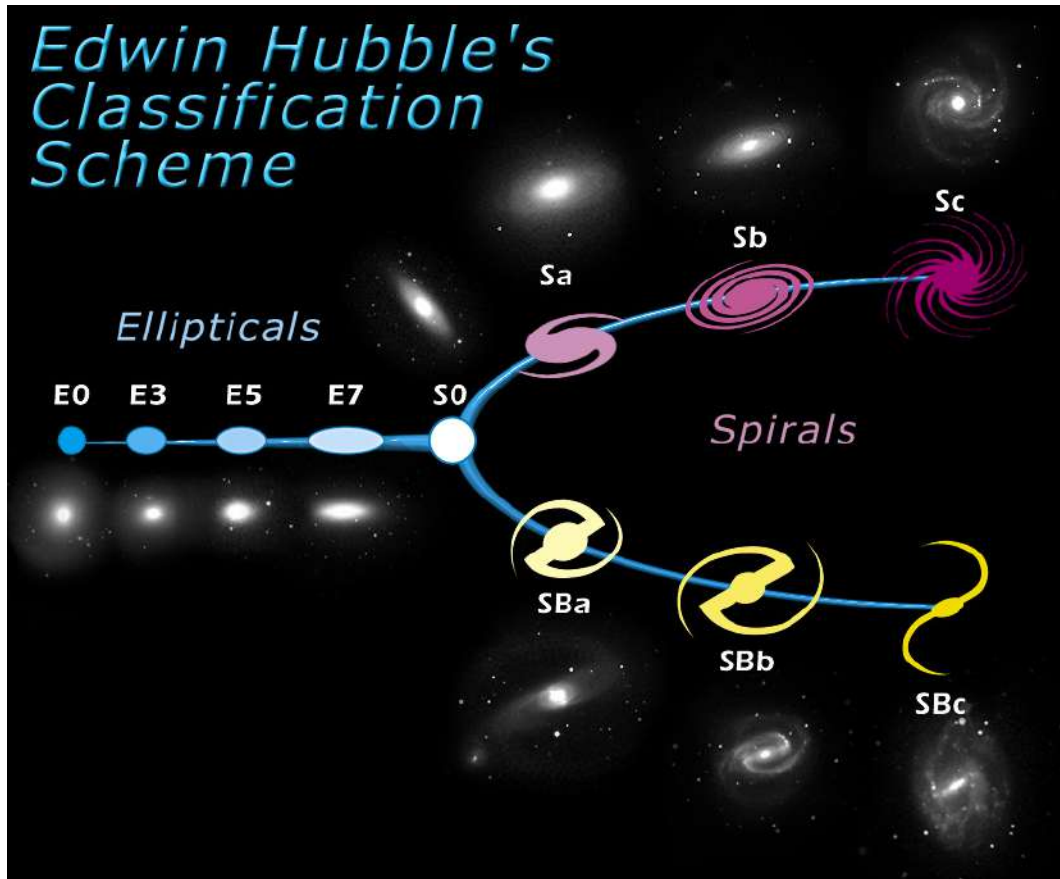


Figure 1.1.3: The Hubble tuning-fork diagram is used to classify galaxies based on their morphology. Credit: NASA & ESA

ies, implying an old stellar population and lack of star formation. In contrast, spiral galaxies showcase prominent spiral arms and contain abundant gas and dust, their active star formation leads them their bluer colors. Lenticular galaxies possess a disk resembling spirals but lack well-defined arms, and their color can vary depending on their star-formation activity. Meanwhile, irregular galaxies not have a distinct regular shape, and do not fall into any of the regular classes of the Hubble sequence. Furthermore they can display a wide range of colors depending on their recent star formation history. The study of galaxy shapes offers valuable insights into the distribution of baryonic matter, their interactions with the environment, and the dark matter halos. In this thesis primarily focuses on the analysis of spiral galaxies, as we will discuss in detail, their stellar and gas distribution in their disk component provide unique information about very relevant process behind galaxy formation, such as star formation history, chemical enrichment, dynamics and dark matter distribution, among others. In particular, we will primarily focus on Milky Way-like galaxies, with the goal of placing our own Galaxy within a broader cosmological context. In the following, we will give a brief description of the components of spiral galaxies.

## 1.2 Spiral galaxies

Spiral galaxies represent approximately two-thirds of the massive galaxies in the present-day Universe and, as such, they are the most common type of galaxy (Lintott et al., 2011; Willett et al., 2013). They have a distinctive structure, typically with a spheroidal central component, known as the bulge, surrounded by a disk of stars and gas. Within the disk we find spiral arms, regions of intense star formation. Like all galaxies, spiral galaxies are enveloped with a stellar and dark matter halo, which surrounds the galaxy and provides gravitational support.

The Hubble classification system divides spiral galaxies into two main types: classical spiral galaxies (S) and barred spiral galaxies (SB). Classical spirals exhibit a central bulge and spiral arms, while barred spirals showcase a central bar extending from the center, with spiral arms stemming from the ends of the bar. Additionally, within the spiral galaxies classification, there are sub-classifications denoted as Sa, Sb, and Sc for classical spirals, and SBa, SBb, and SBc for barred spirals. These designations denote variations in the openness and definition of their spiral arms and the size relation between the bulge and disk. Notably, Sa/SBa galaxies possess a prominent bulge with tightly wound arms, while Sc/SBc galaxies feature loosely wound arms and a smaller bulge, with SBb or Sb galaxies falling in between. Interestingly, Sa/SBa galaxies have a lower star formation rate, lower metallicity, and an older stellar population compared to Sc/SBc galaxies.

As previously discussed, spiral galaxies are stellar systems with a substantial star formation rate, particularly concentrated in their spiral arms, where gas and dust are abundant. The stars can produce supernovae events, expelling gas and dust from the galaxy. This ejected material then contributes to the formation of new stars in a continuous cycle, leading to an enrichment of the galaxy's metallicity of the galaxy over time. This feedback of the stellar activity shapes the fascinating evolution of galaxies. The stellar halo in disk galaxies provides valuable information about the assembly history of the galaxy itself, as we will see in the next sections. Its dynamical and chemical properties can shed light on its accretion history, mergers, gravitational interactions, dark matter distribution, and other aspects of its formation and evolution (Tissera et al., 2013, 2014; Monachesi et al., 2013, 2019; Conroy et al., 2021; Khoperskov et al., 2023).

## 1.3 The matter distribution of disk galaxies

### 1.3.1 Bulge and bar

The bulge and bar of a galaxy are important components that can have a significant influence on the formation and evolution of the galaxy. The bulge takes the form of an ellipsoidal structure in the central region of the galaxy, while other disk galaxies have a bar-shaped structure. Both components are composed mainly of older stars, and are therefore reddish in color.

The formation of bulges and bars is a complex process that depends on various factors. Bulges can form through violent processes such as galaxy mergers, where the gravitational interactions between galaxies lead to the redistribution of stars and gas towards the center. Pseudo-bulges (or disk-like bulges, Athanassoula (2005)), on the other hand, could form through secular processes driven by the internal dynamics of the galaxy and hierarchical evolution as mergers (Gargiulo et al., 2019; Brooks & Christensen, 2016; Gozman et al., 2023). Kinematically, these are hot components, having a velocity dispersion support

greater than their rotational support. Furthermore, due to the lack of dust and gas component, bulges tend to have almost no star formation. The distribution of light is described by a Sersic profile (Sérsic, 1963; Sersic, 1968, usually  $n > 2$  for bulges and  $n < 2$  for pseudo-bulges, where  $n$  is the Sersic index). The metallicity of bulges can vary depending on their formation mechanisms. Classical bulges are typically metal-rich, similar to elliptical galaxies, while pseudo-bulges can have a range of metallicities, including both metal-rich and metal-poor populations. Bars, on the other hand, are elongated structures that can form through gravitational instabilities in the disc, or they can be triggered by interactions with companion galaxies. They are characterized by a distortion in the shape of the disc, with stars and gas moving along elongated orbits. Bars play a crucial role in the secular evolution of disk galaxies. They redistribute angular momentum within the galaxy, causing material to be emitted from the bar's inner Lindblad resonance and absorbed by the spheroid and outer disk. Bars can also drive the formation of substructures such as spirals and rings

The kinematics of bulges and bars are closely related to their formation and evolution. Bulges can have a range of kinematic properties, including rotation and dispersed motions. Classical bulges often have a more pressure-supported kinematics, while pseudo-bulges can exhibit both rotation and random motions ( $\langle B/T \rangle = 0.16$  in contrast to  $\langle B/T \rangle = 0.41$  for bulges, where  $\langle B/T \rangle$  is the bulge-to-total ratio (Fisher & Drory, 2008)). Bars are elongated, symmetric structures found in well-defined stellar disks. They dynamically interact with other components such as the disk, the bulge, if present, and the dark matter halo (Debattista & Sellwood, 2000).

### 1.3.2 Disc

The analysis of the stellar content in disks is one of the classical approaches to study the processes that the galaxies have undergone during their formation history, as well as the evolution of their structural information such as mass distribution, age, luminosity, chemical abundance, and others (e.g. MacArthur et al., 2009; Roediger et al., 2011; Sánchez-Blázquez et al., 2011; Perez et al., 2011; Erwin et al., 2008; Pohlen & Trujillo, 2006). Early studies suggested that the stellar density distribution of disk galaxies decreases exponentially with radius (Patterson, 1940; Freeman, 1970). This has been suggested to be the result of the initial angular momentum distribution of the gas cloud as it collapsed to form the disk (Fall & Efstathiou, 1980; Dalcanton et al., 1997; Mo et al., 1998). However, studies by van der Kruit (1979) found that such an exponential distribution does not extend to large radii for most galaxies. Indeed, later studies by Erwin et al. (2008); Pohlen & Trujillo (2006) showed that in fact a majority of galaxies do not have a well defined exponential behavior in their stellar distribution. In their study they defined three classes of surface brightness behavior considering a double-exponential profile: Those galaxies that show a deficit of light in the outer exponential with respect to the inner exponential (Type II), those galaxies with an excess of light in the outer exponential with respect to the inner exponential (Type III). Finally, the disk galaxies in the intermediate cases correspond to galaxies that display a pure exponential well defined all radii (Type I). In chapter 3 we discuss the three classes of double-exponential profiles in disk galaxies with respect to their stellar content.

The cooling of atomic hydrogen (HI) and the presence of warm molecular hydrogen (H<sub>2</sub>) serve as the fundamental building blocks from which stars are born (Hodge, 1986; Kennicutt, 1989, 1998; Bigiel et al., 2008). HI is particularly valuable for studying the kinematics of the disk due to its Doppler-shifted line emission at 21 cm. The dominant motion in a spiral galaxy is rotation, with HI exhibiting a

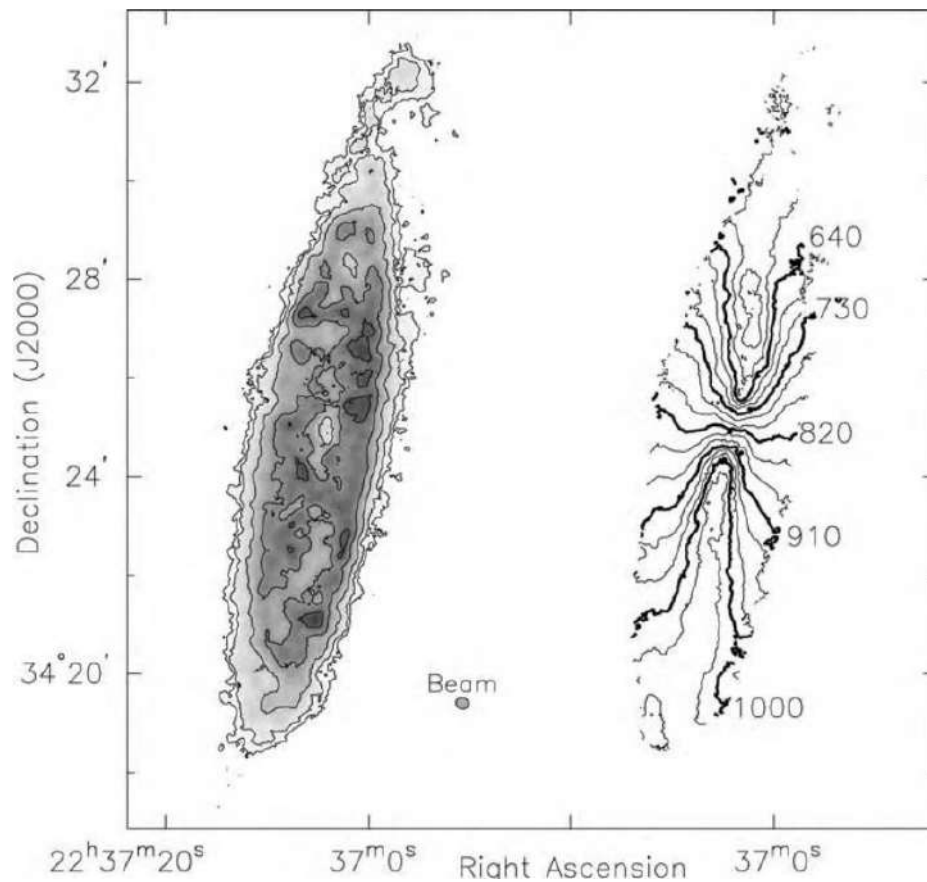


Figure 1.3.1: HI gas within NGC 7331, as captured by the Very Large Array (VLA) telescope, is presented. On the left panel, the distribution of gas surface density is depicted. At a distance of  $d=14$  Mpc, an observation reveals a total of  $11.3 \times 10^9 M_{\odot}$  of HI gas. The external contour delineates diffuse gas at  $N_{\text{H}} = 2.8 \times 10^{19} \text{ cm}^{-2}$ ; subsequent tiers are at levels of 1.2, 3.3, 6.4, and  $9.5 \times 10^{20} \text{ cm}^{-2}$ . On the right panel, contours illustrate the velocity  $V_r$  of the gas, spaced at intervals of 30 km/s. Credit: M. Thornley and D. Bambi, L. Sparke and J. Gallagher

typical dispersion velocity ranging between 8-10 km/s. The distribution of HI gas can provide valuable insights into the structure of the disk (Dib et al., 2021; Vollmer et al., 2016). For example, in Fig 1.3.1, we can observe the HI gas distribution in galaxy NGC 7331. The left panel displays the gas surface density, while the right panel shows contours of gas radial velocity. This distribution map can be used to trace asymmetrical distributions or signs of interaction with other galaxies (Phookun & Mundy, 1995; Noordermeer et al., 2005; Holwerda et al., 2011; van Eymeren et al., 2011). Observations of gas emission with respect to radial velocity have also been used to study the distribution of dark matter in galactic discs. The rotation curves of galaxies have revealed that the mass distribution in galaxies is not solely due to visible matter. The observed velocities of gas in the outer regions of galaxies are higher than expected based on the visible matter alone (Fig. 1.3.2), indicating the presence of dark matter (de Blok et al., 2008). These observations have supported the development of the theory of dark matter, which posits that the majority of matter in the universe is composed of non-luminous, or dark matter.

The chemical content within the disk stores important information about the formation history of the disk and other processes, such as migration and interactions with bars or other galaxies. Gas flows are

one of the mechanisms that shape the stellar metallicity in a disk galaxy, from gas accretion processes that contribute to galaxy growth and chemical enrichment, to outflow processes such as Active Galactic Nuclei (AGN) or supernova feedback. The composition of the gas may change due to mixing with the diverse Interstellar Medium (ISM) or dilution caused by the inflow of pristine gases from the intergalactic medium (e.g. Kereš et al., 2005; Brooks et al., 2007; Gibson et al., 2013). For example, Tissera et al. (2016) analyzed the relationship between galaxy gas-phase metallicity gradients, stellar masses, and star formation rates using simulated galaxies. They found that low-mass galaxies tend to have more diverse gas metallicity gradients. Another mechanism influencing stellar metallicity is stellar migration, in which stars change their positions due to orbital changes, including disk heating or radial migration driven by bars or spiral arms (Binney & Tremaine, 1987). This process is thought to influence the evolution of stellar population gradients, although its efficiency has been challenging to quantify. Using galaxies from the CALIFA survey, Sánchez-Blázquez et al. (2014) found no differences in metallicity or age gradients between galaxies with and without bars. Stronger evidence for stellar migration processes comes mainly from simulations and detailed studies of the Milky Way (MW), such as the work of Sellwood & Binney (2002) and Roediger et al. (2012). External perturbations such as galaxy accretion, interactions, or mergers can redistribute the positions and angular momenta of matter. Consequently, the merger history plays an essential role in shaping the metallicity gradient of the entire galaxy, especially the halo (e.g. Hirschmann et al., 2014). Some studies suggest that metallicity gradients,  $\nabla_{O/H}$ , in massive isolated spiral galaxies, at least within the local Universe, exhibit a wide range of metallicity slopes (e.g. Lequeux et al., 1979; Zaritsky et al., 1994). Furthermore, studies with cosmological simulations show that the oxygen gradient is clearly correlated with the gas disk size, resulting in shallower abundance slopes for larger gas disk sizes (e.g. Tissera et al., 2019).

### 1.3.3 Halo

Galaxies reside within the gravitational potential well of their associated dark matter halos, highlighting the important role of this component in the complex processes of galaxy formation and evolution. The halo of a spiral galaxy extends far beyond its visible disc, encompassing a mixture of baryonic and dark matter. With respect to the stellar disc, the stellar halo is composed stars that, typically, are older and more metal poor, and shows a higher velocity dispersion. The distribution of dark matter in a galaxy's halo has been thoroughly studied using a variety of observational and theoretical methods (Cole & Lacey, 1996; Gao & White, 2006). Observational studies have used techniques such as stellar dynamics and gravitational lensing to infer the complex distribution of dark matter within galaxies. In the case of gravitational lensing, the bending of light due to the curvature of space-time around massive object provides valuable insights into the mean density of dark matter, its relative density compared to baryonic matter, its size, and even its interaction strength with various fundamental forces (Massey et al., 2010). Interestingly, a local perturbation of the surface brightness distribution of the Einstein ring can be caused by the presence of a low-mass substructure in the lens galaxy (e.g., Vegetti et al., 2012). Furthermore, as discussed in Section 1.3.2, the analysis of rotation curves and the kinematics of gas and stars helps to solve the puzzle of the mass distribution of the dark matter halo. Although dark matter halos are often thought to be spheroidal or ellipsoidal, their structures frequently undergo mergers or gravitational interactions that can perturb their mass distribution. These perturbations can impact the baryonic distribution in its interior and lead to perturbations in the position and kinematics of this component, suggesting a close

connection between the dark and visible matter distributions.

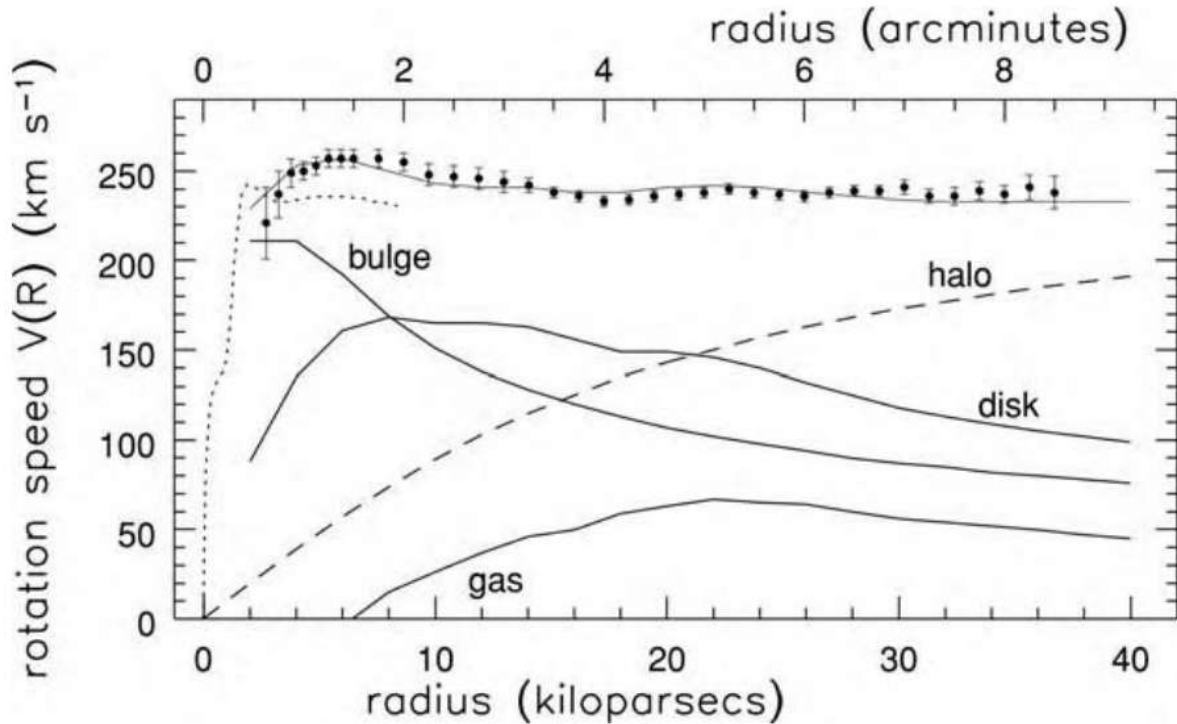


Figure 1.3.2: The data points represent the rotation profile of NGC 7331, derived from the HI map illustrated in Fig. 1.3.1, with the vertical bars indicating associated uncertainties. The CO gas distribution (dotted lines), observed at a finer spatial resolution, portrays a swifter ascent. The lower solid curves delineate the individual contributions to the velocity  $V(R)$  from the gas disc, the bulge, and the stellar disc. The sum of these components does not agree with the observed velocities, which are compensated by an additional dark halo. Credit: M. Thornley and D. Bambi, L. Sparke and J. Gallagher

Simulations have played an important role in understanding the dark matter distribution in the Universe (see Sec. 2). In particular, hydrodynamical simulations allow us to carefully analyze the profound influence of dark matter halos on the baryonic components and their consequent evolution and galaxy formation. These simulations provide a deeper understanding of the large-scale structure of the Universe as predicted by the  $\Lambda$ CDM paradigm, including large structures such as galaxy clusters and filaments. Modeling the density distribution of this of this galactic component is essential to understand the structure and evolution of a galaxy. Among the commonly used density profiles are the Navarro-Frenk-White (NFW) profile (Navarro et al., 1995, 1996) and the Hernquist profile (Hernquist, 1990). The NFW profile (equation 1.3.1) is an important profile that has been found to hold for a wide range of halo masses and redshifts (Jing, 2000), implying that the shape of the DM halo density profile is universal. The NFW profile is described by  $\rho_s$  and  $R_s$ , which represent the normalization factor and the scale radius, respectively. This equation can be divided into two regions: one describes the inner parts of a DM halo, between the center of the halo and the scale radius. This region describes a shallow slope of  $\rho(r) \propto r^{-1}$ . On the other hand, the outer region has a steeper slope than the inner region and is described by  $\rho(r) \propto r^{-3}$ . Furthermore, the equation 1.3.1 describes that halos with larger scale radii have small central densities,

and viceversa.

$$\rho(r) = \frac{\rho_s}{\frac{r}{R_s} \left(1 + \frac{r}{R_s}\right)^2} \quad (1.3.1)$$

Similarly, the Hernquist profile shows a gradual decrease in density towards the edge of the DM halo, described by the equation 1.3.2. The profile differs from the NFW profile only in the outer parts, where it varies as  $\rho(r) \propto r^{-4}$ .

$$\rho(r) = \frac{\rho_s}{\frac{r}{R_s} \left(1 + \frac{r}{R_s}\right)^3} \quad (1.3.2)$$

In addition to the DM halo, galaxies host an additional spheroidal component known as the stellar halo. The stellar populations in these outer galactic components provide a unique window into the galaxies' merger histories. The composition of the stellar halo is often composed of the oldest and metal-poor stars, providing a snapshot of the early evolutionary history of the galaxies. According to the  $\Lambda$ CDM model, halos grow mainly by merging with smaller subhalos, while the disk of the galaxy undergoes kinematic heating. As a result, the stellar halo takes on a diffuse structure that is intimately linked to the growth and assembly history of the halo system. Stellar halos often exhibit low surface brightness, reaching about  $\mu_r \sim 31$  mag arcsec $^{-2}$ , and are often well described by a power-law density profile of  $r^{-3}$  (Zibetti et al., 2004). Furthermore, studies by Monachesi et al. (2016, 2019) of six Milky Way-mass disk galaxies from the GHOST survey showed that these galaxies extend to about  $\sim 50$  kpc to 70 kpc. This extension is correlated with their mass, with massive disk galaxies having very extended stellar envelopes beyond the region where the disk dominates. The accreted stellar mass in the halo is also correlated with metallicity, with massive halos tending to have higher metallicities. This can be attributed to the fact that most of their stars are derived from a more massive, metal-rich progenitor (e.g. Harmsen et al., 2017; D'Souza & Bell, 2018; Monachesi et al., 2019). Therefore, the stars in a halo are mainly contributed by the largest (one or a few) merger partners. The disruption of satellite galaxies in the stellar halo by the host tidal field results in significant substructure. This includes extended stellar streams and small satellite galaxies (e.g. Johnston et al., 1996; Helmi & White, 1999; Bullock & Johnston, 2005; Cooper et al., 2010; Gómez et al., 2010, 2013; Belokurov & Kravtsov, 2022). In addition, stellar halos exhibit substantial halo-to-halo variations in their properties due to stochastic variations in their merger history (e.g. Bullock & Johnston, 2005; De Lucia & Helmi, 2008; Cooper et al., 2010; Gómez et al., 2012; Tissera et al., 2012, 2013, 2014; Monachesi et al., 2019, 2016). The Milky Way's halo has been extensively studied to unravel its history and its interactions with neighboring galaxies. In particular, some observational and theoretical analyses have focused on our neighboring galaxies, one of them being the Large Magellanic Cloud (LMC), and its interactions with our Milky Way. These studies have provided compelling evidence that advances our understanding of the galactic halo and sheds light on the complex interaction history of the Milky Way and its neighboring galaxies (e.g. Weinberg, 1995; Kalberla & Dedes, 2008; Gómez et al., 2015; Garavito-Camargo et al., 2019; Besla et al., 2019; Patel et al., 2020). Despite these advances, their nature, distribution, and connection to the baryonic and dark matter in galactic halos remain active areas of research. In this Thesis, we explore the complex influence of the dark matter halo on the morphology of disk galaxies.

## 1.4 Perturbations in disk galaxies

Spiral galaxies evolve continuously, exposed to various perturbations. These perturbations arise from interactions with neighboring galaxies, gravitational torques from perturbed dark matter halos, internal processes within the galaxy itself, among other relevant mechanisms. Their deep influence reverberates through galaxy formation histories, triggering alterations in morphology, size, and rotational features. The comprehensive study of the perturbations within disk galaxies is of paramount importance, providing insights into their evolution and formation. In particular, it allows us to explore the merger history of galaxies and reveal the distribution of the dark matter that surrounds their baryonic components. In this section, we delineate two distinct categories of perturbations: those that arise within the galactic plane and those that manifest within the galactic halo.

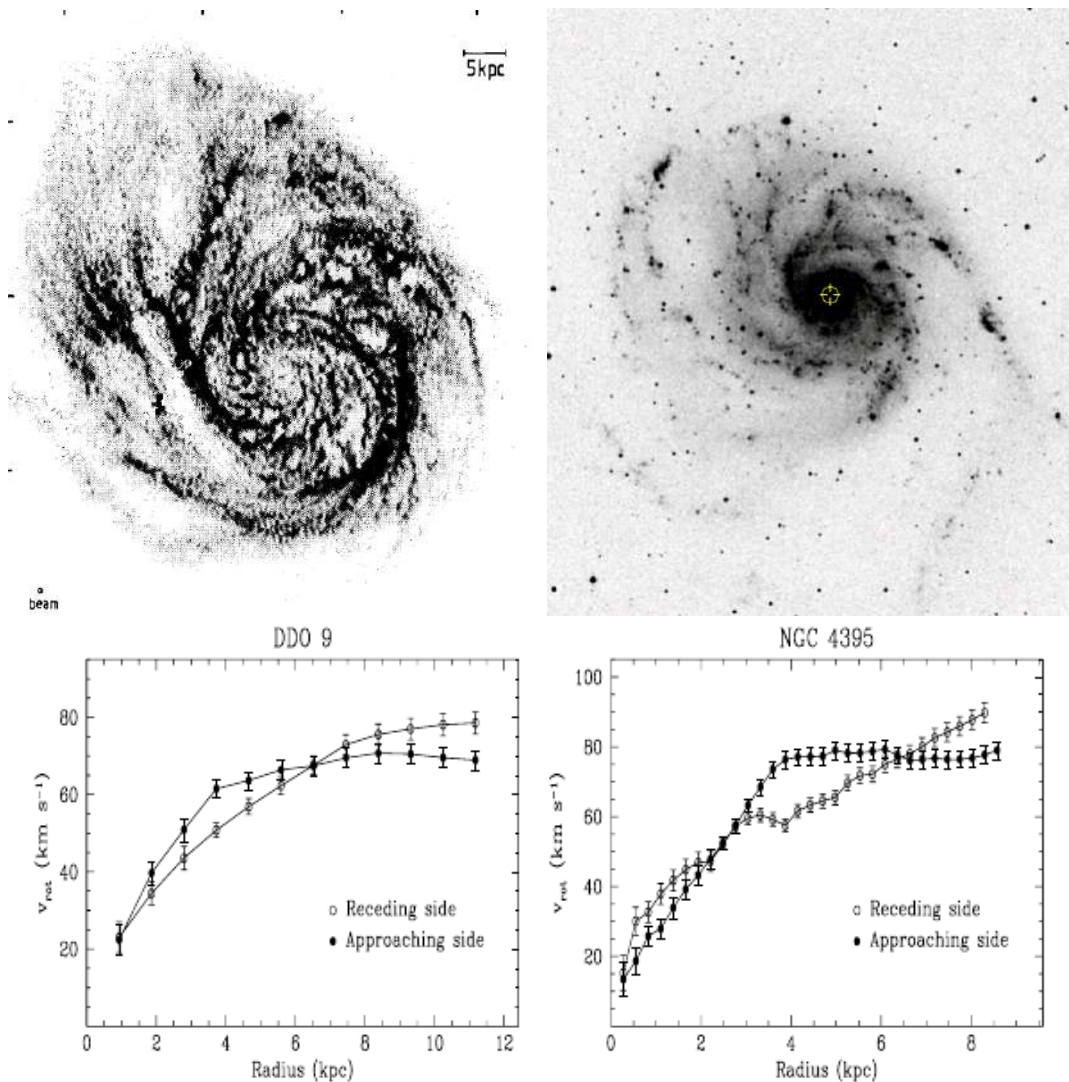


Figure 1.4.1: The lopsided galaxy M101 in their HI distribution (left panel) and stars distribution (right panel). Credits: Jog & Combes (2009) and Swaters et al. (1999)

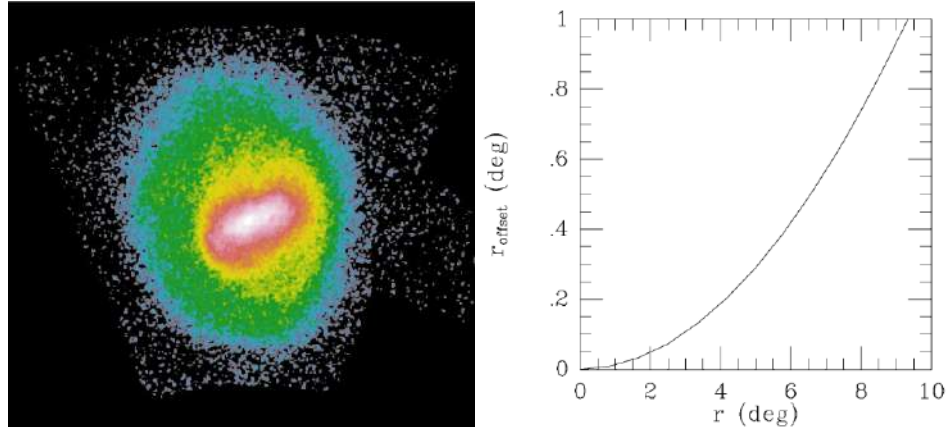


Figure 1.4.2: Surface number density distribution on the sky of RGB and AGB stars in the LMC from 2MASS and DENIS data (left panel). The distance  $r_{\text{offset}}$  by which the center shifts depends on the semimajor-axis (right panel). Credits: van der Marel (2001)

Within the galactic plane, different types of perturbations can occur, both in the in-plane distribution and in the vertical distribution. Such perturbations include lopsidedness, lopsided bars, warps, vertical corrugations, rings, among others. A lopsided galaxy displays an uneven disk mass distribution, with one side extending farther than the other. This asymmetry can be seen in both the gas and stellar distributions (see Figure 1.4.1). One of the first studies of these perturbations were presented by Baldwin et al. (1980), who proposed a model to explain the rotation of matter and its long-lasting perturbation. They based their model on a sample of 20 lopsided galaxies in the HI distribution. The lopsidedness could have significant effects on the dynamics and evolution of the galaxy, including its star formation and black hole growth (Jog & Combes, 2009). In fact, (Dolfi et al., 2023) found that simulated Milky Way-like galaxies that are lopsided in their stellar distribution have a significantly different star forming history compared to non-lopsided galaxies. The kinematics of lopsided galaxies also result in an asymmetric rotation curve (see the bottom panels in Figure 1.4.1). This asymmetry is often measured using the  $m=1$  Fourier amplitudes ( $A_1$ ) in the stellar surface mass density (Rix & Zaritsky, 1995; Zaritsky & Rix, 1997; Quillen et al., 2011). Early studies found that about 30 percent of late-type galaxies in the nearby Universe have this perturbation (Zaritsky & Rix, 1997; Bournaud et al., 2005). This suggests that lopsidedness is a common perturbation. Furthermore, as we will show later in Chapter 4, this morphological asymmetry could provide information about the distribution of their dark matter halo, suggesting an interesting galaxy-halo connection. The inner regions of disk galaxies can also show asymmetric distributions. For example, the bar in the Large Magellanic Cloud (LMC) (Fig. 1.4.2) is considered to be lopsided because of its off-center position with respect to the disk (van der Marel, 2001; Jacyszyn-Dobrzaniecka et al., 2016). It also appears to be asymmetric in its intrinsic shape. The strength of the bar in spiral galaxies can be estimated by the  $m=2$  Fourier amplitude, while the lopsided distribution of the bar can be measured by the odd modes of the Fourier amplitudes (e.g.,  $m=1, 3, 5$ ). A recent study by Łokas (2021) using the TNG100 simulation from IllustrisTNG (see Section 2.2) found that the asymmetry of bars is a long-lived feature. They also suggested two scenarios for the formation of lopsided bars: one involving a disk galaxy interacting with a massive companion, and the other involving an off-center disk with respect to its dark matter halo. According to the authors, the latter scenario is likely to be the most probably. Regarding vertical perturbations, warps are deformations in the outer parts of disk galaxies that are per-

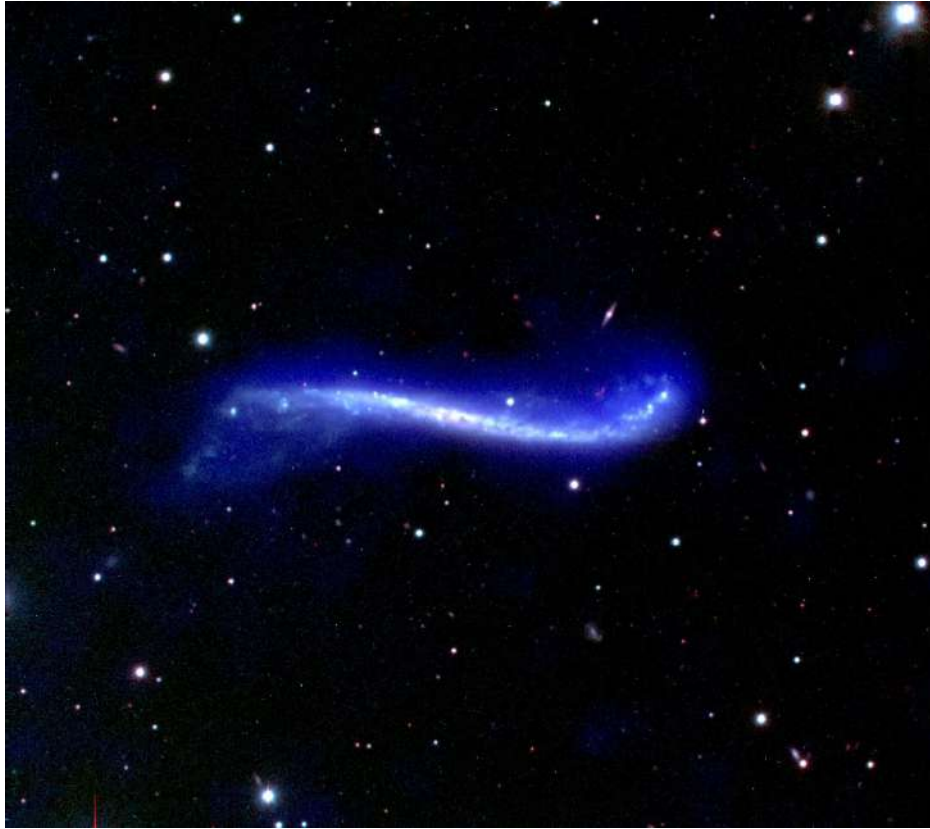


Figure 1.4.3: UGC 3697, the “Integral Sign” galaxy, presents an edge-on spiral configuration marked by a distinct warp in both its stellar and gaseous discs. Its neutral hydrogen gas, depicted in blue, overlays an optical star image. Unusual to typical spiral galaxies, the highest concentration of neutral hydrogen is not situated near the galaxy’s center but along its western periphery, where the Very Large Array (VLA) has identified a prominent, expansive emission zone. Moreover, gas plumes extend significantly above and below the galactic disc. Credit: NRAO/AUI/NSF

pendicular to the disc’s plane (see Fig. 1.4.3). They are often observed in both neutral hydrogen (HI) and optical light (Bosma, 1981; García-Ruiz et al., 2002). Warps can manifest as bending or twisting of the disk plane. The study of warps is important because it can provide insights into galaxy formation, interactions, dynamics, and mass distribution. Our current understanding of warps comes from statistical analyses of observations and simulations, which have revealed a wide range of amplitudes and characteristics. Early studies suggested that around 50 percent of stellar disks exhibit warps (Sánchez-Saavedra et al., 1990). However, more recent analyses indicate that the prevalence of warps is higher, with approximately 70 percent of galaxies displaying warps and other vertical perturbations (Reshetnikov & Combes, 1998; Ann & Park, 2006; Gómez et al., 2017). The recurring occurrence of warps suggests that they are either continuously regenerated or are long-lasting perturbation (Sellwood, 2013a). Warps can have a complex nature, and the observational characterization can be challenging. Their measurement of their main properties can be affected by factors such as such as inclination, measurement techniques, and morphology. Traditionally, two types of warp morphology have been identified: U-shaped and S-shaped warps, with the latter being the most common. However, there is another type of vertical perturbation known as the

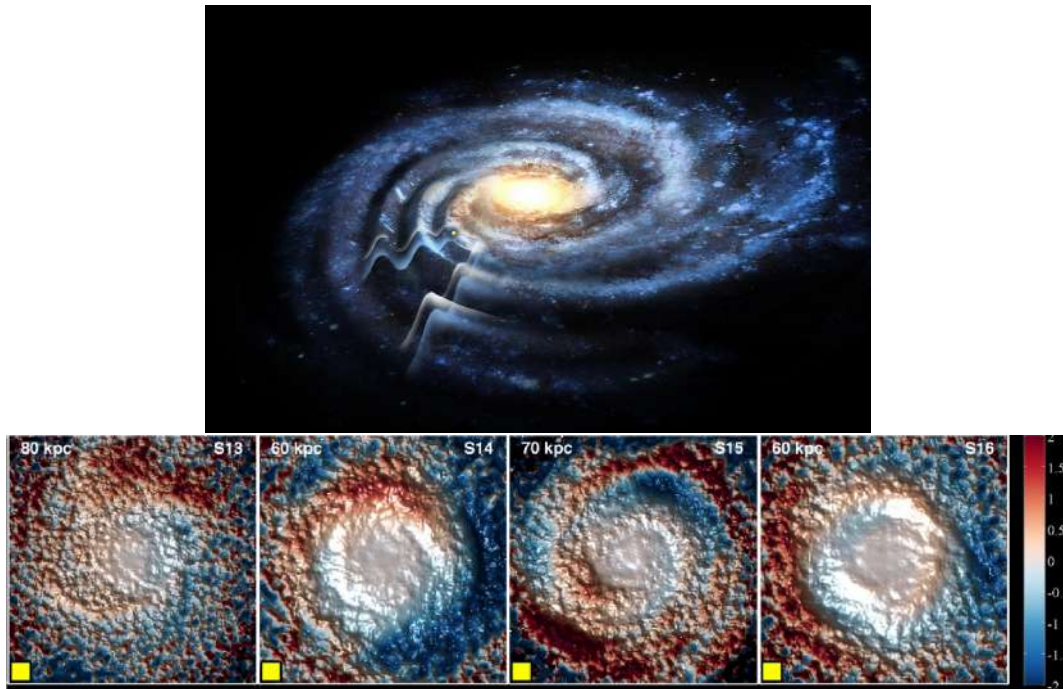


Figure 1.4.4: Representation of the corrugation pattern in the Milky Way disk (top panel). Maps of the mass-weighted mean height of the galaxies in the simulated disk with a corrugated pattern (bottom panels). Credits: Rensselaer Polytechnic Institute and Gómez et al. (2017), respectively.

corrugation pattern (Fig. 1.4.4). This pattern involves an extended and oscillatory vertical displacement of the disk with respect to the overall midplane of the disc. The importance of understanding corrugation patterns in the context of galaxy dynamics is evident from studies based on cosmological simulations (Gómez et al., 2016, 2017). These simulations suggest that corrugation patterns are expected to be prevalent in late-type galaxies. Evidence for more complex corrugation patterns in external galaxies remains very limited (Fridman et al., 1998; Alfaro et al., 2001; Sánchez-Gil et al., 2015; Gómez et al., 2021; Urrejola-Mora et al., 2022). This is because the morphological signatures of corrugation patterns can be diluted due to projection effects, regardless of the disc’s inclination. A methodology that can be used to unveil corrugation patterns is to analyze line-of-sight velocity fields,  $V_{\text{los}}$ . This approach takes advantage of the expected phase difference of approximately 90 degrees between the local disc’s mean height ( $\langle Z \rangle$ ) and mean vertical velocity ( $\langle V_z \rangle$ ). In a recent study, Gómez et al. (2021) used this methodology to analyze the 2D  $V_{\text{los}}$  field of the late-type galaxy VV304a, obtained through  $H_\alpha$  Fabry–Perot observations. They found coherent and global motions consistent with corrugation patterns for VV304a galaxy. Urrejola-Mora et al. (2022) followed this method to analyze a sample of 40 nearby low-inclination disk galaxies, using  $H_\alpha$  Fabry-Perot observations from the Waves in Nearby Disk galaxies Survey (WiNDS), and found 8 new vertically perturbed galactic discs. Particularly, the Milky Way galaxy present a ring structure called as Monoceros ring, which exhibits stream-like features and sharp edges formed by passing a satellite. Later studies linked this structures with a corrugation pattern that covers the outer disk structure ( $R_{\text{gal}} \gtrsim 6$  kpc), which could have been induced by the recent interaction between the Milky Way and its satellite galaxy, the Sagittarius dwarf (Gómez et al., 2016; Laporte et al., 2018b,a). These studies provide new insights into the nature of corrugation patterns in spiral galaxy discs. Further research is

needed to understand the formation and evolution of these patterns, and their role in galaxy dynamics. Ring galaxies offer a unique glimpse into galactic dynamics. They feature a distinctive circular arrangement of stars and gas encircling a central nucleus. Ring galaxies can be formed by two main mechanisms (Few & Madore, 1986): interactions or mergers with companion galaxies (P-types), or gas accumulation at Lindblad resonances under the continuous influence of gravity torques from the bars (O-type). These structures provide a valuable lens through which to understand the complex forces shaping galaxy formation and evolution. Ring galaxies are identified by analyzing their radial flux profile and distinguishing them from other morphological structures. Studying ring galaxies is important to understand the formation and evolution of galaxies. They provide information about the physical features of galaxies, such as their star forming history and dynamical structure. Hydrodynamical simulations, such as the EAGLE simulations, have revealed that many ring galaxies emerge from interactions with companion galaxies, where the drop-through collision with the companion(s) is responsible for diluting the metallicity and pressure of the gas, forming the ring structure (Elagali et al., 2018). This deepens the understanding of the complex interplay between gravitational forces, gas dynamics, and stellar processes, enhancing our knowledge of galactic evolution.

Stellar streams are fossil signatures of accretion events, which can be used to study the merging history of host galaxies. In observational surveys, the detection of external galaxies is often based on surface brightness maps obtained from integrated photometry, and the frequency of detection depends on the limiting surface brightness. In particular, for the Milky Way, the detection can be done photometrically, through color-magnitude diagrams, analyzing the phase-space distributions of large number of stars (Gaia Collaboration et al., 2018), or chemically, thanks to large samples of stars observed spectroscopically (Bundy et al., 2014; Sánchez et al., 2023). In theoretical studies, cosmological simulations are used to interpret observations and connect observable quantities with the accretion history of galaxies. For example, a study by Vera-Casanova et al. (2022) used hydrodynamical cosmological simulations from the Auriga project (Grand et al., 2017) to analyze the information that can be extracted from the brightest streams progenitors (BSP) in each halo in regards to their host merging activity. They noted that stellar streams are not detectable at surface brightness levels  $\leq 25$  mag arcsec $^{-2}$ , becoming discernible between 28 and 29 mag arcsec $^{-2}$ . BSPs stem from diverse infall times spanning 1.6 to 10 Gyrs ago, with a majority formed through early accretion events, while only 25 percent occurred in the past 5 Gyr. Additionally, they observed that BSPs with larger infall masses tend to be accreted during later times, and in the majority of cases, they do not constitute the primary contributor to the accreted stellar halo within their galaxy sample.

In our own Galaxy, we can see the field of streams, shown in Figure 1.4.5. This picture was taken by Belokurov et al. (2006), who analyzed data from the Sloan Digital Sky Survey II (SDSS-II). The area is named “field of streams” for its numerous crossing trails of stars. The Field of Streams is dominated by the Sagittarius Stream, which originates from the Sagittarius Dwarf Elliptical Galaxy. This stream is a product of multiple orbits around the Milky Way Galaxy, and it exhibits a bifurcated nature. The overlapping of the Sagittarius Stream with other stellar streams has provided invaluable insights into the structural organization of dark matter within the inner halo of the Milky Way. The stream’s bifurcated nature suggests that the dark matter distribution is spherical, rather than the flattened spheroid that was previously expected (Fellhauer et al., 2006). Recent studies, however, yielded divergent findings (Vasiliev et al., 2021)

However, not only does baryonic matter exhibit perturbations in its distribution within the halo. The

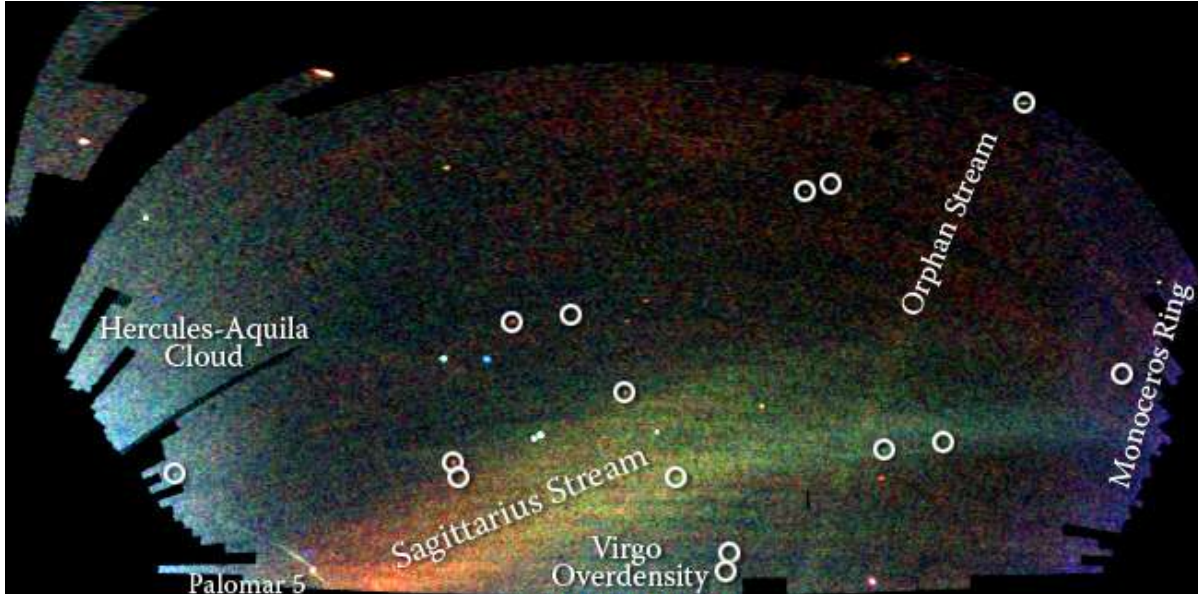


Figure 1.4.5: A map of stars in the outer regions of the Milky Way Galaxy, extracted from SDSS images capturing the northern sky, displayed in a projection reminiscent of Mercator. The color corresponds to star distance, while the brightness signifies star density across the celestial expanse. Notable features depicted in this visualization encompass streams of stars that have been dislodged from the Sagittarius dwarf galaxy, a smaller 'orphan' stream intersecting the Sagittarius streams, the 'Monoceros Ring' encircling the Milky Way's disc, pathways of stars being stripped from the Palomar 5 globular cluster, and aggregations of stars in excess within the Virgo and Hercules constellations. Enclosed circles highlight newfound companions of the Milky Way, ascertained through the SDSS; these include faint globular star clusters and modest dwarf galaxies. Credit: V. Belokurov and the Sloan Digital Sky Survey.

dark matter halo can also be perturbed by merger events or by the passage of a satellite, for example. Regarding the latter, satellite galaxies orbiting within the dark matter halos of their hosts can induce perturbations through dynamical friction (Chandrasekhar, 1943). Satellite galaxies have been studied to generate density wakes through direct gravitational interactions between particles. These interactions cause the satellite to lose angular momentum and energy (Binney & Tremaine, 2008). Tremaine & Weinberg (1984) found that local gravitational scattering is a response to the resonant nature of the system, in which resonances occur between the orbital frequencies of the dark matter particles in the halo and the satellite galaxy. These resonances can induce a global exchange of angular momentum from the satellite to the dark matter halo (White, 1983; Weinberg, 1998). In its first orbit around a host galaxy, the satellite produces the classical conic wake (Chandrasekhar, 1943). As the satellite continues to orbit the host galaxy, the orbital frequencies of its DM particles narrow, leading to resonances at specific frequencies. The conic wake weakens, and these resonances create overdensities and underdensities within the dark matter halo, affecting its kinematics. In Garavito-Camargo et al. (2019) these perturbations are identified as the Transient Response and the Collective Response. The first corresponds to the classical Chandrasekhar wake (described in Chandrasekhar, 1943) that follows the satellite galaxy. The collective response is described as the overdensities and underdensities that do not trail the satellite, but are generated mainly by the center of mass (COM) displacement of the halos. In particular, Garavito-Camargo et al. (2019)

used eight N-body simulations to explore the global patterns of density and kinematic perturbations in the stellar halo that are correlated with the orbital motion of the LMC-MW system and the identification of the LMC dark matter wake. The associated torque of the wake, exerted on the embedded disc, can lead to the formation of morphological disturbances seen in this section, such as vertical patterns (warps and corrugation patterns, Weinberg (1998); Gómez et al. (2016); Antoja et al. (2018); Laporte et al. (2018a,b)) and axisymmetric perturbations like lopsidedness (Zaritsky & Rix, 1997; Varela-Lavin et al., 2023). This suggests a strong connection between the kinematics and density distribution of the dark matter halo and the disk galaxy, which we will explore in the next chapters.

## 1.5 This thesis

As we have observed, the distribution of stars in disks provides a valuable tool for understanding the diverse physical processes that shape the different components of a galaxy. For example, they provide insights into the distribution of dark matter, star formation history, metallicity, and chemical distribution. Additionally, they can complement the study of the merger history and dark matter perturbations. In this thesis, our goal is to study phenomena like radial stellar distribution and its different behaviors, seeking connections with the stellar content of the galaxy and its environment. Furthermore, we will investigate the relationship between the galaxy's halo and its disk, focusing on morphological asymmetries. This investigation will shed light on the properties of the dark matter halo, which remains invisible to current light-based observations.

To accomplish this, we have harnessed the power of state-of-the-art cosmological hydrodynamical simulations from prominent projects such as EAGLE, IllustrisTNG, and Auriga. These simulations have proven to be powerful tools for analyzing galaxy evolution in a statistical context. In particular, they allow us to perform a comprehensive analysis of galaxies across different epochs and to explore different components such as metallicity, stellar age, kinematical properties, and positional information of the constituent particles, among others. By exploiting the capabilities of these simulations, we have extensively studied the stellar distributions of central subhalos similar to those of the Milky Way, allowing us to provide essential insights into the relationships we have previously discussed.

In Chapter 2, we provide a comprehensive overview of the simulations employed in this thesis. We explore the pivotal role of cosmological simulations, demonstrating their value as tools that offer crucial insights into the formation and evolution of galaxies. These simulations serve as complements to observational astronomical data, significantly enriching our understanding of the intricate cosmic processes at play. Moreover, we delve into the fundamental characteristics of prominent projects, such as EAGLE, IllustrisTNG, and Auriga, highlighting the strengths and unique attributes of each.

Chapter 3 is dedicated to characterizing the diverse behavior of the outer regions of the radial stellar distribution in disk galaxies within a statistical framework. This chapter explores a variety of properties associated with stellar content, including mono-age distributions, star formation activity, and angular momentum content. Through careful analysis, we unravel the relationship between the stellar content and the diverse outer distributions surrounding disk galaxies. Additionally, we discuss how these distributions are intimately linked to the surrounding galactic environment, further enhancing our comprehension of the complex interplay that shapes these radial stellar distributions.

In Chapter 4, we undertake a thorough analysis of asymmetrical morphologies in disk galaxies, particularly focusing on lopsidedness. Using a carefully selected sample of galaxy models from the IllustrisTNG

project, we perform a detailed statistical analysis. Within this chapter, we meticulously characterize the key physical conditions that give rise to lopsided perturbations, exploring their structural properties, self-gravitational cohesiveness, tidal interactions with massive satellites, dark matter distribution, and angular momentum content. We also study the time evolution of these aspects, unraveling the different processes that govern lopsided galaxies and contrasting them with those that do not exhibit this asymmetry. This analysis provides insights into the structural complexity within disk galaxies, furthering our understanding of their formation and evolution mechanisms.

In Chapter 5, we present our preliminary results, focusing on a sample of disk galaxies with Milky Way-like halos obtained from the Auriga project. To do this, we employ the pyEXP code, a powerful tool that uses Basis Function Expansions (BFE) to decompose the dark matter and stellar disk density components into various modes and radial orders. This method allows us to estimate the gravitational potential energy of particles based on the mass distribution profile. Our research goal is to explore how dark matter overdensity wakes perturb the galaxy's disk, and whether these perturbations are connected to morphological features like lopsidedness and warps. We will study the impact of the torques induced by the wakes in the halo on these asymmetrical features. Through this detailed analysis, we will gain valuable insights into the dynamic interactions that shape the formation and evolution of disk galaxies, as well as their intriguing relationship with the overdensities in their dark matter halos. Finally, in Chapter 6 we summarize the main conclusions of this thesis and discuss future work that could be done to improve our understanding of the matter.

# Chapter 2

## Numerical models of cosmological galaxies

### 2.1 The role of cosmological simulations and some definitions

Cosmological simulations play an important role in contemporary astronomical analysis, providing valuable insights into various areas of astrophysical research. These simulations serve as powerful tools for studying the dynamics and evolution of the universe, facilitating our understanding of a diverse range of astronomical phenomena, among other things, they allow us to study the non-linear interplay that takes between known relevant process during the formation and evolution of galaxies, such as star formation, AGN, supernovae feedback, gas colling, etc. Cosmological simulations also allow us to interpret the gas kinematics within galaxies and their intergalactic medium. The simulations incorporate stellar evolution models allowing to follow the evolution of different stellar populations. Cosmological simulations are a powerfull tool for understanding the distribution and properties of dark matter in the Universe according to the  $\Lambda$ CDM model. By simulating the hierarchical growth of cosmic structure under the influence of the gravitational pull of dark matter, we can gain insight into the large-scale distribution of dark matter halos and their impact on galaxy formation and evolution. In summary, cosmological simulations are an indispensable tool in astronomy, allowing the study of a wide range of astronomical phenomena and the testing of theoretical predictions against observational data. These simulations bridge the gap between theory and observation, advancing our knowledge of the structure, evolution, and fundamental properties of the Universe.

In this Thesis, we use cosmological simulations that use two of the most prominent techniques to model fluid dynamics: the Smoothed Particle Hydrodynamics (SPH) method and the AREPO (Springel, 2010) adaptive mesh method. Smoothed Particle Hydrodynamics (SPH) is based on the representation of the fluid based on a set of discrete particles that carry information about local properties such as density, pressure, and temperature. These particles interact with each other through smoothing functions that allow realistic modeling of the dynamics and evolution of astrophysical systems. An outstanding implementation of SPH in astrophysics is the GADGET-3 code (Springel, 2005), which is used to simulate processes such as the formation of galaxies, the evolution of star clusters. On the other hand, the AREPO is uses a fully dynamic and unstructured mesh, based on a moving and adaptive grid, as opposed to the static grids used in other methods such as adaptive mesh refinement (AMR). This mesh adapts and changes in real time as the simulation evolves. The traditional SPH formulation has certain inherent shortcomings that can lead to inaccurate results, such as the artificial suppression of fluid instabilities. On the other

hand, codes based on Eulerian grids, the most common alternative, also have disadvantages, such as the lack of Galileon invariance in the fixed grids. In contrast, *Arepo*, a novel moving-mesh hydrodynamics code presented by Springel (2010), combines the advantages of SPH, such as Galileo invariance, with accurate resolution of fluid instabilities by solving the Eulerian equations on a mesh that moves with the fluid. Although there are similarities in terms of overall results, such as star formation histories and black hole growth, detailed differences emerge in the gas morphologies between the SPH and *Arepo* simulations, with SPH showing more pronounced hot halos and artificial cluster structures, while *Arepo* exhibits greater effectiveness in dissipating clusters and cooling the gas from the hot halos. These distinctions are crucial when considering the accuracy of the results in astrophysical simulations. However, gas tracking is one of the disadvantages of *AREPO*. In SPH, the gas is represented as a collection of particles, so it is relatively easy to track its motion. In *AREPO*, the gas is represented as an adaptive mesh, and the cells can change shape and size as the gas moves. This can make it difficult to track the motion of the gas over time. Also, *AREPO* could take  $\sim 30$  percent more CPU time than SPH with the same initial number of resolution elements, and both codes start from identical initial conditions Torrey et al. (2012).

In the following sections, we describe the general characteristics of the cosmological simulations used in this Thesis. All the simulations analyzed in this work used the same methodology that was applied to identify halos and their corresponding galaxies. To identify haloes and their associated subhaloes, the Friends of Friends (FoF) algorithm (Davis et al., 1985) and the *SUBFIND* algorithm (Springel et al., 2001; Dolag et al., 2009) are used. FoF is a tool for identifying groups of particles in a simulation. In practice, the FoF algorithm creates networks of linked particles, taking into account a linking length parameter. A given particle is directly bound to all other particles within a distance of the linking length (its friends), and indirectly linked to all particles associated with its friends (its friend-of-friends). For the next simulations, the linking length used is the standard 0.2 times the mean interparticle distance of the dark matter (e.g. Frenk et al., 1988; Lacey & Cole, 1994). The *SUBFIND* algorithm identifies and isolates particles that belong to gravitationally bound structures within each FoF halo. The primary mass component of each subhalo is the dark matter, then the baryons (gas, stars, and black hole particles) are associated with nearest group of dark matter particles. These elements are exclusive to their respective subhalos and do not overlap with material from other subhalos. Galaxies in this context are defined as subhaloes with non-zero stellar mass, excluding those with less than 20 percent of their mass in dark matter (see Section 5.2 of Nelson et al., 2019a). The sample of galaxies in these simulations includes both central and satellite galaxies. A central galaxy typically represents the most massive subhalo within its FoF halo, and may be associated with one or more satellites. Satellites are galaxies identified by the *SUBFIND* algorithm that are part of their parent FoF group, regardless of their radial distance from the group center. Thus, in this thesis, the terms “FoF halo” or “halo” all refer to structures designed by FoF. The terms “subhalo”, “galaxy”, or “satellite galaxy” all refer to substructures identified by *SUBFIND*.

## 2.2 EAGLE simulations.

In this section, we provide a brief summary of the main characteristics of the EAGLE simulations<sup>1</sup> that are used in the Chapter 3. For a more in-depth description of the cosmological simulation, readers can refer to Schaye et al. (2015) and Crain et al. (2015). The EAGLE project is a set of cosmological hydrody-

---

<sup>1</sup><http://eagle.strw.leidenuniv.nl>

namical simulations, each variant varying in terms of volume, numerical resolution, and galaxy formation subgrid models. A modified version of the N-Body Tree-PM Smoothed Particle Hydrodynamics (SPH) code GADGET-3 was used to facilitate the execution of EAGLE (Springel et al., 2005). The modifications include the SPH formulation collectively known as ANARCHY (Schaye et al., 2015; Schaller et al., 2015), the utilization of the  $C_2^2$  kernel from Wendland (1995), the pressure-entropy SPH formulation from Hopkins (2013), the incorporation of time-step limiters by Durier & Dalla Vecchia (2012), the implementation of the artificial viscosity switch by Cullen & Dehnen (2010), and the integration of a mild thermal conduction term following the form proposed by Price (2008).

All simulations adopt a flat  $\Lambda$ -CDM cosmology with parameters taken from the Planck mission (Planck Collaboration et al., 2014):  $\Omega_\Lambda = 0.693$ ,  $\Omega_m = 0.307$ ,  $\Omega_b = 0.04825$ ,  $\rho_8 = 0.8288$ ,  $h = 0.6777$ ,  $n_s = 0.9611$  and  $Y = 0.248$ . In section 1.1, we discuss that  $\Omega_\Lambda$ ,  $\Omega_m$ ,  $\Omega_b$  correspond to the cosmological parameter of the average densities of dark energy, dark matter and baryonic matter in units of the critical density  $z = 0$ ,  $\rho_8$  is the square root of the linear variance,  $h$  is the Hubble parameter ( $H_0 \equiv h \text{ } 100 \text{ km s}^{-1}$ ),  $n_s$  is the scalar power-law index of the power spectrum of primordial perturbations, and  $Y$  is the primordial mass fraction of helium. Initial conditions were formulated using second-order Lagrangian perturbation theory (Jenkins, 2010), supplemented by phase data extracted from the publicly available PANPHISA dataset (Jenkins, 2013). The simulation was run over three cubic periodic volumes with box lengths of 25, 50, and 100 comoving megaparsecs (cMpc), as detailed in Table 2.2.1. Furthermore, both baryonic (gas, stars, and massive black holes) and non-baryonic (dark matter) particles were traced from an initial redshift of  $z = 127$  through to the present day.

Subgrid source and sink terms are implemented in the differential equations for processes not resolved by the numerical scheme. These schemes are as simple as possible, depending only on the local hydrodynamic properties. This ensures that galactic winds develop without pre-determined mass loading factors<sup>3</sup> or directions, and without any direct dependence on halo or dark matter properties. The radiative cooling, at  $T > 10^4$  K, and photoheating implementations are described in Wiersma et al. (2009a) for eleven chemical elements: H, He, C, N, O, Ne, Mg, Si, S, Ca, and Fe, in an element-by-element fashion. Additionally, the time-dependent stellar mass loss due to winds from massive stars and AGB stars, core collapse supernovae, and type Ia supernovae is tracked (Wiersma et al., 2009b). Star formation is implemented stochastically following the pressure-dependent Kennicutt-Schmidt relation (Schaye & Dalla Vecchia, 2008), accounting for a metal-dependent star formation threshold proposed by Schaye (2004), in order to track the transition from warm atomic gas to the unresolved cold molecular gas. The initial stellar mass function is that given by Chabrier (2003). Following the method of Dalla Vecchia & Schaye (2012), the feedback from star formation events is implemented thermally and stochastically. Black holes with mass  $1.48 \times 10^5 M_\odot$  are placed in the centers of haloes greater than a threshold mass  $1.48 \times 10^{10} M_\odot / h$  and tracked following the methodology of Springel et al. (2005) and Booth & Schaye (2009). A modified version of the Bondi-Hoyle accretion rate is implemented for gas accretion onto black holes (Rosas-Guevara et al., 2015; Schaye et al., 2015). The implementation of feedback is performed by employing the stochastic AGN heating scheme described in Schaye et al. (2015), incorporating the energy threshold described by Booth & Schaye (2009).

In Table 2.2.1, we present a summary of the EAGLE database, which includes the comoving cubic

<sup>2</sup>This kernel inhibits particle pairing Dehnen & Aly (2012).

<sup>3</sup>The mass loading factor quantifies the efficiency of outflows in removing gas from the galaxy in comparison to star formation. In low-mass galaxies, outflows can remove up to 10 times more gas than what is converted into stars.

Table 2.2.1: Parameters describing the available simulations. From left-to-right the columns show: simulation name suffix, comoving box size, total number of particles, initial baryonic particle mass, dark matter particle mass, comoving Plummer-equivalent gravitational softening length, maximum physical softening length and the subgrid model parameters that vary:  $n_{\text{H},0}$ ,  $n_{\text{n}}$ ,  $C_{\text{visc}}$ ,  $\Delta T_{\text{AGN}}$  control, the characteristic density and the power-law slope of the density dependence of the energy feedback from star formation, the sensitivity of the BH accretion rate to the angular momentum of the gas, and the temperature increase of the gas during AGN feedback, respectively.

Identifier	L [cMpc]	N	$m_{\text{g}}$ [ $M_{\odot}$ ]	$m_{\text{dm}}$ [ $M_{\odot}$ ]	$\epsilon_{\text{com}}$ [ckpc]	$\epsilon_{\text{phys}}$ [pkpc]
Ref-L0025N0376	25	$2 \times 376^3$	$1.81 \times 10^6$	$9.70 \times 10^6$	2.66	0.70
Ref-L0025N0752	25	$2 \times 752^3$	$2.26 \times 10^5$	$1.21 \times 10^6$	1.33	0.35
Recal-L0025N0752	25	$2 \times 752^3$	$2.26 \times 10^5$	$1.21 \times 10^6$	1.33	0.35
Ref-L0050N0752	50	$2 \times 752^3$	$1.81 \times 10^6$	$9.70 \times 10^6$	2.66	0.70
AGNdT9-L0050N0752	50	$2 \times 752^3$	$1.81 \times 10^6$	$9.70 \times 10^6$	2.66	0.70
Ref-L0100N1504	100	$2 \times 1504^3$	$1.81 \times 10^6$	$9.70 \times 10^6$	2.66	0.70

Identifier	$n_{\text{H},0}$ [ $\text{cm}^{-3}$ ]	$n_{\text{n}}$	$C_{\text{visc}}$	$\Delta T_{\text{AGN}}$ [K]
Ref-L0025N0376	0.67	$2/\ln 10$	$2\pi$	$10^{8.5}$
Ref-L0025N0752	0.67	$2/\ln 10$	$2\pi$	$10^{8.5}$
Recal-L0025N0752	0.25	$1/\ln 10$	$2\pi \times 10^3$	$10^{9.0}$
Ref-L0050N0752	0.67	$2/\ln 10$	$2\pi$	$10^{8.5}$
AGNdT9-L0050N0752	0.67	$2/\ln 10$	$2\pi \times 10^2$	$10^{9.0}$
Ref-L0100N1504	0.67	$2/\ln 10$	$2\pi$	$10^{8.5}$

box length, the baryonic and non-baryonic particle masses, and the gravitational softening lengths. The simulations are identified by their box length (e.g., L0100) and the cube root of the initial number of particles per species (e.g., N1504). For example, a simulation with a box length of 100 cMpc and approximately  $1504^3$  particles is named L0100N1504. Note that simulations with the prefix ‘‘Ref-’’ correspond to the primary run. For these simulations, three box sizes are run: 25, 50, and 100 cMpc, along with three variations of total particles: approximately  $376^3$ , approximately  $752^3$ , and approximately  $1504^3$ . The L0025N0752 simulation was performed with a re-calibrated subgrid model, denoted by the prefix ‘‘Recal-’’. Additionally, the intermediate 50 cMpc simulation was re-run with a modification of the gas temperature rise during AGN feedback,  $\Delta T_{\text{AGN}} = 10^9$  K, the increase of  $\Delta T_{\text{AGN}}$  yield more energetic feedbacks events, resulting in reduced radiative losses, also the ambient density of gas to the central black hole of galaxies is greater than that of star-forming gas distributed throughout their discs. This simulation is denoted by the prefix ‘‘AGNdT9’’.

In Chapter 3, we use the galaxy sample constructed by Tissera et al. (2019) from Ref-L100N1504 simulation. To summarize, this galaxy catalog includes only central galaxies (i.e., no satellite galaxies were included) with more than 1000 baryonic particles and more than 100 star-forming gas particles in the

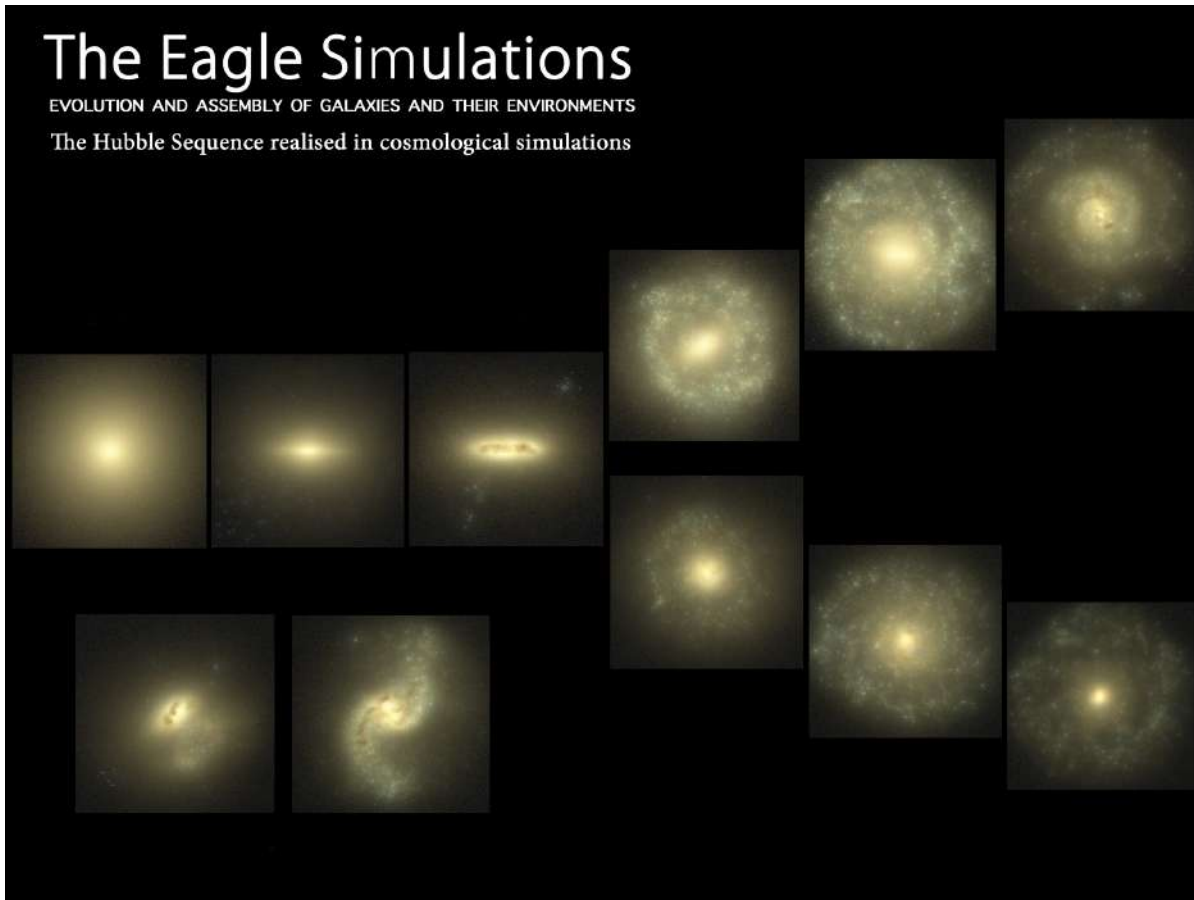


Figure 2.2.1: Sample of galaxies simulated from Ref-L100N1504 EAGLE simulation showing the Hubble sequence. Images are made using a composition of the monochromatic u,g and r band SDSS filters, accounting for dust extinction. Credit: EAGLE Website

disk component, resulting in a sample of 592 discs. The galaxy components have been dynamically decomposed into bulge and disk using the method and criteria described by Tissera et al. (2012).

## 2.3 IllustrisTNG project

In this Section we introduce the numerical simulations considered in the Chapter 4, which are taken from the Illustris-The Next Generation project (IllustrisTNG hereafter Pillepich et al., 2018; Nelson et al., 2018, 2019a; Marinacci et al., 2018; Springel et al., 2018; Naiman et al., 2018).

The IllustrisTNG project is a set of gravo-magnetohydrodynamics cosmological simulation, run with the moving-mesh code Arepo (Springel, 2010). It comprises three large simulation volumes: TNG50, TNG100, and TNG300, enclosing volumes of  $\sim 50^3$  cMpc,  $100^3$  cMpc and  $300^3$  cMpc, respectively (See Fig. 2.3.1). Each volume has a variation that includes baryonic and dark matter particles, and other with only dark matter particles. All TNG simulations are evolved from  $z = 127$  to the present day ( $z = 0$ ) considering the standard  $\Lambda$ CDM model, with parameters based on the Planck Collaboration et al. (2016)

Run	Volume [cMpc <sup>3</sup> ]	$L_{\text{box}}$ [cMpc/h]	$N_{\text{GAS,DM}}$ -	$N_{\text{TRACER}}$ -	$m_{\text{baryon}}$ [ $M_{\odot}/h$ ]	$m_{\text{DM}}$ [ $M_{\odot}/h$ ]	$m_{\text{baryon}}$ [ $10^6 M_{\odot}$ ]	$m_{\text{DM}}$ [ $10^6 M_{\odot}$ ]
TNG50-1	51.7 <sup>3</sup>	35	2160 <sup>3</sup>	1 × 2160 <sup>3</sup>	5.7 × 10 <sup>4</sup>	3.1 × 10 <sup>5</sup>	0.08	0.45
TNG50-2	51.7 <sup>3</sup>	35	1080 <sup>3</sup>	1 × 1080 <sup>3</sup>	4.6 × 10 <sup>5</sup>	2.5 × 10 <sup>6</sup>	0.68	3.63
TNG50-3	51.7 <sup>3</sup>	35	540 <sup>3</sup>	1 × 540 <sup>3</sup>	3.7 × 10 <sup>6</sup>	2.0 × 10 <sup>7</sup>	5.4	29.0
TNG50-4	51.7 <sup>3</sup>	35	270 <sup>3</sup>	1 × 270 <sup>3</sup>	2.9 × 10 <sup>7</sup>	1.6 × 10 <sup>8</sup>	43.4	232
TNG100-1	106.5 <sup>3</sup>	75	1820 <sup>3</sup>	2 × 1820 <sup>3</sup>	9.4 × 10 <sup>5</sup>	5.1 × 10 <sup>6</sup>	1.4	7.5
TNG100-2	106.5 <sup>3</sup>	75	910 <sup>3</sup>	2 × 910 <sup>3</sup>	7.6 × 10 <sup>6</sup>	4.0 × 10 <sup>7</sup>	11.2	59.7
TNG100-3	106.5 <sup>3</sup>	75	455 <sup>3</sup>	2 × 455 <sup>3</sup>	6.0 × 10 <sup>7</sup>	3.2 × 10 <sup>8</sup>	89.2	478
TNG300-1	302.6 <sup>3</sup>	205	2500 <sup>3</sup>	1 × 2500 <sup>3</sup>	7.6 × 10 <sup>6</sup>	4.0 × 10 <sup>7</sup>	11	59
TNG300-2	302.6 <sup>3</sup>	205	1250 <sup>3</sup>	1 × 1250 <sup>3</sup>	5.9 × 10 <sup>7</sup>	3.2 × 10 <sup>8</sup>	88	470
TNG300-3	302.6 <sup>3</sup>	205	625 <sup>3</sup>	1 × 625 <sup>3</sup>	4.8 × 10 <sup>8</sup>	2.5 × 10 <sup>9</sup>	703	3760
TNG50-1-Dark	51.7 <sup>3</sup>	35	2160 <sup>3</sup>	-	-	3.7 × 10 <sup>5</sup>	-	0.55
TNG50-2-Dark	51.7 <sup>3</sup>	35	1080 <sup>3</sup>	-	-	2.9 × 10 <sup>6</sup>	-	4.31
TNG50-3-Dark	51.7 <sup>3</sup>	35	540 <sup>3</sup>	-	-	2.3 × 10 <sup>7</sup>	-	34.5
TNG50-4-Dark	51.7 <sup>3</sup>	35	270 <sup>3</sup>	-	-	1.9 × 10 <sup>8</sup>	-	275
TNG100-1-Dark	106.5 <sup>3</sup>	75	1820 <sup>3</sup>	-	-	6.0 × 10 <sup>6</sup>	-	8.9
TNG100-2-Dark	106.5 <sup>3</sup>	75	910 <sup>3</sup>	-	-	4.8 × 10 <sup>7</sup>	-	70.1
TNG100-3-Dark	106.5 <sup>3</sup>	75	455 <sup>3</sup>	-	-	3.8 × 10 <sup>8</sup>	-	567
TNG300-1-Dark	302.6 <sup>3</sup>	205	2500 <sup>3</sup>	-	-	7.0 × 10 <sup>7</sup>	-	47
TNG300-2-Dark	302.6 <sup>3</sup>	205	1250 <sup>3</sup>	-	-	3.8 × 10 <sup>8</sup>	-	588
TNG300-3-Dark	302.6 <sup>3</sup>	205	625 <sup>3</sup>	-	-	3.0 × 10 <sup>9</sup>	-	4470

Run	$\epsilon_{\text{DM},*}^{z=0}$ [kpc]	$\epsilon_{\text{DM},*}$ [ckpc/h]	$\epsilon_{\text{gas,min}}$ [ckpc/h]	$r_{\text{cell,min}}$ [pc]	$\bar{r}_{\text{cell}}$ [kpc]	$\bar{r}_{\text{cell,SF}}$ [pc]	$\bar{n}_{\text{H,SF}}$ [cm <sup>-3</sup> ]	$n_{\text{H,max}}$ [cm <sup>-3</sup> ]
TNG50-1	0.29	0.39 → 0.195	0.05	8	5.8	138	0.8	650
TNG50-2	0.58	0.78 → 0.39	0.1	19	12.9	282	0.7	620
TNG50-3	1.15	1.56 → 0.78	0.2	65	25.0	562	0.6	80
TNG50-4	2.30	3.12 → 1.56	0.4	170	50.1	1080	0.5	35
TNG100-1	0.74	1.0 → 0.5	0.125	14	15.8	355	1.0	3040
TNG100-2	1.48	2.0 → 1.0	0.25	74	31.2	720	0.6	185
TNG100-3	2.95	4.0 → 2.0	0.5	260	63.8	1410	0.5	30
TNG300-1	1.48	2.0 → 1.0	0.25	47	31.2	715	0.6	490
TNG300-2	2.95	4.0 → 2.0	0.5	120	63.8	1420	0.5	235
TNG300-3	5.90	8.0 → 4.0	1.0	519	153	3070	0.4	30

Table 2.3.1: Table of physical and numerical parameters for each volume variation of TNG simulations. The physical parameters are: the box volume, the box side-length, the initial number of gas cells, dark matter particles, and Monte Carlo tracer particles. The target baryon mass, the dark matter particle mass, the  $z = 0$  Plummer equivalent gravitational softening of the collisionless component, the same value in comoving units, and the minimum comoving value of the adaptive gas gravitational softenings. Additional characterizations of the gas resolution, measured at redshift zero: the minimum physical gas cell radius, the median gas cell radius, the mean radius of star-forming gas cells, the mean hydrogen number density of star-forming gas cells, and the maximum hydrogen gas density

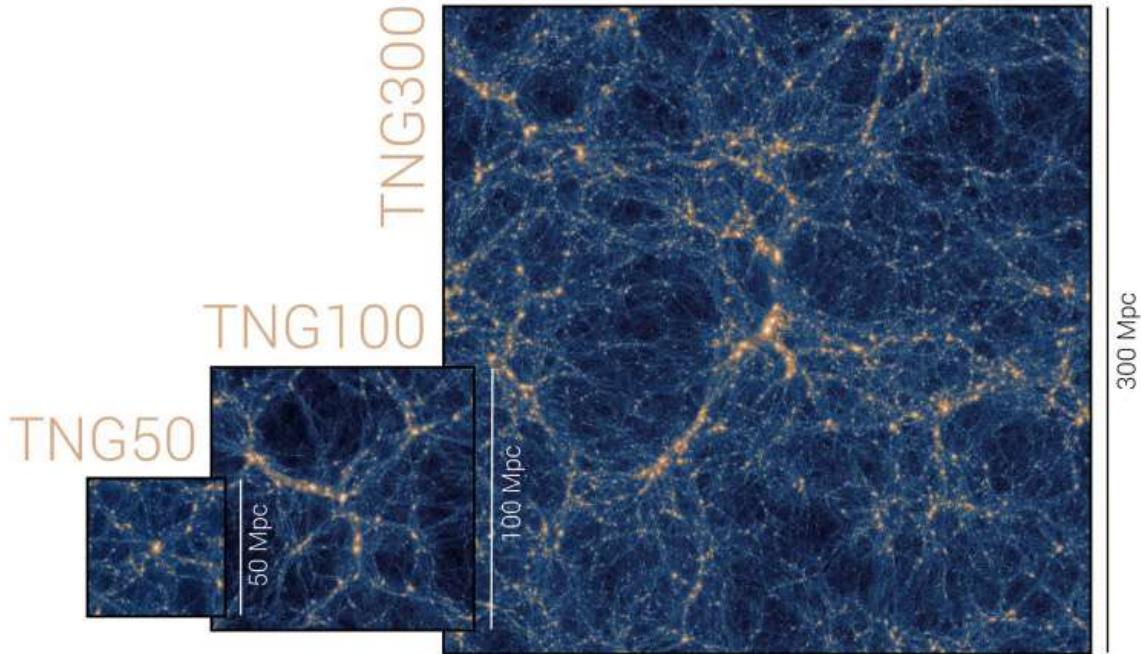


Figure 2.3.1: The three IllustrisTNG simulation volumes: TNG50, TNG100, and TNG300. The images show dark matter density distribution. Credit: TNG Collaboration.

results:  $\Omega_m = 0.3089$ ,  $\Omega_\Lambda = 0.6911$ ,  $\Omega_b = 0.0486$ ,  $h = 0.6774$ ,  $\sigma_8 = 0.8159$ ,  $n_s = 0.9667$ , with Newtonian self-gravity solved in an expanding Universe. In the table 2.3.1, we show a summary of the physical and numerical parameters for each of the resolution levels of the three flagship TNG simulations. TNG300 is the largest volume simulation of the project. It allows to study galaxy clustering and provides unparalleled statistics of the galaxy population as a whole. On the other hand, TNG50 is the highest mass resolution of the project, allowing the study small-scale structures, such as galaxies, in great detail (Nelson et al., 2019b).

The IllustrisTNG<sup>4</sup> is the successor of the Illustris project (Vogelsberger et al., 2014b,a; Genel et al., 2014; Nelson et al., 2015), containing updated models for the physical processes that are relevant for galaxy formation and evolution. The galaxy formation model includes several key components, such as stochastic star formation based on gas density thresholds, the evolution of mono-age stellar populations represented by stellar particles, chemical enrichment of the interstellar medium (ISM) tracing nine different chemical elements (H, He, C, N, O, Ne, Mg, Si, Fe), and total gas metallicity. It also includes processes such as gas cooling, heating, and feedback from supernovae in the form of galactic winds. Furthermore, the model considers the seeding and growth of supermassive black holes, and the injection of energy and momentum from these black holes into the surrounding gas. All aspects of the model, including parameter values and the simulation code, are thoroughly detailed in the two IllustrisTNG method papers (Weinberger et al., 2017; Pillepich et al., 2018) and remain entirely unchanged for our production simulations. One specific numerical adjustment has been implemented for the TNG50 simulation, involving a modification to the effective equation of state of star-forming gas. This change aims to rapidly convert high-density gas into

<sup>4</sup><https://www.tng-project.org>

Table 2.4.1: Summary of the numerical resolution for each level in Auriga project. The columns are: resolution “level” of the run, dark matter particle mass, baryonic target particle/cell mass, softening length, and the number of simulations available to the date (December 2023).

Level	$m_{DM}$ ( $M_{\odot}$ )	$m_b$ ( $M_{\odot}$ )	$h_b$ (pc)	$n_{sim}$
2	$4.6 \times 10^3$	$8.5 \times 10^2$	94	1
3	$3.6 \times 10^4$	$6.7 \times 10^3$	188	7
4	$2.9 \times 10^5$	$5.4 \times 10^4$	375	39
5	$2.4 \times 10^6$	$4.4 \times 10^5$	750	5
6	$2.0 \times 10^7$	$4.2 \times 10^6$	1500	1

stars and thus avoid time steps as small as 10 years at the TNG50 resolution. Importantly, this adjustment is motivated solely by numerical considerations and does not impact galactic properties or statistics at any cosmic epoch (refer to Section 2.2 of Nelson et al. (2019a) for comprehensive details).

In this thesis, we focus on the model TNG50-1 (Pillepich et al., 2019; Nelson et al., 2019b) and its dark matter only counterpart. TNG50-1 (hereafter TNG50) is the highest resolution run within the TNG project. Its high resolution allows us to better analyze the azimuthal distribution of stellar mass in the outskirts of Milky Way-like galaxies.

## 2.4 Auriga project

In chapter 5 we explore the dark matter halos simulated as part of the Auriga project (Grand et al., 2017). The Auriga project provides simulations at 5 different resolution levels (Level 2, 3, 4, 5, and 6). The characteristics and differences between the resolution levels are summarized in Table 2.4.1. In Chapter 5 of this Thesis, we focus on the level 3 resolution simulation, which gives access to halos (Fig. 2.4.1). At this resolution, the simulation has  $3.6 \times 10^4$  and  $6.7 \times 10^3 M_{\odot}$  per dark matter and baryonic particle, respectively, with a softening length of 188 pc.

The Auriga simulations consist of cosmological zoom-in re-simulations focused on haloes with virial masses in the range of 1 to  $2 \times 10^{12}$  solar masses. These halos are initially identified as isolated on the  $z = 0$  snapshot of the L100N1504 dark matter-only simulation of the EAGLE project (Schaye et al., 2015). Initial conditions for the zoom re-simulations were set at  $z = 127$  following the Zel’dovich (1970) approximation, the procedure for which is outlined in Jenkins (2010) and adopting the cosmological parameters provided by Planck Collaboration et al. (2014):  $\Omega_m = 0.307$ ,  $\Omega_b = 0.048$ ,  $\Omega_{\Lambda} = 0.693$ ,  $n_s = 0.9611$ ,  $\rho_8 = 0.8288$ ,  $Y = 0.248$ , and a Hubble constant of  $H_0 = 100h \text{ km s}^{-1} \text{ Mpc}^{-1}$ , where  $h = 0.6777$ . The halos are then re-simulated with full baryonic physics, with improved resolution around the primary halo.

These simulations were conducted using the magnetohydrodynamic (MHD) code AREPO (Springel 2010) and a comprehensive galaxy formation model, as described in Vogelsberger et al. (2013); Marinacci et al. (2014); Grand et al. (2016). Gravitational and collisionless dynamics are estimated by standard Tree-PM method (e.g. Springel, 2005) and discretized the MHD equations on a dynamic unstructured Voronoi

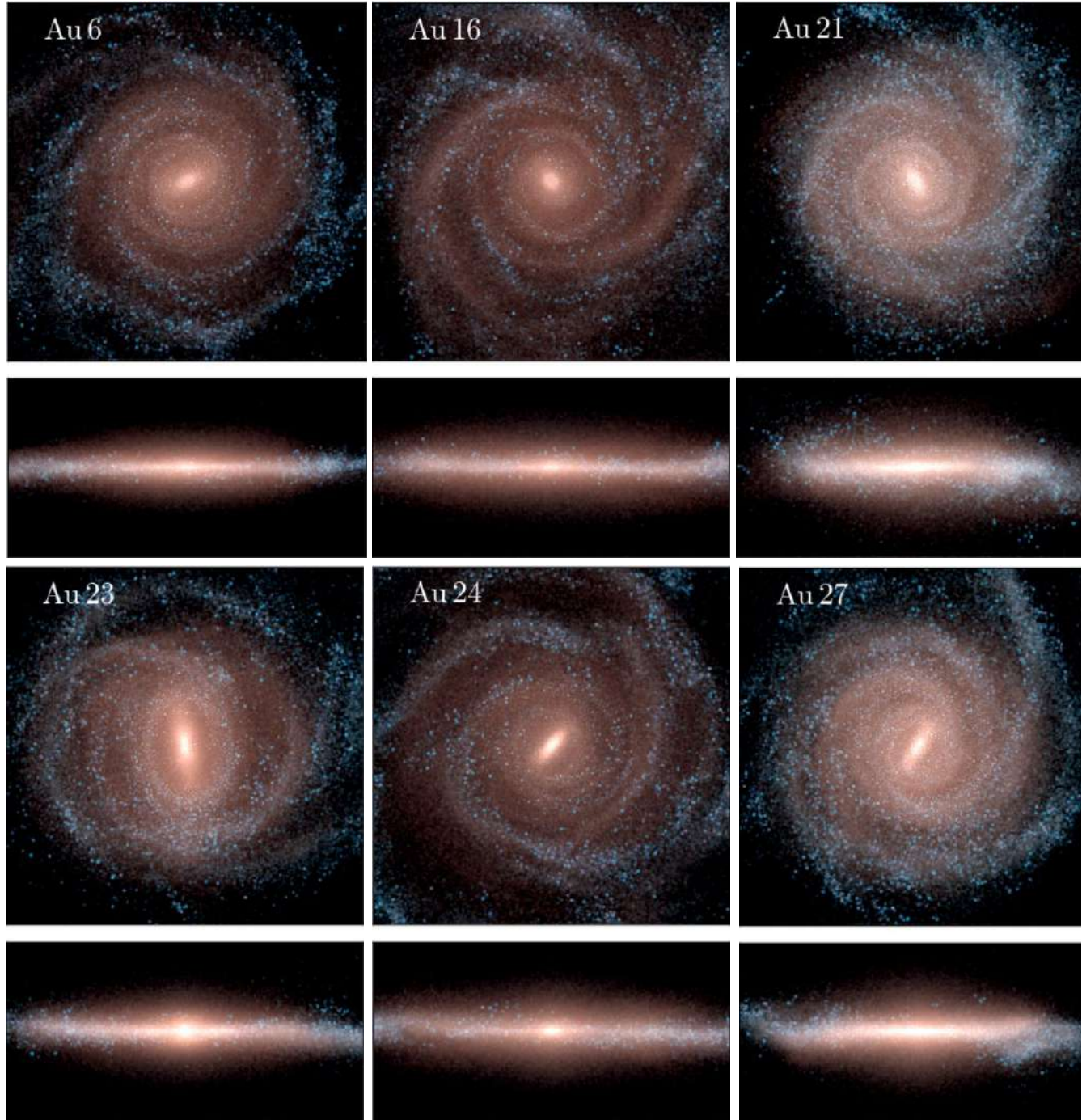


Figure 2.4.1: The face-on and edge-on projected stellar density at  $z = 0$  for level 3 simulations from Auriga project (simulation used in chapter 5). The images are performed from a projection of the K-, B- and U-band luminosity of stars. Younger (older) star particles are therefore represented by bluer (redder) colours. The plot dimensions are  $50 \times 50 \times 25$  kpc. Credit: Grand et al. (2017)

mesh. That equations are solved with a second-order Runge-Kutta integration (Pakmor et al., 2016). The gravitational formation model encompasses various elements such as atomic and metal-line cooling (Vogelsberger et al., 2013), a spatially uniform UV background (Faucher-Giguère et al., 2009), a subgrid model for the interstellar medium and star formation (Springel & Hernquist, 2003), magnetic fields, and self-consistent stellar evolution, including metal enrichment from various sources.

As in other models, each star particle represent a single stellar population (SSP), which is characterized by a given age and metallicity. The initial stellar mass function that is include for each SSP is given by Chabrier (2003). The galaxy formation model used for this simulations incorporates feedback from core collapse supernovae through a non-local effective wind model that transports energy, mass, metals, and momentum from star-forming regions. The model also accounts for the growth, feedback, and seeding of supermassive black holes (Springel, 2005). Gas accretion onto black holes is determined by the Bondi–Hoyle–Lyttleton model (Bondi & Hoyle, 1944; Bondi, 1952), while thermal energy feedback is injected into surrounding gas cells. Thermal energy is also provided to create hot gas bubbles in the halo, based on the model of Nulsen & Fabian (2000). The mass and metals are then distributed among nearby gas cells with a top-hat kernel. A total of nine elements are tracked: H, He, C, O, N, Ne, Mg, Si, and Fe. The Auriga model has demonstrated its ability to generate realistic spiral disk galaxies that align well with various observations. These include factors such as the star formation histories, stellar masses, sizes, and rotation curves of Milky Way-sized galaxies (Grand et al., 2017), the characteristics of stellar halos in local galaxies Monachesi et al. (2019), their HI gas distribution Marinacci et al. (2017), the occurrence and main properties of stellar disk warps Gómez et al. (2017), the attributes and prevalence of galactic bars (Fragkoudi et al., 2020) and bulges (Gargiulo et al., 2019), as well as the properties of magnetic fields within nearby disk galaxies (Pakmor et al., 2017, 2018).

Overall, the AURIGA simulations provide a detailed and comprehensive approach to understanding the formation and evolution of galaxies within a cosmological context. In chapter 5, we analyse the level 3 of resolution in Auriga project, which is a set of six fully cosmological magnetohydrodynamical simulations Milky Way-like galaxies. This simulation have around  $\sim 10^3 M_{\odot}$  of baryonic mass resolution and  $\sim 10^4 M_{\odot}$  of dark matter resolution, which it is a perfect set of galaxies to study the stellar and dark matter components with a great detail.

## 2.5 Resolution and numerical heating

In N-body simulations, artificial heating arises from two-body interactions between point-mass particles, scattering them into orbits of higher random energy. Studies such as Fujii et al. (2011) and Sellwood (2013b) have shown that the amount of numerical heating is significantly affected by the simulation resolution. Numerical heating is more pronounced in simulations with smaller numbers of particles. In general, there is a consensus that simulations with  $N > 10^6$  particles modeling the disk experience an acceptable level of numerical heating, while smaller particle numbers are more susceptible to this effect (e.g., Ludlow et al., 2021). In addition, gravitational interactions are softened on small scales in these simulations to avoid unphysical two-body scattering between nearby particles. This softening ensures that the particle collection represents a smoothed density field, with various kernel-based smoothing techniques implemented. In the following sections, we briefly and cursory discuss how numerical heating and softening could affect the simulations used in this thesis, aiming to ensure that simulation resolution and softening length do not play a significant role in the evolution of galactic disks.

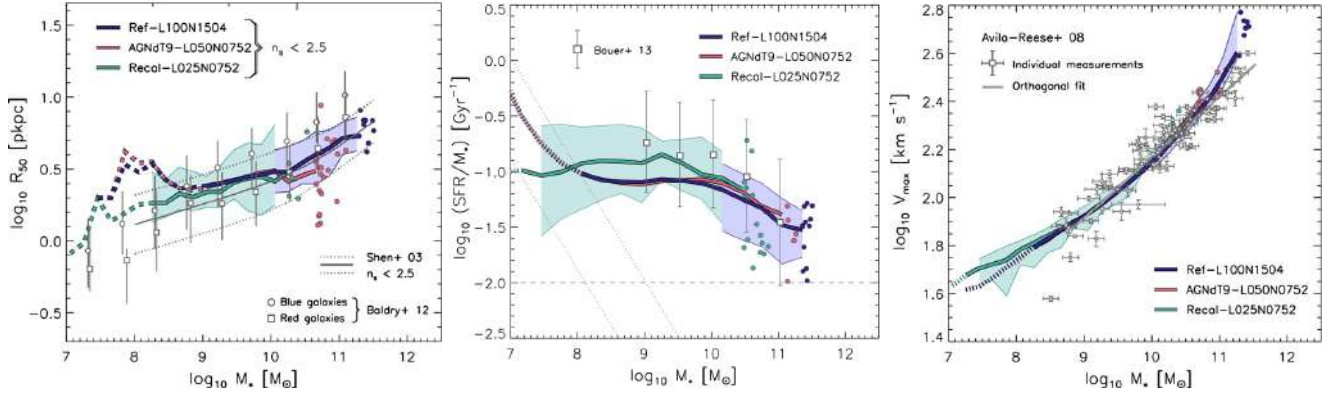


Figure 2.5.1: Left Panel: Relationship between galaxy size and stellar mass for galaxies at  $z = 0.1$  in physical kiloparsecs (pkpc). The depicted curves represent the median values of the projected half-mass radii for the simulations, with shaded areas indicating the corresponding  $1\sigma$  scatter. Middle Panel: Specific star formation rate (SSFR) for actively star-forming galaxies plotted against stellar mass at  $z = 0.1$ . Galaxies are categorized as star-forming if their SSFR exceeds  $10^{-2} \text{ Gyr}^{-1}$ , as denoted by the horizontal dashed line. Simulation medians are illustrated by colored curves, accompanied by shaded regions representing the  $1\sigma$  scatter. Right Panel: Tully–Fisher-like relation, correlating the maximum rotation curve with stellar mass for late-type galaxies at  $z = 0.1$ . The colored curves depict simulation medians, with dotted sections indicating values below the resolution limit of 100 stellar particles. In cases where there are fewer than 10 galaxies per bin, individual objects are represented by filled circles. The shaded regions convey the  $1\sigma$  scatter observed in the simulations. Credit:Schaye et al. (2015)

## 2.5.1 EAGLE project

Several analyses have been performed to study the convergences within the EAGLE simulations. Ludlow et al. (2021) studied the spurious collisional heating of simulated stellar disks, examining how the resolution and mass of dark matter particles can affect the vertical and radial kinematics of disk stars, and consequently the structure of their stellar distribution. The study proposes an empirical model to describe these results and applies it to current cosmological simulations. In particular, they find that for a Milky Way-type galaxy to remain unaffected by vertical collisional heating, it must have more than  $\sim 10^6$  particles, suggesting that dark matter particles should be  $\lesssim 6 \times 10^5 M_\odot$ . In EAGLE’s Ref-L0100N1504 simulation, dark matter particles are  $9.7 \times 10^6$ , and for a Milky Way-like galaxy with a ratio of vertical velocity dispersion to the characteristic velocity of its dark matter halo fraction ( $V_{200}$ ) greater than 0.1, it has about  $1.2 \times 10^6$  particles. According to the empirical model, EAGLE’s dark matter particles exceed this threshold, suggesting possible effects of collisional heating. However, other studies have explored the resolution effects in these simulations.

Schaye et al. (2015) performed several analyses comparing each EAGLE simulation with observational results. One aspect studied was galaxy sizes. Figure 2.5.1 left panel shows galaxy sizes (parameterized by the half-mass radius,  $R_{50}$ ) in relation to their stellar mass. These relationships were compared with the observations of Shen et al. (2003) and Baldry et al. (2012) using SDSS and GAMA data, respectively. While all simulations appear to be in agreement with observations at high masses, differences emerge for low-mass galaxies, possibly due to resolution limitations or other deficiencies in the simulations or halo finders, as well as observational effects such as neglecting variations in the stellar mass-to-light ratio and dust extinction. Schaye et al. (2015) also examined specific star formation rates as a function

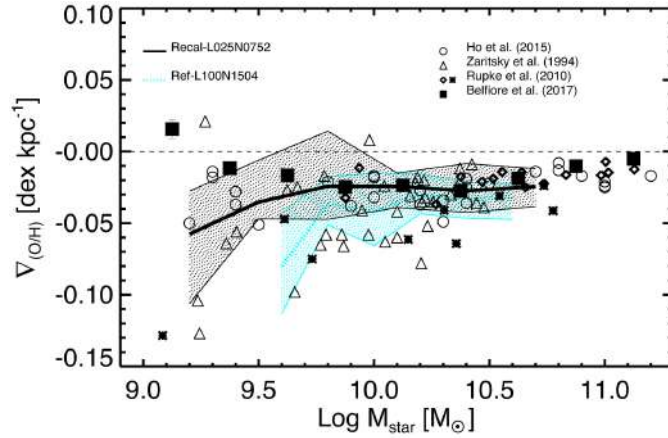


Figure 2.5.2: Median  $\nabla_{O/H}$  estimated for the star-forming disk components as a function of the stellar mass of the EAGLE galaxies in for the Recal-L025N0752 run (black solid lines). For comparison, the simulated relation for the discs in low-density environments of the Ref-L100N1504 are also shown (cyan lines) Credit:Tissera et al. (2019)

of stellar mass (Figure 2.5.1, middle panel), revealing differences between intermediate resolution (Ref-L100N1504) and higher resolution simulations. Although Ref-L100N1504 is statistically consistent with (Bauer et al., 2013) using GAMA data, the authors suggest that this may be a numerical effect. The specific star formation rate then converges to higher-mass galaxies. In the right panel of Figure 2.5.1, the authors test the Tully-Fisher relation (Tully & Fisher, 1977) by comparing the maximum rotation curve as a function of stellar mass with Avila-Reese2008 observations. All simulations show good numerical convergence, in agreement with observations for masses between  $10^9 < M_{\star}/M_{\odot} < 10^{10}$ , with differences less than 0.03 dex. At larger masses the differences with observations increase to 0.12 at  $M_{\star} = 10^{11.3} M_{\odot}$ . Schaye et al. (2015) emphasize the importance of resolution by focusing on feedback effects from star formation and AGN. They conclude that these processes can be effectively anticipated due to subgrid model dependencies, spurious losses from limited resolution, and other factors. Despite the limitations, they achieve relatively good agreement with several galactic and intergalactic metallicity observations, pointing out the need for interpretation and highlighting resolution improvements to address issues such as metallicity in dwarf galaxies.

Tissera et al. (2019) also explored resolution effects, focusing on metallicity profiles. They compared metallicity gradients as a function of stellar mass in two EAGLE simulations with different resolutions, Ref-L100N1504 and Recal-L025N0752, the latter being higher resolution (Fig. 2.5.2). This comparison, including observations, shows consistent trends, especially in high-mass galaxies. In Recal-L025N0752, all selected galaxies belong to low-density regions, indicating consistent relationships, with smaller galaxies showing more negative metallicity gradients, although Recal-L025N0752 disks tend to have slightly flatter gradients.

Lagos et al. (2017) analyzed the specific angular momentum as a function of stellar mass in three low-volume simulations at different redshifts. Ref-L025N0376 has the same subgrid physics and resolution as Ref-L0100N1504. Figure 2.5.3 illustrates this relationship, considering all stellar particles within the half-mass radius (left column) and within a fixed 10 pkpc aperture (right column). Interestingly, all simulations converge, with Ref-L025N0376 producing slightly smaller  $j_{\text{stars}}(10\text{pkpc})$  in low-mass

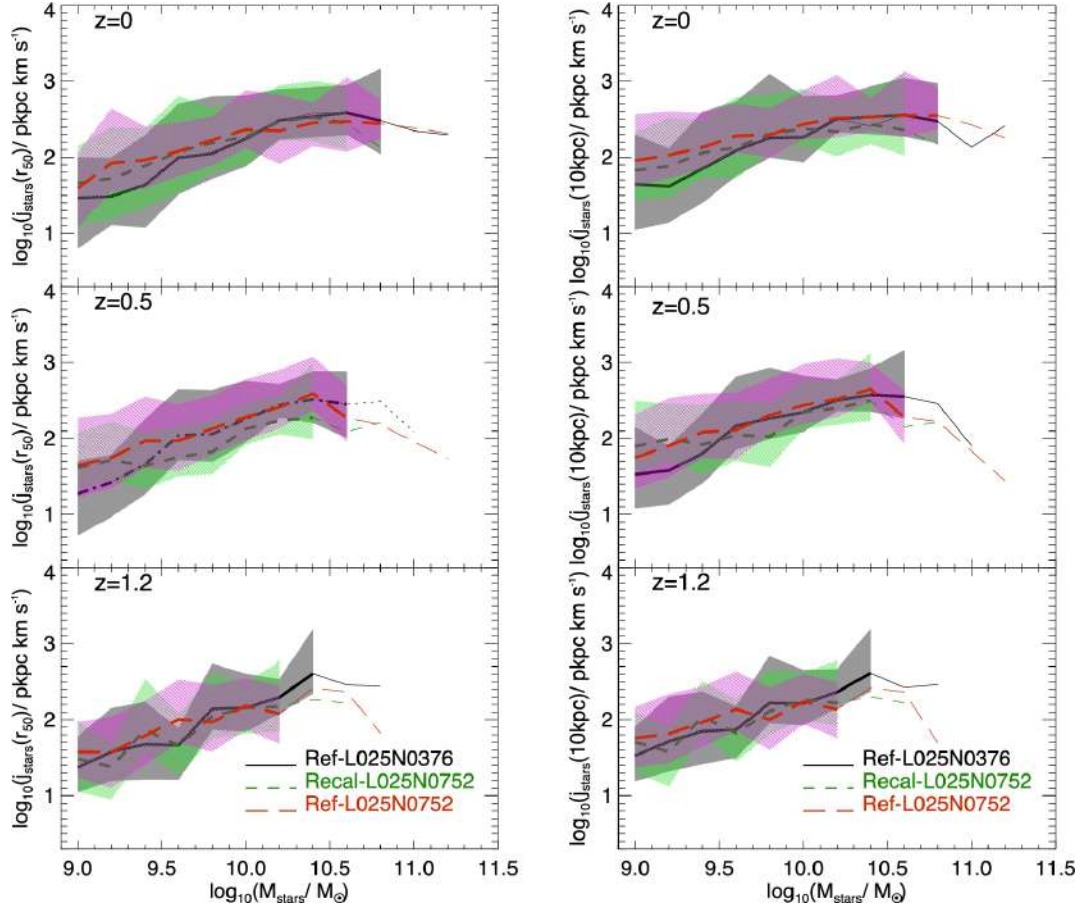


Figure 2.5.3: The  $j_{stars}$ –stellar mass correlation is depicted at three distinct redshifts,  $z = 0, 0.5, 1.2$ , for the simulations Ref-L025N0376, Ref-L025N0752, and Recal-L025N0752, as indicated. Two measurement scenarios are presented: one within the half-mass radius of the stellar component (left-hand panels) and the other within a fixed aperture of 10 pkpc. Median relations are represented by lines, and the 16th–84th percentile ranges are shown as shaded regions. The latter are displayed exclusively for bins containing  $\lesssim 10$  galaxies, while bins with fewer objects are depicted as thin lines. Credit:Lagos et al. (2017)

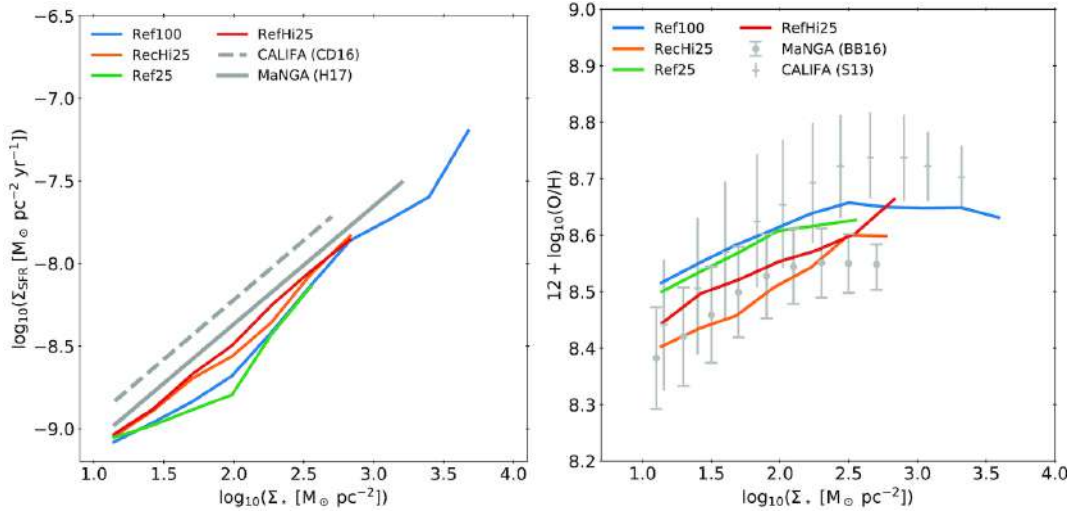


Figure 2.5.4: The resolved main sequence of star formation (rSFMS) is analyzed across diverse simulations to assess the impact of numerical convergence and volume selection effects. The comparison between Ref100 and Ref25 highlights the influence of volume effects, while the comparisons between Ref25 and RefHi25, and Ref25 and RecHi25 demonstrate ‘strong’ and ‘weak’ convergence properties, respectively (see Schaye et al., 2015). It is observed that the rSFMS exhibits reasonably effective convergence. Credit:Trayford & Schaye (2019)

galaxies, although not consistently across all redshifts, possibly due to statistical variations. The authors explored this specific angular momentum-mass relationship with other measurements and found similar agreements.

Finally, Trayford & Schaye (2019) presents the resolved star formation main sequence (rSFMS, Figure 2.5.4), which correlates the surface star formation rate with the surface stellar density, focusing on convergence tests for Ref100 (Ref-L100N1504), RefHi25 (Ref-L025N0752) and Ref25 (Ref-L025N0376) simulations. Overall, volume sampling and resolution effects have a minor influence on the rSFMS. However, a consistent shift of about 0.15 dex below the MANGA relation is observed, due to differences in the integrated star formation rates in EAGLE galaxies compared to observational studies. Despite this shift, the values and trends remain consistent with observations, indicating consistency within uncertainties. These convergence tests in EAGLE simulations highlight that resolution can introduce variations in results that require careful consideration. In our case, the intermediate resolution Ref-L100N1504 simulation shows some variations in the convergence tests, especially for low-mass galaxies and star formation rate analyses, showing a slight deviation from certain observations. However, for higher-mass galaxies, the convergence improves and even agrees with observations. This consistency is encouraging because in Chapter 3, where we use the Ref-L0100N1504 simulation, we explore breaks in the stellar density profiles in galaxies with masses in the range  $10^{10-11.5} M_\odot$ . We also assume that these breaks in the surface density profiles of galactic disks are global rather than local behaviors, and thus should not be significantly affected by numerical heating due to simulation resolution.

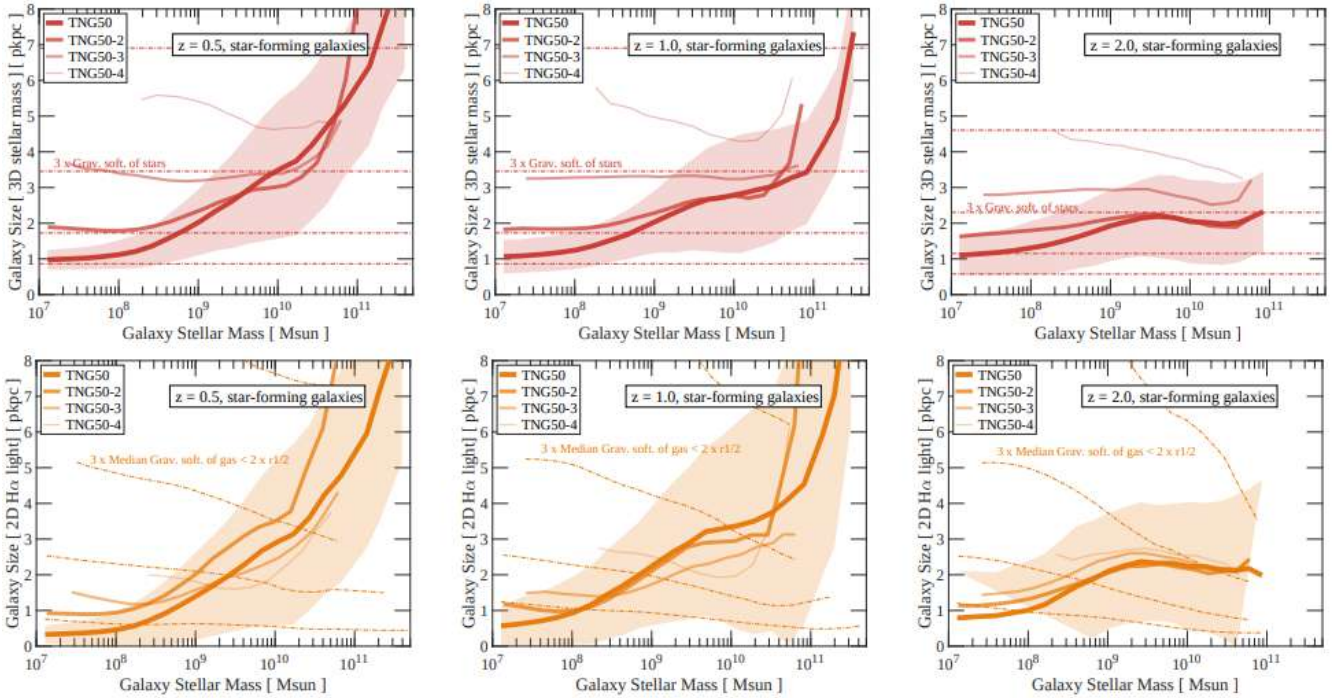


Figure 2.5.5: Median galaxy sizes varying with stellar mass in different resolution scenarios within the same cosmological volume. Thicker, darker curves represent improved numerical resolution. Presented at three redshifts, 3D stellar half-mass radii (upper panels) and 2D  $H\alpha$  half-light radii (lower panels) show  $1-\sigma$  galaxy-to-galaxy variation in TNG50. Dashed lines indicate three times the typical gravitational softening lengths. In IllustrisTNG, size convergence occurs across mass scales and times, especially at higher redshifts. Galaxy sizes above a certain stellar mass show a non-trivial softening length dependence. Credit: Pillepich et al. (2019)

## 2.5.2 IllustrisTNG project

As presented in Section 2.3, the IllustrisTNG simulations are distributed over three box volumes, each with different levels of resolution. Additionally, each variant has its dark matter-only counterpart. In this thesis, we use the TNG50-1 simulation, which is characterized by the highest resolution within the set (see Table 2.3.1). Previous publications on IllustrisTNG provide initial results for each simulation variant, allowing comparisons in terms of resolution, subgrid physics, etc. This section focuses specifically on resolution.

The Pillepich et al. (2019) studies explored galaxy size, disk height, and kinematics across different resolution variations of TNG50 simulations. Among the different TNG50 variations, simulations such as TNG50-2 and TNG50-3 can have resolutions similar to TNG100 and TNG300, while TNG50-1 has a substantially higher resolution by factors of 16.4 and 132, respectively. The relationship between size and mass at different resolutions for the same halo can be observed in Figure 2.5.5. The higher resolutions are represented by darker, thicker lines. This relationship is shown for three representative times,  $z = 0.5$ ,  $z = 1$ , and  $z = 2$  (from left to right). The upper panels show sizes using stellar mass, while the lower panels are calculated using 2D  $H\alpha$  gas. For a given stellar mass for a fixed galaxy, the median relations indicate that better resolution generally yields smaller galaxy sizes in both distributions for low-mass galaxies ( $< 10^{9-10} M_{\odot}$ ). At lower redshifts, a break is observed between low-mass and high-

mass galaxies, possibly related to different star-halo ratios at different resolutions. Furthermore, lower-resolution galaxies are more extended, which influences higher-mass galaxies due to their intrinsic size, and galactic mergers with lower-mass galaxies contribute to this extension. In summary, the improved numerical resolution of TNG50-1 allows reliable studies of galaxy structure. In Figure 2.5.5, the dashed and dotted curves mark the location of three times the typical gravitational softening lengths for stellar particles and gas cells in different simulations and galaxies. These curves indicate the boundary between smoothed and fully Newtonian forces. The gas softening scale is related to spatial size, with low-density regions being more affected. Despite the different trends over time, it is clear that softening does not determine the physical dimensions of galaxies in the TNG50 simulations, except at low masses and low redshifts.

The analysis continues in Figure 2.5.6, which compares disk heights at different numerical masses and spatial resolutions. The upper panel shows measurements based on stellar mass, while the lower panel uses the  $H_\alpha$  height. Similar to the previous figure, wider and darker lines represent better resolution. The distributions of galactic disk heights for  $10^{9-10} M_\odot$  at  $z = 0.5$  are analyzed (left column). The plots highlight the fundamental role of resolution in this mass range, with the authors concluding that the resolution dependence on disk height is less pronounced at higher redshifts ( $z > 0.5$ ). Moreover, it is less prominent for more massive galaxies than those shown in Fig. 2.5.6.  $H_\alpha$  heights converge more rapidly than stellar heights, regardless of resolution changes and at higher redshifts. Gravitational softening lengths decrease with time, but disk heights do not follow the same trend in all cases. The authors emphasize that the galactic structure is not directly related to the softening lengths. In Appendix B of Pillepich et al. (2019), a test is performed to explore the effect of softening lengths on disk heights. They find in some cases that reducing gravitational softening can increase both the height and size of the disks in TNG50.

The TNG50-1 simulation used in this work shows convergence in size and height for galactic disks, being less extended and thinner with better resolution. Despite the differences in resolution between the variants, both the surface and morphological distribution of galactic disks should not be significantly affected.

### 2.5.3 Auriga project

In Grand et al. (2016), tests were conducted to explore the impact of resolution and numerical heating on galactic disks in Auriga. Despite exceeding  $10^7$  particles in both the stellar and dark matter components at the level 3 used in this thesis, it is crucial to ensure that resolution-dependent numerical heating does not significantly affect galaxy evolution. Two additional simulations of the Au 16 halo were performed at level 4, one with a high resolution increased by a factor of 8 compared to level 4, and one with a low resolution reduced by a factor of 8. The results are presented in Fig. 2.5.7, which shows age-velocity dispersion profiles over a 10 Gyr range. The results show remarkable similarity, with deviations in the vertical velocity dispersion of less than 8 km/s for each age. This suggests that Level 4 simulations are not predominantly affected by resolution-dependent numerical heating, but rather by physical heating mechanisms. This provides a favorable context for the analysis of our thesis, as we use a higher resolution than level 4.

In Grand et al. (2017), the studies focused on levels 3, 4, and 5. To assess convergence, three galactic halos (Au 6, Au 16, and Au 24) were analyzed across the three resolution levels. Figure 2.5.8 shows the

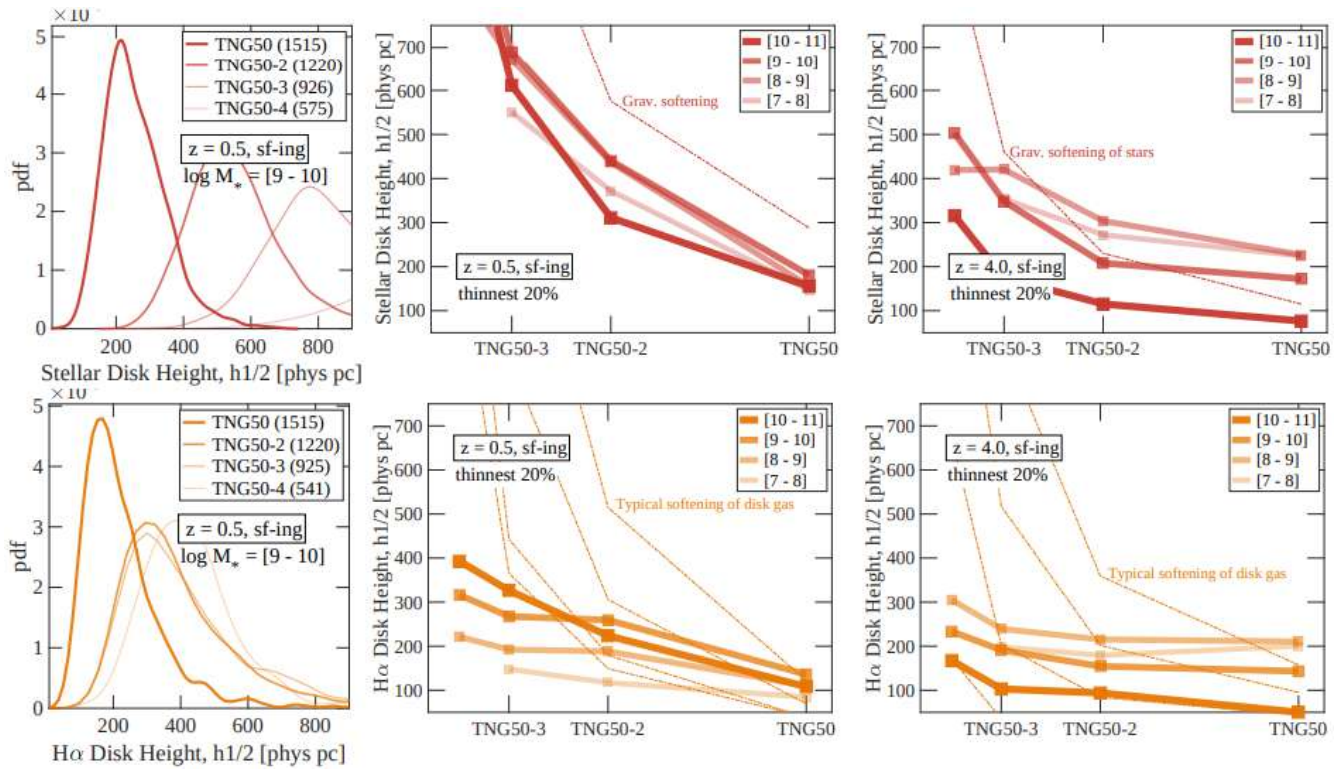


Figure 2.5.6: Galaxy heights in different resolution scenarios within the same cosmological volume: improving resolution is indicated by thicker, darker curves. Stellar mass and  $H\alpha$  light disk heights are shown at the top and bottom, respectively. Credit: Pillepich et al. (2019)

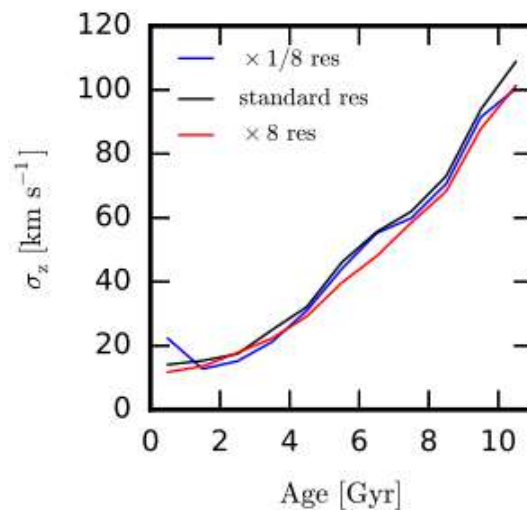


Figure 2.5.7: The age-velocity dispersion relation for Au 16 at the standard resolution (black), 8 times higher resolution (red) and 8 times lower resolution (blue). Credit: Grand et al. (2016)

surface density profiles and orbital circularity distributions, top and second rows respectively. Circularities and total disk mass fractions are very similar for each halo at all three resolution levels, suggesting that the kinematic structure of the disk and bulge remains relatively unchanged. Surface density profiles show some variation in Au 6, while Au 16 and Au 24 appear to be relatively more stable. The study also takes into account the star formation history, which remains consistent across all halos, with a slight increase in star formation at higher resolutions (more details in Grand et al., 2017). In the third row of Figure 2.5.8 evaluates the velocity curves of the halos, showing in particular sharper curves near the center at higher resolutions, reflecting a more compact core. The authors attribute this to variations in the highly nonlinear black hole accretion and feedback loops that help regulate central star formation. In the lower part of Fig. 2.5.8, the vertical disk structure, estimated from the radial profile of the root mean square height for stellar disk particles, is evaluated. It is observed that the disks are slightly thinner at higher resolution, although they have similar height profiles. The authors conclude that the vertical structure of the disk is well-converged. However, these slight variations could be due to the softening lengths, which the authors test in Fig. 2.5.9. Here, the authors run the Au 6 simulation with ten times smaller softening lengths (Au6lowsoft) and replicate the radial profile of the root mean square height, and find that the difference in vertical thickness between the two simulations is negligible, both for the young population and for all stars, demonstrating that shorter softening lengths do not lead to thinner disks. The authors conclude that the softening length should not be considered as a resolution limit, since gravity does not simply disappear below the softening length scale.

In conclusion, Auriga simulations are well converged at the resolution levels seen in these publications. Within these simulations, the level 3 used in our thesis provides a solid framework for interpreting astrophysical phenomena and understanding the evolution of galactic disks and their dark matter halos.

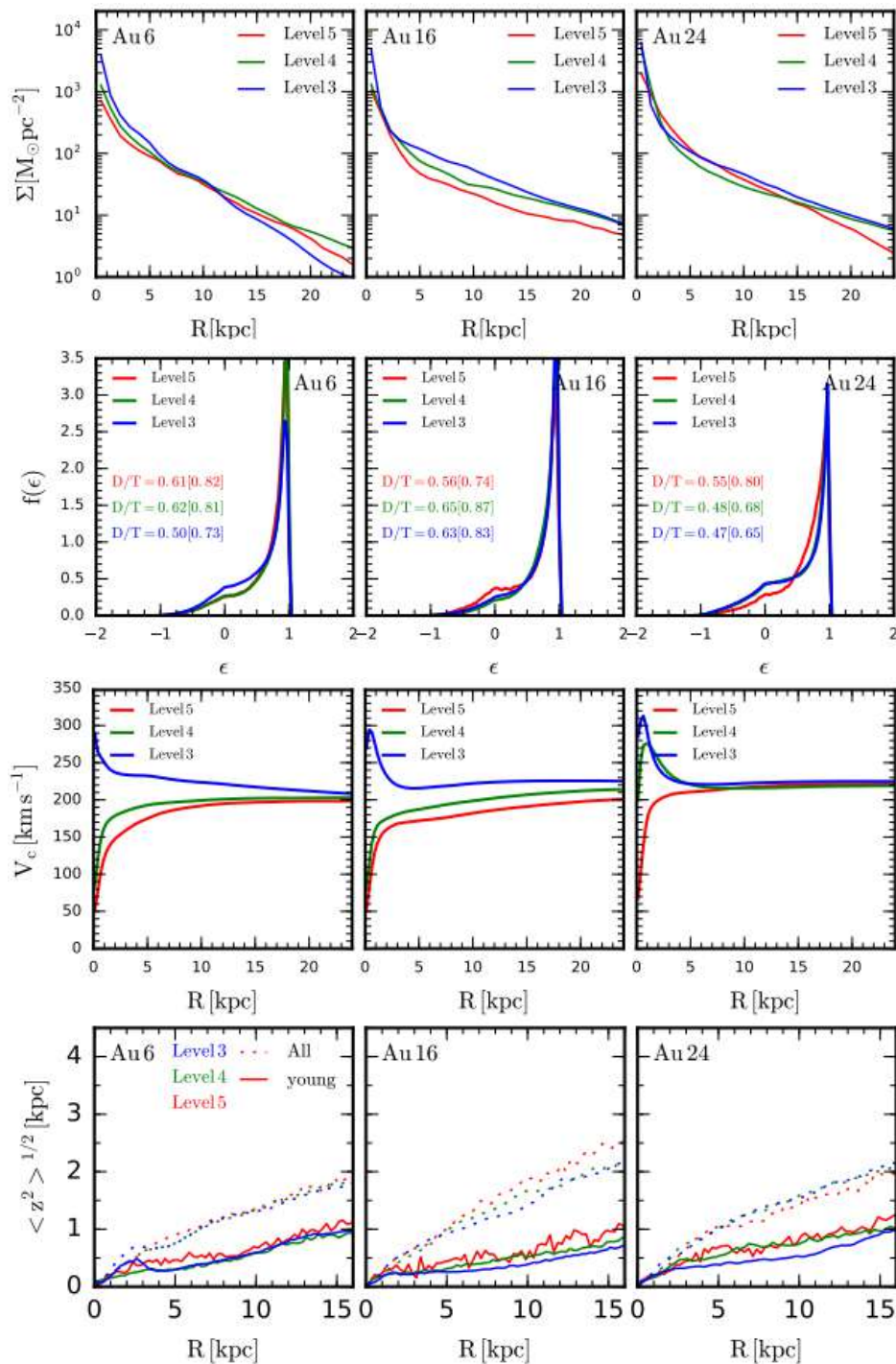


Figure 2.5.8: Stellar surface density profiles (top row), orbital circularity distribution (second row), the radial profiles of the circular velocity (third row) and the root mean square height (fourth row) for all star particles (dotted lines) and for star particles younger than 3 Gyr (solid lines). Haloes Au 6 (first column), Au 16 (middle column) and Au 24 (third column) at three different resolution levels. Credit: Grand et al. (2017)

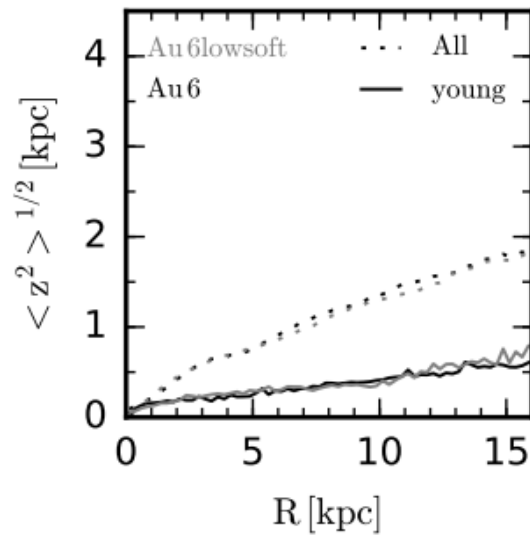


Figure 2.5.9: The radial profile of the root mean square height of simulation Au 6 and a re-run of the same halo with ten times lower softening lengths. Credit: Grand et al. (2017)

# Chapter 3

## Exploring the outskirts of the EAGLE disc galaxies

### Abstract<sup>1</sup>

Observations show that the surface brightness of disk galaxies can be well-described by a single exponential (TI), up-bending (TIII) or down-bending (TII) profiles in the outskirts. Here we characterize the mass surface densities of simulated late-type galaxies from the EAGLE project according to their distribution of mono-age stellar populations, the star formation activity and angular momentum content. We find a clear correlation between the inner scale-lengths and the stellar spin parameter,  $\lambda$ , for all three disk types with  $\lambda > 0.35$ . The outer scale-lengths of TII and TIII disks show a positive trend with  $\lambda$ , albeit weaker for the latter. TII disks prefer fast rotating galaxies. With regards to the stellar age distribution, negative and U-shape age profiles are the most common for all disk types. Positive age profiles are determined by a more significant contributions of young stars in the central regions, which decrease rapidly in the outer parts. TII disks prefer relative higher contributions of old stars compared to other mono-age populations across the disks whereas TIII disks become progressively more dominated by intermediate age (2-6 Gyrs) stars for increasing radius. The change in slope of the age profiles is located after the break of the mass surface density. We find evidence of larger flaring for the old stellar populations in TIII systems compared to TI and TII, which could indicate the action of other processes. Overall, the relative distributions of mono-age stellar populations and the dependence of the star formation activity on radius are found to shape the different disk types and age profiles.

---

<sup>1</sup>Based on Varela-Lavin et al. (2022), published in MNRAS

### 3.1 Introduction

Stellar populations store important information on the evolution of galaxies and the physical processes that shaped their morphologies, star formation histories and chemical properties, among others. In the case of spiral galaxies, powerful information can be readily obtained through their surface brightness (SB) profiles. Disk components are typically consistent with well-behaved exponential profiles (Patterson, 1940; Freeman, 1970). To first order, their formation can be explained by the so-called standard model for disk formation (Fall & Efstathiou, 1980) which is based on the specific angular momentum conservation of baryons. However, within the current cosmological paradigm, galaxy formation proceeds in a non-linear way so that mergers and interactions with other galaxies, or with the global environment, can disturb galactic disks causing a redistribution of angular momentum (e.g. Pedrosa & Tissera, 2015; Teklu et al., 2015; Lagos et al., 2017), the formation of non-symmetric features (e.g. Gómez et al., 2016, 2017, 2021; Grand et al., 2016) and the loss of material via tidal stripping (Barnes & Hernquist, 1996), among others. It has become clear that not all spiral galaxies can be described by a single exponential profile extended to arbitrarily large radii (van der Kruit, 1979). Thus, while the SB distributions of some disks can be well-described by an exponential profile all the way out (TI), other disks show a brightness deficiency (TII) or excess (TIII) with respect to a single exponential profile. Such disks are better described by double exponential fits (e.g. Pohlen & Trujillo, 2006) with a characteristic break radius ( $R_{br}$ ). Observational studies suggest a correlation between the Hubble type and the disk type. TIII systems are reported to be more frequent in early-type spirals while TII ones are more common in late-type ones (Erwin et al., 2008; Pohlen & Trujillo, 2006; Gutiérrez et al., 2011).

Several theoretical and observational works have analysed the characteristics of outer regions of disk galaxies (e.g. Roškar et al., 2008b,a; Sánchez-Blázquez et al., 2009; Minchev et al., 2012a; Bakos et al., 2008; Yoachim et al., 2012; Ruiz-Lara et al., 2016). Yet, the origin of the deviation from a single exponential disk is still unclear. Variations of star formation efficiency, migration, accretion of small satellites, or a combination of all of them could be behind this. The main hypotheses formulated to explain "breaks" in the SB profiles are related to angular momentum redistribution (Debatista et al., 2006) and to the existence of a star formation threshold (Elmegreen & Hunter, 2006). Additionally, several works have reported a link between an outer upturn ("U-shape") in the age profiles and the TII profile, with the age up-turn causing the lack of light in the outer regions (Bakos et al., 2008; Roškar et al., 2008a; Sánchez-Blázquez et al., 2009; Martínez-Serrano et al., 2009; Yoachim et al., 2012). According to Sánchez-Blázquez et al. (2009), the origin of TII and TIII galaxies arises from a combination of two processes: (1) an abrupt change of slope in the radial star formation profile and (2) the effects of stellar radial migration inside-outside of  $R_{br}$ . The first is due to a change in the gas volume density profile, which would cause the bending down in the stellar density profile. The second is due to radial migration of stars formed in the inner parts towards locations beyond  $R_{br}$ . In addition, these authors proposed that the different types of stellar density profiles could be a consequence of a variation of efficiencies of both mechanisms. Ruiz-Lara et al. (2017b) reported different stellar age and metallicity inner gradients for galaxies displaying TI, TII and TIII SB profiles. Those results are interpreted as outcome of a gradual increase in the radial migration efficiency of stars from TII to TI and TIII galaxies.

Ruiz-Lara et al. (2016) analysed 44 spiral galaxies selected from the CALIFA survey (Walcher et al., 2014, see also Ruiz-Lara et al. 2017b). They compared the SB and age profiles in order to find differences between profile types (I and II). They also reported a U-shape in the age profiles of 17 galaxies that were

either TII or TI. However in their sample, the U-shape feature is only observable in light-weighted age profiles. They claim that the mechanisms shaping the SB and stellar population distributions are not directly coupled and that the U-shape in age profiles would be due to an early formation of the disk followed by an inside-out quenching of the star formation.

On the other hand, Herpich et al. (2015, 2017) investigated the role of the halo spin parameter ( $\lambda$ ) in shaping the outer SB profiles by analysing a set of simulations of isolated controlled galaxies. They found a clear transition from TIII galaxies, displaying low spin parameters to TII galaxies, showing higher values. TI disks are reported to have intermediate values,  $\lambda \sim 0.035$ . Recently, Wang et al. (2018) found that the formation of TIII galaxies were linked to high HI-richness and low spin  $\lambda$  of the inner stellar disc. Hence there are still open questions regarding the origin of these characteristics features in the SB profiles. While the smooth formation of disks with global angular momentum conservation would lead to a correlation between scale-lengths and spin parameter  $\lambda$  (Mo et al., 1998), these distributions could be disturbed by variety of physical processes such as stellar migration, dynamical heating, satellite accretion, bar formation, among others.

Clearly, the origin of the spread observed in the properties of galactic disc, such as surface density and brightness profiles, is complex and involves the action of several physical mechanisms. As such, these profiles can provide very rich information regarding the formation and evolution of galactic disc. For this purpose, we analyse the stellar surface density of disk galaxies selected from the simulation with the largest volume of the EAGLE Project (Schaye et al., 2015). The EAGLE simulations have been shown to reproduce several galaxy relations such as the gas content of galaxies at a given mass (Lagos et al., 2015; Bahé et al., 2016; Crain et al., 2017), the evolution of the galaxy stellar mass function (Furlong et al., 2015), the scale-resolved metallicity-star formation relation (Trayford & Schaye, 2019), the metallicity gradients as a function of stellar mass (Tissera et al., 2019, 2022) and the azimuthal variation of the metallicity gradients at  $z = 0$  (Solar et al., 2020). Our goal is to characterize the origin of the different surface density and age profiles in a cosmological context. In this chapter, we focus on the analysis of stellar populations and their age distributions in central disk galaxies. The stellar surface density profiles,  $\Sigma(r)$ , are statistically analysed with the goal of identifying correlation between the distribution of mono-age stellar populations and the star formation activity.

The chapter of this thesis is organized as follows. In Section 3.2 we describe the main characteristics of the EAGLE simulations, the selected galaxy sample and the algorithm that is be applied to classify the different  $\Sigma(r)$ . Section 3.3 describes the analysis and results. In Section 3.4 we discuss and summarize our main findings.

## 3.2 Simulated galaxies

For this chapter we will use largest simulation (Ref-L100N1504) of the EAGLE Project<sup>1</sup> (Schaye et al., 2015; Crain et al., 2015). The initial conditions are consistent with the Planck Cosmology parameters (Planck Collaboration et al., 2014):  $\Omega_\Lambda = 0.693$ ,  $\Omega_m = 0.307$ ,  $\Omega_b = 0.04825$ ,  $\sigma_8 = 0.8288$ ,  $h = 0.6777$ ,  $n_s = 0.9611$  and  $Y = 0.248$  where  $\Omega_\Lambda$ ,  $\Omega_m$  and  $\Omega_b$  are the average densities of dark energy, matter and baryonic matter in units of the critical density at  $z = 0$ ,  $\sigma_8$  is the square root of the linear variance of the

<sup>1</sup>In <http://eaglesim.org>, <http://eagle.strw.leidenuniv.nl> a global description of the project as well as access to movies and images and the database of galaxies can be found (McAlpine et al., 2016).

matter distribution when smoothed with a top-hat filter of radius  $8h^{-1}$  cMpc,  $h$  is the Hubble parameter ( $H_0 \equiv h100\text{kms}^{-1}$ ),  $n_s$  is the scalar power-law index of the power spectrum of primordial perturbations, and  $Y$  is the primordial mass fraction of helium. The subgrid physics parameters were calibrated to reproduce the galaxy mass function and the observed sizes of galaxies at  $z = 0.1$  (Schaye et al., 2015). In addition, other variations of the subgrid physics were explored as presented in Crain et al. (2015). The Ref-L100N1504 run simulates a cubic volume of side 100 Mpc. The setup of the initial conditions provides a mass resolution of  $9.7 \times 10^6 M_\odot$  for dark matter and an initial mass of  $1.81 \times 10^6 M_\odot$  for baryonic particles. The gravitational calculations between particles are computed with a Plummer equivalent softening length of 2.66 comoving kpc limited to a maximum physical size of 0.70 pkpc ( $\epsilon_{\text{grav}}$ ). This simulation provides a large number of galaxies formed in a variety of environments.

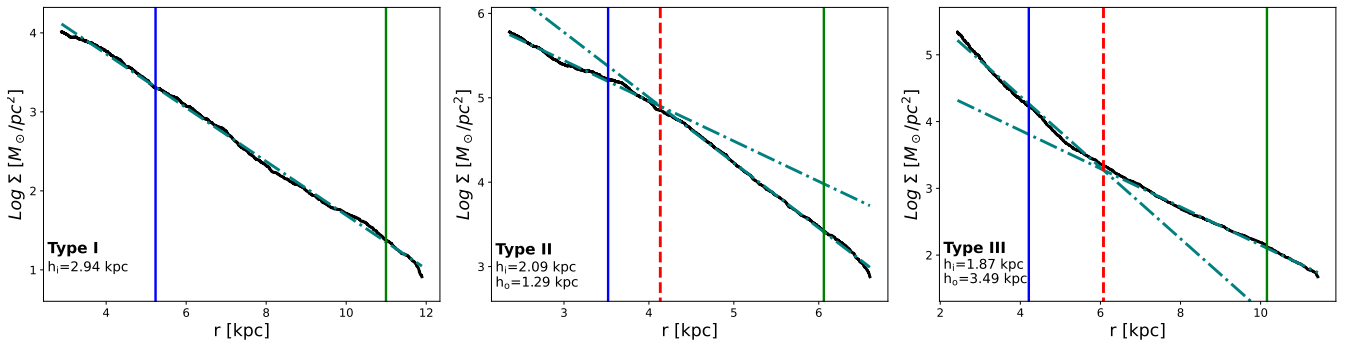


Figure 3.2.1: Examples of typical TI (left panel), TII (middle panel) and TIII (right panel)  $\Sigma(r)$  profiles in the EAGLE disks (black lines). The linear regression for TI and the double exponential fits for TII and TIII are also shown (cyan, dashed dot lines). The characteristics scales,  $R_{\text{eff}}$  (blue, solid lines),  $R_{\text{opt}}$  (green, solid lines) and  $R_{\text{br}}$  (red, dashed vertical lines) are also depicted, together with the inner  $h_i$  and outer  $h_o$  scale-lengths.

### 3.2.1 The simulated galaxy sample

We use the galaxy catalogue constructed by Tissera et al. (2019) from the Ref-L100N1504 at  $z=0$ . Only central galaxies within a given halo are analysed (i.e. no satellite galaxies have been included). The spheroidal and disk components were separated by applying a dynamical criterion based on the angular momentum content and the binding energy. This is done by estimating  $\epsilon = J_z / J_{z,\text{max}}(E)$ , where  $J_z$  is the angular momentum component in the direction of the total angular momentum, and  $J_{z,\text{max}}(E)$  is the maximum  $J_z$  over all particles at a given binding energy  $E$  (see Tissera et al., 2012, for details on the procedure and conditions used). With this algorithm, the disk and bulge components are identified. The disc-to-total stellar mass ratio ( $D/T$ ) is used to classify galaxies according to their morphologies. In order to analyze galactic disks with morphologies and environments similar to those of the Milky Way, central galaxies with  $D/T > 0.5$  are selected. Additionally, only those with disk components resolved with more than 5000 stellar particles are considered. As a consequence, our sample comprises 1012 disk galaxies with stellar mass within the mass range  $[10^{10}, 10^{11.5}] M_\odot$ . For each galaxy we calculated the optical radius,  $R_{\text{opt}}^{\text{disc}}$ , as the radius that enclosed  $\sim 83$  percent of the stellar mass of a disk (Sáiz et al., 2001), and the effective radius,  $R_{\text{eff}}$ , as the radius that enclosed half of the disk stellar mass.

Hereafter, the  $\Sigma(r)$  profiles of the disk components of the selected galaxies are defined by projecting the

stellar mass onto the rotational plane of the disks, from  $3\epsilon_{\text{grav}}$  to  $1.5 R_{\text{opt}}$ . This is performed after the galaxies are rotated to have their z-axis aligned with the total angular momentum of the stellar disks. To minimize potential issues due to numerical resolution or very local inhomogeneities, the  $\Sigma(r)$  profiles are calculated using moving averages. In practice, for a given galaxy, the azimuthally averaged disk surface density,  $\Sigma(r_i)$ , is estimated at the galactocentric distance of each disk stellar particle,  $r_i$ . Here  $i = 1, \dots, N_{\text{disc}}$  where  $N_{\text{disc}}$  is the total number of disk particles. To do so, we first sort all disk stellar particles with respect to  $r_i$  in ascending order. We compute  $\Sigma(r_i)$  by selecting both the 10 percent of disk particles that are located at  $r > r_i$  and the 10 percent of disk particles that are located at  $r < r_i$ . In other words, a total of 20 percent of disk stellar particles are considered at each  $r_i$ . We then add the mass of all selected disk stellar particles and compute the surface density considering the area enclosed by the selected subset<sup>2</sup>.

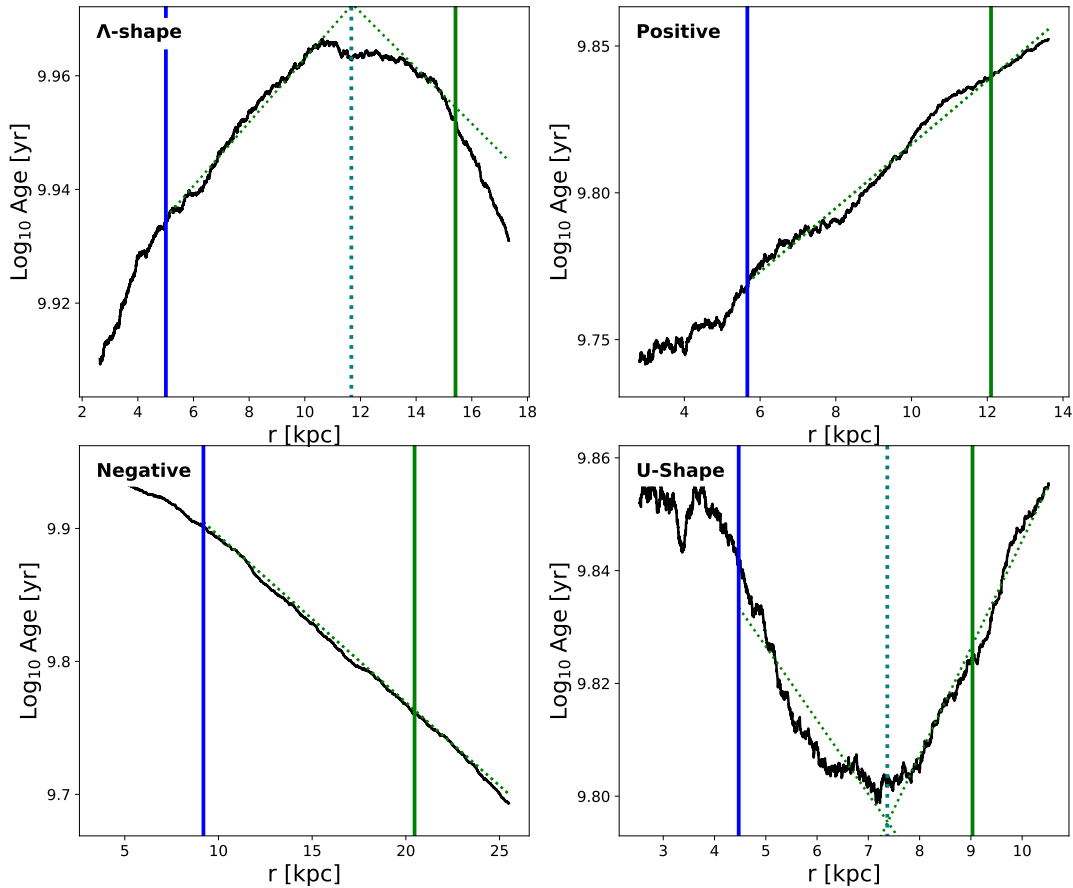


Figure 3.2.2: Four different age profiles identified in EAGLE disks are shown for illustration purposes (black lines). The linear regressions are also depicted (green dotted lines). The characteristics scales,  $R_{\text{eff}}$  (blue solid lines),  $R_{\text{opt}}$  (green solid lines) are included. Additionally, for the U-shape and  $\Lambda$ -shape profiles  $R_{\text{min}}$  and  $R_{\text{max}}$  are depicted (green short-dashed lines).

<sup>2</sup>Note that, to always use the same number of particles when estimating  $\Sigma(r_i)$ , for the first and last 10 percent of the sorted disk particles,  $\Sigma(r_i)$  is not computed.

### 3.2.2 Break-Finder (BF) algorithm

In order to characterize the  $\Sigma(r)$  profiles, we follow a methodology similar to that established by previous authors (Erwin et al., 2008; Muñoz-Mateos et al., 2013), where  $\Sigma(r)$  profiles are presented as a double power-law piece-wise joined by an inflection point (see Erwin et al., 2008, equations 5 and 6). For this, we fit the profiles using the following piece-wise function:

$$\log_e \Sigma_i(r) = \log_e \Sigma_{0,i} - \frac{r}{h_i} \quad \text{if } r \leq R_{\text{br}}, \quad (3.2.1)$$

$$\log_e \Sigma_o(r) = \log_e \Sigma_{0,o} - \frac{r}{h_o} \quad \text{if } r > R_{\text{br}}, \quad (3.2.2)$$

where the two parts are joined at the break radius,  $R_{\text{br}}$ . Here  $h_i$  and  $h_o$ ; inner and outer scale lengths,  $\Sigma_{0,i}$  and  $\Sigma_{0,o}$ ; inner and outer central densities and  $R_{\text{br}}$ . Note that, the value of  $\Sigma_{0,o}$  is set by the values of the remaining four parameters. Equations 3.2.1 and 3.2.2 are used to characterize the inner and outer regions of the disks, respectively.

Our BF fitting procedure considers star particles within  $0.5 R_{\text{eff}}$  to  $1.5 R_{\text{opt}}$ . The BF algorithm is sensitive to breaks. A potential problem with the methods arises at the disk outer and inner most edges, where spurious inflection point could be defined. To avoid spurious results we allow  $R_{\text{br}}$  to only vary within  $0.5 R_{\text{eff}}$  to  $R_{\text{opt}}$ . The remaining parameters are forced to be greater than 0. The parameter fitting is performed using a robust least squares optimization method for bounded problems called Trust Region Reflective algorithm<sup>3</sup>. The best fit minimizes the sum of squared residuals, which is quantified through the  $\chi^2$ . The result is always a double exponential. The type of profiles are defined according to the criteria described in section 3.3.1

## 3.3 Analysis

### 3.3.1 Stellar surface density profiles

We analyse the  $\Sigma(r)$  of the selected disk galaxies and classify them as TI, TII and TIII profiles. For this purpose, the BF algorithm described in Section 3.2.2 is applied to the  $\Sigma(r)$  of all galaxies in our sample. The classification is performed by comparing the  $h_i$  and  $h_o$  scales. The strength of the break is quantified by defining

$$\beta = h_i - h_o.$$

Following Ruiz-Lara et al. (2017b), we define TII disks are those with  $\beta \gtrsim 0.5$  kpc, TIII disks have  $\beta \lesssim -0.5$  kpc, and TI disks have with  $|\beta| \leq 0.5$  kpc. This value corresponds to the quarter of  $\beta$  standard deviation. Then, for TI disks, we perform a single power-law fit. In Fig. 3.2.1, we show the result of applying the fitting algorithm to three typical examples. Clearly, TII and TIII disks show double exponential profiles, with the inner disk defined for  $r < R_{\text{br}}$  (the cyan, dashed vertical line), and the outer disk for  $r > R_{\text{br}}$ .

Finally, we use the  $\chi^2$  of the best fits to eliminate from the samples those disks that have more complex structure and hence require more than two exponentials to describe the  $\Sigma(r)$ . These disks are strongly

<sup>3</sup>We implement Trust Region Reflective algorithm using the CURVE\_FIT function from the SCIPY library. More details can be found at <https://scipy.org>

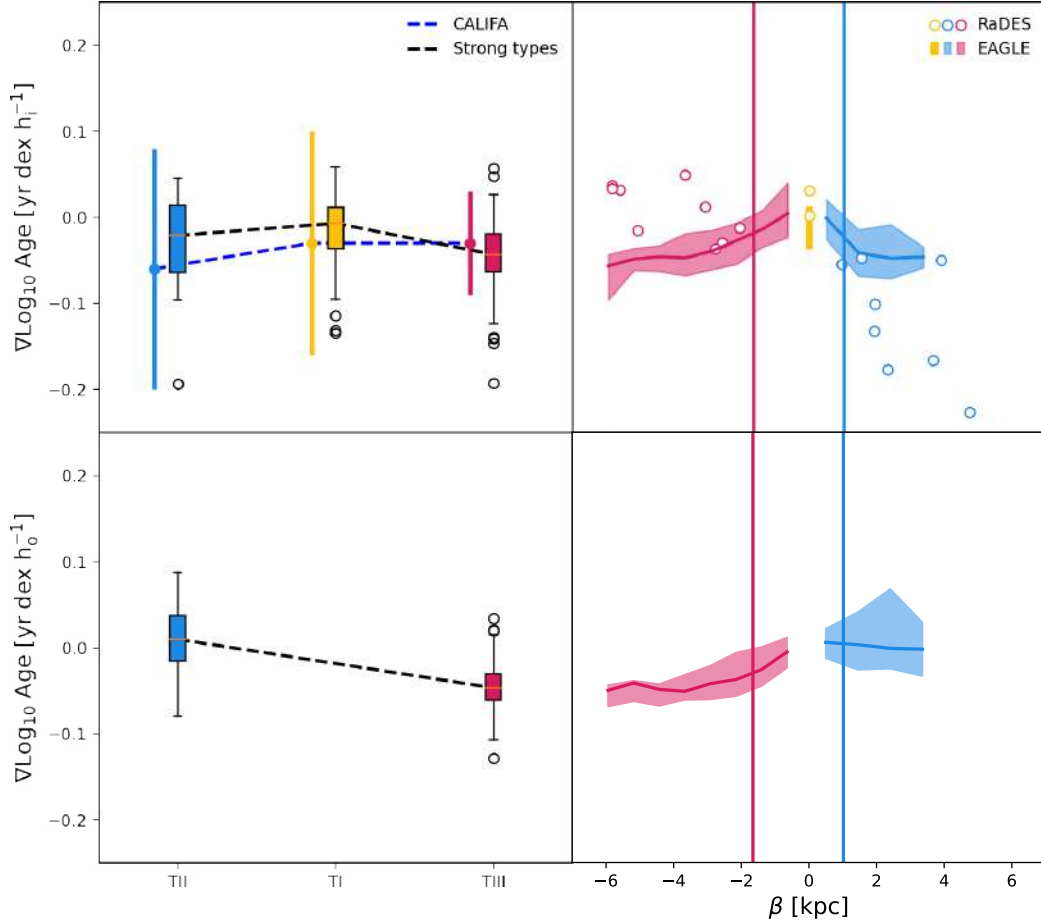


Figure 3.3.1: Analysis of the gradients of the inner and outer age profiles for different disk types (top and bottom panels, respectively). In the left panels, the age gradients for the inner (upper) and outer (lower) disks as a function of disk types for our EAGLE sample are shown. The median age gradients for the strong types subsamples (blue, yellow and red boxes for TII, TI and TIII, respectively and dashed black lines) are included. The size of the boxes denote the 25<sup>th</sup> and 75<sup>th</sup> percentiles (open black circles show the outliers). For comparison the median mass-weighted ages gradients for the inner disks reported by Ruiz-Lara et al. (2017b) for galaxies in the CALIFA survey (dashed blue line) are also depicted (the error bars correspond to the dispersion as given by their table 4). In the right panels, the median age gradients for the inner and outer disks are shown for TI, TII and TIII galaxies. The shaded regions are enclosed by the 25 – 75<sup>th</sup> percentiles of the corresponding distributions. The red and blue vertical lines depict the medians of  $\beta$  for the TIII and TII profiles, respectively. These are used to define strong TII and TIII types (Sec. 3.3.1). The results of Ruiz-Lara et al. (2017a) using the RaDES simulated galaxies (red and blue open points) are also included).

Table 3.3.1: Distribution of the disk types in the EAGLE sample.

	$N_{\text{T}}$	$N_{\text{TI}}$	$N_{\text{TII}}$	$N_{\text{TIII}}$
All Types	912	301 (33%)	116 (13%)	495 (54%)
Strong Types	607	301 (49%)	58 (10%)	248 (41%)

disturbed and are not suitable for the study of this Chapter. For this purpose, only galaxies with  $\chi^2 < \hat{\chi}^2 + \sigma_{\chi^2}$ , where  $\hat{\chi}^2$  is the median and  $\sigma_{\chi^2}$  is the standard deviation of the  $\chi^2$  distribution for our total sample. In this way, we eliminate the outliers of  $\chi^2$  at  $1 - \sigma$  level, and build a well-fitted subsample of simulated galaxies whose  $\Sigma(r)$  can be described by either a pure or a double exponential. Our final sample comprises 912 galaxies.

With the aim of analysing a more trustworthy sample, we quantify the strong TII and TIII types groups by selecting the fifty percent of galaxies of each  $\Sigma$  type which have the strongest deviation between the inner and outer disks. For this purpose, the median of the  $\beta$  distribution for each  $\Sigma$  type is calculated. Strong TII are galaxies that have  $\beta$  larger than  $\hat{\beta} = 1.02$  kpc, while strong TIII galaxies have  $\beta$  less than  $\hat{\beta} = -1.66$  kpc. Of course, there are no strong types for TI disks. In Table 3.3.1, we show the numbers of members and percentages of galaxy types in the total and strong samples. We can see that TIII is the most frequent type overall in the analysed sample. However TI are more frequent if we only consider the strong TII and TIII subsamples. The less frequent galaxy type in both EAGLE samples is TII. Hereafter, we will only consider the strong-type disks in the analysis with the purpose of disentangling clearly the similarities and differences among them.

As can be seen from Table 3.3.1, TI and TIII are the most frequent types in our simulated sample. This seems at odd with observations, which find TII to be the most common profile. However, observations also suggest that the fractions of galaxies with different disk types vary with morphology and probably with the environment. TII disks are reported to be more frequent in late-type galaxies while TIII disks tend to be identified in early-types. For example, Pohlen & Trujillo (2006) analysed a sample of 93 late-type galaxies and found a distribution of 10%:60%:30% for types TI:TII:TIII, respectively. Using 66 early-type spiral galaxies, Erwin et al. (2008) reported percentiles of 27%:42%:27%, and Gutiérrez et al. (2011) also detected a trend for TII to be more frequent in late-type spirals using a sample of 47 face-on early-type unbarred galaxies, they reported a global breakdown of 21%:50%:38%. As it will be discussed in Sec. 3.3.3, this dependence on morphology is reproduced by the EAGLE simulations. Although the frequencies between our EAGLE sample and the observations are not similar, recent work with galaxy triplets finds a high frequency of TIII galaxies in this environment. Members of such triplets typically show signs of interactions, highlighting the relevance of environment (Tawfeek et al., 2021). We note that, in our work, galaxies are located in different environments (Tissera et al., 2019) and that this aspect will be addressed in a forthcoming study.

### 3.3.2 Age profiles

To understand the origin of the different types of  $\Sigma(r)$  profiles, and to confront them with observations, we also estimate age profiles for each galaxy. As for the  $\Sigma(r)$  profiles, the mass-weighted stellar age profiles are constructed by using stars located between  $3\epsilon_{\text{grav}}$  and  $1.5 R_{\text{opt}}$  and are estimated by using

Table 3.3.2: Age profile type frequencies in TI, TII and TIII disks. The fractions of galaxies with a given age profiles in a given  $\Sigma$  type subsample are provided within parenthesis.

	TI	TII	TIII
Negative	85 (0.29)	13 (0.22)	120 (0.50)
U-shape	101 (0.34)	25 (0.43)	110 (0.46)
Positive	49 (0.17)	14 (0.24)	6 (0.02)
$\Lambda$ -shape	59 (0.20)	6 (0.10)	5 (0.02)

moving averages. We note that the age profiles have been calculated within the same radial range used for the surface density profiles in order to be able to correlate their trends.

Then a double-linear piece-wise function is fitted within the radial range  $[R_{\text{eff}}, 1.5R_{\text{opt}}^{\text{disc}}]^4$  using our BF algorithm. The profiles were fitted using logarithmic scale. In this way the inner,  $a_{\text{in}}$ , and outer,  $a_{\text{out}}$ , slopes and the inflection point are obtained (see Section 3.2.2). To classify the age profiles, we use the  $a_{\text{in}}$  and  $a_{\text{out}}$  slopes. We define four different behaviours by applying the criteria described below:

$$\begin{aligned}
 a_{\text{in}} < 0 & \begin{cases} \text{U-shape} & \text{if } a_{\text{in}} < a_{\text{out}} \\ \text{Negative} & \text{if } a_{\text{in}} \geq a_{\text{out}} \end{cases} \\
 a_{\text{in}} > 0 & \begin{cases} \text{Positive} & \text{if } a_{\text{in}} \leq a_{\text{out}} \\ \Lambda\text{-shape} & \text{if } a_{\text{in}} > a_{\text{out}} \end{cases}
 \end{aligned}$$

For the U-shape profiles, we refer the radial position at which the profiles with slopes  $a_{\text{in}}$  and  $a_{\text{out}}$  intersect each other as  $R_{\text{min}}$ . For the  $\Lambda$ -shape profiles this radial position is referred as  $R_{\text{max}}$ . These definitions are related to the position of the minimum and maximum age, respectively. Fig. 3.2.2 show typical examples of positive, negative U- and  $\Lambda$ -shape age profiles. These different types of age profiles are found in simulated disks regardless of their  $\Sigma(r)$  type (i.e. TI, TII and TIII). However, their frequencies change for TI, TII and TIII disks as summarized in Table 2. On the one hand, the U-shape profile is found to be the dominant class in TI and TII disks while for TIII disks the most frequent are negative and U-shaped age profiles. On the other hand, positive and  $\Lambda$ -shape age profiles are the least frequent in TIII galaxies (where together represent only 4 percent to the total TIII), but are more numerous in TI where they are found in  $\sim 37$  per cent of the total TI galaxies. Observationally, Roediger et al. (2012) reported 15% of the TI and 36% of TII and TIII to have U-shape profiles. They also reported 30% of TI to have negative age slopes. Our estimations for the EAGLE galaxies are in general agreement with these observations. Roediger et al. (2012) also found that more than 50% of galaxies in their Virgo sample had positive age gradients regardless of the disk types, indicating the possible action of environmental effects. However, we have not found any report of  $\Lambda$ -shape age profiles in observations yet.

We compare our results with Ruiz-Lara et al. (2017a), where 214 spiral galaxies selected from the CALIFA survey are analysed. They estimated both the light-weighted and mass-weighted age profiles. To

<sup>4</sup>The radial range have been extend towards larger radii to ensure the detection of any change of slope in the age profiles since they are found to occur at larger galactocentric distances than the  $R_{\text{br}}$ .

make a fair comparison with our simulated data, we adopted the slopes of the linear regression fits of their mass-weighted age profiles. We also consider the definitions proposed by Ruiz-Lara et al. (2017b) to compute the inner and outer gradients. The inner disks are defined between  $0.5R_{\text{eff}}$  and  $R_{\text{br}}$  for TII and TIII disks, and between  $0.5R_{\text{eff}}$  and  $1.5R_{\text{opt}}$  for TI disks. The outer regions in TII and TIII disks are calculated from  $R_{\text{br}}$  to  $1.5R_{\text{opt}}$ . The inner gradients are normalized by the inner scale-length  $h_i$  and  $h_o$  for outer gradients.

In the left panel of Fig. 3.3.1, we display the age gradients for TI, TII and TIII, including the observational results presented in Ruiz-Lara et al. (2017b). Our sample is represented by the colored boxes in the left panels. As can be seen, the simulated age profiles for each  $\Sigma(r)$  type are within the observed range. However, there is a trend for the simulated age gradients to be slightly shallower for TI and TII.

In the top right panel of Fig. 3.3.1 the median age gradients for the strong TII and TIII for our EAGLE sample are displayed as a function of  $\beta$  and compared with the results of RaDES simulated disks (Ruiz-Lara et al., 2017b, open circles). We note that these authors estimated light-weighted age profiles using the r-band SDSS luminosities and this might introduce difference with our results. The EAGLE disks show a weak correlation for TIII and anticorrelation for TII between the inner age gradients with  $\beta$ . The Pearson correlation factor of each one are 0.37 and  $-0.30$  respectively. Regarding TIII disks, RaDES reported an anticorrelation while EAGLE is consistent with the opposite trend. These differences could originate by the different subgrid physics implemented in RaDES and EAGLE simulations. Hence, the information stored in both age and  $\Sigma$  profiles could help to constrain the galaxy formation models.

In the lower panels of Fig. 3.3.1 we also include similar relations for the age gradients in the outer regions using  $h_o$ . This plot can be done only for TII and TIII disks. As can be seen the age profiles are shallower/positive for TII, while the outer regions of TIII disks show stronger negative age profiles and a trend for stronger TII to have more negative outer age gradients.

### 3.3.3 The angular momentum content

As mentioned in Section 4.1, different mechanisms could simultaneously act to shape the  $\Sigma(r)$  profiles. Here, we explore the connection between disk type and degree of galaxy rotation. To analyse this, we use the D/T ratio (Tissera et al., 2019), the stellar spin parameter,  $\lambda$ , and the ratio between the rotational velocity,  $v$ , and the dispersion velocity,  $\sigma$ , of galaxies,  $v/\sigma$  (Lagos et al., 2018). All these parameters can be used to quantify the degree of stellar rotational support of galaxies. We highlight that, while D/T values are estimated using 3D information of the particle distributions and their angular momentum content, the  $\lambda$  and  $v/\sigma$  are 2D parameters obtained from a mock catalogue constructed by Lagos et al. (2018). From this catalogue, in this work we adopted the  $\lambda$  and  $\sigma$  values obtained when taking edge-on orientations of the galactic disks. These parameters are r-band luminosity-weighted within half-mass radius. Hence,  $\lambda$  and  $\sigma$  provides a more direct comparison with observations while D/T ratios measure the actual degree of rotation.

In Fig. 3.3.2, the D/T distribution for the three  $\Sigma$  types are shown. As can be seen, TII disks tend to have larger contributions of galaxies with  $D/T > 0.70$  while TI and TIII have larger number of galaxies with  $D/T < 0.65$ . The median D/T for the three samples are:  $0.64 \pm 0.08$ ,  $0.68 \pm 0.08$ ,  $0.63 \pm 0.07$  for TI, TII, TIII, respectively (the errors correspond to the standard deviation). These trends are in agreement with observations that reported a trend for TII disks to be more frequent in late-type galaxies while TIII profiles, in more dispersion-dominated disk galaxies (Erwin et al., 2008; Pohlen & Trujillo, 2006;

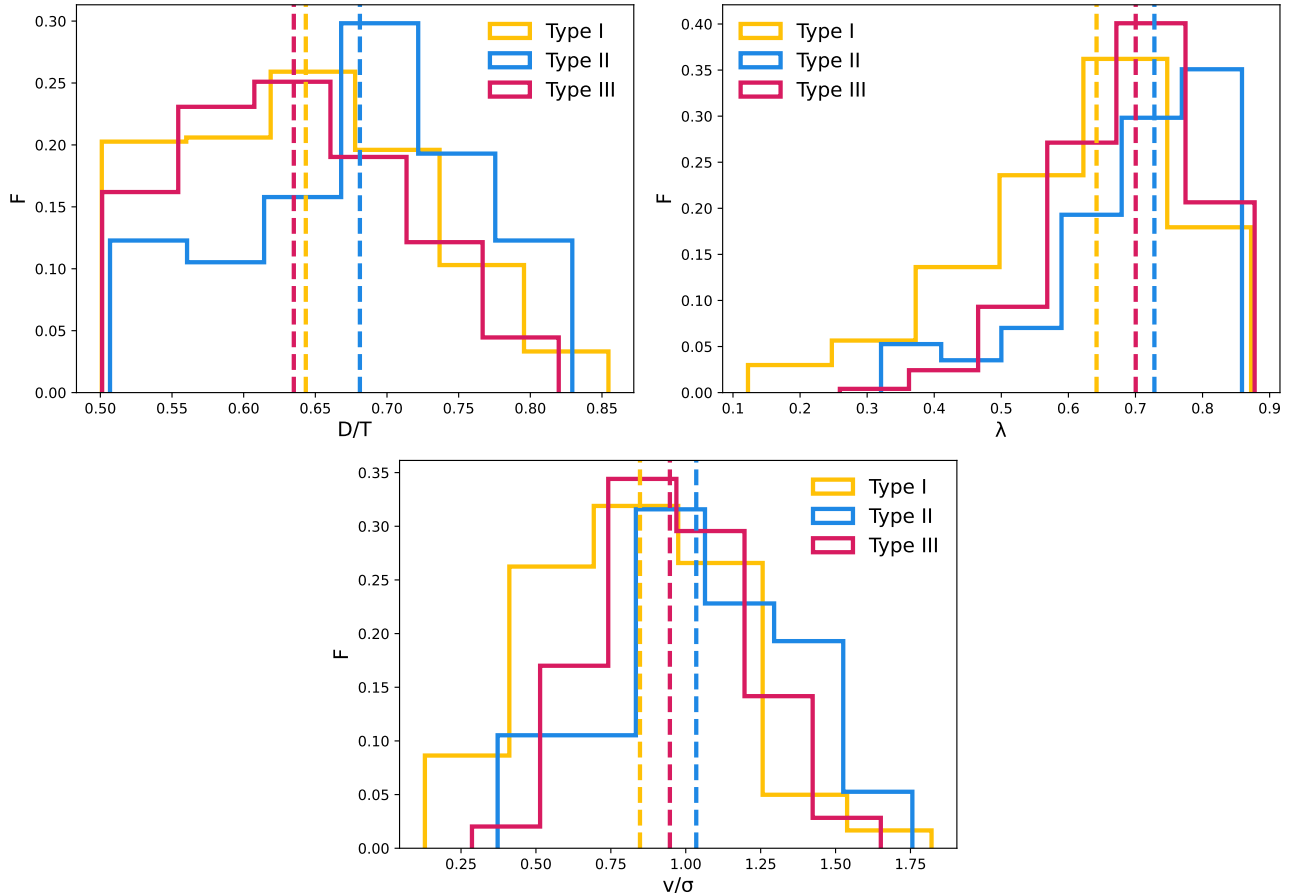


Figure 3.3.2: Distribution of galaxies with TI, TII and TIII disks as a function of  $D/T$  (left upper panel),  $\lambda$  (right upper panel) and  $v/\sigma$  (lower panel). The median values for each sub-sample are shown as indicated in the legend. The histograms are normalized by the total number of elements in each subsample.

Gutiérrez et al., 2011; Debattista et al., 2017).

Values for the spin parameter  $\lambda$  and the  $v/\sigma$  distributions of galaxies for each disk type are taken from Lagos et al. (2018). Clear disc-dominated systems are expected to have  $\lambda > 0.6$  approximately. However, in the middle panel of Fig. 3.3.2 we can see a small tail towards lower  $\lambda$  values which can be explained by the fact that these two parameters are estimated along the line-of-sight of edge-on projections (see also figure 4 in Rosito et al., 2019a). In Fig. 3.3.3 we explore the relations between  $D/T$  and  $\lambda$  for the three types of disks. Which they trace each other very well with Pearson correlation factors of 0.65, 0.611, 0.67 for TI, TII and TIII disks, respectively. However, that the dispersion increases for decreasing  $D/T$ , i.e. as the bulge component becomes more important to equal the disc. In this range of  $D/T \approx 0.5$  there is more variation of  $\lambda$  which could be due to projection effects. The  $v/\sigma$  provides an alternative quantification of the level of rotational support of galaxies. As can be seen from the middle panel of Fig. 3.3.2, the three  $\lambda$  distributions are skewed to low  $\lambda$  values, with the median values at  $0.64 \pm 0.15$ ,  $0.73 \pm 0.12$ ,  $0.70 \pm 0.1$  for TI, TII and TIII, respectively. The errors correspond to the standard deviations of each subsample. TII galaxies tend to have larger  $\lambda$  parameters while TI and TIII profiles tend to have larger contributions of galaxies with smaller  $\lambda$ .

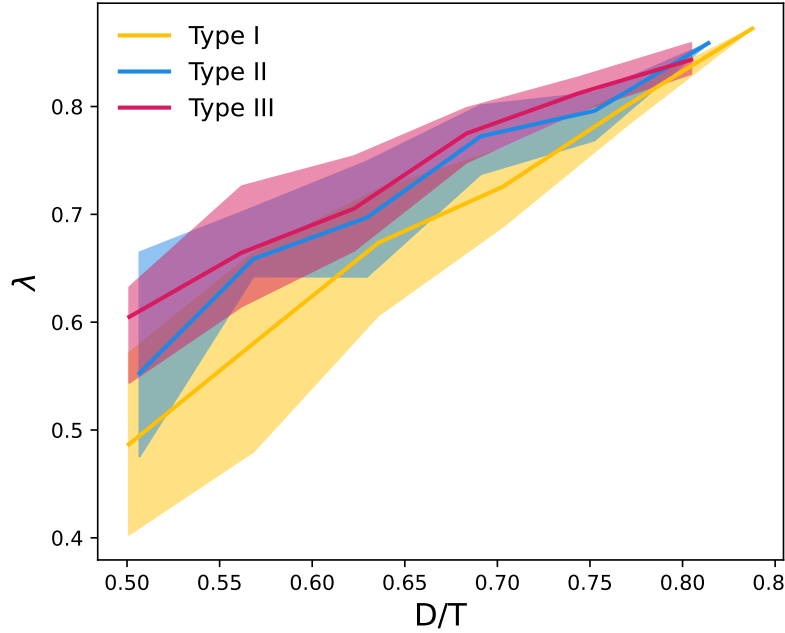


Figure 3.3.3: Correlation between  $\lambda$  and  $D/T$  for galaxies with TI (yellow), TII (blue) and TIII (pink) disks. The medians are shown by solid lines and the 25-75th are used to determine the shade areas.

In the lower panel of Fig. 3.3.2, the distributions for  $v/\sigma$  are shown with similar results. The median values of the  $v/\sigma$  distributions are  $0.85 \pm 0.3$ ,  $1 \pm 0.32$ ,  $0.95 \pm 0.24$  for TI, TII and TIII.

To assess the statistical significance of these findings, we applied a Kolmogorov-Smirnov test (KS test) to the  $\lambda$ ,  $v/\sigma$ ,  $D/T$  distributions. Table 3.3.3 shows the p-values corresponding to the comparison between the different distributions shown Fig. 3.3.2. It provides, for different parameters, an assessment of how different/similar the samples are between them. In the case of  $D/T$ , the KS analysis is consistent with the trend for TII to prefer disc-dominated galaxies.

TI and TIII show a trend to prefer galaxies less rotationally supported and, likely, with more significant inner spheroidal components or bulges. Conversely, disc-dominated galaxies have a larger fraction of TII profiles. We note that these are only global trends since there is a variety of galaxies with different morphologies for a given disk type. This finding suggests that, although the angular momentum content of the galaxies is relevant to shape the stellar mass distribution, and its disk scale-length, it is certainly not the only physical mechanisms at play.

To get further insight into the relation between the degree of rotation and the disk types, in Fig. 3.3.4 we show the inner scale-lengths, the outer scale-lengths and the  $R_{br}$  as a function of  $\lambda$ . We note that for TI disks only one scale-length can be defined and hence, there is no  $R_{br}$  for these galaxies. Similar trends are found if  $v/\sigma$  is used instead of  $\lambda$ . From the upper panel of Fig. 3.3.4, it is clear that, galaxies with  $\lambda \gtrsim 0.35$ ,  $h_i$  increases with increasing  $\lambda$ , for all types of disks. This is the expected trend when disks form under global angular momentum conservation (Mo et al., 1998). However, the trends change for  $\lambda \lesssim 0.35$  in TI disks, where an anticorrelation is detected. We estimated that the Pearson correlation is  $r = 0.55$  for  $\lambda \gtrsim 0.35$  and  $r = -0.35$  for  $\lambda \lesssim 0.35$ , for TI disks. Galaxies in this last range of  $\lambda$  have less significant disks than bulges and they might have been more affected by mergers and interactions

Table 3.3.3: Statistical analysis: p-values for the KS test applied to the  $\lambda$ ,  $v/\sigma$ ,  $D/T$  and stellar mass distributions for each type disks: TI, TII and TIII.

disk type	p-value $_{\lambda}$	p-value $_{v/\sigma}$	p-value $_{D/T}$
TI vs TII	0.0006	0.0003	0.01
TI vs TIII	0	0	0.43
TII vs TIII	0.39	0.08	0.0003

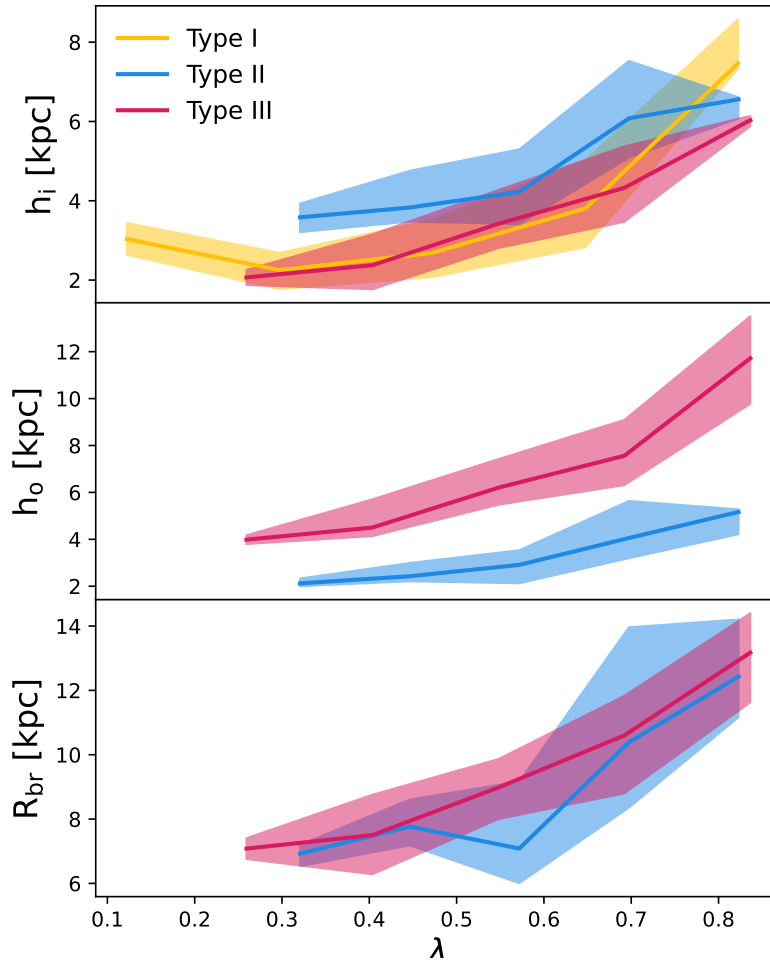


Figure 3.3.4: Median characteristic scales for the three disk types as a function of  $\lambda$ :  $h_i$  (upper panel),  $h_o$  (middle panel), and  $R_{br}$  (lower panel). The shaded regions denote the 25-75<sup>th</sup> percentiles.

(Lagos et al., 2018; Rosito et al., 2019a). From this figure, we can also see that, at a given high  $\lambda$ ,  $h_i$  increases systematically from TI, TIII and TII disks. This suggests the action of various processes during disk formation beyond the global conservation of angular momentum, such as the redistribution of gas and/or stellar populations, e.g. due to the accretion of satellites, which inspire angular momentum into the disc; also disk perturbations such as bars, spirals, and lopsided modes could be related to this trend

(see discuss in section 4.4.4.1). The tendency for  $h_i$  to be larger in TIII than in TI is agreement with the observational results reported by Gutiérrez et al. (2011).

Regarding TII and TIII disks, we can extend the comparison to  $h_o$  and  $R_{br}$  as shown in the middle and lower panels of Fig. 3.3.4. As can be seen, the  $h_o$  for TIII disks are systematically larger than those of TII disks at given  $\lambda$ . The  $h_o$  of both disk types increase with increasing  $\lambda$ . However, the processes that shape the  $\Sigma$  profiles in the outskirts of strong TII produce a different dependence of  $h_o$  on  $\lambda$ . TIII and TII disks show clearly correlations between  $\lambda$  with  $h_o$  and  $R_{br}$ . We estimated Pearson correlation factors of  $r \sim 0.51$  for both relations for TIII disks and for TII disks, we obtained  $r = 0.48$  and  $r = 0.44$ , respectively.

The  $R_{br}$  values are similar for TII and TIII profiles at a given  $\lambda$ , in both cases, showing a positive trend, so that more rotationally supported disks break at larger galactocentric radius. Larger galactocentric radius could be linked to angular momentum increase from quiescent mergers as well as strong AGN feedback (Grand et al., 2017). This could be connected to the discussion in section 4.4.4.1.

Our results show that TII disks are preferentially found in galaxies which are strongly dominated by rotation.

### 3.3.4 Distributions of $R_{min}$ , $R_{max}$ and $R_{br}$

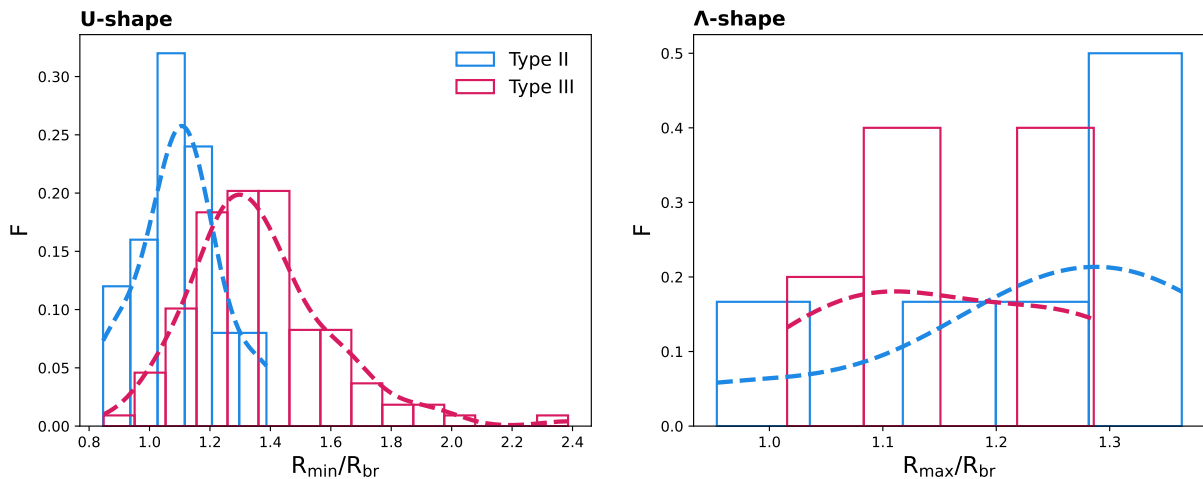


Figure 3.3.5: Distributions of  $R_{min}/R_{br}$  (left panel) and  $R_{max}/R_{br}$  (right panel) for U-shape and  $\Lambda$ -shape age profile, respectively, in TII (cyan, dashed lines) and TIII (pink, dashed, lines) disks.

In order to better quantify the relative position of  $R_{min}$  and  $R_{max}$  of the age profiles with respect to  $R_{br}$  of the  $\Sigma$  profiles, the distributions of these parameters are included in the next sections, we estimated the ratios  $R_{min}/R_{br}$  and  $R_{max}/R_{br}$  for TII and TIII disks.

In Fig. 3.3.5 we show the probability density function (PDF) by using the Kernel Density Estimation. As can be seen from the top panel, galaxies with U-shape age profiles have different values and distributions of  $R_{min}/R_{br}$ . TII disks show this ratio with a maximum frequency at  $R_{min}/R_{br} \approx 1$  and the distribution are more concentrated around this value. Conversely, TIII disks have a more extended distribution, which

cover a larger values of  $R_{\min}/R_{\text{br}}$ , indicating that in these disks the minima in the age profiles are located further out in the disks with respect to  $R_{\text{br}}$ . This means that the upward bend of the U-shape age profile for TII galaxies is closer to  $R_{\text{br}}$  than for TIII, as we will show in the next sections. The larger variety of  $R_{\min}/R_{\text{br}}$  detected for TIII disks, most of them larger than 1, suggest that the physical mechanisms behind the change in age might not be directly related with the star formation process and hence, could be more associated to environmental effects or migration.

Similar estimations were performed for  $R_{\max}/R_{\text{br}}$ . As can be seen from the right panel of Fig. 3.3.5, the distributions are very noisy because of the low number of galaxies with this particular age profile. There is a weak trend for TII to have slightly larger values. However considering the low number of members of this subsample, we prefer to be cautious and not draw a conclusion.

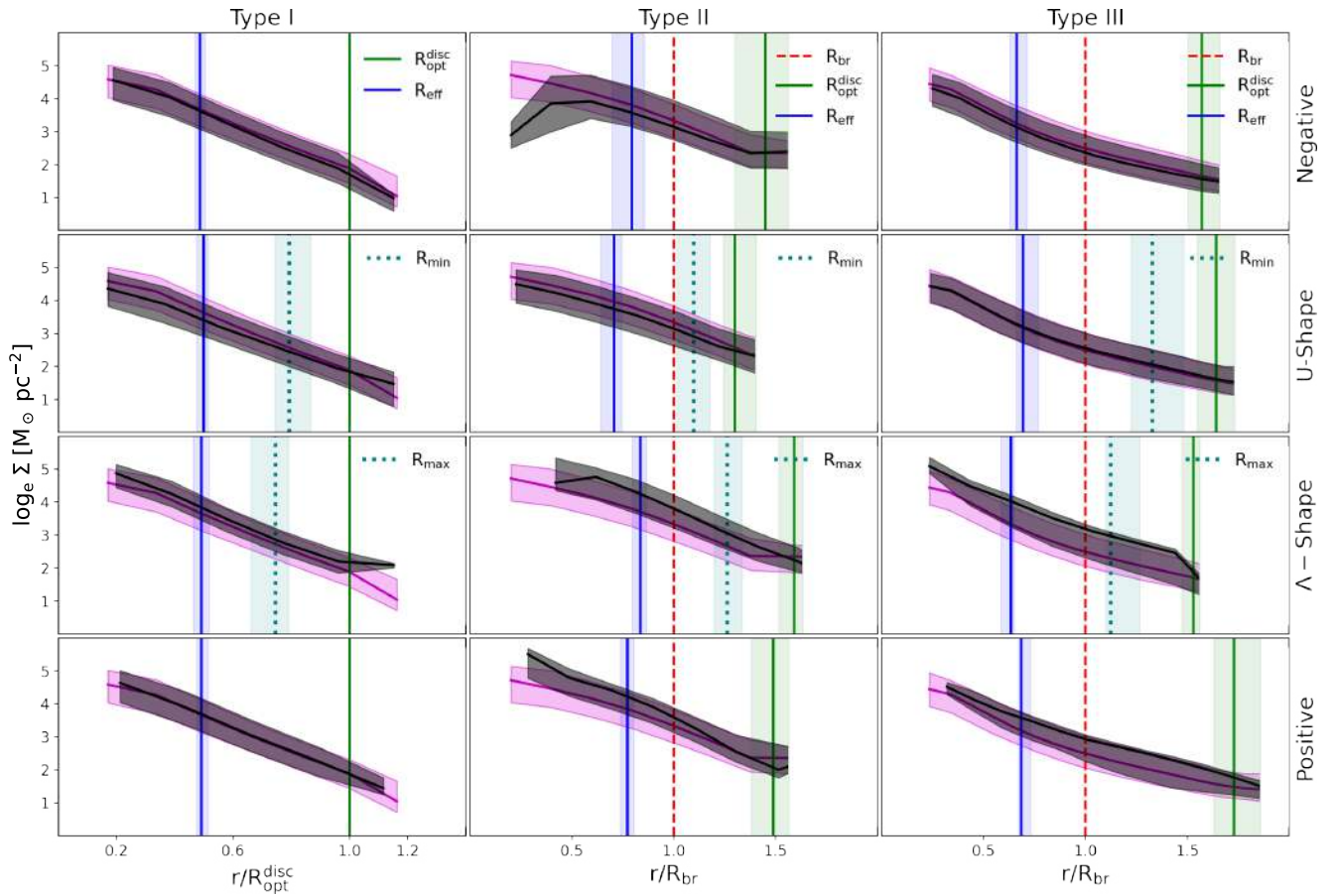


Figure 3.3.6: Median  $\Sigma$  for TI (left column), TII (middle column) and TIII (right column) stacked profiles of disks with different age profiles (grey shaded region). For comparison, the median  $\Sigma$  stacked according only to  $\Sigma$  profiles are shown (violet shaded region). Shaded regions encompass the 25 – 75<sup>th</sup> percentiles (and each profile stacked were created between  $0.5R_{\text{eff}}$  to  $1.5R_{\text{opt}}^{\text{disc}}$ ). The medians and shaded regions defined by the 25 – 75<sup>th</sup> percentiles of  $R_{\text{br}}$ ,  $R_{\text{opt}}^{\text{disc}}$ ,  $R_{\text{eff}}$ ,  $R_{\min}$ ,  $R_{\max}$  are also depicted.

### 3.3.5 Statistical analysis of $\Sigma$ and the age profiles

As we mentioned above, three types of  $\Sigma$  and four different types of age profiles are defined and identified in the EAGLE sample. In order to further explore the connection between characteristics of the  $\Sigma$  and the distribution of stellar age in the disks, in Fig. 3.3.6 we show the median  $\Sigma$  for a given disk type (violet lines and shaded region): TI (left column), TII (middle column) and TIII (right column). For each disk type subsample, we subdivided and stacked the  $\Sigma$  profiles according to the corresponding four age profiles (rows panels). The resulting median of each subpopulation is shown by a black solid line and shaded region. To perform the stacking of  $\Sigma$  profiles, they were first normalised by a characteristic radius. For the double-exponential  $\Sigma$ , i.e. TII and TIII, the median distributions are normalized by  $R_{\text{br}}$ , while for TI galaxies by  $R_{\text{opt}}^{\text{disc}}$ <sup>5</sup>. The vertical green and blue solid lines show the medians of  $R_{\text{opt}}^{\text{disc}}$  and  $R_{\text{eff}}$ , respectively.  $R_{\text{br}}$  is shown with a dashed red line while both  $R_{\text{min}}$  and  $R_{\text{max}}$  (depending on the  $\Sigma$  and age type) with cyan dashed lines, respectively. These last two radii denote the location of the minimum and maximum of the age profiles, respectively. All shaded areas shown in this figure are defined by the 25<sup>th</sup> and 75<sup>th</sup> percentiles of the corresponding distributions.

As can be seen from Fig. 3.3.6, TI disks show very similar  $\Sigma$  for all age profiles. The positive and  $\Lambda$ -shape profiles show slightly higher densities than the global stacked profile. Certain trends can be also noticed in the distributions of the characteristic radii, namely  $R_{\text{br}}$ ,  $R_{\text{opt}}^{\text{disc}}$ ,  $R_{\text{eff}}$ ,  $R_{\text{min}}$  and  $R_{\text{max}}$  (the latter two only correspond to the U-shape and  $\Lambda$ -shape age profiles, respectively). For TI profiles, both  $R_{\text{min}}$  and  $R_{\text{max}}$  tend to be located within  $R_{\text{opt}}^{\text{disc}}$ , whereas for TII and TIII these radii are located between  $R_{\text{br}}$  and  $R_{\text{opt}}^{\text{disc}}$ . In general, if we focus on the disks with the U-shape profiles, we note the upward bend of the age profile for TII galaxies (see  $R_{\text{min}}$ ) is located closer to  $R_{\text{br}}$  than for the TIII type, where  $R_{\text{min}}$  tends to be at larger radii on average (but still within  $R_{\text{opt}}^{\text{disc}}$ ). These differences between the distributions of those scalelengths are discussed in Sec. 3.3.4 for TII and TIII. This suggests that TII disks with U-shape age profiles, where  $R_{\text{min}}$  is closer to  $R_{\text{br}}$  in general, experience a sharp decrease of star formation rate giving rise to an outer disk with older population. In the case of the TIII profiles the change of the star formation activity may occur further out in the disks. As a result the TIII disks could be populated by younger/intermediate age stars out to larger radii. In the following sections, we will analyse the distribution of stellar populations by age and the star formation rate density. We also acknowledge the fact that other processes such as mergers, radial migration or environmental effects could also contribute with old stars to the outer regions of TIII, particularly.

### 3.3.6 Distribution of the mono-age stellar populations

In order to understand the origin of the different  $\Sigma$  profiles in relation to the characteristics of their age distributions, we compute the stellar mass fraction profiles for each galaxy by considering three different age intervals: young stars ( $< 2$  Gyr), intermediate age stars (2-6 Gyr) and old stars ( $> 6$  Gyr). They will be considered as three mono-age stellar populations. TI galaxies are normalised by  $R_{\text{opt}}^{\text{disc}}$ , while TII and TIII galaxies are normalised by  $R_{\text{br}}$ . In this way, they can be stacked according to galaxies disk types and age profiles. For each subsample, the median stellar mass fraction for mono-age stellar populations is estimated as a function of radius. The mass fraction is calculated with respect to the total stellar mass per

<sup>5</sup>The normalization of double-exponential galaxies aims to compare the differences between the inner and outer regions relative to  $R_{\text{br}}$ . Type I galaxies, which by definition have no  $R_{\text{br}}$ , are normalized on the basis of their  $R_{\text{opt}}^{\text{disc}}$ . Nevertheless, we take this distinction into account in our comparisons.

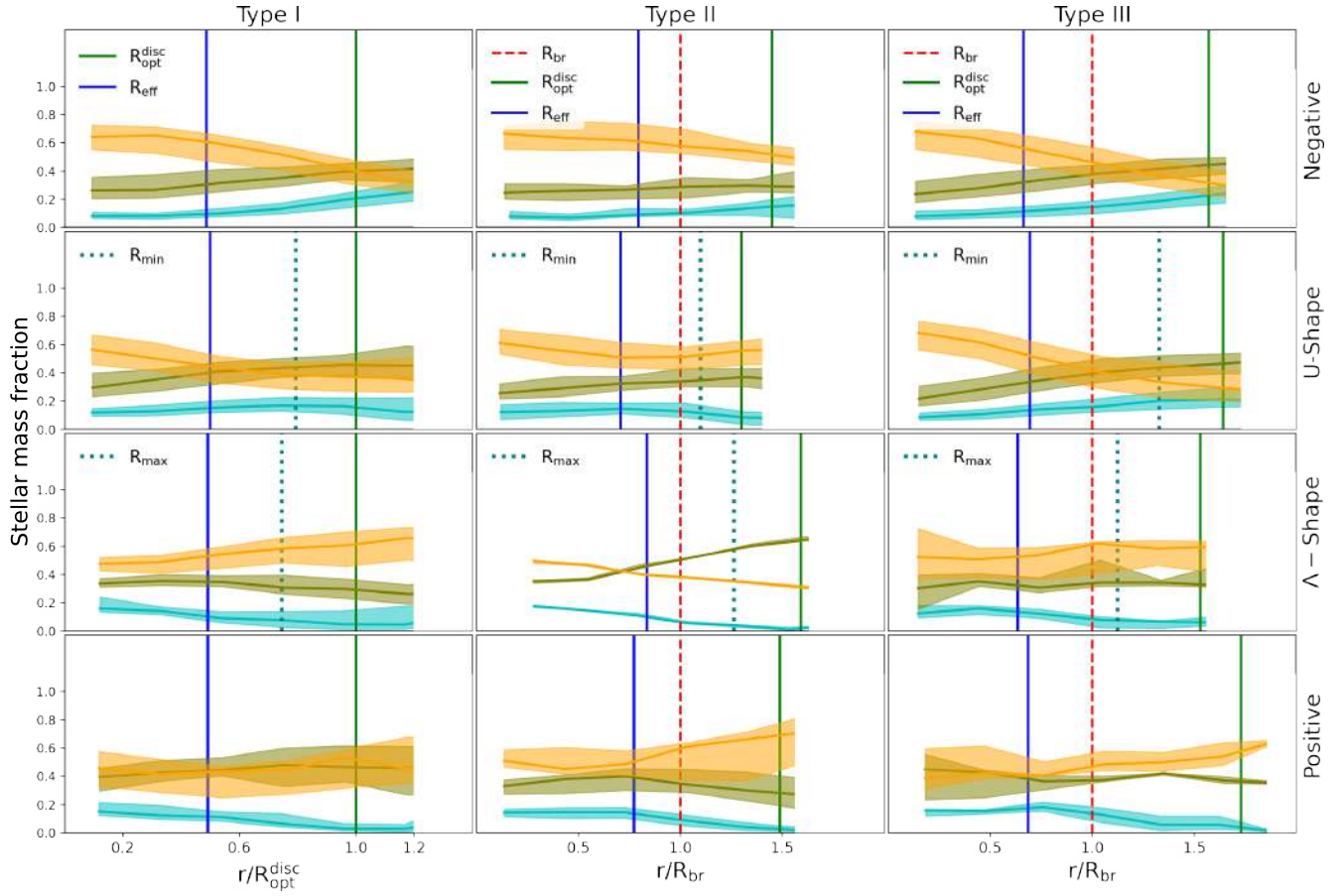


Figure 3.3.7: Median stellar mass fractions a function of the normalised radius for TI (left panels), TII (middle panels) and TIII (right panels) disks, separated according to their age profiles: negative (upper panels), U-shape (second upper panels),  $\Lambda$ -shape (third panels) and positive (fourth panel). Stellar populations are divided into three age groups: young stars,  $< 2$  Gyr (cyan lines), intermediate stars,  $2 - 6$  Gyr (olive lines) and old stars,  $> 6$  Gyr (orange lines). The shaded regions are defined by the 25 – 75<sup>th</sup> percentiles. The following median characteristics radii are included:  $R_{br}$ ,  $R_{opt}^{disc}$ ,  $R_{eff}$ ,  $R_{min}$ ,  $R_{max}$ .

radial interval. Figure 3.3.7 shows the stacked stellar mass fractions of disks for each of  $\Sigma$  type and each age type. TI, TII and TIII (left, middle, and right column respectively) and negative, U-shape,  $\Lambda$ -shape, and positive age profiles (top/first, second, third, bottom/fourth rows, respectively). The corresponding characteristics radii are also included. The shaded colored regions correspond to young, intermediate and old age intervals (cyan, olive and orange regions respectively), and are enclosed by 25<sup>th</sup> and 75<sup>th</sup> percentiles of the stacked profiles each subsample. For these stacked profiles,  $R_{eff}$ ,  $R_{br}$ ,  $R_{min}$  and  $R_{max}$  are the corresponding medians for each  $\Sigma$  and age types. Hereafter, we will only use these medians for reference.

As can be seen from Fig. 3.3.7, TI profiles with the U-shape and negative age profiles tend to have larger mass fractions of old populations than intermediate ones in the central region. In fact, approximately 60 per cent of the stellar mass corresponds to old stars. The contribution of these mono-age populations decreases rapidly for increasing radius. Meanwhile, the fraction of young stellar populations varies

slightly within  $R_{\text{opt}}^{\text{disc}}$ , increasing systematically with increasing radius for disks with negative age profiles so that it reaches 20% at  $R_{\text{opt}}^{\text{disc}}$ . For TI systems with U-shape age profiles, the fraction of young stars are similar, with a weak increase around  $R_{\text{min}}$ . However, at this characteristic radius the contribution of intermediate age stars is more important than the old stars, explaining the change in slope of the U-shaped age profile with TI galaxies. For  $\Lambda$ -shape and positive profiles, the relative fractions of the old and intermediate populations are dominant throughout the disks. However, they have higher concentration of young stars in the central regions than the outskirts. This concentration diminishes significantly at about  $R_{\text{max}}$  for  $\Lambda$ -shape and close to  $R_{\text{opt}}^{\text{disc}}$  for the positive profiles.

For TII disks with U-shape and negative age profiles, the old population represents the largest mass contribution on the whole disc, representing more 60 per cent in the central regions. It is interesting to note the change of trends in the old populations from  $R_{\text{min}}$  in U-shape profiles. For instance, intermediate age stars have an increasing contribution from the inner to the outer regions in U-shape age profiles, while negative age profiles is almost constant. In particular, the mass fraction of young populations for negative profiles tend to be almost constant within  $R_{\text{opt}}^{\text{disc}}$ . However, for systems with U-shape profiles, there is clear decrease of the contribution of young population from  $R_{\text{min}}$ . The latter suggests a drop in star formation activity at large galactocentric distances. For galaxies with positive age profiles, there is an important contribution of old stars populations in the outer region ( $r > R_{\text{br}}$ ), and a decrease of young and intermediate populations. Conversely, the mass fractions of young and intermediate stellar populations increases in the central regions. However, we stress that for  $\Lambda$ -shape age profiles the number of galaxies is very small to draw a robust conclusion.

For TIII disks with negative and U-shape age profiles we also find larger fractions of old populations in the inner regions. The old disk decrease rapidly for  $r > R_{\text{br}}$  while the intermediate age populations have more contribution at the same radial range. This might indicate the presence of an old inner disk which is more concentrated than TII galaxies. Furthermore, the outer disks are more dominated by intermediate age stars from  $R_{\text{min}}$  in U-shape and from  $R_{\text{opt}}^{\text{disc}}$  for negative age profiles. The young populations tend to increase in the outer region, even are similar to the contribution of old stars in the very outskirts of the disks. Similar to TII, the low number of galaxies in the  $\Lambda$ -shapes and positive age profiles are not enough to draw a robust conclusion.

In summary, we find different contributions of mono-age stellar populations in the three defined disk types, which modulate their  $\Sigma$  profiles. We note the physical meaning of  $R_{\text{min}}$  in U-shape age profiles, which might highlight the locus of a drop in star formation activity in TII profiles (and probably the origin of the break in these types) and the dominance of the intermediate population, even over the old stellar population for  $r > R_{\text{br}}$  in TIII galaxies. We will explore this issue in more detail in the following section.

### 3.3.7 Statistical analysis of the star formation activity

In this section, we explore the star formation rate surface density,  $\Sigma_{\text{SFR}}$ , for galaxies with different  $\Sigma$  and age profiles to provide an interpretation on the origin of the behaviours described above. To estimate the current star formation activity, the  $\Sigma_{\text{SFR}}$  is computed considering stars particles younger than 2 Gyr. For this estimation, only galaxies with more than 500 young stars particles were considered<sup>6</sup>. The  $\Sigma_{\text{SFR}}$

<sup>6</sup>We acknowledge the fact that this is a relative large age interval. However, adopting a shorter one results in significant reduction of the number of galaxies. Consequently, it would affects our statistics. On the other hand, 2 Gyr is the same threshold assumed to define young stellar populations. This allow us to correlate the results of Fig. 6 and Fig. 7 more directly.

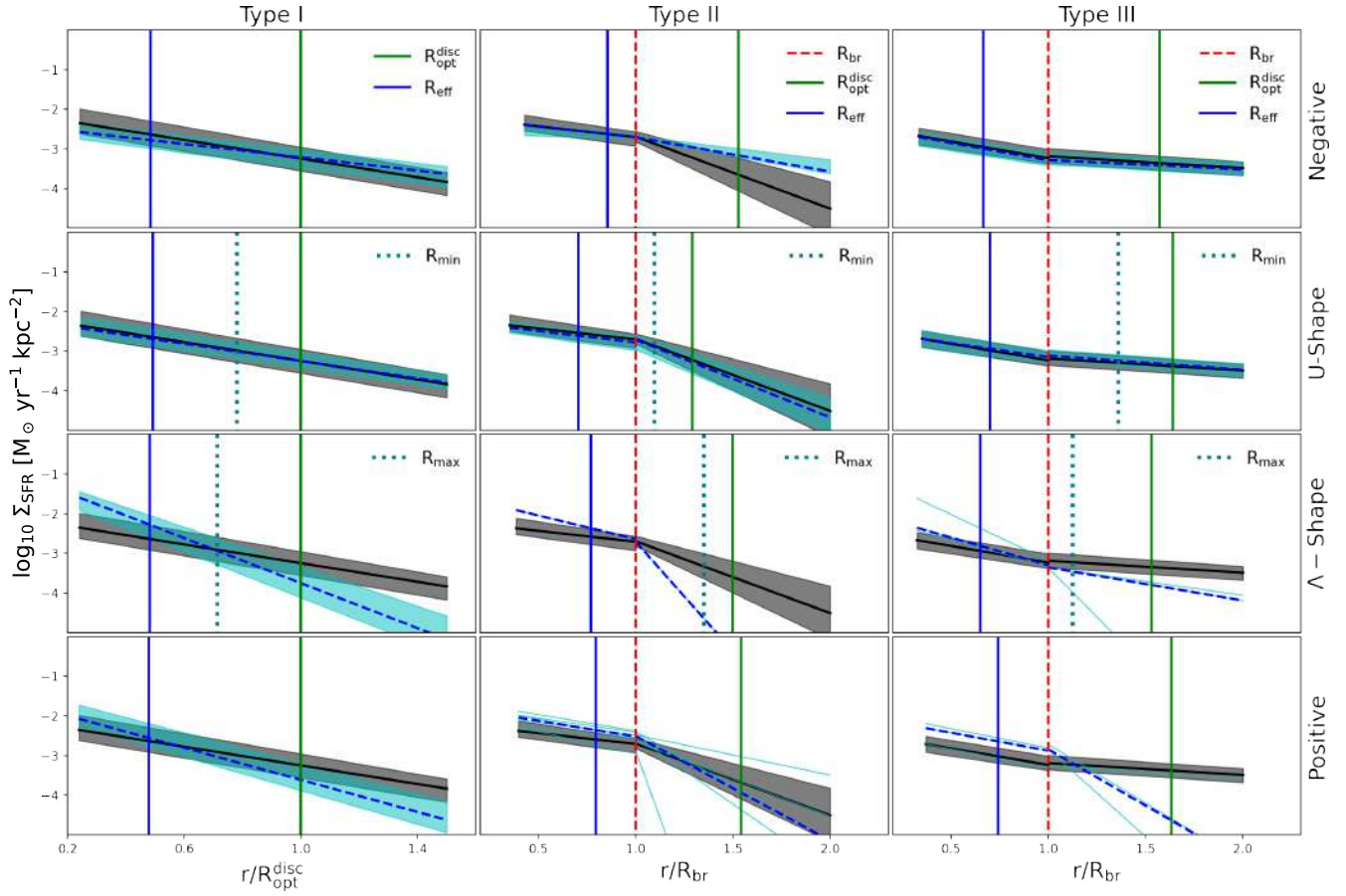


Figure 3.3.8: Median  $\Sigma_{\text{SFR}}$  profiles for different types of  $\Sigma$  and ages profiles (dashed blue lines). For comparison, the median  $\Sigma_{\text{SFR}}$  profiles of each disk type are included (gray solid line). The shaded regions cover 25-75<sup>th</sup> percentiles of the corresponding relations (gray and cyan shaded areas). The characteristics radii,  $R_{\text{br}}$ ,  $R_{\text{opt}}^{\text{disc}}$ ,  $R_{\text{eff}}$ ,  $R_{\text{min}}$ , and  $R_{\text{max}}$ , are included when corresponding.

profiles are estimated by using moving averages. The aim of this section is to analyse the changes of  $\Sigma_{\text{SFR}}$  profiles between the inner and outer zones of the disks. For TII and TIII disks,  $\Sigma_{\text{SFR}}$  profiles are normalized by  $R_{\text{br}}$  while for TI disks, they are normalized by  $R_{\text{opt}}^{\text{disc}}$ . Then we fitted a linear regression between  $0.5R_{\text{eff}}$  and  $1.5R_{\text{opt}}^{\text{disc}}$  for the TI galaxies, and applied a double linear regression to the TII and TIII galaxies (see Section 3.2.2), within the radial range  $[0.5R_{\text{opt}}^{\text{disc}} - R_{\text{br}}]$  and  $[R_{\text{br}} - 1.5R_{\text{opt}}^{\text{disc}}]$ . We then estimate the median gradients and the 25<sup>th</sup> and 75<sup>th</sup> percentiles for each corresponding subsample. The results of this procedure are shown in Fig. 3.3.8. The black solid lines show the overall median  $\Sigma_{\text{SFR}}$  profile for TI (left panels), TII (middle panels) and TIII (right panels) type disks, and has been included for reference. The blue, dotted lines show the median profiles obtained by subdividing the samples according to their age profiles. The shaded regions (cyan) correspond to 25-75<sup>th</sup> percentiles of the corresponding subsample. Due to the low number of galaxies with enough young stars, TII and TIII galaxies with positive and  $\Lambda$ -shape age profiles are shown individually.

As can be seen from Fig. 3.3.8, the negative and U-shaped age profiles show a slightly lower  $\Sigma_{\text{SFR}}$  in the inner regions than the overall TI profile. This is agreement with our previous results that show that

the old populations dominate the inner regions while the intermediate stellar populations become more important in the outer regions as expected in a inside out formation model. Both types of age profiles are the most numerous in TI. Indeed, the general shape for TI galaxies (black region) is mainly determined by the U- and negative age profiles. We note that the  $\Sigma_{\text{SFR}}$  profiles in TI disks with U-shape age profiles does not show a break, in agreement with Fig. 3.3.6 where we can see that the intermediate age stars seem to be responsible of the shape of age profiles. TI disks with positive or  $\Lambda$ -shape age profiles show a clear change in the median slope of  $\Sigma_{\text{SFR}}$  with respect to the overall TI profiles, indicating higher level of star formation activity in the inner regions than in the outer parts. TI galaxies with  $\Lambda$ -shape show the highest SFR density in the central regions and the lower one in the outskirts.

TII disks have mainly negative and U-shape profiles. Those with negative slopes have higher  $\Sigma_{\text{SFR}}$  profiles than average for  $r > R_{\text{br}}$ . These SFR profiles can be well fitted by a single exponential (the change in slopes between the  $r > R_{\text{br}}$  and  $r < R_{\text{br}}$  is very small). TII systems with U-shape age profiles have a SFR distribution consistent with  $\Sigma$  profiles, i.e. they show a clear break at about the  $R_{\text{min}}$ . The higher star formation activity in the central region keeps reinforcing the break in the  $\Sigma$  profiles. In TII disks there is only one  $\Lambda$ -shaped age profile, indicating that the rest of the galaxies in this group have few young stellar particles. These systems have higher SFR in the inner region and a sharp decrease for  $r > R_{\text{br}}$ . We emphasize that the change of slopes of the age profiles at  $R_{\text{max}}$  is due to higher contributions of the intermediate and old stellar populations in the outer regions. Finally those disks with positive profiles have higher inner SFR and slightly lower one in the outer parts.

TIII disks show  $\Sigma_{\text{SFR}}$  profiles with similar breaks and change of slopes for disks with negative and U-shape age profiles. The change in slope is consistent with a slight increase of the SFR in the outer regions, for  $r > R_{\text{br}}$ , but the  $R_{\text{min}}$  is further away from  $R_{\text{br}}$ . This could suggest that U-shape profile might be modulated by other processes beyond the star formation activity in the galaxy. Those with positive and  $\Lambda$ -shape age distributions show again higher SFR in the central regions as expected. We recall that there are fewer than 10 galaxies in these subsamples. Hence TIII tend to have negative and U-shape profiles, as mentioned in the previous section. The U-shape in age profiles can be associated to both a decrease of the SF activity with decreasing radius and the more significant contribution of intermediate age stars in the outskirts as discussed in the previous section.

In summary, the  $\Sigma_{\text{SFR}}$  profiles vary differently for different disk types. TI disks have  $\Sigma_{\text{SFR}}$  gradients that vary for different age profiles, being negative steeper for disks with positive gradients. The TII and TIII disks have  $\text{Sigma}_{\text{SFR}}$  profiles that change slopes according to their  $\text{Sigma}$  profile, with slopes breaking slightly downward and slightly upward for  $r > r_{\text{break}}$ , respectively. In the case of TIII profiles the break in the U-shape age profiles are further out, overall, in comparison with the break in the  $\Sigma$  profiles, suggesting that the other mechanisms could contribute to shape them.

### 3.3.8 Statistical analysis of the median vertical height profiles

Radial migration via scattering by non-asymmetric perturbations or churning might have an impact on the outskirts of disk galaxies (Debattista et al., 2017). The contribution of stellar migration to vertical heating in the outskirts and secular evolution in disk galaxies could also lead to flaring (Minchev et al., 2012b), although mergers and interactions are also proposed to be the main cause for the effects (García de la Cruz et al., 2021; Grand et al., 2017). disk flaring increases with radius in older stellar populations, while flaring in younger populations is reported to be weaker (Minchev et al., 2015). Thus, a thick disk compo-

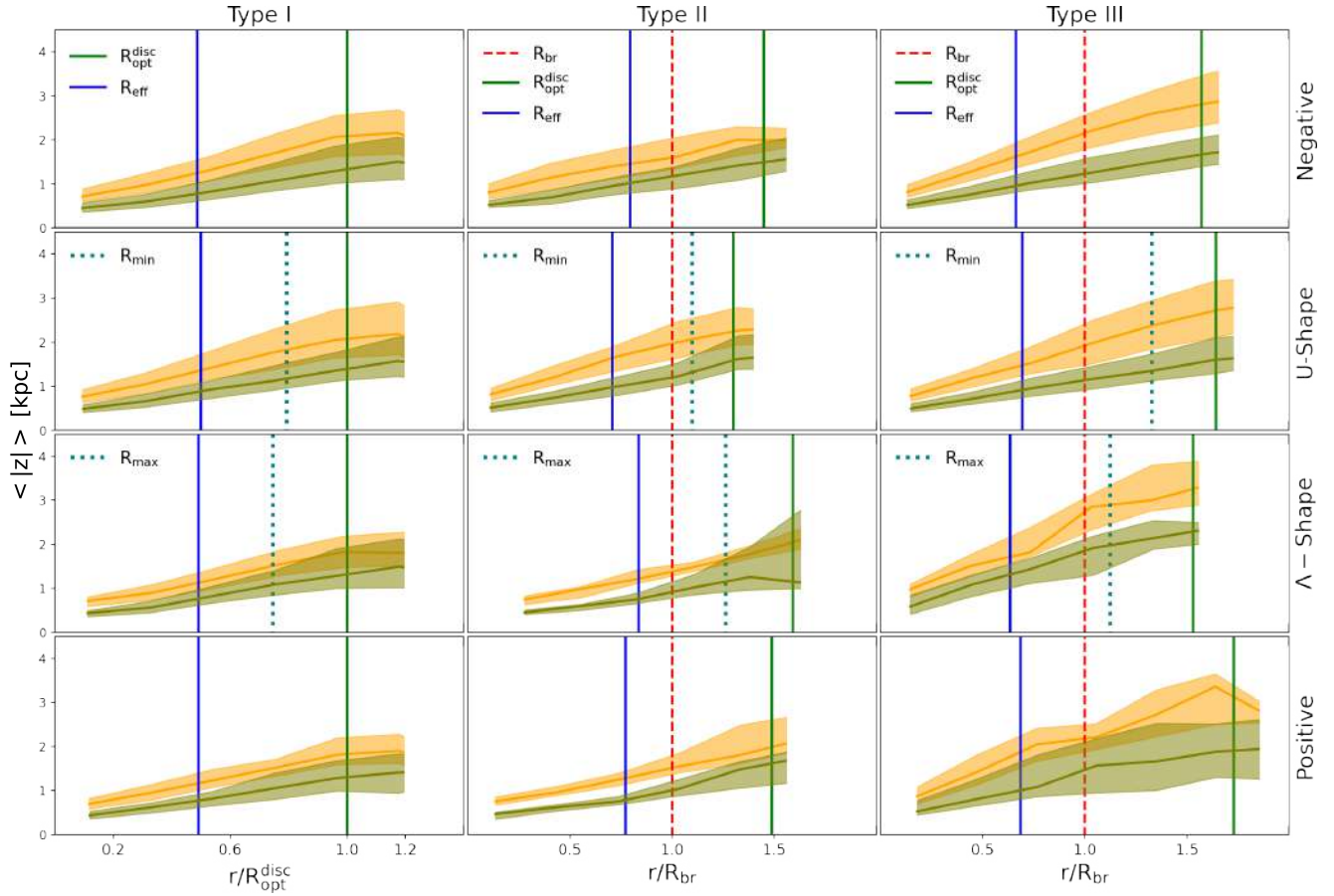


Figure 3.3.9: Distribution of the median height ( $\langle |z| \rangle$ ) with respect to the midplane galactic as a function of galactocentric distances. These profiles are stacked according to the  $\Sigma$  and age types. The shaded regions are enclosed by corresponding 25-75<sup>th</sup> percentiles. The orange shaded regions correspond to the old stars with ages  $> 6$  Gyr and the olive shaded regions, to the intermediate age stars, 2-6 Gyr.

ment and a high velocity dispersion of the old stellar populations in the disk outskirts could indicate the action of scattering (Minchev & Famaey, 2010) or radial migration (Minchev et al., 2012a). Nevertheless the effect of radial migration on disks is still a controversial issue with many works providing different results (Roškar et al., 2013; Grand et al., 2016).

While it is beyond the scope of this Chapter to study in detail the impact of these mechanisms<sup>7</sup>, we can assess the behaviour of the flaring in the median absolute heights,  $\langle |z| \rangle$ , for different types of disks. For this purpose we estimate the heights of the old ( $> 6$  Gyr) and intermediate (2-6 Gyr) age stellar populations with respect to the galactic mid-plane as a function of radius (normalized by  $R_{br}$  in double exponential types and  $R_{opt}^{disc}$  for TI disks) for the different disk types. Then, the distributions are stacked per  $\Sigma(r)$  and age profile types.

In Fig. 3.3.9 we show the  $\langle |z| \rangle$  profiles stacked for the old stars (orange regions) and intermediate stars

<sup>7</sup>We will not analyse in detail the displacement of stellar particles from their birth radius due to the low number of snapshots available to follow the orbits. This introduces numerical noise which does not allow a clear estimation of the fraction of migrated stars.

(olive regions).

For TIII disks the old stellar populations tend to have the larger flaring with respect to other two disk types. This trend is present for disk with different age profiles. disks with positive and  $\Lambda$ -shape age profiles have larger variations due to the low number of members (i.e. less than 10 galaxies in the sub-samples). TI and TII disks have similar level of flaring but TII systems show very low variety (quantified by the 25-75<sup>th</sup> percentiles). These trend suggest that TIII would be more affected by radial migration or by the accretion of satellites in the outer parts (Debattista et al., 2017).

### 3.4 discussion and Conclusions

In this Chapter we explored the shape of the surface density profiles,  $\Sigma$ , of disk-dominated galaxies selected from the largest-volume simulation of the EAGLE Project. Our sample of simulated galaxies was required to have  $D/T > 0.5$  and their disk components were classified according to their  $\Sigma(r)$  as types TI, TII and TIII. To obtain reliable results, we focused our statistical analysis on the so-called strong type, i.e., those galaxies identified to have the strongest breaks on their density distribution.

We also analysed the age profiles, the SFR surface densities, the mono-age stellar distributions and variation of the vertical height and its dispersion of galaxies belonging to the three defined disk type. Our main results can be summarized as follows:

- The EAGLE disks show the three expected  $\Sigma(r)$  distributions so that they can be classified as TI, TII and TIII disks. We find that, in this simulation and for mass-weighted  $\Sigma(r)$ , TIII and TI are the more frequent types in our EAGLE sample. We note that the simulated galaxies can be located in different kind of environment.
- Overall, there is a trend between the morphology (i.e. quantified by  $D/T$ ) and the disk types. TII disks are more frequent in late-type spirals, while TI and TIII tend to be detected in more early-type spiral systems. These trends are in agreement with observations (Pohlen & Trujillo, 2006; Gutiérrez et al., 2011). However, we note that there is a large variety of morphologies for galaxies with different disk types, which suggests the action of other physical mechanisms on the distributions of the stellar populations in the disks.
- Our analysis shows a clear correlation between the inner disk scale-lengths and the stellar spin parameter,  $\lambda$  for all three disk types with  $\lambda \geq 0.35$ . Additionally, at a given  $\lambda$ , there is a systematic increase of the inner disk scale-lengths from TI to TIII and TII, in that order. Indeed, TII disks have the larger inner disk scale-lengths in agreement with observations. Regarding the outer disk scale-lengths, both TII and TIII disks show a positive correlation with  $\lambda$  and that the outer scale-lengths of TIII are systematically larger. This suggests that the outer disk regions in the TII disks might have grown by a weak star formation activity, maybe fed by smooth accretion (Fig. 3.3.8), whereas in TIII disks other mechanisms associated with the local environment, such as galaxy interactions, could have affected the distribution of stellar populations (Younger et al., 2007; Laine et al., 2014) or stellar migration of intermediate age stars.
- Four types of age profiles are identified in disks regardless of their  $\Sigma$  type: negative, U-shape, positive and the so-called  $\Lambda$ -shape age profiles. The U-shape is the most frequent type followed

by the negative one. Together they represent  $\sim 70$  percent of the strong types subsamples. The positive and  $\Lambda$ -shape age profiles are found mainly in TI and TII galaxies, together accounting for 37 and 34 percent, respectively.

While U-shape, negative, and positive age profiles have been reported in previous works (e.g. Debattista et al., 2017), we also identify  $\Lambda$ -shape profiles in the few simulated disks. In this simulation, this age profile is produced by a significant increase of the star formation activity in the inner disk regions, together with a slight increase of the intermediate populations (2-6 Gyr old) in the outer regions. However, we note that previous studies of dispersion-dominated galaxies in the EAGLE simulations have also reported larger star formation activity in the central regions than expected, which might suggest the need for a more efficient AGN feedback, which could prevent late star formation activity (Rosito et al., 2019b,a; Lagos et al., 2020). This could be also true for our sample which is composed by disc-dominated galaxies.

- TI disks show the distributions of mono-age stellar populations consistent with an inside-out formation scenario, and have  $\Sigma_{\text{SFR}}$  profiles that decay systematically with increasing galactocentric distances. The U-shape profiles can be associated to larger contributions of intermediate age stellar populations. In fact, the minimum median age is statistically located at a radius from which the frequency of intermediate stars surpass those of the others mono-age stellar populations. TI disks with positive and  $\Lambda$ -shape age profiles have both similar fractions of old and intermediate stars and more significant contributions of young stars in the central regions. The larger star formation activity in the central regions is accompanied by a shirking of the SFR in the outer regions. The overall median  $\Sigma_{\text{SFR}}$  is well approximated by a single exponential law but with a shorter typical scale-length than TI with negative and U-shape age profiles. The triggering of star formation activity in the inner regions could have been produced by recent interactions with nearby galaxies that destabilized the gaseous disks, transporting material to the centre. This would feed the star formation and the bulge component. This is consistent with the fact that TI disks tend to be found in early-type spirals. These events together with radial migration could also explain the increasing flaring detected in TI disks.
- TII disks tend to have mainly negative or U-shape profiles. The inner regions are dominated by old stars whose fractions decrease steadily with increasing radius. Those with negative age profiles have smaller fractions of young stars than those with U-shape ones. In the latter case, the median  $R_{\text{br}}$  and  $R_{\text{min}}$  are very similar, indicating that the break in the density profiles is immediately followed by a change of slope in age distributions. This change is produced by a lower contribution of young stars as a result of the sharper truncation of the star formation activity. The few TII disks found to have positive/ $\Lambda$ -shape age profiles have larger star formation activity in the central region, which is strongly truncated in the outskirts. Additionally, they have larger contributions of young stars in the inner disks as expected. TII disks also show flaring in the heights but with the smallest dispersion.
- The up-bending of TIII disks coincides with a sharp decrease in the fraction of old stars that dominate within  $R_{\text{br}}$ . For  $r > R_{\text{br}}$  intermediate and young stars contribute more significantly than old ones. In case of U-shape and negative age profiles the fractions of young stars are almost constant as a function of radius. Additionally, the  $\Sigma_{\text{SFR}}$  for  $r > R_{\text{br}}$  is higher than expected from a simple

extrapolation of the inner  $\Sigma_{SFR}$ . The  $R_{\min}$  of the U-shape age profiles are located further out in the disks in comparison with those of TII disks. We also note that the fact that there are very few positive age profiles in TIII disks suggests that these disks could be more stable to perturbations that drive gas inflows to the inner regions and trigger central star formation activity, reinforcing the speculation that accreted material from interactions or minor mergers in the outer regions could be a crucial mechanism to shape the  $\Sigma$  profiles (see also Fig.3.3.7 where the contribution from different mono-age stellar populations are displayed).

We identified disks with the three expected  $\Sigma$  types in the EAGLE simulations, which can be associated with different relative contributions of mono-age stellar populations, SFR activity across the disks and angular momentum content of the galaxies. In a future work, we will focus on the role of environment, mergers and interactions. In this chapter we explore the stellar content of the disk, looking in particular at breaks in the stellar surface density profiles. These distributions, along with others presented, serve as manifestations of baryonic matter influenced by interactions with neighboring galaxies, environmental effects, and other processes. Furthermore, such processes can induce morphological perturbations, including lopsidedness and warps, in the baryonic distributions of the galactic disk. In the following chapter, we will study the formation and evolution of lopsided galaxies and explore their relation to the DM halo.

# Chapter 4

## Lopsided Galaxies in a cosmological context: a new galaxy-halo connection

### Abstract<sup>1</sup>

Disc galaxies commonly show asymmetric features in their morphology, such as warps and lopsidedness. These features can provide key information regarding the recent evolution of a given disc galaxy. In the nearby Universe, up to  $\sim 30$  percent of late-type galaxies display a global non-axisymmetric lopsided mass distribution. However, the origin of this perturbation is not well understood. In this work, we study the origin of lopsided perturbations in simulated disc galaxies extracted from the TNG50 simulation of the IllustrisTNG project. We statistically explore different excitation mechanisms for this perturbation, such as direct satellite tidal interactions and distortions of the underlying dark matter distributions. We also characterize the main physical conditions that lead to lopsided perturbations. 50 percent of our sample galaxy have lopsided modes  $m = 1$  greater than  $\sim 0.12$ . We find a strong correlation between internal galaxy properties, such as central stellar surface density and disc radial extension with the strength of lopsided modes. The majority of lopsided galaxies have lower central surface densities and more extended discs than symmetric galaxies. As a result, such lopsided galaxies are less self-gravitationally cohesive, and their outer disc region is more susceptible to different types of external perturbations. However, we do not find strong evidence that tidal interactions with satellite galaxies are the main driving agent of lopsided modes. Lopsided galaxies tend to live in asymmetric dark matter halos with high spin, indicating strong galaxy-halo connections in late-type lopsided galaxies.

---

<sup>1</sup>Based on Varela-Lavin et al. (2023), published in MNRAS

## 4.1 Introduction

In the nearby Universe spiral galaxies, such as our own, show different morphological asymmetries such as warps, lopsidedness and polar rings, among others. Lopsided perturbations in disc galaxies are one of the most common. It is described as a morphological distortion in which a side of the disc is more elongated than the other. Such global non-axisymmetric perturbation is typically quantified through a Fourier decomposition of the mass or light distribution, focusing on the  $m = 1$  mode,  $A_1$  (Rix & Zaritsky, 1995; Quillen et al., 2011). Rix & Zaritsky (1995) showed that, for lopsided galaxies, the amplitude of  $A_1$  increases with radius in the outer galaxy regions. Clear examples of lopsided galaxies include M101 or NGC1637.

One of the first studies reporting this perturbation was presented by Baldwin et al. (1980), who analyzed the spatial distribution of HI gas in the outer regions of a sample of galaxies. Lopsidedness has been studied in the stellar (Rix & Zaritsky, 1995) and HI gas distributions (Richter & Sancisi, 1994; Haynes et al., 1998) of galaxies, as well as on their large-scale kinematics (Swaters et al., 1999; Schoenmakers et al., 1997; Khademi et al., 2021), and compared against numerical models (Ghosh et al., 2022; Łokas, 2022). In the nearby Universe 30 percent of late-type galaxies show high values of  $A_1$  (Zaritsky & Rix, 1997; Bournaud et al., 2005). On the other hand, for early-type galaxies the frequency with which this perturbation arises is close to 20 percent (Rudnick & Rix, 1998). This higher frequency of lopsidedness in late-type galaxies was confirmed by Conselice et al. (2000), who analyzed a sample of 113 galaxies both early and late-type. Lopsidedness in this sample was quantified using the  $180^\circ$  rotational asymmetry measure,  $A_{180}$ . They found a strong relation between morphology and lopsidedness, showing that early-type galaxies (elliptical and lenticular) tend to systematically have lower values of  $A_{180}$ .

A more recent study from Reichard et al. (2008, hereafter R08) measured the asymmetries in galaxies through  $A_1$  using their surface brightness distribution in three different bands. Their sample consisted of more than 25000 galaxies from Sloan Digital Sky Survey (SDSS). They showed that the occurrence and strength of lopsidedness has a strong dependency with galaxy structural properties. Disc galaxies with higher  $A_1$  tend to have low stellar mass, concentration and high central stellar density. The latter is the parameter that most clearly correlates with the lopsidedness. As in Rix & Zaritsky (1995), R08 shows that the amplitude of the  $m = 1$  mode is negligible in the very inner regions of galactic discs due to its strong self-gravitating nature. However a systematic increase of the  $A_1$  parameter with galactocentric radius is observed in the outer galactic regions of lopsided galaxies. In addition R08 finds that the lopsided light distributions are primarily caused by lopsided distributions in the stellar mass.

As discussed by Jog & Combes (2009), lopsidedness can have very significant effects on the evolution of galaxies. In particular, for disc galaxies it can induce the redistribution of stellar mass due to angular momentum transport and the modulation of hosts star formation histories. In addition, the internal torques induced by such  $m = 1$  modes can result in the loss of angular momentum by the host gaseous disc, thus affecting the growth of the central supermassive black hole. As a result, lopsided perturbations could allow us to place important constraints on the recent interaction history of galaxies.

Several studies that have tried to characterize the main mechanisms driving lopsided perturbations. Possible proposed mechanisms are minor mergers (Walker et al., 1996; Zaritsky & Rix, 1997; Ghosh et al., 2022) and tidal interactions due to close encounters between galaxies of similar mass (Kornreich et al., 2002). Indeed, low density galaxies and, in particular the outskirts of galactic disc, are likely to be more susceptible to tidal stress. However, a study of 149 galaxies observed in the near-infrared from

the OSUBGS sample (Eskridge et al., 2002) by Bournaud et al. (2005) found that the amplitude of the  $m = 1$  mode is uncorrelated with the presence of companions. Instead, they suggested that asymmetric gas accretion is an important driver of lopsidedness. Similarly, Łokas (2022) used a sample of simulated galaxies extracted from the TNG100 simulation of the IllustrisTNG project (Nelson et al., 2019a) to study the origin of these perturbations. They concluded that the most frequent mechanism for the formation of lopsided discs is asymmetric star formation, probably related to gas accretion. However, they also observed that the distortions in the gas and stars were not strongly correlated. Recent studies have reported the presence of lopsided galaxies or unwinding spirals in galaxy clusters, attributed to ram pressure (Bellhouse et al., 2021; Vulcani et al., 2022).

Another plausible mechanism driving lopsided discs relates to perturbations in the density field of the underlying galactic dark matter (DM) halo. These asymmetries in a DM halo could be produced by a resonant interaction between the DM halo particles and an orbiting satellite. The resulting asymmetry of the DM overdensity field, or wake, can be thought of as a superposition of different modes excited by such resonant interaction. The wake’s associated torque, exerted on the embedded disc, could lead to the formation of strong morphological disturbances such as lopsidedness and warps, among others. Indeed, Weinberg (1998) showed that such perturbations can induce the formation of vertical patterns, such as warps and corrugation patterns. These results were later confirmed using fully cosmological hydrodynamical simulations (Gómez et al., 2016) as well as carefully tailored simulations to study the response of the Milky Way halo to a recently accreted Large Magellanic Cloud satellite (Laporte et al., 2018a; Garavito-Camargo et al., 2019). Furthermore, as discussed by Jog (1999), these DM halo asymmetries can also induce the formation of lopsided perturbations, and sustain them for long periods of time. Using the Millennium simulation (Springel et al., 2005), Gao & White (2006) characterized asymmetries in DM halos within a mass range of  $\sim 10^{12}$  to  $10^{15} M_{\odot}$ . The asymmetries were quantified based on shifts between the overall DM halo center of mass (CoM) and its center of density (cusp). Shifts between the a system’s CoM and cusp can be thought as the a dipolar component of a wake (Weinberg, 1998; Garavito-Camargo et al., 2021), and typically have the strongest amplitude of all modes. They showed that such asymmetries were not uncommon and that the frequency with which they arose depended on the host mass. While 20 percent of cluster haloes have CoM separated from their cusp by distances larger than 20 per cent of the virial radius, only 7 per cent of the Milky Way-mass haloes show such large asymmetries. Despite all these studies, several questions remain to be answered regarding lopsided galaxies, including the main driver and longevity of such perturbation. Additionally, we do not yet understand whether lopsidedness can be linked to fundamental properties of the structure and evolution of the host galaxy and its halo. In this work we analyze a large sample of late-type galaxies, extracted from the Illustris TNG50 project (Nelson et al., 2019a; Pillepich et al., 2019) to shed light on these issues. This highly-resolved fully-cosmological hydrodynamical simulation includes, in a self-consistent manner, the different physical processes that have been proposed as the main drivers of morphological perturbations. In particular, we focus on Milky Way mass-like halos, whose stellar disc can be resolved with the available mass resolution. In Section 4.2 we discuss the details of the numerical simulation, as well as the selection criteria for our galaxy sample. The methods to characterize the properties of the stellar discs, and to quantify the presence of a lopsided mode on their density distribution, are introduced in Section 4.3. In Section 4.4 we present our results. Our conclusion and discussion are summarised in Section 4.5

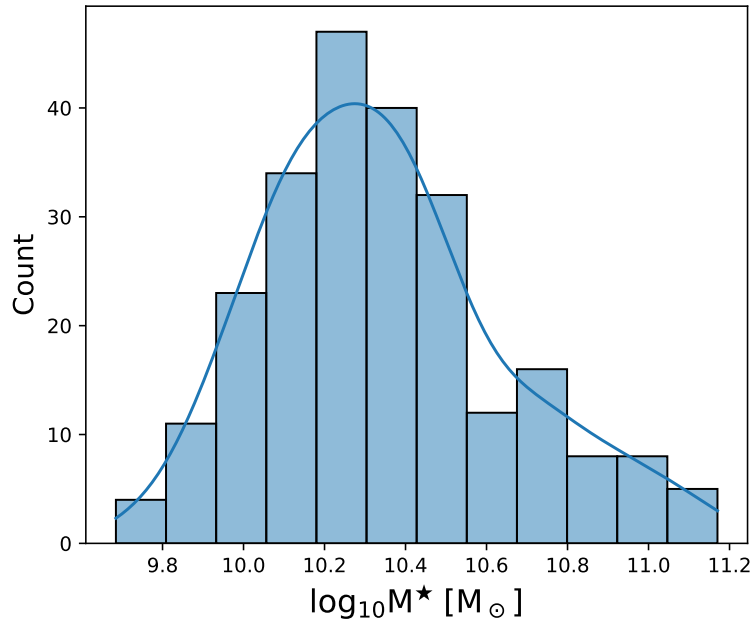


Figure 4.1.1: Stellar mass distribution of our selected sample (see Section 2.2). The solid line depicts a KDE of this distribution.

## 4.2 Simulations

In this Section we introduce the numerical simulations considered in this work, which are taken from the Illustris-The Next Generation project (IllustrisTNG hereafter Pillepich et al., 2018; Nelson et al., 2018, 2019a; Marinacci et al., 2018; Springel et al., 2018; Naiman et al., 2018). We also describe the criteria applied to select galaxies from the corresponding large cosmological boxes.

### 4.2.1 The IllustrisTNG project

The IllustrisTNG project is a set of gravo-magnetohydrodynamics cosmological simulation, run with the moving-mesh code Arepo (Springel, 2010). It comprises three large simulation volumes: TNG50, TNG100, and TNG300, enclosing volumes of  $\sim 50^3$  cMpc,  $100^3$  cMpc and  $300^3$  cMpc, respectively. All these TNG runs follow the standard  $\Lambda$ CDM model, with parameters based on the Planck Collaboration et al. (2016) results:  $\Omega_m = 0.3089$ ,  $\Omega_{\Lambda} = 0.6911$ ,  $\Omega_b = 0.0486$ ,  $h = 0.6774$ ,  $\sigma_8 = 0.8159$ ,  $n_s = 0.9667$ , with Newtonian self-gravity solved in an expanding Universe. The IllustrisTNG<sup>1</sup> is the successor of the Illustris project (Vogelsberger et al., 2014b,a; Genel et al., 2014; Nelson et al., 2015), containing updated models for the physical processes that are relevant for galaxy formation and evolution (Weinberger et al., 2017; Pillepich et al., 2018), such as radiative cooling, stochastic star-formation in dense interstellar stellar medium, and an updated set of sub-grid physics models for stellar evolution, black hole growth, stellar and AGN feedback.

<sup>1</sup><https://www.tng-project.org>

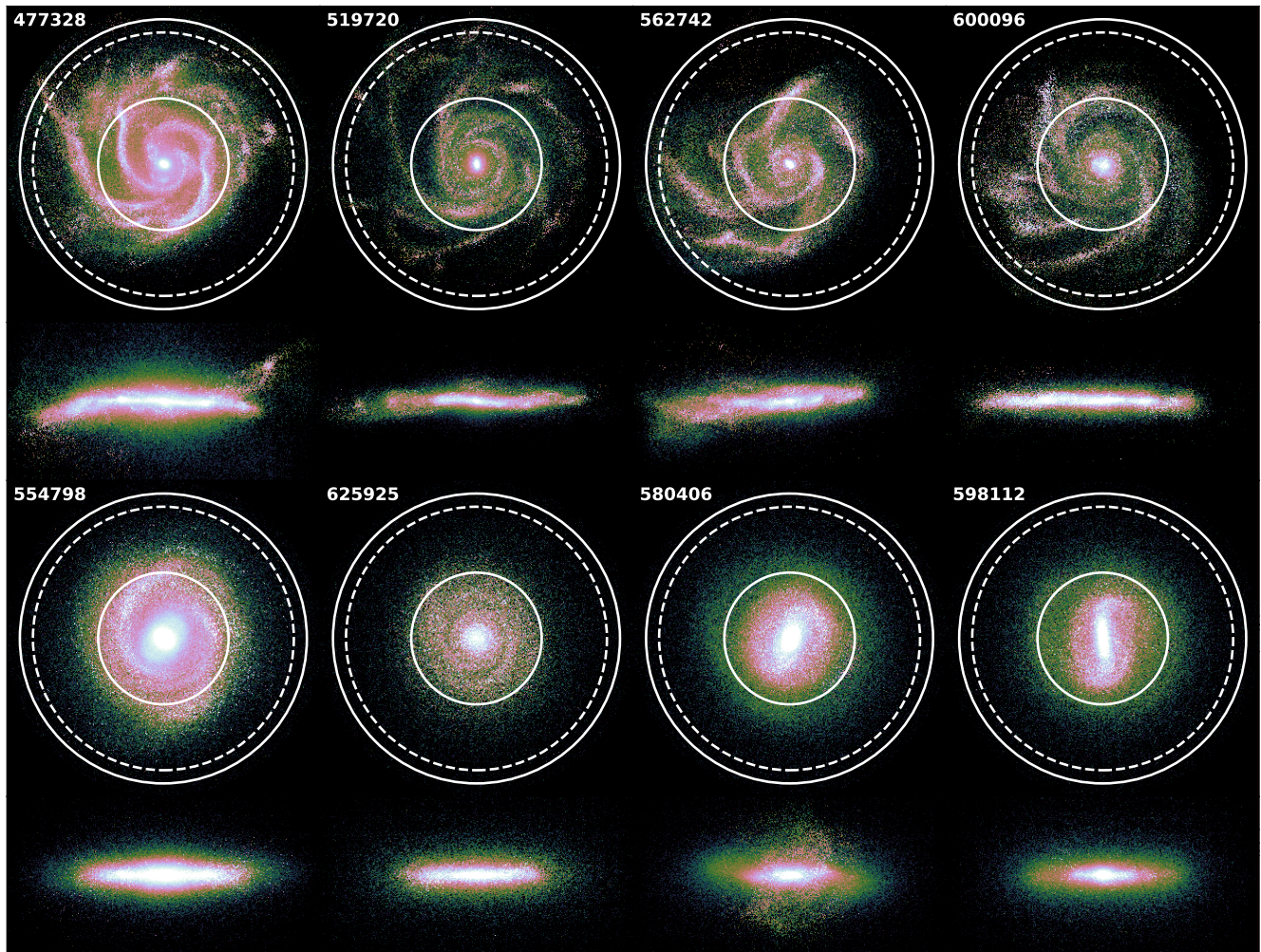


Figure 4.1.2: Face-on and edge-on projected stellar density for eight galaxies from our TNG50 sample at  $z = 0$ . The images at the top correspond to the most lopsided galaxies while those at the bottom to the most symmetrical ones. The dashed circle indicates  $R_{26.5}$ . The solid circles represent the lower and upper radial limit considered to compute  $A_1$ , which are between  $0.5R_{26.5}$  and  $1.1R_{26.5}$ , respectively. More details in Section 4.3.2.

In this work, we focus on the model TNG50-1 (Pillepich et al., 2019; Nelson et al., 2019b) and its DM only counterpart. TNG50-1 (hereafter TNG50) is the highest resolution run within the TNG project. Its high resolution allows us to better analyze the azimuthal distribution of stellar mass in the outskirts of Milky Way-like galaxies. In Table 4.2.1 we list the main parameters of this simulation.

The TNG50 database provides a catalogue of magnitudes in eight bands (SDSS  $g,r,i,z$ , Buser U,B,V and Palomar K) for each stellar particle. To estimate them, each stellar particle is assumed to represent a single stellar population of a given age and metallicity, consistent with a Chabrier IMF (Chabrier, 2003). Their energy spectral distributions (SEDs) are obtained from the Bruzual & Charlot (2003) populations

synthesis models (e.g. Tissera et al., 1997). We note that possible effects by dust obscuration have not been considered.

## 4.2.2 Selection criteria

In this work, we seek to characterize the properties and main physical mechanism that give rise to disc galaxies displaying a non-axisymmetric global mass distribution of type  $m = 1$ , better known as lopsided galaxies (Jog & Combes, 2009).

We built our sample focusing on host late-type galaxies embedded in DM haloes with a  $M_{200}$  between  $10^{11.5}$  and  $10^{12.5} M_{\odot}$ , where  $M_{200}$  is defined as the total mass of the halo enclosed in a sphere whose mean density is 200 times the critical density of the Universe at  $z = 0$ . We considered only central galaxies, so we do not consider satellites within our sample. To properly quantify lopsidedness in the galaxies outskirts, we selected well-resolved galaxies with more than 10000 stellar particles, identified and assigned to each host by the SUBFIND algorithm (Springel et al., 2001). Finally, we selected disc-dominated galaxies by requiring the Disc-to-Total mass ratio (D/T) to be greater than 0.5. This last parameter was extracted from a catalogue provided by Genel et al. (2015), and represents the fractional stellar mass within  $10 \times R_{50}^2$  with a circularity parameter  $|\epsilon| > 0.7$ . That last parameter is defined as  $\epsilon = J_z/J(E)$ , where  $J_z$  is the angular momentum component perpendicular to the disc plane of a stellar particle with orbital energy  $E$ , and  $J(E)$  is the (estimated) maximum possible angular momentum for the given  $E$  in a circular orbit (Tissera et al., 2012). That last selection about D/T place a strong limit on the mass contribution of the spheroidal components to the simulated galaxies.

After applying the selection criteria, the final sample comprises 240 late-type galaxies at  $z = 0$ . In Figure 4.1.1, we show the total stellar mass distribution of the selected sample. The stellar mass distribution of our TNG50 sample ranges from  $10^{9.5} M_{\odot}$  to  $10^{11.2} M_{\odot}$ . The mean stellar mass of our galaxy sample is  $\sim 10^{10.3} M_{\odot}$ . In Section 4.4.5, we expand our sample to compare with previous results from the literature. Only for this purpose, we select central haloes with  $M_{200}$  ranging from  $10^{11}$  to  $10^{13} M_{\odot}$ .

## 4.3 Methods

### 4.3.1 Characteristic scales

To measure asymmetries in the mass and light distribution of the disc component of our simulated galaxy suite, it is important to define the different radial scales within which the analysis will be performed. In our work, these characteristic scales are estimated by using the projected stellar mass and light onto the rotational plane of the disc. First, we generate radial surface brightness (SB) profiles in the V photometric band. The SB profiles are created through the binning of the luminosity distribution of the stellar particles in radial annuli of 0.5 kpc of width. For better accuracy, we have smoothed the SB profile with a polynomial fit. This smoothed profile is used to define the position outermost edge of the disc,  $R_{26.5}$ , as the radius where the SB profile falls to a magnitude of 26.5 mag arcsec<sup>-2</sup>.  $R_{26.5}$  is also known as optical radius, and here it is used as a proxy of the size of galaxies. The  $R_{26.5}$  in our TNG50 sample are within the range [9.5, 46.75] kpc with a median of 22.53 kpc. In Figure 4.1.2 we show examples of four lopsided

<sup>2</sup>The stellar half-mass radius,  $R_{50}$  is defined as the radius that encloses 50 percent of the total stellar mass of a subhalo.

Table 4.2.1: Main parameters of the TNG50 simulation: the comoving volume and the box side-length (1-2<sup>th</sup> rows), the number of initial gas cells and dark matter particles (2-4<sup>th</sup> rows), the mean baryonic and dark matter particle mass resolution (4-6<sup>th</sup> rows), the minimum allowed adaptive gravitational softening length for gas cells (comoving Plummer equivalent) (7<sup>th</sup> row) and the redshift zero softening of the collisionless components (8<sup>th</sup> row).

Run Name		TNG50
Volume	[cMpc <sup>3</sup> ]	51.7 <sup>3</sup>
L <sub>box</sub>	[cMpc/h]	35
N <sub>GAS</sub>	-	2160 <sup>3</sup>
N <sub>DM</sub>	-	2160 <sup>3</sup>
m <sub>baryon</sub>	[M <sub>⊙</sub> ]	8.5x10 <sup>4</sup>
m <sub>DM</sub>	[M <sub>⊙</sub> ]	4.5x10 <sup>5</sup>
ε <sub>gas,min</sub>	[pc]	74
ε <sub>DM</sub>	[pc]	288

and four symmetric discs galaxies in our sample (top and bottom panel, respectively). In this figure, we also illustrate the sizes of the galaxies as measured by  $R_{26.5}$  (white dashed circles), illustrating how well this parameter traces the size of disc galaxies with different characteristics.

From now on, we consider all star particles located within a sphere of radius  $R_{26.5}$ , to estimate the parameters in this subsection. We define the stellar half-mass radius,  $R_{50}^*$  as the position that enclosed the 50 percent of stellar mass,  $M_{50}^*$  of the corresponding disc. Similarly, we define  $R_{90}^*$  as the position that enclosed 90 percent of the disc stellar mass,  $M_{90}^*$ . We find that  $R_{50}^*$  varies between 2.02 and 13.69 kpc with a median of 6.57 kpc, while  $R_{90}^*$  varies within 5.91 and 36.26 kpc, with a median of 15.81 kpc. These parameters allow the estimation of the stellar concentration defined as  $C_* = R_{90}^*/R_{50}^*$ , and central stellar density,  $\mu_* = M_{50}^*/\pi R_{50}^{*2}$ .

### 4.3.2 Quantification of $m = 1$ asymmetries

In order to quantify the asymmetry in the mass and light distributions of the disc stellar component of our galaxies, we adopt the Fourier mode approach (Rix & Zaritsky, 1995; Zaritsky & Rix, 1997; van Eymeren et al., 2011; Grand et al., 2016; Quillen et al., 2011). In particular, we focus our analysis on lopsided perturbations, which can be characterized as a displacement of the center of stellar mass with respect to its center of density. Such asymmetric perturbations can be quantified through the amplitude of the  $m = 1$  Fourier mode.

Within a given thin radial annulus,  $R_j$ , the complex coefficients of the  $m$  Fourier mode can be estimated from a discrete distribution as

$$C_m(R_j) = \sum_i^N M_i^* e^{-im\phi_i} \quad (4.3.1)$$

where  $M_i^*$  and  $\theta_i$  are the mass and azimuthal coordinate of the  $i$ -th stellar particle that belongs to the

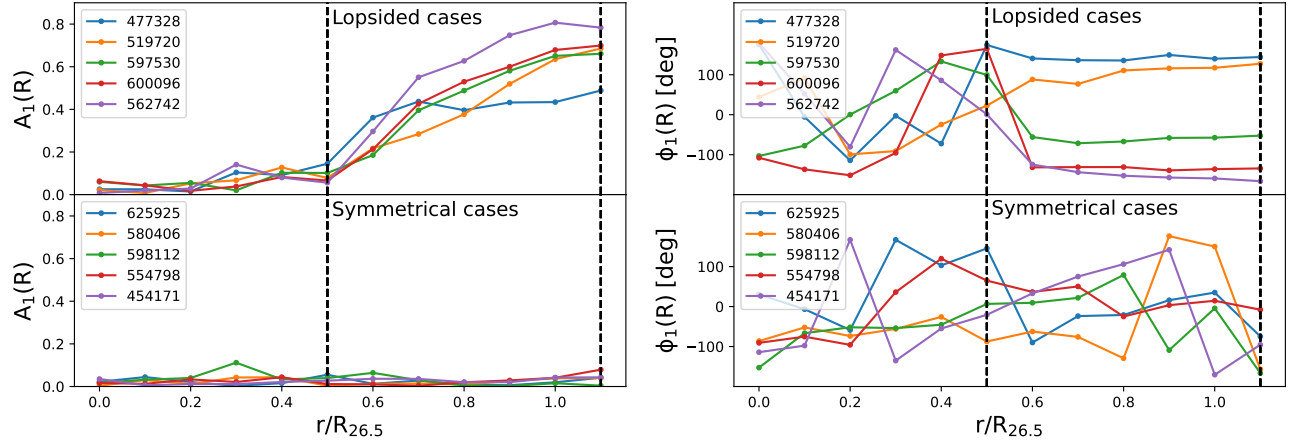


Figure 4.3.1: *Left panel:* Radial distribution of the amplitude  $m = 1$  Fourier mode ( $A_1(R)$ ), for five galaxies lopsided of  $A_1$  (top sub-panel) and five symmetrical galaxies (bottom sub-panel). The black dashed lines indicate the lower and upper radial limits considered to compute a global mass-weighted mean of  $m = 1$  Fourier amplitudes,  $A_1$  for each galaxy. Note that lopsided cases show an increase of  $A_1(R)$  when increasing radius, and for symmetrical cases  $A_1(R)$  approaches zero in the whole galaxy (see Section 4.3.2). *Right panel:* Radial distribution of phase angle of the  $m = 1$  component,  $\phi_1(R)$ . Similar to the top panel, we show five lopsided and symmetrical disc examples. The lopsided galaxies show a nearly constant phase angle in their outer disc, in agreement with previous studies (Li et al., 2011; Zaritsky et al., 2013).

$j$ -th radial annulus in a given galaxy. the angle  $\phi_i$  is defined as  $\phi_i = \text{atan2}(y_i, x_i)$ , where  $x_i$  and  $y_i$  are the cartesian coordinates of the  $i$ -th stellar particle for galaxies oriented in a face-on configuration<sup>3</sup>. Then we define the amplitude of  $m$ -th Fourier mode as,

$$B_m(R_j) = \sqrt{a_m(R_j)^2 + b_m(R_j)^2} \quad (4.3.2)$$

where  $a_m$  and  $b_m$  are the real and imaginary part of  $C_m$  (equation 4.3.1). The amplitude  $B_1(R_j)$  corresponds to the strength of the  $m = 1$  mode within a given  $j$ -th radial annulus. Finally, since each radial annulus has a different total stellar mass, we express  $B_1(R_j)$  relative to the corresponding  $m = 0$  mode,

$$A_1(R_j) = \frac{B_1(R_j)}{B_0(R_j)}, \quad (4.3.3)$$

where  $B_0$  is given by eqn. 4.3.2 for  $m = 0$ , and it is equal to the total mass in the given  $j$ -th radial annulus. Thus, eqn. 4.3.3 corresponds to the mass-weighted amplitude of the  $m = 1$  Fourier mode as a function of radius.

In Fig. 4.3.1 we show the radial  $A_1$  profile (left panel) obtained from five of our most lopsided (top sub-panel) and five of our most symmetrical models (bottom sub-panel). We note that all galaxies, independently of whether they are lopsided or not, show very small  $A_1$  values within  $R \sim 0.5 R_{26.5}$ . However, for lopsided galaxies,  $A_1$  starts to rapidly increase after this galactocentric distance. The radial distribution

<sup>3</sup> $\text{atan2}()$  is a function of two parameters that returns the phase angle of the position of a  $i$ -th star particle in the respective quadrant, thus phase angles have values within the range  $-\pi$  to  $\pi$ .

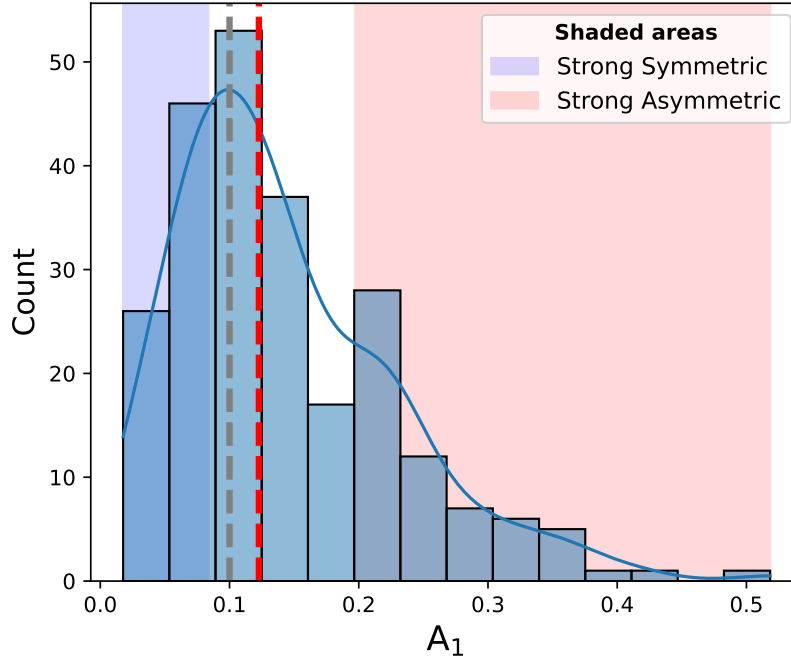


Figure 4.3.2: Distribution of the sample of global (mean)  $A_1$  parameter computed for each simulated galaxy in our sample at  $z = 0$ . The solid blue line shows the  $A_1$  distribution built using KDE method. The dashed red line is the median of  $A_1$  distribution,  $\hat{A}_1 \approx 0.12$ , which is used to differentiate between symmetric and asymmetric galaxies, the gray dashed line correspond to 0.1 threshold, typically used to defined lopsided galaxies, note that  $\hat{A}_1 > 0.1$ , this means that a little more than half of our sample has  $A_1 > 0.1$  values. The blue and red shaded areas indicate the first and fourth quartiles of the distribution, used to define the sub-sample of strong symmetric and asymmetric groups, respectively.

of  $A_1(R)$  in our model is similar to that found in Rix & Zaritsky (1995), who used near-IR observations from a sample of 18 galaxies to characterise the properties of lopsided galaxies. Rudnick & Rix (1998) and Bournaud et al. (2005) also found that the amplitude of the lopsided perturbations increases steadily ( $A_1 > 0.1$ ) within the outer disc regions (radial range of  $\approx 1.5$  to  $2.5$  exponential disc scalelengths). Jog (2000) suggested that the self-gravitational potential of the galaxy exerts a resistance to some external gravitational perturbation. However, the resilience exerted by self-gravity is more significant at smaller radii, and indeed the values of  $A_1(R)$  are low in the inner disc. For lopsided galaxies, the gravitational pull by self-gravity is weaker at larger radii, so  $A_1(R)$  grows. Otherwise, the symmetric cases could be gravitationally more cohesive, and consequently the radial distribution of  $A_1(R)$  keeps lower values in the whole disc. In Section 4.4.3, we explore this in detail.

In the right panel of Fig. 4.3.1, we show the radial phase angle of the  $m = 1$  component,  $\phi_1(R)$ . Note the nearly constant value of  $\phi_1(R)$  in the outer disc for lopsided examples, region where the corresponding asymmetry becomes significant. This feature is typical in lopsided galaxies (Zaritsky & Rix, 1997; van Eymeren et al., 2011; Ghosh et al., 2022). The radial variation of  $\phi_1(R)$  is a useful tool for understanding the nature of the lopsidedness and how long it takes to wind around the galaxy (Baldwin et al., 1980). Previous results (Saha et al., 2007; Ghosh et al., 2022) suggest that, in lopsided galaxies, the outer galaxy

region does not wind up as quickly as their inner region, suggesting a weak self-gravity in these galaxies. Since the outer region of galactic discs is more prone to developing lopsidedness, we estimate, for each galaxy, a unique global mass-weighted mean of the  $m = 1$  Fourier mode, hereafter  $A_1$ . This allow us to compare the level of lopsidedness among galaxies in our sample. The global  $A_1$  is computed by taking the mean of the  $A_1(R)$  in outer galaxy regions. We consider eight (8) radial annular region, of width  $0.075R_{26.5}$ , located within the interval  $0.5R_{26.5}$  to  $1.1R_{26.5}$ . This region is highlighted by the dashed lines in Fig. 4.3.1 and the solid circles shown in Fig. 4.1.2).

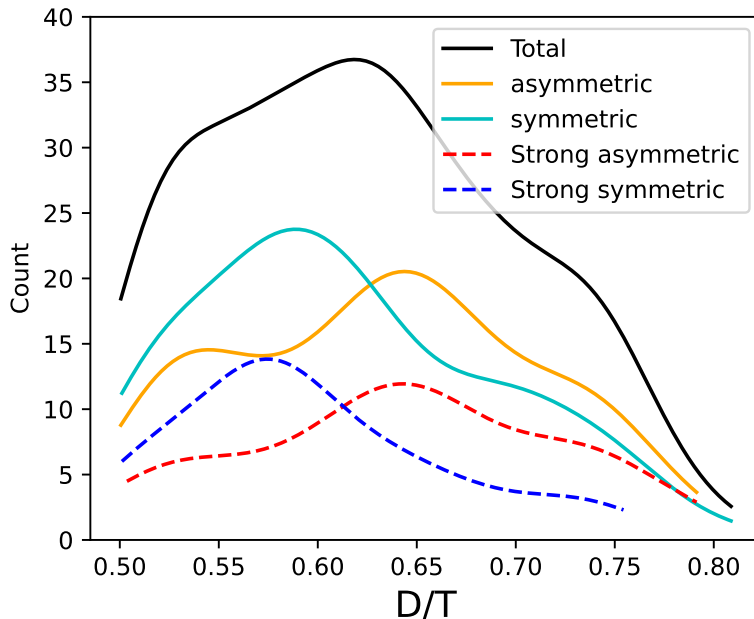


Figure 4.3.3: Distribution of Disc-to-Total mass ratio,  $D/T$ , for the total sample (black line), only asymmetrical galaxies (orange line) and only symmetrical galaxies (cyan). The red and blue dashed lines correspond to strong asymmetric and symmetric subsamples, respectively. The distribution were obtained using a KDE method. Asymmetrical galaxies tend to be more disc-dominated than their symmetrical counterpart. The medians for each group are 0.61 and 0.64, respectively. A similar trend is observed for the strong sub-samples.

### 4.3.3 Estimating the asymmetries in DM haloes and stellar component

In this work we are interested in characterizing the origin and evolution of lopsided perturbations. A possible mechanism triggering such perturbation is the response of the galactic disc to a distorted DM halo. As discussed in Sec.4.1, these halo distortions arise as a result of interactions between the host DM particles and an external agent (Jog, 1997, 1999; Gómez et al., 2016; Gao & White, 2006; Laporte et al., 2018b). To quantify such distortions in the DM halo of our numerical models, we focus on offsets of the halo center of mass with respect to its density cusp. Typically, the dipolar response of the DM halo density field is the strongest. Thus, it can be used to identify perturbed DM distributions.

Here we follow the analysis performed by Gao & White (2006). First, we identify the DM halo density cusp,  $r_{\text{cusp}}$ , based on the position of the most bound particle of the central halo, given by SUBFIND. We

then computed the DM halo center of mass,  $r_{\text{DM}}$ , considering all DM particles located within the inner three and five times  $R_{26.5}$ . We note that, as shown by Gómez et al. (2016), perturbations in the DM halo at further galactocentric distances are not efficient at disturbing the embedded galactic disc. Nonetheless, to compare with Gao & White (2006) we also compute  $r_{\text{DM}}$  considering all DM particles assigned to the main host halo by SUBFIND ( $R_{200}$ ). Finally we compute the offset of  $r_{\text{DM}}$  with respect to  $r_{\text{cusp}}$  as

$$\Delta r_{\text{DM}}^i = |r_{\text{cusp}} - r_{\text{DM}}^i|, \quad (4.3.4)$$

where the supra index  $i = 3R_{26.5}, 5R_{26.5}$  and  $R_{200}$  indicates the spatial region within which  $r_{\text{DM}}$  is calculated.

## 4.4 Results

### 4.4.1 General disc morphological properties

In this Section we analyze the main morphological characteristics of the 240 stellar discs, selected according to the criteria defined in Section 4.2. In Fig. 4.3.2 we show the distribution of the global  $A_1$  parameter, which correspond to the average  $A_1(R)$  values computed within the radial range  $[0.5 - 1.1R_{26.5}]$  (see Sec. 4.3.2). We note that the distribution is similar to the one reported by R08 (see their figure 10), obtained using a sample 25155 galaxies from the SDSS. It is worth noting that, even though the stellar mass range of our sample (Fig. 4.1.1) is similar to that in R08 ( $10^8 - 10^{11}M_{\odot}$ , see figure 8 in R08), the latter includes a population of early type galaxies, which are missing from our sample. Nonetheless, the R08 sample is dominated by late-type objects, allowing us to compare our results with the data. The characteristic galaxy  $A_1$  values in R08 were obtained by averaging over the radial range between  $R_{50}$  and  $R_{90}$ . The outer radius limit is imposed due to limitation with the observational data (see Sec. 2.2 of R08 for more details). We have computed our distribution considering smaller outer limits, finding no significant variation in our results. Similar results were obtained by previous works such as Rix & Zaritsky (1995); Bournaud et al. (2005).

The red dashed line in Fig. 4.3.2 indicates the median of the  $A_1$  distribution, which takes a values of  $\hat{A}_1 \approx 0.12$ . This  $\hat{A}_1$  is used from now on to differentiate galaxies between symmetric ( $A_1 < \hat{A}_1$ ) and asymmetric or lopsided cases ( $A_1 > \hat{A}_1$ ). We note that this value is only slightly larger than the 0.1 threshold, typically used to define lopsided discs (Bournaud et al., 2005; Zaritsky & Rix, 1997; Jog & Combes, 2009). We further subdivide our sample into strongly symmetric and asymmetric cases by selecting galaxies located in the first and fourth quartiles of the  $A_1$  distribution, respectively. The strong cases are highlighted in Fig. 4.3.2 with shaded areas.

We now explore whether there are correlations between the D/T (see Sec. 4.2.2) of our simulated galaxies and the symmetry of their azimuthal mass distribution. We recall that the parameter D/T allows the quantification of the disc mass contribution to the galaxy's total stellar mass. The black solid line in Fig. 4.3.3 shows the D/T density distribution obtain using the Kernel Density Estimation (KDE)<sup>4</sup> of the D/T values obtained from our full sample. Note that our selection criteria imposes a lower D/T limit of

<sup>4</sup>We implement KDE using the `GAUSSIAN_KDE` function from the `SCIPY` library. More details can be found at <https://scipy.org>

0.50. The distribution has a median value of  $\approx 0.62$ , indicating a significant presence of strongly disc-dominated galaxies in our sample. Interestingly, asymmetric galaxies tend to be more disc dominated than their symmetric counterparts, with medians of 0.64 and 0.61, respectively. The blue and red dashed lines show the same distribution, now for the strong-asymmetric and strong-symmetric samples. The difference in the median D/T values are slightly more pronounced than in the previous subsamples, with values of 0.64 and 0.58 for the asymmetric and symmetric subsamples, respectively. This suggests that the presence of more significant central pressure supported component could be playing a role on limiting the strength of lopsided perturbations. This is further explored in Section 4.4.3.

## 4.4.2 Structural properties of lopsided galaxies

As discussed in the previous Section, our sample of disc-dominated galaxies show different degrees of lopsided asymmetry, as quantified by the value of their  $A_1$  parameter. In this Section,  $R_{50}^*$ , stellar mass concentration,  $C_*$ , and central stellar surface density,  $\mu_*$ , present significant differences between the asymmetric and symmetric sub-samples.

To highlight the main differences between the asymmetric discs and their symmetrical counterparts, we focus on the strongly symmetric and strongly asymmetric galaxy samples defined in Fig. 4.3.2. The left upper panel of Fig. 4.4.1 shows the distribution of  $R_{50}^*$  and  $\mu_*$ . The distributions are represented with a two dimensional kernel density estimation (KDE). The top and the right sub panels show the marginalized 1D distribution for  $R_{50}^*$  and  $\mu_*$ , respectively. Interestingly, both strong types show different distributions in this plane. We find that asymmetric galaxies tend to have larger  $R_{50}^*$  than their symmetric counterparts. In addition, they tend to show lower values of  $\mu_*$  at given  $R_{50}^*$ . These differences are highlighted on the 1D KDE, with median values of  $R_{50}^*$  and  $\mu_*$  for the symmetric and asymmetric sub samples of (4.62, 7.22) kpc and  $(10^{8.39}, 10^{7.75}) M_\odot \text{ kpc}^{-2}$ , respectively.

Following R08, on the right upper and bottom panels we show 2D KDE of our simulated galaxy sample in  $\mu_*$  versus total stellar mass,  $M^*$ , and in  $M^*$  versus stellar concentration,  $C_*$ , respectively. R08 shows that, among these structural parameters, the strongest correlation with  $A_1$  is obtained for  $\mu_*$ . Indeed, our results are in good agreement with these observations. Note that the most pronounced difference between the distributions of these strong types is obtained for  $\mu_*$ . The marginalized  $C_*$  distribution (bottom panel) shows that both type of galaxies present nearly indistinguishable distribution of stellar concentration. Interestingly, within the stellar mass range considered in this work, we find that symmetric galaxies tend to be slightly more massive than lopsided galaxies. In addition, the lopsided sub-sample shows a narrower distribution in  $M^*$ . To quantify these results, we estimate Pearson correlations coefficient between the previously defined parameters. In Table 4.4.1, we show both the correlation coefficient obtained using only the strong samples and also using all lopsided and symmetrical galaxies (fourth column). As previously indicated, the strongest (anti)correlation is obtained between  $A_1$  and  $\mu_*$ . This significant anti correlation is obtained for both the strong and the complete samples.

## 4.4.3 The role of the central mass distribution

As discussed in the previous Section, our sample of galactic models shows a significant correlation between  $A_1$  and the central stellar density,  $\mu_*$ . Galaxies with lower  $\mu_*$  typically show higher values of  $A_1$ . Additionally we also find that lopsided galaxies tend to show larger values of  $R_{50}^*$ . This suggest that

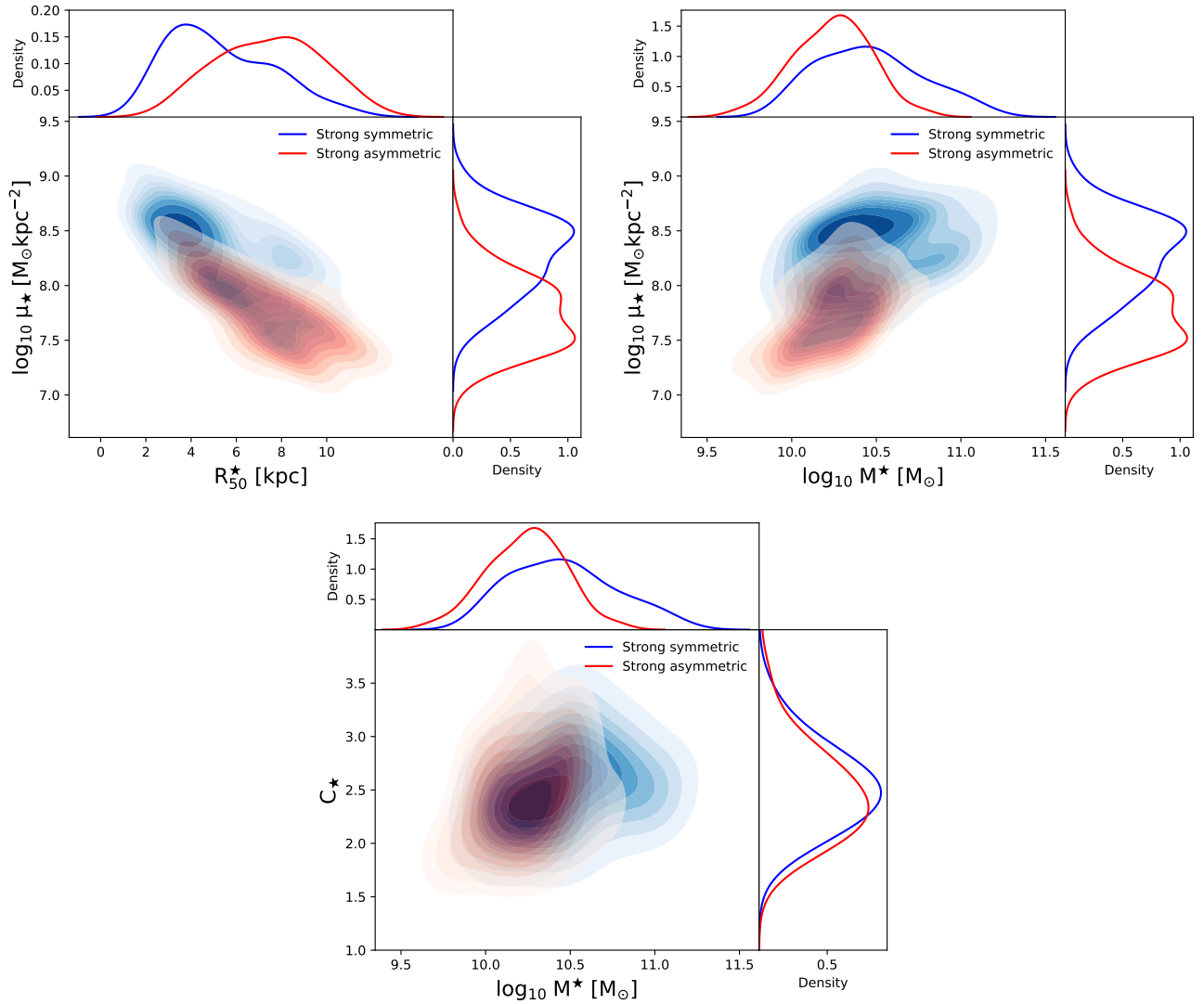


Figure 4.4.1: *Left upper panel:* Central stellar density,  $\mu_*$ , as a function of stellar half-mass radius,  $R_{50}^*$ , for the strong symmetric and asymmetric sub-samples that are defined in Fig. 4.3.2. *Right upper panel:*  $\mu_*$  as a function by the total stellar mass,  $M_{90}^*$ . *Bottom panel:* Stellar mass concentration,  $C_*$ , as a function  $M_{90}^*$ . These panels were built using KDE bivariate distribution for the central sub-panel, and simple KDE distribution for edge sub-panels. The strong sub-sample was separated between strong symmetric (blue region) and strong asymmetric (red region). Note that strong asymmetric galaxies tend to have their central regions more extended and slightly less massive than symmetric galaxies. Furthermore, A clear difference between both sub-samples are in their central stellar density, where in asymmetric galaxies tend to be lower ones.

galaxies with lower density and more extended central regions could be more prone to develop lopsided perturbations.

Indeed, discs with denser inner regions are likely to be more gravitationally cohesive. To explore whether the disc self-gravity plays a significant role in the onset and amplitude of lopsided perturbations we

Table 4.4.1: Correlations coefficients for relations between the analysed parameters discussed in in Section 4.3.3 and 4.4.3.

P1	P2	Correlation Coefficient	
		Strong sample	All sample
$\log_{10} A_1$	$\log_{10} \mu_*$	-0.68	-0.54
$\log_{10} A_1$	$R_{50}^*$	0.53	0.37
$\log_{10} A_1$	$C_*$	-0.03	-0.01
$\log_{10} A_1$	$\log_{10} M_{50}/R_{26.5}^3$	-0.72	-0.60
$\log_{10} \mu_*$	$\log_{10} M_{50}/R_{26.5}^3$	0.60	0.52

show, in Fig. 4.4.2, the distribution of  $M_{50}/R_{26.5}^3$  versus  $\mu_*$  for all galaxies in the strong symmetric and asymmetric samples. Here,  $M_{50}$  represents the total mass of all particles enclosed in a sphere of radius  $R_{50}^*$ , and includes contributions from the stellar, the gas and the dark matter components. We note that the quantity  $M_{50}/R_{26.5}^3$  represents a proxy of the tidal force exerted by the inner galaxy region ( $R < R_{50}^*$ ) on material located at distances equal to the disc optical radius,  $R_{26.5}$ . As before, we focus on the strong symmetric and asymmetric types. From this figure we observe that these two subgroup represent very distinct populations in  $M_{50}/R_{26.5}^3$  versus  $\mu_*$  space. Present-day asymmetric galaxies exert a much lower tidal field on their outer disc regions, where lopsided perturbations show the strongest amplitudes. This is clearly shown on the 1D KDE histogram displayed in the top panel. Indeed, the (anti)correlation between  $A_1$  and  $M_{50}/R_{26.5}^3$  is the strongest among the structural parameters explored in this work. This is quantified in Table 4.4.1, which also highlights that this anti-correlation is even greater than the one found between  $A_1$  and  $\mu_*$ . We emphasize that the anti-correlation is not limited to the strong subtypes, and that it remains large even if we consider the all galaxies in the sample, as can be seen from the rightmost column of Table 4.4.1.

Several previous studies have explored different scenarios for the origin of lopsided modes based on environmental interactions, such as fly-bys, minor and major mergers, perturbed underlying dark matter density field, and misaligned accretion of cold gas, among others (Weinberg, 1994; Jog, 1997, 1999; Kornreich et al., 2002; Walker et al., 1996; Zaritsky & Rix, 1997; Bournaud et al., 2005; Levine & Sparke, 1998; Noordermeer et al., 2001; Gómez et al., 2016; Garavito-Camargo et al., 2019). Our results instead hint toward a population of galaxies susceptible to develop lopsidedness, and not to a particular external perturbation source. In other words, galaxies with weakly cohesive inner regions could develop a lopsided mode when faced with any sort of external perturbation. Indeed, as we show later in Section 4.4.5, the strong present-day connection between the strength of the lopsided modes and of the inner tidal force field is independent of the past interaction history of our simulated galaxies with their environment.

#### 4.4.4 Evolution of lopsided galaxies

Around the 30 percent of late-type galaxies in the nearby Universe show lopsided perturbations (Rix & Zaritsky, 1995; Jog & Combes, 2009). This could indicate that either lopsided perturbations are long lived, or that a significant fraction of galaxies are prone to develop such perturbations even in absence of

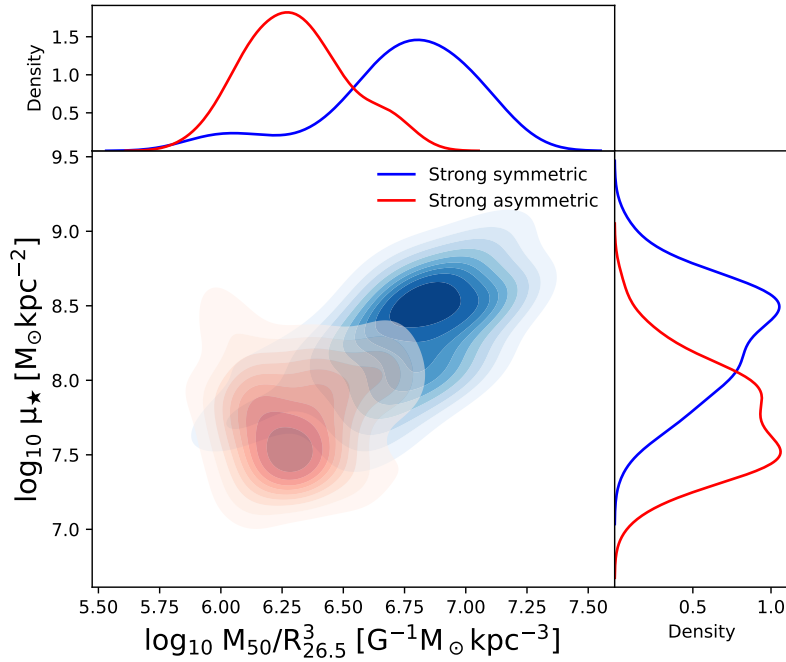


Figure 4.4.2: Distribution of the proxy of the tidal force exerted by the inner disc on its outskirts,  $M_{50}/R_{26.5}^3$ , versus central stellar density,  $\mu_*$ , for all galaxies in the strong symmetric and asymmetric samples. The top and right panels show the corresponding one dimensional distribution. All distributions were obtained using a KDE method. A clear correlation between  $\mu_*$  and  $M_{50}/R_{26.5}^3$  is seen. Strong asymmetric galaxies tend to have lower values of  $M_{50}/R_{26.5}^3$ , suggesting that weakly gravitationally cohesive galaxies are susceptible to lopsided distortions in their stellar distribution.

significant external interactions, as suggested in the previous Section. Here we explore the time evolution of the main structural parameters that differentiate symmetric and lopsided galaxies, as well as the time evolution of the amplitude of the lopsided mode.

#### 4.4.4.1 Time evolution of structural parameters

As previously discussed, lopsided galaxies tend to show lower values of  $\mu_*$  as well as larger  $R_{50}^*$  at the present-day. In Fig. 4.4.3 we explore how these structural parameters evolved over time. As before we focus on the strong types to better highlight the differences between perturbed and unperturbed galaxies. The left panel shows the time evolution of the central stellar surface density,  $\mu_*$ , over the last 6 Gyr. The blue and red solid lines depict the median  $\mu_*$  obtained after stacking the strong asymmetric and symmetric subsamples, respectively. The shaded areas are determined by the 25th and 75th percentiles of both distributions. It is interesting to note that, at the present-day, the difference in  $\mu_*$  is very significant, and that this difference increased over the last 6 Gyr. In particular, we notice a significant decay of  $\mu_*$  over time for the strong lopsided cases, while for the symmetric counterparts  $\mu_*$  remain nearly constant. To understand what is behind this decay, we show in the middle panel of Fig. 4.4.3 the time evolution of the stellar mass enclosed within the stellar half-mass radius,  $M_{50}^*$ . We notice that, on average, lopsided

galaxies tend to enclose less stellar mass within  $R_{50}^*$ . However the difference in  $M_{50}^*$  between symmetric and asymmetric galaxies remains nearly constant over the last 6 Gyr. This is in contrast for the time evolution of  $R_{50}^*$ , shown in the right panel. Note that 6 Gyr ago, both subsamples had, on average, very similar values of  $R_{50}^*$ . However, lopsided galaxies experienced a significant growth of  $R_{50}^*$  while, for symmetric galaxies, it remained nearly constant, specially over the last 3 Gyr.

The previous analysis shows that what drives the decay of  $\mu_*$  for lopsided galaxies is mainly the growth of the stellar disc size. Using the Auriga simulations, Grand et al. (2017) investigated the mechanisms that set present-day disc sizes, and found that they are mainly related to the angular momentum of halo material. In their models, the largest discs are produced by quiescent mergers that inspiral into the galaxy and deposit high-angular momentum material into the pre-existing disc. This process simultaneously increases the spin of dark matter and gas in the halo. On the other hand early violent mergers and strong AGN feedback strongly limits the final disc size by destroying pre-existing discs and by suppressing gas accretion on to the outer disc, respectively. Interestingly, they find that the most important factor that leads to compact discs, however, is simply a low angular momentum for the halo. To explore whether the halo spin,  $\lambda$  (see eq. 12 Grand et al., 2017) plays a role on the development of lopsided galaxies by partially setting the size of the disc and thus their radial mass distribution, in Fig. 4.4.4 we show the distribution of  $\lambda$  versus  $M_{50}/R_{26.5}^3$  for galaxies in our sample. The color coding indicates the strength of the  $A_1$  mode. Interestingly, we find that galaxies with high  $\lambda$  typically show smaller values of  $M_{50}/R_{26.5}^3$  and high values of  $A_1$ . On the other hand, galaxies with low  $\lambda$  values are dominated by strongly self gravitating discs and, thus, low  $A_1$  values. Interestingly, using the EAGLE and Fenix simulations Cataldi et al. (2021) reported that haloes with less concentration tend to host extended galaxies. These results highlight an interesting morphology–halo connection for late type galaxies.

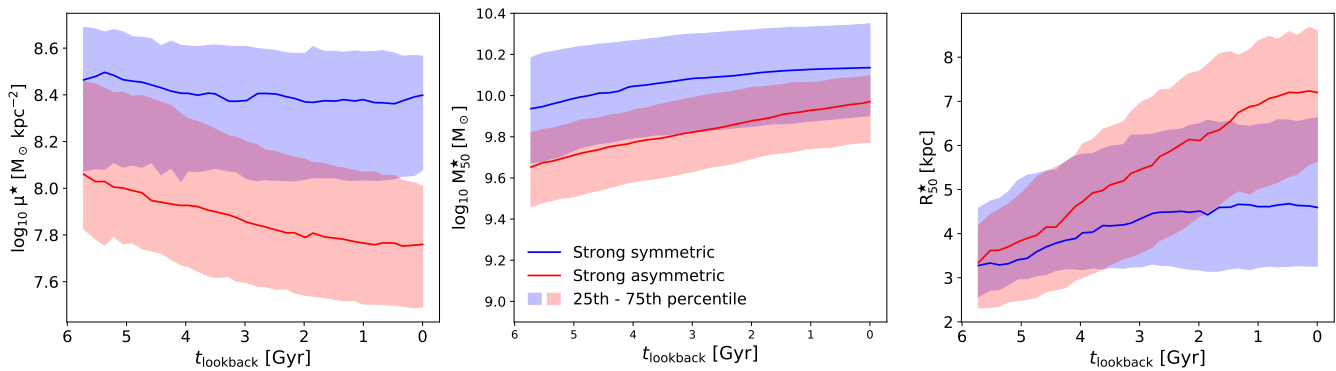


Figure 4.4.3: Time evolution of the central stellar density, the stellar half-mass, and stellar half-mass radius (from left to right). Quantities are shown as a function of lookback time. The solid blue and red lines show the median of the distributions obtained from the strong symmetric and asymmetric subsamples, respectively. The shaded areas highlight indicate the 25th and 75th percentiles of the corresponding distributions. The central stellar density evolution of the strong asymmetric sub-sample tend to have a sharp decrease in time compared to strong symmetric sub-sample. This is a consequence of the rapid growth of  $R_{50}^*$  over time.

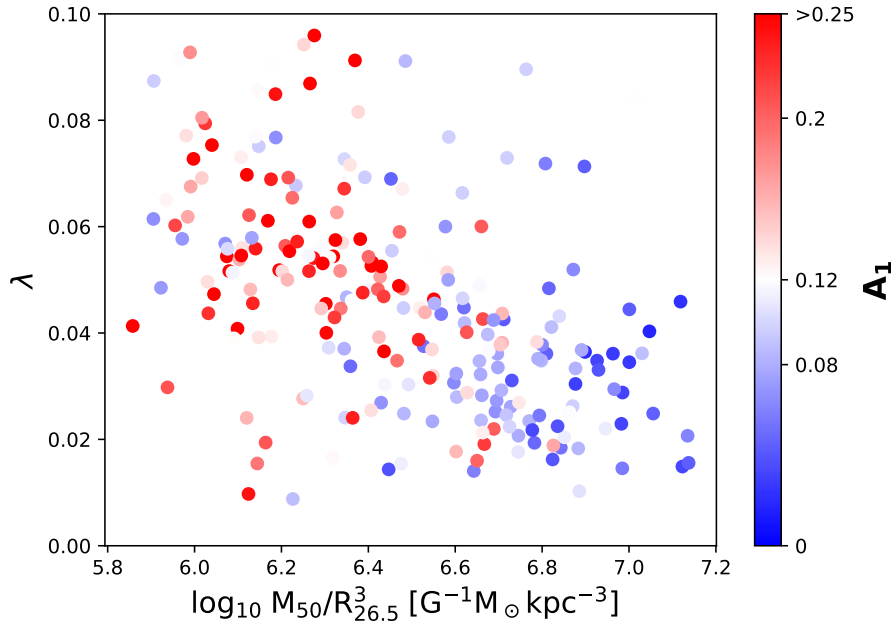


Figure 4.4.4: Distribution of halo spin parameter,  $\lambda$ , versus proxy of the tidal force exerted by the inner disc on the its outskirts,  $M_{50}/R_{26.5}^3$ . The dots are colored according to the present-day value of  $A_1$ . Which the palette of colors was centered around  $\hat{A}_1 \sim 0.12$ , while 0.08 and 0.2 values correspond to the 25<sup>th</sup> and 75<sup>th</sup> percentiles of  $A_1$  distribution, used to define strong sub-sample. Note that asymmetrical galaxies tend to have higher halo spin than their counterpart symmetrical.

#### 4.4.4.2 Frequency of $A_1$

As previously discussed, Fig. 4.3.2 shows that, at the present-day, a 62 percent of our simulated galactic discs are significantly lopsided ( $A_1 > 0.1$ ). This suggest that this type of perturbations are either long-lived (e.g. Jog & Combes, 2009), or short-lived but repeatedly re-excited by subsequent perturbations (see e.g. Ghosh et al., 2022). We explore this by following the time evolution of our simulated galaxies, and quantifying the fraction of time they present a significant lopsided perturbation over the last 6 Gyr. In practice, we proceed as follow. We identify our galactic models in the 36 snapshots available during the last 6 Gyr of evolution and compute, on each of them, the  $A_1$  parameter. This parameter is calculated by fixing the value of  $R_{26.5}$  at its present-day value. We have tested that our results do not significantly vary if we take into account the evolution of the optical radius. In Fig. 4.4.5, we explore the distribution of  $A_1$  in our sample over the past 6 Gyr (bottom panel). The median of  $A_1$  (green line) is around 0.125 during this period. The green region cover the 25<sup>th</sup> to 75<sup>th</sup> percentiles of the  $A_1$  distribution of our sample, which does not exceed 0.2 for the 75<sup>th</sup> percentile and does not fall below 0.075 for the 25<sup>th</sup> percentile. In the top panel we show the fraction of galaxies that display a high amplitude of  $m = 1$  component ( $A_1 > 0.1$ ), showing that around 60 to 70 percent of the galaxies in our sample exhibit high lopsidedness during this time range. That suggests that lopsided perturbation is a very frequent phenomenon for disc galaxies.

Fig. 4.4.6 shows the distribution of galaxies in  $\mu_*$  versus  $M_{50}/R_{26.5}^3$  space, colour coded according to the fraction of time each simulated galaxies experienced  $A_1 > 0.1$  within the last 6 Gyr. Present-day lopsided

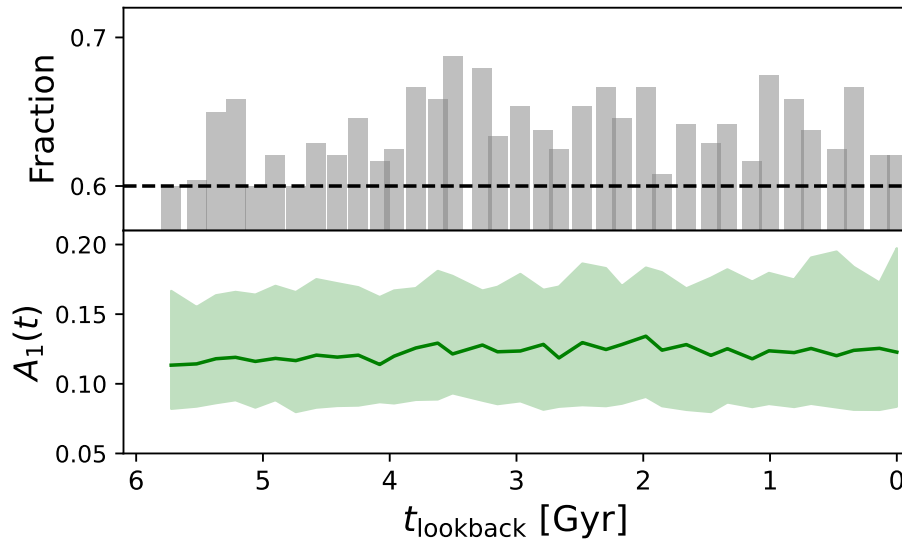


Figure 4.4.5: *Top panel:* Fraction of galaxies that show  $A_1 > 0.1$  during the last 6 Gyr. *Bottom panel:* Distribution of  $A_1$  in the sample in function of time. The green line correspond to the median of  $A_1$  and the green region covers the 25<sup>th</sup> to 75<sup>th</sup> percentile of the  $A_1$  distribution. We see that the medians of  $A_1$  are around 0.125 during the last 6 Gyr. Our sample show that the fraction of galaxies with high lopsidedness are between 60 to 70 percent in that range of time

galaxies, defined as in Section 4.4.1, are shown with star symbols, whereas their symmetrical counterparts, with square symbols. In general, we find that symmetric galaxies (high  $\mu_*$  and  $M_{50}/R_{26.5}^3$  values), show low  $A_1$  values throughout the latest 6 Gyr of evolution. In other words, strongly gravitationally cohesive galaxies have remained symmetric over most of the corresponding period of time (blue colors). On the other hand, we find that lopsided galaxies (typically weakly gravitationally cohesive) have remained lopsided ( $A_1 > 0.1$ ) over a significant fraction of the latest 6 Gyr (red colors). There are however several examples of galaxies that have been lopsided over most of this period, but at the present day have a symmetric configuration (see red squares). Note as well that it is less common to find present-day lopsided galaxies with low frequency of  $A_1$ .

Our results suggest that lopsided perturbation are typically long-lived, rather than short-lived but repeatedly re-excited. We further explore this in the following Section, where we follow the time evolution of a number representative galaxy models.

#### 4.4.5 Main driving agents

As discussed in Section 4.1, several different mechanism have been proposed as main driving agents for this type of morphological perturbation. The mechanisms range from direct tidal perturbations from relatively massive satellites, torques associated with perturbed underlying DM halos, and the non-axisymmetric accretion of cold gas, among others. In this Section we explore whether there is a dominant mechanism driving lopsidedness in our simulated galaxies.

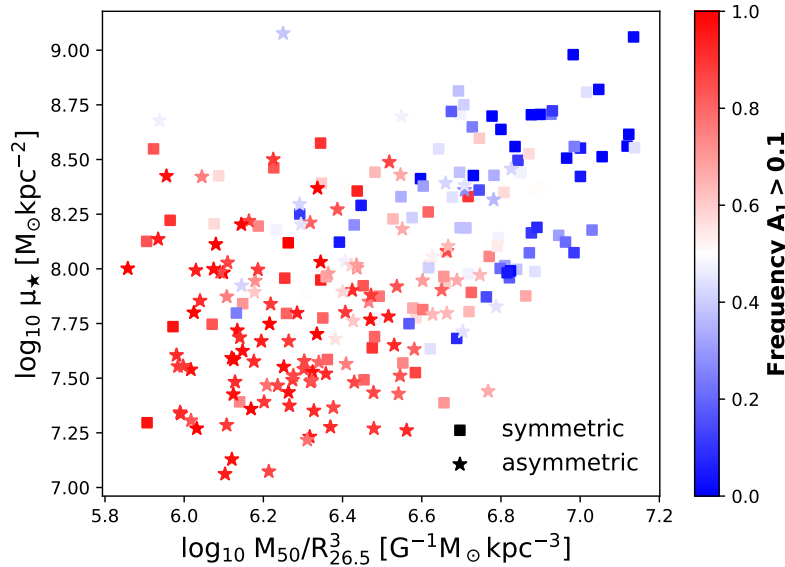


Figure 4.4.6: Distribution of the central stellar density versus  $M_{50}/R_{26.5}^3$ , which is a proxy of the tidal force exerted by the inner disc on its outskirts. Galaxies are separated between symmetric (squared) and asymmetric (star), using  $A_1$  at  $z = 0$ . The symbols are colour coded according to the fraction of time they experienced of significant lopsided perturbation ( $A_1 > 0.1$ ) during the last 6 Gyr of evolution. Galaxies with lower  $M_{50}/R_{26.5}^3$  tend to show lopsided distortions for longer periods. Interestingly, there are symmetric cases at the present-day that have spent long periods as lopsided (red squares). This galaxies typically show low  $M_{50}/R_{26.5}^3$ . Conversely, it is less common to see present-day lopsided galaxies with small  $A_1 > 0.1$  frequency.

#### 4.4.5.1 Individual examples

Before analyzing the whole sample of galaxy models in a statistical manner, we first analyze in detail a couple of typical examples of present-day symmetric and lopsided galaxies.

We first focus on two examples of typical present-day symmetric galaxies. The top panels of Fig. 4.4.7 show that, as discussed in Sec 4.4.4.1, symmetric galaxies typically do not experience a substantial growth in size over the last 6 Gyr of evolution. Both discs show nearly constant  $R_{50}^*$  and  $R_{90}^*$  values over this period of time. In the second panel (top to bottom) we show the time evolution of  $\mu_*$ . As expected, both galaxies show  $\mu_*$  values larger than the  $z = 0$  median (red dashed line,  $\hat{\mu}_* = 10^{7.98}$ ). In addition  $\mu_*$  show nearly constant values over this period of time. The large central surface density and small size render strong cohesiveness and thus resilience to perturbations. Indeed, as shown in the third panel, their  $A_1$  value remains mainly below the  $\hat{A}_1$  threshold, indicating that these galaxies have remained symmetric over most of this period. We note, however, that the evolution of  $A_1$  shows moderate increments over short spans of times. For example, for galaxy **S1**,  $A_1$  rises over  $\hat{A}_1$  at a lookback time,  $t_{lb} \sim 5$  Gyr. To explore the origin of this short-lived lopsided mode we quantify in the fourth and fifth panels the interaction of this galactic disc with its environment. We first look at the time evolution of the offset of the halo center of mass, CoM, with respect to its density cusp,  $\Delta r_{DM}^i$  (fourth panel). Interestingly,  $\Delta r_{DM}^i$  peaks during the same period. This is noticeable when considering DM particles up to a distance of  $5R_{26.5}$ . Note as well that this offset of the DM halo CoM is short lived and directly related to a strong

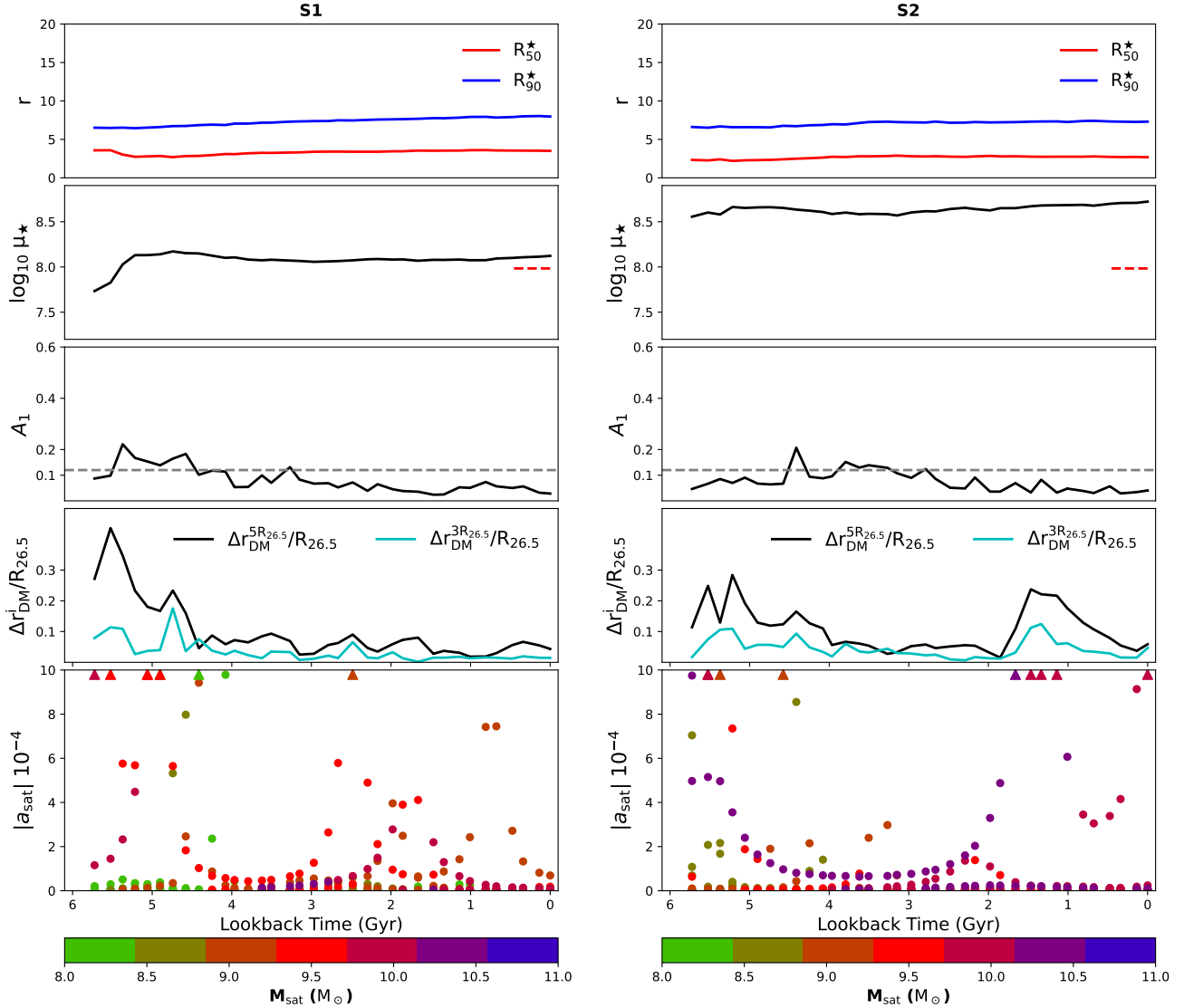


Figure 4.4.7: Examples of two typical present-day symmetric galaxies, S1 and S2. *From top to bottom, First panel:* Time evolution of the scale length parameters,  $R_{50}^*$  and  $R_{90}^*$ , during the last 6 Gyr of evolution. *Second panel:* Evolution of the central surface density,  $\mu_*$ . The red dashed line on the right side of each panel shows the corresponding present-day median of  $\mu_*$ . *Third panel:*  $A_1$  as a function of time. The black dashed line correspond to the  $\hat{A}_1$  threshold, extracted from the full sample distribution at  $z = 0$ . *Fourth panel:* Time evolution of the offset between the DM halo center of mass and its density cusp,  $\Delta r_{\text{DM}}^i$ . We show the evolution of  $\Delta r_{\text{DM}}^i$  calculated within two spatial regions,  $3R_{26.5}$  and  $5R_{26.5}$  (see Sec. 4.3.3). *Fifth panel:* Time evolution of tidal field exerted on the host galaxy by its 10 most massive satellites. Triangles indicate tidal field values that are above the Y-axis limit. Symbols are colour coded as a function of the total mass of the corresponding satellite.

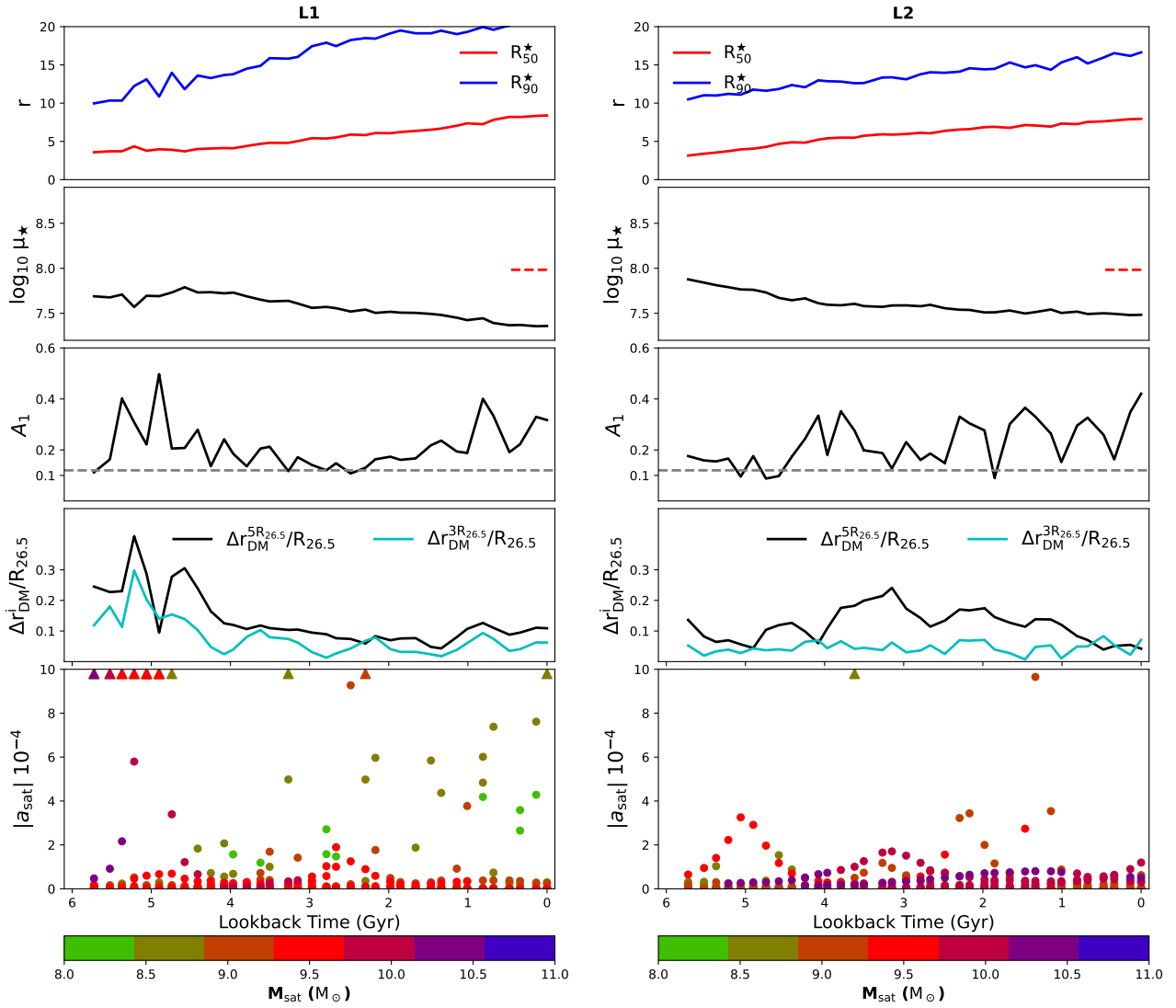


Figure 4.4.8: As in Fig. 4.4.7, for two typical present-day Lopsided galaxies, L1 and L2.

tidal interaction with a massive satellite galaxy. This is shown on the bottom panel, where we show the time evolution of tidal field exerted on the host by its 10 most massive satellites as a function of time, i.e.  $|a_{\text{sat}}| = GM_{\text{sat}}/R_{\text{sat}}^3$ . Here  $M_{\text{sat}}$  and  $R_{\text{sat}}$  are the total mass of the satellite and the distance between the satellite and its host galaxy. We notice that the galactic disc strongly interacts with a massive satellite ( $M_{\text{sat}} \sim 10^{10} M_{\odot}$ ) at  $t_{\text{lb}} \sim 5$  Gyr. This strong interaction is behind the brief distortion of the host outer DM halo, and the temporary onset of a mild  $A_1$  perturbation. For this large  $\mu_*$  simulated galaxy, and in agreement with Ghosh et al. (2022), the perturbation rapidly dissipates and the amplitude of the disc  $m = 1$  mode remains below  $\hat{A}_1$  for the rest of the period, even though a second significant interactions

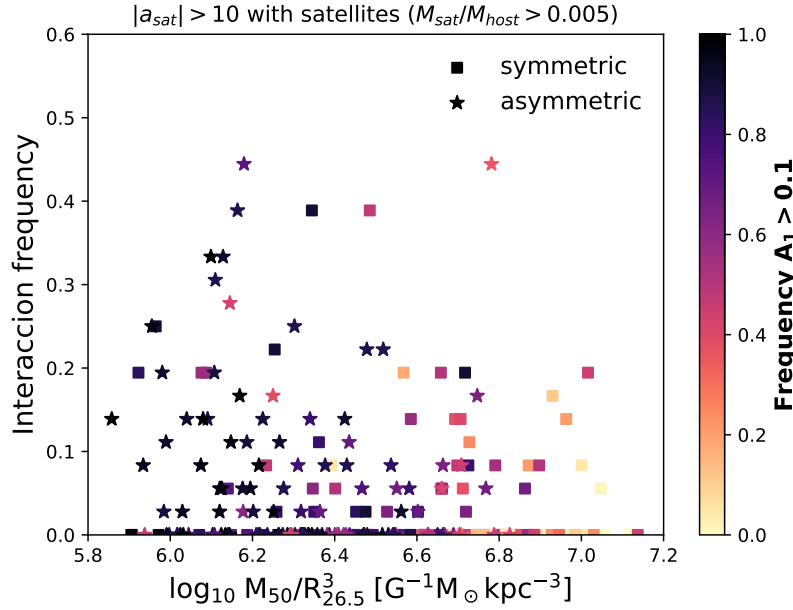


Figure 4.4.9: Fraction of time that a given host has strongly interacted with satellites of  $M_{\text{sat}} \geq 10^{9.5} M_{\odot}$  during the last 6 Gyr of evolution in function of self-gravity proxy. The color coding indicated the fraction of time galaxies presented a strong lopsided perturbation ( $A_1 > 0.1$ ). The different symbols indicated whether galaxies are symmetric or asymmetric at the present-day. Note that no significant correlation is found between the fraction of time galactic discs display lopsided perturbations and the fraction of time they experienced significant satellite tidal interactions.

takes place later on ( $t_{\text{lb}} \sim 2.5$  Gyr).

In the right panels of Fig. 4.4.7 we analyze a second example, S2, of a present-day symmetric galaxy. As before, the galaxy shows small and nearly constant scale lengths over the whole the last 6 Gyr of evolution. It shows as well a nearly constant  $\mu_{\star}$  value, but with a value larger than in the previous example, S1. The  $A_1$  parameter typically remains below  $\hat{A}_1$ , except for short periods where it slightly raises over this threshold. When inspecting interactions with its environment, we observe that S2 experienced two very strong interactions with a satellite galaxy of  $M_{\text{tot}} \approx 10^{10.5} M_{\odot}$ . These interactions take place at  $t_{\text{lb}} \approx 5.5$  and 1.5 Gyr (fifth panel), and both resulted in significant perturbations of the host DM halo (fourth panel). Yet, due to the large  $\mu_{\star}$ , no associated response is observed in the evolution of the  $A_1$  parameter.

In Fig. 4.4.8 we now explore two examples of strongly lopsided galaxies, L1 and L2. The top panels show that, contrary to the symmetric cases, these galaxies experienced a consistent growth in size over the latest 6 Gyr, which resulted in a decrement of their  $\mu_{\star}$ . As a result, the central surface density of these simulated galaxies is significantly lower (second panels) than in the symmetric examples. The third panels show that, in both cases,  $A_1$  has mainly remained above our threshold,  $\hat{A}_1$ , indicating long lived lopsided modes. In particular, for L1 (left panels), we find that the galaxy experienced a relatively strong tidal interaction with a satellite of  $M_{\text{sat}} \sim 10^{10.5} M_{\odot}$  at  $t_{\text{lb}} \approx 5$  Gyr. Due to the low values of  $\mu_{\star}$ , and contrary to the S1 case, this interaction excited a strong lopsided mode as well as a shift of the DM

CoM with respect to its density cusp. The lopsided perturbation slightly wanes over time, but it always remains over  $\hat{A}_1$ . At  $t_{1b} \approx 2$  Gyr the disc experienced a second significant tidal interaction ( $M_{\text{sat}} \sim 10^{10} M_{\odot}$ ) that enhances the lopsided perturbation, raising the value of  $A_1 \approx 0.35$  until the present-day. On the other hand even though L2 (right panels) shows a value of  $A_1 > \hat{A}_1$  over most of the last 6 Gyr, it did not experience any significant interaction with massive satellites ( $M_{\text{sat}} > 10^{10} M_{\odot}$ ). Interestingly, the CoM of outer DM halo shows a significant shift with respect to its cusp during this period, with values  $\Delta r_{\text{DM}}^{5R_{26.5}}$  as large as 20 percent of  $R_{26.5}$ . Such perturbed DM halo could be behind the long lived lopsided perturbation in this galactic disc (see e.g. Jog & Combes, 2009). We will explore in detail this particular kind of models in a follow up study.

#### 4.4.5.2 Statistical characterization of the impact of interactions

In the previous Section we discussed two examples of stellar discs that interacted with their nearby environment and developed very strong lopsided perturbations. On the other hand, we also discussed examples of galaxies that strongly interacted with their environments but did not develop significant lopsided modes on their discs. The main difference between these two sets of objects is their central surface density,  $\mu_*$ , which set the gravitational cohesiveness of the disc outskirts. In this Section we explore what are the main agents driving lopsided perturbations in low  $\mu_*$  galaxies.

We start by quantifying significant tidal interaction with satellite galaxies within the last 6 Gyr of evolution. As in Section 4.4.5.1, for each galaxy in our sample, we compute  $|a_{\text{sat}}|$  as function of lookback time. Based on Figures 4.4.7 and 4.4.8, and the results shown in Gómez et al. (2017), we first quantify the fraction of time galactic discs were exposed to  $|a_{\text{sat}}| > 10$  from satellites with mass ratios  $M_{\text{sat}}/M_{\text{host}} > 0.005$ . Lower values of  $|a_{\text{sat}}|$  do not yield to global perturbations in the discs. For a MW-mass host, the chosen threshold in the mass ratio allows interaction with satellites of  $M_{\text{sat}} \geq 10^{9.5} M_{\odot}$ . Lower mass satellite are unlikely to induced significant global vertical perturbations (Gómez et al., 2017). Figure 4.4.9 shows our sample of galactic discs in satellite interaction frequency versus  $M_{50}/R_{26.5}^3$  space. Points are color coded by the fraction of time each disc presents a significant lopsided perturbation (see Sec.4.4.4.2). As before, we notice that galaxies with lower frequencies of  $A_1 > 0.1$  (light colors) tend to have lower values of  $M_{50}/R_{26.5}^3$ . Interestingly we find no significant correlation between the fraction of time galactic discs display lopsided perturbations and the fraction of time they experienced significant satellite tidal interactions. In particular, a significant number of simulated disc galaxies (35 per cent of the full sample) did not experience significant interactions during the last 6 Gyr, but nevertheless, have a long-lasting lopsided perturbation over most of that period. This supports our conclusion that direct tidal interaction with satellites galaxies is just one plausible channel for inducing lopsided perturbation, and not the main driving agent. Our results are in agreement with those presented by Bournaud et al. (2005) who shows with a sample of 149 observed galaxies that the  $m = 1$  amplitude is uncorrelated with the presence of companions.

In addition to direct tidal torques exerted by satellites, galactic discs can respond to the gravitational interaction with a distorted DM halo (Gómez et al., 2015; Garavito-Camargo et al., 2019; Laporte et al., 2018a). One of the first attempts to statistically study asymmetries in the inner regions of dark haloes, and their possible relation to the accretion of external material on to these regions, was provided by Gao & White (2006, hereafter GW06). Based on the large statistic provided by the Millennium Simulation (Springel et al., 2005), they studied asymmetries in the density distribution of DM halos, selected with masses ranging from MW-mass to cluster mass hosts. They showed that such asymmetries are not un-

common, and that the frequency with which they arise depends on host mass. While 20 per cent of cluster haloes have density centres that are separated from barycentre by more than 20 per cent of the virial radius, only seven per cent of MW haloes have such large asymmetries.

Following GW06, we examine the distribution of the offsets of central DM halos extracted from the TNG50-1 simulation and its DM only simulation counterpart. Our goal is to test whether we recover the results presented in GW06, based purely on DM only models, and test whether the addition of baryons has an effect on this statistics. Since our work is centered around late type galaxies, we focus on three sets of models selected by halo mass,  $M_{200}$ . The less massive set contains haloes with  $M_{200}$  between  $10^{11}$  to  $5 \times 10^{11} M_{\odot}$ ; the intermediate set between  $5 \times 10^{11}$  to  $10^{12} M_{\odot}$ , and the more massive between  $10^{12}$  to  $5 \times 10^{12} M_{\odot}$ . In the table 4.4.2 we show the results of this selection for each simulation.

For each simulated galaxy, we compute  $\Delta r_{\text{DM}}^{\text{R}200}$  (see Eq.4.3.4) at the present-day considering DM particles within  $R_{200}$ . In the top panel of Figure 4.4.10, we show the  $\Delta r_{\text{DM}}^{\text{R}200}$  cumulative distribution function (CDF) for the three halo subsets. The solid and dashed lines show the results obtained from the full hydrodynamical simulation and the DM only, respectively. To facilitate the comparison between these different haloes, each  $\Delta r_{\text{DM}}$  has been normalized by the corresponding  $R_{200}$ . Our results based on the DM only simulations are in good agreement GW06. We find that more massive haloes tend to have larger asymmetries. Indeed, while  $\sim 8$  percent of halos with  $10^{12} < M_{200} < 5 \times 10^{12} M_{\odot}$  show  $\Delta r_{\text{DM}}^{\text{R}200} > 20$  percent, for haloes with  $10^{11} < M_{200} < 5 \times 10^{11} M_{\odot}$  only  $\sim 1.5$  percent show such large asymmetries. Comparison with the results obtained with the full-physics models shows that these trends are not significantly affected by the addition of baryons. The shaded areas highlight the differences between the DM only and the hydrodynamical simulations. Note that only the larger mass halo subset shows a slightly larger fraction of halos with  $\Delta r_{\text{DM}}^{\text{R}200} \gtrsim 0.15$  in the hydrodynamical simulation. However, this difference mainly arise from the low number statistics associated to mass bin<sup>5</sup>. The similarities between both simulations are better highlighted in the bottom panel of Fig. 4.4.10, where we show the difference between both CDFs.

As previously discussed in GW06, these DM halo asymmetries could be related to visible asymmetric phenomena in galaxies, among them lopsidedness. To explore this, we show the  $\Delta r_{\text{DM}}^i$  CDF, now considering only galaxies selected by the criteria defined in Section 4.2.2. For this analysis we focus on perturbations within the inner DM halo,  $3 \times R_{26.5}$  (Figure 4.4.11), since this is the region that can exert significant torque on the embedded discs (e.g Gómez et al., 2016). We first explore the subset of galaxies that are strongly symmetric and strongly lopsided. The corresponding CDFs are shown in solid red and blue lines respectively. The vertical green line indicates the mean of the gravitational softening length,  $\epsilon_{\text{DM}}$  (see table 4.2.1), obtained after normalizing  $\epsilon_{\text{DM}}$  by the  $R_{26.5}$  of each galaxy. The shaded region covers 25th and 75th percentiles of this distribution. The figure clearly shows that symmetric galaxies tend to have small  $\Delta r_{\text{DM}}^{3R_{26.5}}$ , indicating very similar spatial location for the DM CoM of the center of density. Only 5 percent of the symmetric galaxies show values of  $\Delta r_{\text{DM}}^{3R_{26.5}} > 0.05$ . The CDF for the asymmetric galaxies shows a different behaviour. It is clear that asymmetric galaxies tend to show significantly large  $\Delta r_{\text{DM}}^{3R_{26.5}}$  than their symmetric counterparts. Indeed,  $\approx 30$  percent of the disc galaxies shows  $\Delta r_{\text{DM}}^{3R_{26.5}} > 0.05$ . Yet, as discussed in Section 4.4.5.1, we find a large number of lopsided galaxies show very small  $\Delta r_{\text{DM}}^{3R_{26.5}}$ , indicating that this is not necessarily the main driver behind their perturbations.

<sup>5</sup>We have confirmed that his difference is due to low number statistics by repeating the analysis on the larger volume simulations TNG100-1.

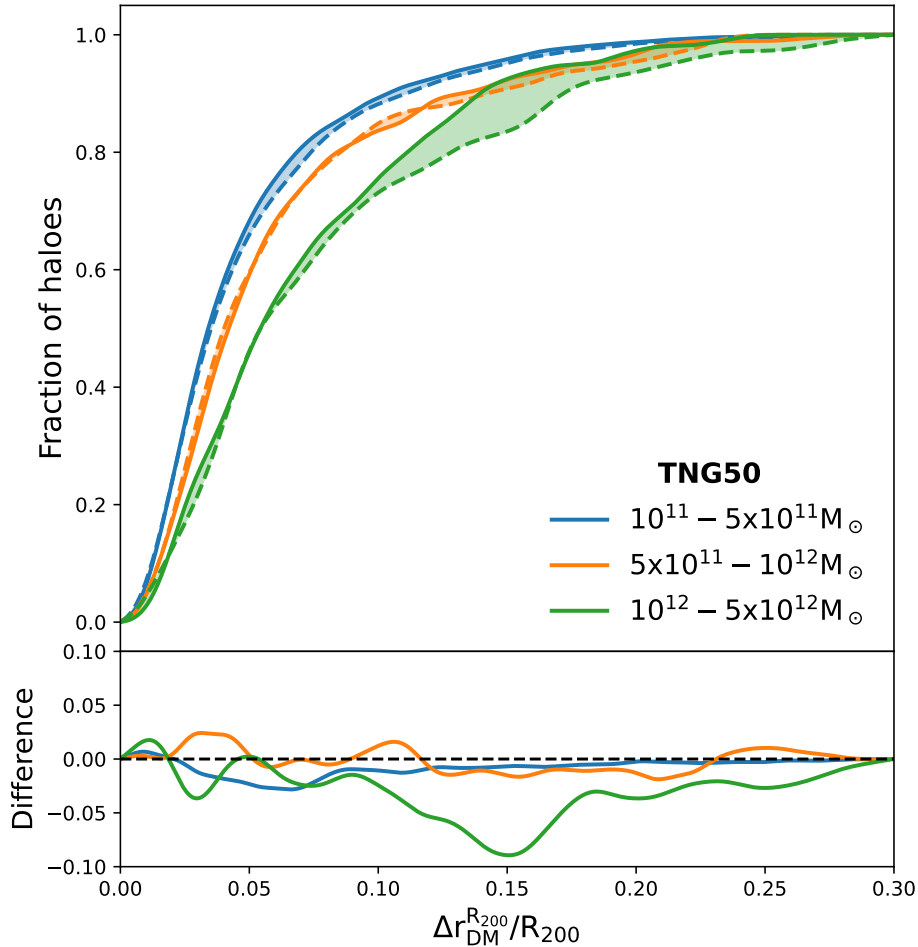


Figure 4.4.10: Top panel: Cumulative distribution function of offset between the halo center of mass and their density cusp,  $\Delta r_{\text{DM}}$ . The colour coded lines show the results obtained from different halo mass ranges. For this calculation DM particles within each halo’s  $R_{200}$  are considered. Solid and dashed lines show the results obtained from the full hydrodynamical and the DM only simulations, respectively. Bottom panel: differences between cumulative distribution function calculated from the full hydrodynamical and the DM only simulations.

## 4.5 Conclusions and discussion

In this Chapter, we have studied disc galaxies that display a global  $m = 1$  non-axisymmetric perturbation in their stellar mass distribution, more commonly known as a lopsided perturbation. We focused the analysis on a sample of MW-mass like galaxies from the fully cosmological hydrodynamical simulation, TNG50 from IllustrisTNG project. Our sample was built selecting central subhalos with  $M_{200}$  within the range  $10^{11.5}$  to  $10^{12.5} M_{\odot}$ . To consider well-resolved disc-dominated galaxies we imposed a threshold in the D/T ratio of 0.5, and only selected galaxies with more than  $10^4$  stellar particles within a subhalo. From this criteria, 240 late-type galaxies with total stellar mass between  $10^{9.5}$  and  $10^{11.2} M_{\odot}$  were selected. Lopsidedness in the discs were quantified by computing the amplitude of the  $m = 1$  Fourier mode of the

Table 4.4.2: Number of haloes for each  $M_{200}$  range between the two homologous runs; baryonic + DM simulation and only DM.

<b>TNG50-1</b>		
	Baryon+DM	DM only
$10^{11} - 5 \times 10^{11} M_{\odot}$	1251	1352
$5 \times 10^{11} - 10^{12} M_{\odot}$	190	185
$10^{12} - 5 \times 10^{12} M_{\odot}$	168	172

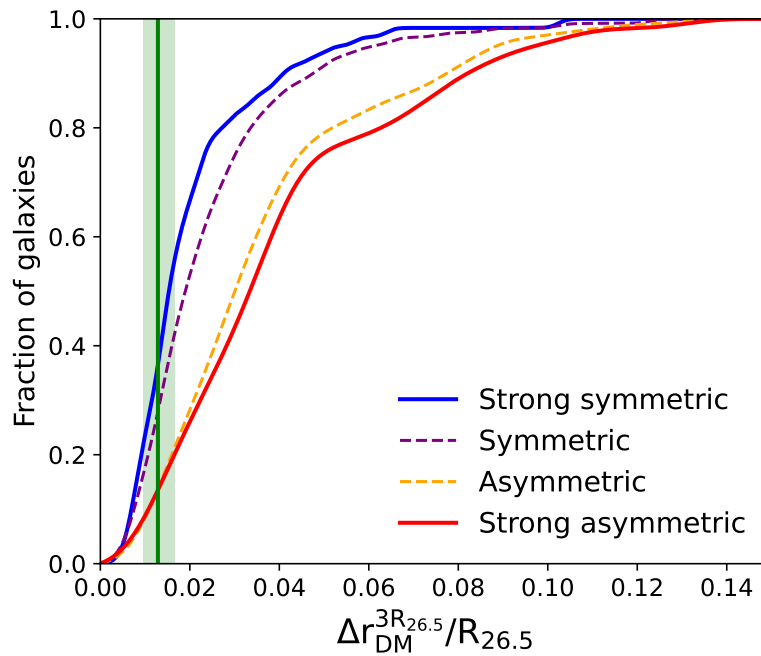


Figure 4.4.11: Cumulative distribution function of the offset between the halo center of mass and their density cusp,  $\Delta r_{\text{DM}}^{3R_{26.5}}$ . For this calculation DM particles within each galaxy  $3 \times R_{26.5}$  are considered. The dashed purple (solid blue) and orange (red) lines show the results obtained from the (strong) symmetric and asymmetric subsamples, respectively. The vertical green line indicates the median of the distribution obtained after normalizing the gravitational softening,  $\epsilon_{\text{DM}}$ , by the  $R_{26.5}$  of each galaxy. The shaded green area encloses the 25th and 75th percentile of the corresponding distribution.

stellar density distribution,  $A_1$ . Based on this parameter, we classified our galaxies as symmetrical and asymmetrical (i.e. lopsided) cases.

We find that in our simulated galaxy sample the main characteristics of such lopsided perturbations are in good agreement with observations. In lopsided galaxies, the radial profile of the  $m = 1$  mode amplitude,  $A_1(R)$ , increases with radius in the outer disc regions, while in the inner parts it remains flat and close to zero. The radius at which the transition takes place is  $\approx 0.5R_{26.5}$ , in agreement with previous observational works (e.g. Rix & Zaritsky, 1995; Bournaud et al., 2005). Furthermore, lopsided galaxies

exhibit a nearly constant or mildly varying radial distribution of phase angles, indicating a slow winding of the phase angle in the outer disc (Saha et al., 2007; Ghosh et al., 2022). Based on this, we computed for each simulated galaxy a characteristic  $A_1$  value, which corresponds to the average of  $A_1(R)$  between  $0.5R_{26.5} < R < 1.1R_{26.5}$ . We find that the distribution of this characteristic  $A_1$  parameter is also in good agreement with observations, that measured in large observational samples the  $A_1$  distribution, considering similar galactic regions (Bournaud et al., 2005; Reichard et al., 2008). To highlight differences between lopsided and symmetrical galaxies, we focus on the analysis on the first and fourth quartiles of the  $A_1$  distribution. We call these subsets strong symmetric and strong asymmetric galaxies, respectively. When analyzing the present-day structural parameters of our sample, we find that lopsided galaxies tend to be more disc-dominated than their symmetrical counterparts. This trend suggests that the presence of a centrally pressure supported component plays an important role on setting the lopsidedness strength. This is in agreement with previous works, which found that the fraction of lopsided galaxies increases with galaxy Hubble type, being late-type galaxies the population with the highest fraction (Rix & Zaritsky, 1995; Bournaud et al., 2005; Conselice et al., 2000). Following R08, we also characterized our sample through the following present-day structural parameters: stellar half-mass radius,  $R_{50}^*$ , total stellar mass,  $M^*$ , central surface density,  $\mu_*$  and stellar concentration,  $C_*$ . Focusing on the strong subsamples, we find that both lopsided and symmetric galaxies show very similar  $C_*$  distributions. We also find that strongly lopsided galaxies tend to have more extended central regions and to be slightly less massive than their symmetrical counterpart. However, the most strong (anti)correlation we find is between  $\mu_*$  and  $A_1$ . Indeed, the strong subsamples show very different distributions of  $\mu_*$ , with lopsided disc systematically showing lower  $\mu_*$  values. These results are consistent with the observational findings from R08, suggesting that galaxies with lower central density could be more susceptible to different types of interaction and, thus, more prone to the excitation of lopsided modes. Based on these results, we show that what regulates whether a galaxy develops strong lopsided modes is the self-gravitating nature of the inner galactic regions. Discs with denser inner regions are more gravitationally cohesive and thus, less prone to develop lopsided perturbations in their external regions. Hence, our results hint toward a population of galaxies susceptible to lopsided perturbations, and not to a particular external driving source.

We have explored the time evolution of the main structural parameters that differentiate symmetric and lopsided galaxies, as well as the time evolution of the amplitude of the lopsided modes. We focus on their behaviour during the last 6 Gyr of evolution. We observed that the percentage of galaxies in our sample with  $A_1 > 0.1$  are between 60 and 70 during this range of time. Interestingly, we find that, while for symmetric galaxies  $\mu_*$  remains nearly constant through time, a significant decay of  $\mu_*$  is observed in lopsided galaxies. The main reason for this is the faster growth of the half-mass radius,  $R_{50}^*$ , displayed by lopsided galaxies with respect to their symmetric counterparts. While both galaxies experienced similar growth rates of their  $M_{50}^*$ , lopsided galaxies grow faster in size thus reducing their inner self-gravitational cohesion. Following Grand et al. (2016), we analyzed whether the halo spin,  $\lambda$ , is behind this faster growth rate of  $R_{50}^*$  in lopsided objects. Interestingly, we find that galaxies with higher present-day  $\lambda$  are typically less cohesive and show higher values of  $A_1$ . On the other hand, galaxies with low  $\lambda$  values are dominated by strongly self-gravitating discs and, thus, low  $A_1$  values. Our results highlight an interesting morphology–halo connection for late type galaxies.

We have also analyzed the main agents driving these perturbations. In agreement with previous studies, we have shown that satellite interactions can excite lopsided modes (Weinberg, 1995; Zaritsky & Rix, 1997; Bournaud et al., 2005). However, we find that up to  $\sim 35$  per cent of the sample galaxy shows

significant lopsided perturbations but, during the last 6 Gyr of evolution, did not experienced interactions with any satellite of mass ratio  $M_{\text{sat}}/M_{\text{host}} > 0.005$ . Interestingly those galaxies present low values of  $\mu_*$ . This supports the conclusion that direct tidal interaction with satellite is a possible channel for inducing lopsided perturbation, but not the main driving agent. Our results are in agreement with those presented by Bournaud et al. (2005) who shows with a sample of 149 observed galaxies that the  $m = 1$  amplitude is uncorrelated with the presence of companions.

Several studies have shown that galactic discs can also respond to tidal torques exerted by global perturbations of the host DM halo density distribution (Weinberg, 1998; Gómez et al., 2016; Laporte et al., 2018a,b; Hunt et al., 2021; Grand et al., 2022). To examine whether this mechanism is an important driving agent of lopsided perturbations in our simulations, we quantified the distribution of offsets between the CoM DM halo and the density cusp,  $r_{\text{cusp}}$ , of our halos,  $\Delta r_{\text{DM}}^{\text{R}200}$ . Previous studies based on the dark matter-only Millenium simulations (Gao & White, 2006) found that significant distortions in the DM halos are not uncommon, and that the frequency with which they arise depends on host mass. Our analysis, based on simulations that incorporate a self-consistent treatment for the evolution of baryons, yielded very similar results. While  $\sim 8$  percent of halos with  $10^{12} < M_{200} < 5 \times 10^{12} M_{\odot}$  show  $\Delta r_{\text{DM}}^{\text{R}200} > 20$  percent, only  $\sim 1.5$  percent of halos with  $10^{11} < M_{200} < 5 \times 10^{11} M_{\odot}$  show such large asymmetries. Given this result, we studied whether halos with large offsets typically host lopsided galactic discs. Interestingly, we find that symmetric galaxies tend to have smaller distortions in their inner DM halos (within  $3 \times R_{26.5}$ ) than their lopsided counterparts. While only five percent of the symmetric galaxies show values of  $\Delta r_{\text{DM}}^{3\text{R}26.5} > 0.05$ ,  $\approx 30$  percent of the lopsided galaxies do so. This results place torques from DM halo overdensity wake as another important mechanism behind the excitation of lopsided modes in galaxies with low central surface densities. In a follow up study we will quantify such torques by decomposing the density and potential distributions using basis function expansions (BFEs Garavito-Camargo et al., 2021; Cunningham et al., 2020; Johnson et al., 2023; Lilleengen et al., 2023). Furthermore, we found that lopsided galaxies tend to live in high spin dark matter halos. Using the same simulation suite Grand et al. (2017) showed that the present-day size of a stellar disc is strongly related to the the spin of its halo. High spin halos tend to host extended galaxies with lower central surface densities, thus prone to develop lopsided perturbations. This result, together with the lopsided response of discs to overdensity wakes, indicates a new direction for understanding the halo-galaxy connection in lopsided galaxies.

In this work, we have shown that lopsidedness is a very frequent phenomenon in the history of galaxies. The discs of these galaxies are extended with low central surface densities. Their self-gravity makes them cohesively weak, and therefore easily susceptible to any type of interaction such as tidal torques exerted by distorted DM halos and minor mergers. Such galaxies tend to reside in high-spin and often highly asymmetric DM halos, revealing a connection between the halos and lopsided discs.

## Chapter 5

# The effects of the DM overdensity wakes on disk galaxies

### Abstract

In this chapter we present preliminary results from an ongoing project that explored the effects that overdensity wakes in dark matter halos can produce on their host galactic disks. We are set to quantify the associated torques from such wakes and to explore the generation of morphological perturbations in disk galaxies. To achieve this goal, we decompose the density and potential field of MW-like galaxies, extracted from the Auriga project, using basis function expansions (BFE). Our preliminary results discuss the implementation of the BFE method to fully cosmological simulations and demonstrate its suitability. We show how the basis function reconstructs the potential field at the present-day. We also explore the stability of the constructed basis expansion as a function of time, by attempting to reconstruct DM density field with a basis generated at either later or earlier times.

## 5.1 Introduction

As previously discussed in Chapter 4, the earliest observations of HI gas in disk galaxies revealed that their outer regions exhibit perturbations such as warping (Binney, 1992) or also lopsidedness (Baldwin et al., 1980). These types of asymmetries show significant variations in amplitude and structure from one galaxy to another (e.g., Reshetnikov et al., 2016; Rix & Zaritsky, 1995), indicating that several mechanism behind such perturbations could be at play. Many explanations have been proposed for the formation of perturbations in disk galaxies. Discussed mechanisms range from misaligned halos relative to the disk, misaligned accretion of cold gas in the outer disk, mergers, and tidal interactions with other galaxies or satellites (Weinberg, 1998; Debattista & Sellwood, 1999; Jiang & Binney, 1999; Roškar et al., 2010; Aumer & White, 2013; Gómez et al., 2016, 2017; Walker et al., 1996; Zaritsky & Rix, 1997; Ghosh et al., 2022; Varela-Lavin et al., 2023; Dolfi et al., 2023). In particular, the Milky Way (MW) harbors asymmetric features in its disk. For example, a global perturbation is described in Kalberla & Dedes (2008), where the HI distribution of the MW has a higher gas density in the southern region ( $210^\circ < \phi < 330^\circ$ ) compared to the northern part ( $30^\circ < \phi < 150^\circ$ ). In addition, the Milky Way exhibits a warp in its outer disk region, characterized by a significant amplitude that extends to a height of more than 4 kpc at a galactocentric radius of 25 kpc in the northern region. (Levine et al., 2006; Romero-Gómez et al., 2019). Several authors have provided evidence of the presence of a corrugation patterns in our Galactic disk (Widrow et al., 2012; Widrow & Bonner, 2015; Antoja et al., 2018; Bland-Hawthorn & Tepper-García, 2021; Xu et al., 2015). Such asymmetries and others may result from the tidal interaction between the Milky Way and its satellites, the Large Magellanic Cloud (LMC), the Small Magellanic Cloud (SMC) and Sagittarius dwarf spheroidal galaxy (Sgr) (Weinberg, 1998; Gómez et al., 2013; Laporte et al., 2018a,b; Antoja et al., 2018, 2022)

Interestingly certain morphological asymmetries can result from the response of the disk to a density wake formed in the host dark matter halo by an orbiting satellite (Weinberg, 1998). Resonance dynamics between a satellite and its host dark halo can generate a wake that can exert a torque on a disk (Weinberg, 1998; Weinberg & Katz, 2007; Gómez et al., 2016; Garavito-Camargo et al., 2019, 2021). The resonant response within the halo depend on the orbital frequency and trajectory of the satellite (Choi et al., 2009). Therefore, the precise orbit of the satellite must be taken into account when studying the dark matter halo wake. The resonance orbit between a satellite and its DM halo can satisfy the expression  $l_3\Omega_{pert} = l_1\Omega_1 + l_2\Omega_2$ , where  $\Omega_1$  and  $\Omega_2$  are the radial and azimuthal frequencies of the satellite's orbit, and  $\Omega_{pert}$  is the perturber's frequency (satellite). Here  $l_1$ ,  $l_2$ , and  $l_3$  denote the resonance order, with  $|l_2| \leq l_3 = l$  and  $0 < l_3 = l$ , where  $l$  is the spherical harmonic of the perturber. If  $l_1 = 0$ , then the only resonance occurs at  $\Omega_2 = \Omega_{pert}$ , representing the strongest resonances associated with corotation. For a more detailed discussion of perturbation theory and resonance dynamics, see Tremaine & Weinberg (1984) and Choi et al. (2009). The amplitude of the resonance decays by a factor of  $1/r^l$ , where  $r$  is the distance from the satellite (Weinberg, 1989). This implies that lower resonances dominate the resonant satellite torque. Indeed, in Choi et al. (2009), a number of resonances were examined in terms of energy and angular momentum, and it was found that the resonance  $l_1 = -1$ ,  $l_2 = -2$  and  $l_3 = 2$  dominates in their analysis. The dipole ( $l = 1$ ) and quadrupole ( $l = 2$ ) resonances are the most relevant and give the strongest response.

In this chapter we study dark matter overdensity wakes to understand how torques from resonances can perturb the baryonic component of MW-like halos. We seek to explore the relation between such wakes

and the morphological asymmetries in the galactic disk. To achieve this, we analyze the gravitational potential and dark matter density distribution of MW-like central subhalos from Auriga simulations with their satellites, using BFE. This method allow us to dissect the potential and density fields of dark matter component in different angular and radial terms. In section 5.2 we give a theoretical description of the BFE and discuss its relevance in this work. The data parameters of the Auriga project and information on the simulations used in this study are described in the chapters 5.3 and 2.4. The analysis and preliminary results of this work are presented in section 5.4. The summary and future work are gave in Sec. 5.5

## 5.2 Basis-Function Expansions

To study the potential and density fields of perturbed DM halos, we aim to analyze their perturbations using a set of basis functions that decompose the potential and density field. We aim to identify the particular functions that characterize the perturbations associated with the overall halo potential. This function identification is relevant for a comprehensive analysis of the halo perturbations and their impact on their disk. The analysis of potential and density fields is complex, and a simplified decomposition facilitates the study. It is therefore necessary to be aware of various techniques for calculating the potential fields and individual forces acting on particles within a system.

BFE is a method to calculate density and gravitational potential by decomposing the density distribution using a set of biorthogonal basis functions represented as  $\{\phi_\mu(\mathbf{x}), d_\mu(\mathbf{x})\}$ . The biorthogonal natur of the basis functions guarantees that their inner product is the Kronecker delta (see more detail Petersen et al. (2022)):

$$\int d\mathbf{x} \phi_\mu(\mathbf{x}) d_\nu(\mathbf{x}) = 4\pi G \delta_{\mu\nu} \quad (5.2.1)$$

with  $G$  the universal gravitational constant. They also satisfies the Poisson equation,

$$\nabla^2 \phi_\mu = 4\pi G d_\mu \quad (5.2.2)$$

Then, the density and potential fields can be approximated using a total of  $S$  functions, given by

$$\check{\rho}(\mathbf{x}) = \sum_{\mu=1}^S a_\mu d_\mu(\mathbf{x}) \quad (5.2.3)$$

and

$$\check{\phi}(\mathbf{x}) = \sum_{\mu=1}^S a_\mu \phi_\mu(\mathbf{x}), \quad (5.2.4)$$

respectively. In these equations,  $a_\mu$  corresponds to the amplitudes of coefficients for the  $\mu$ -th functions. Considering the density distribution in a system of  $N$  particles as described as

$$\rho(\mathbf{x}) = \sum_{i=1}^N m_i \delta(\mathbf{x} - \mathbf{x}_i) \quad (5.2.5)$$

where  $m_i$  is the mass of the particle and  $\delta(\mathbf{x} - \mathbf{x}_i)$  is the Dirac delta function in  $\mathbf{x}_i$  position, so  $a_\mu$  is equivalent to

$$a_\mu = \int d\mathbf{x} \rho(\mathbf{x}) \phi_\mu(\mathbf{x}) = \sum_{i=1}^N m_i \phi_\mu(\mathbf{x}_i). \quad (5.2.6)$$

These equations can be utilized by any technique and are collectively BFE method (Clutton-Brock, 1972, 1973; Kalnajs, 1976; Hernquist & Weinberg, 1992; Earn, 1996; Weinberg, 1999; Lowing et al., 2011). Broadly, there are three methods of biorthogonal basis function construction. The first category involves constructing biorthogonal functions using the eigenfunctions of the Laplacian in some conic coordinate system (Fridman & Poliachenko, 1984; Earn, 1996). Although this method requires a large number of terms, it is quite straightforward. The second method is derived from the integral form of the Poisson equation for flat discs. For example, Kalnajs (1976) used Green's function kernel to find two biorthogonal sets: logarithmic spirals and a Jacobi polynomial set. Clutton-Brock (1972, 1973) derived biorthogonal sets for 2D and 3D galaxy models through a Hankel transform. Additionally, other biorthogonal sets are based on the Clutton-Brock formalism, which are derived for specific profiles. An example of this is the Self-Consistent Field (SCF) Method (Hernquist & Ostriker, 1992; Lowing et al., 2011), with the zeroth-order model being a Hernquist (1990) density profile. The third method of biorthogonal basis-function construction involves using the Sturm-Liouville equation (SLE) to derive an empirical set of biorthogonal functions (Weinberg, 1999). The Poisson equation is a particular case of the SLE, which is defined as:

$$\frac{d}{dx}\left[p(x)\frac{d\phi(x)}{dx}\right] - q(x)\phi(x) = \lambda w(x)\phi(x) \quad (5.2.7)$$

where  $\lambda$  is a constant, and the weighting function satisfy  $w(x) > 0$ . The  $\phi(x)$  is the unknown function and  $p(x)$ ,  $q(x)$  and  $w(x)$  are parameter functions related to lower-order term of  $\phi(x)$ . The eigenfunctions  $\phi_\mu$  and eigenvalues  $\lambda_\mu$  of the SLE form (eq. 5.2.7) a complete basis. This formally infinite series in  $\mu$  can be subjected to truncation, as described by Courant & Hilbert (1989). Each of the independent equations for a system of coordinates that separates the Poisson equation is in Sturm-Liouville form and can be solved efficiently by numerical methods (e.g. Ixaru et al., 1999). The lowest-order eigenfunction is  $u(x)$  which is constant by construction, assuming an eigenfunction of the form  $\phi(x) = \phi_o(x)u(x)$ , where  $\phi_o(x)$  is the unperturbed potential for the galaxy density. Consequently, the equilibrium is exactly represented by one term. The higher order basis functions are conditioned on the equilibrium.

When considering the Poisson equation in spherical coordinates, one can separate the variables in the angular and radial terms. The solution takes the form of spherical harmonics for the angular coordinates and Sturm-Liouville equation for the radial equation. In spherical coordinates, the weighting function  $w(x)$  can be chosen to be an equilibrium solution of the Poisson equation. In this chapter, we use the EXP code (Petersen et al., 2022), which takes advantage of this flexibility by choosing a weighting function  $w(x)$  in such a way that the equilibrium potential can be represented by a single term (see Petersen et al., 2021). The lowest-order term is designed to match the unperturbed profile, of which they can accurately represent the potential on selected scales using only a small number of higher-order terms. It is possible to represent the potential with high spatial accuracy as long as the structure continues to resemble the initial model. Considering a spherical system, such as an NFW or Hernquist halo profile, the Poisson equation can be separated into spherical coordinates. The angular solutions are defined as  $P_{lm}$ , where  $l$  and  $m$  represent the degree and order of the associated Legendre polynomial, respectively. Meanwhile, the radial separation follows the form of Equation 5.2.7, where  $x = r$ . In this equation,  $w(r) \propto \rho_o(r)\phi_o(r)$  is used to provide an equilibrium solution of the Poisson equation, representing the parameter corresponding to the unperturbed model.

Now, for the Poisson equation, let's consider that  $\phi(r) = \phi_o(r)u(r)$ . Consequently, the coefficients in

Equation 5.2.7 become as follows<sup>1</sup>:

$$p(r) = r^2 \phi_0^2(r) \quad (5.2.8)$$

$$q(r) = [l(l+1)\phi_0(r) - \nabla_r^2 \phi_0(r)r^2] \phi_0(r) \quad (5.2.9)$$

$$w(r) = -4\pi G r^2 \phi_0(r) \rho_0(r) \quad (5.2.10)$$

For each  $l$  and  $m$ , there exists an eigenfunction  $u_{lm}^j(r)$  that corresponds to a solution of Equation 5.2.7, and its lower-order eigenfunction with  $\lambda = 1$  is  $u_{00}^0(r) = 1$  by construction. As  $j$  increases beyond 0,  $u_{lm}(r)$  acquires an additional radial node. As a result, the potentials become  $\phi_{lm}^j \propto \phi_0(r) u_{lm}^j(r) = \phi_{lm}^j(r) P_{lm}(\theta, \phi)$ . Furthermore, radial boundary conditions can be readily applied at specified locations. This allows for the expansion of nearly spherically symmetric systems, such as dark matter halos, into a concise representation using a limited number of spherical harmonics and radial functions.

## 5.3 Simulation data

As described in more detail in Chapter 2.4, the high numerical resolution of the Auriga cosmological simulations allows to study the dark matter and baryonic distribution of simulated galaxies in great detail. As a result, it serves as an ideal laboratory to study the formation of DM density wakes and their effect on the galactic stellar components. In this Chapter, we use six Milky Way-like halos with  $M_{200}$  ranging from  $10^{12.18}$  to  $10^{12.4} M_\odot$  and  $R_{200}$  ranging from 312.6 to 370.9 kpc at  $z = 0$ . These halos contain more than  $10^7$  particles in both the DM and stellar components, and correspond to third resolution level of the Auriga project (lv13).

To analyse the disk perturbations and the structure of the DM halo, we first rotate each halo such that the embedded galactic disk are projected edge-on. To achieve this rotation, we select all stellar particles within a 10 kpc projection in the X-Y plane. The youngest stars are associated with regions of star formation and the cold gas disk, making them ideal tracers of the galactic disk. To correctly rotate the disks, we include stars younger than 5 Gyr, utilizing their angular momentum. The rotation process is iterative, with each iteration including the rotation of both stars and dark matter particles. Eventually, the rotation plane of the disk aligns with the X-Y plane, and the Z-axis represents height. This rotation is important for analyzing morphological perturbations of the disk, such as lopsidedness and warp, while at the same time studying the effect of wake overdensities in dark matter halos on the stellar component.

## 5.4 Analysis and results

### 5.4.1 Spherical density model

As mentioned above, the EXP code uses the BFE method to expand the potential field of a particle ensemble. These derived basis functions are estimated from an input mass distribution, which can be represented either by an analytical model, such as the NFW or Hernquist profile, or by an empirical profile corresponding to the radial mass distribution profile of the halo.

<sup>1</sup>For more details about this method and the mathematics behind it, see Petersen et al. (2021, 2022) and this webpage

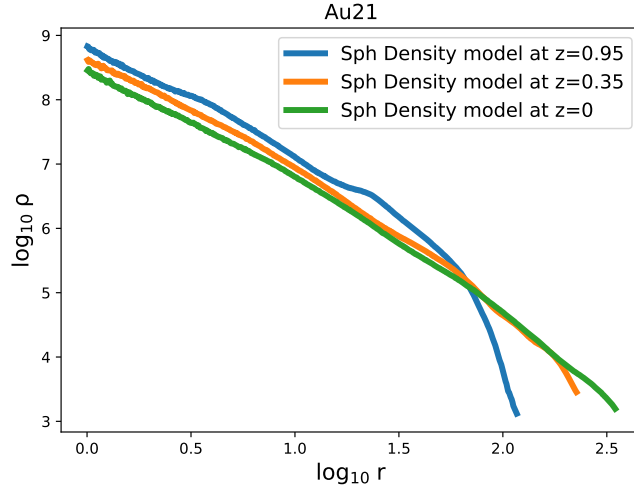


Figure 5.3.1: Spherical density profiles of the dark matter distribution of the Au21 halo at three different redshifts. From these profiles the potential and cumulative mass profiles are estimated, which are used to build the basis functions of EXP.

In this section, we explore how to build suitable basis for the reconstruction of the potential and density fields of the simulated DM halos, at each time step of the simulation. To achieve this, we built three empirical models, each of them based on the DM particles of the central subhalo as identified by Subfind (see Fig. 5.3.1). In this analysis we focus on the results for the Au21 halo because of its interesting satellite interaction activity observed in different snapshots. This halo has a virial radius of  $R_{200} = 349.25$  kpc and a virial mass of  $M_{200} = 10^{12.32} M_{\odot}$ .

The solid lines shown in Fig. 5.3.1 show the density distribution of halo Au21 at three different redshifts,  $z = 0, 0.35, 0.95$ . Notice that, as expected the extension of the DM halo of Au21 increases with time. The density of Au21 in the earliest snapshot reaches 116.67 kpc, while in the present-day it extends to 347.22 kpc. The profile cover the radial extent out to  $R_{200}^2$  of the corresponding redshift. We first start by exploring the stability of the constructed bases as a function of time. To achieve this goal, we will generate basis function at the three different selected redshift.

## 5.4.2 Building basis functions

We start by reconstructing the potential and density profiles described in the previous section. Both potential and density profiles are scaled with respect to their structural parameters, such as  $R_{200}$  and  $M_{200}$ , and from this scaling we compute the unperturbed potential and density profile inputs,  $\phi_{model}(r)$  and  $\rho_{model}(r)$ , respectively. The lowest order monopole function ( $l = n = 0$ ) is tailored to match the density unperturbed profile of the target mass distribution such that  $\rho_{lmn}(r) = \rho_{000}(r) = \rho_{model}(r)$  (similarly for the potential,  $\phi_{lmn}$ ). The basis functions for density and potential are calculated by EXP taking into account that the angular dependence is described by spherical harmonics ( $P_l^m$ ) and the radial dependence

<sup>2</sup>Radius of a sphere centered at the center of the halo whose mean density is 200 times the critical density of the Universe.

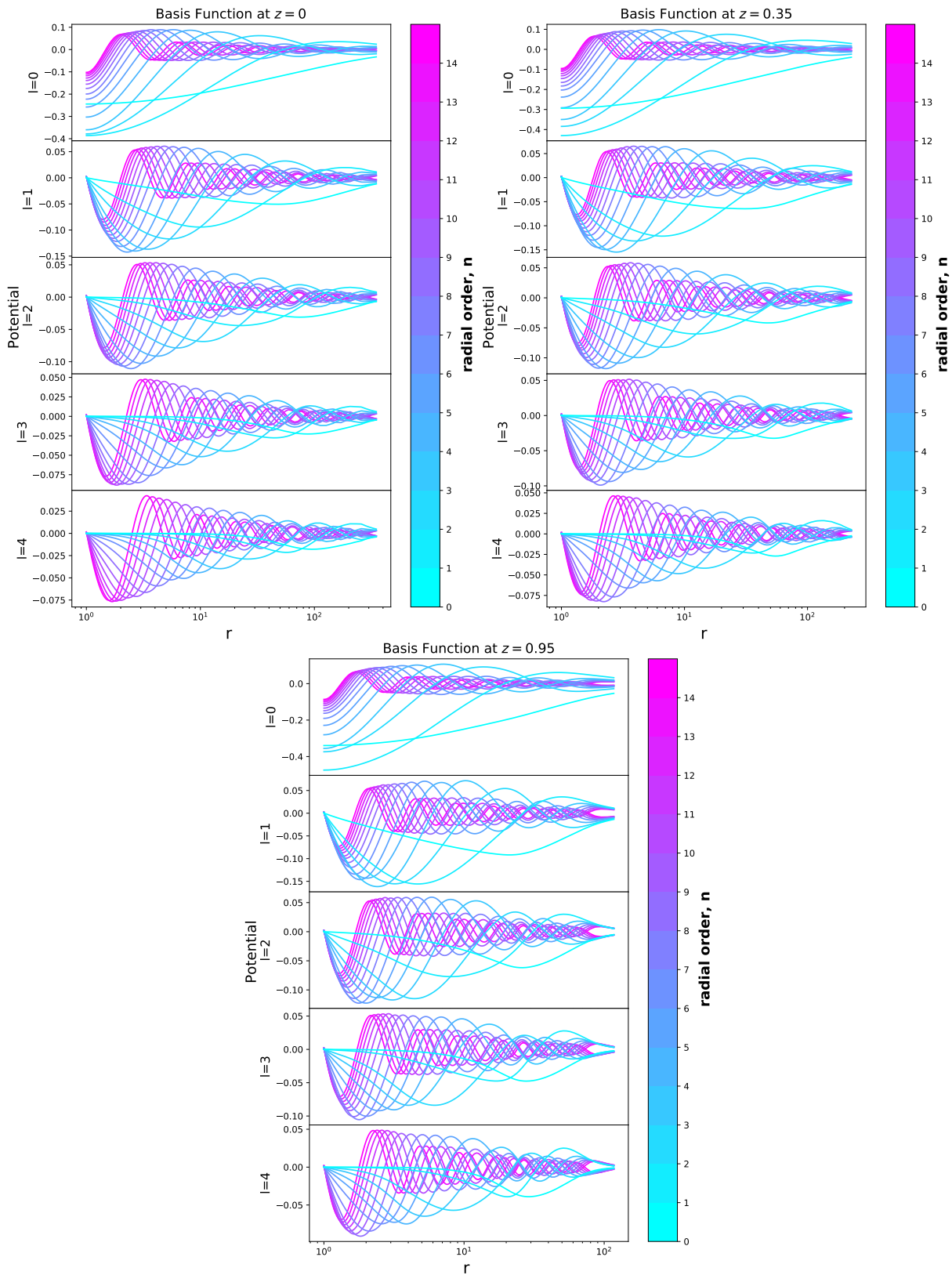


Figure 5.4.1: Basis function for the potential, which is the basis function built using the spherical density model at  $z = 0, 0.35, 0.95$  (top left, top right, and bottom panels, respectively). Each panel shows the basis for the order  $l = 0, 1, 2, 3, 4$ , distributed over the fifty radial orders. The build of those basis functions have a truncation radius of  $R_{200}$  of the corresponding redshift.

is described by the eigenfunctions of the Sturm-Liouville equation (equation 5.2.7) indexed by  $n$ . Similar to previous models (Weinberg & Petersen, 2021; Petersen et al., 2022), we truncate the expansion at  $l_{\max} = 4$  and  $n_{\max} = 15$  for all input empirical models to yield statistically significant coefficients. An  $n_{\max} \approx 16$  minimizes the signal-to-noise ratio<sup>3</sup> and sets the gravitational resolution scale at approximately 20 pc, which is adequate for representing self-gravitating features capable of driving secular evolution. Figure 5.4.1 shows the potential basis functions for each harmonic subspace ( $l = 0, 1, 2, 3, 4$ ) as a function of radius for different radial orders,  $n$ . Each panel represents the basis functions at different epochs. In each harmonic subspace, the number of nodes increases with radial order  $n$ . Also, the radial difference between the nodes decreases with the number of nodes

### 5.4.3 Density field reconstruction

To verify that the basis function is able to reconstruct the density field of the dark matter halo and compare it with the Auriga data particles, we first create a volumetric density map using the dark matter particles from the Auriga simulation. We use a 3D histogram method to construct the volumetric density to compare with the BFE reconstruction. We consider thin slices of 100x100 bins of these volumetric densities. Each slice has a width of 5 kpc. For each bin, the volumetric density represents the total mass per unit volume. To reconstruct the density of the dark matter halo using the EXP code, we obtain the coefficient amplitudes (equation 5.2.6) using the previously defined basis functions by giving as input data the position of the corresponding particles. For this comparison, we focus on the halo at  $z = 0$  and its corresponding basis functions at the same redshift. From the coefficient amplitudes, the EXP code reconstructs the density field (equation 5.2.3) using the terms up to  $l_{\max}$  and  $n_{\max}$ . The reconstructed density field map by EXP is the median of the density field values for the bins using the 3D histogram method. In Figure 5.4.2 we show the comparison between the surface density map using Auriga DM particles,  $\rho_{\text{Auriga}}$  (left panels), and the reconstructed density field map (considering all orders,  $\sum_{lmn} \rho_{lmn}$ ) using EXP,  $\rho_{\text{Exp}}$  (middle panels). The right panels show the residuals between the two density maps, defined as:

$$\rho_{\text{res}} = \frac{\rho_{\text{Auriga}} - \rho_{\text{Exp}}}{\rho_{\text{Auriga}}}. \quad (5.4.1)$$

Each row in the Fig. 5.4.2 corresponds to different slices positioned at different heights. Interestingly, we observe low residual values in the inner regions. However, the values increase at larger radii due to the presence of satellites or more significant substructures. The ring-like shape (top panels in the top region) is due to the fact that the particles identified by SUBFIND were selected based on their greater gravitational binding to the host halo than to the satellite itself. As a result, particles outside the satellite are incorporated into the host halo. Regarding the increased values at large radii, this is also likely due to the fluctuating particle count in the outskirts, rendering the Poisson noise relevant. This is noticeable in the simulated volumetric density panels ( $\rho_{\text{Auriga}}$ , left panels). In contrast, the reconstructed density field map ( $\rho_{\text{Exp}}$ , middle panels) shows a smooth behavior at larger radii. This is because the  $\rho_{\text{Exp}}$  is a smooth function provided by the basis functions used, while  $\rho_{\text{Auriga}}$  represents a limited sample of the underlying density of the system.

<sup>3</sup>The signal-to-noise ratio is defined as the ratio of the rotated coefficients to the square root of the estimated variance normalized by the number of partitions. The number of partitions is defined as the square root of the number of particles. More details in Petersen et al. (2022)

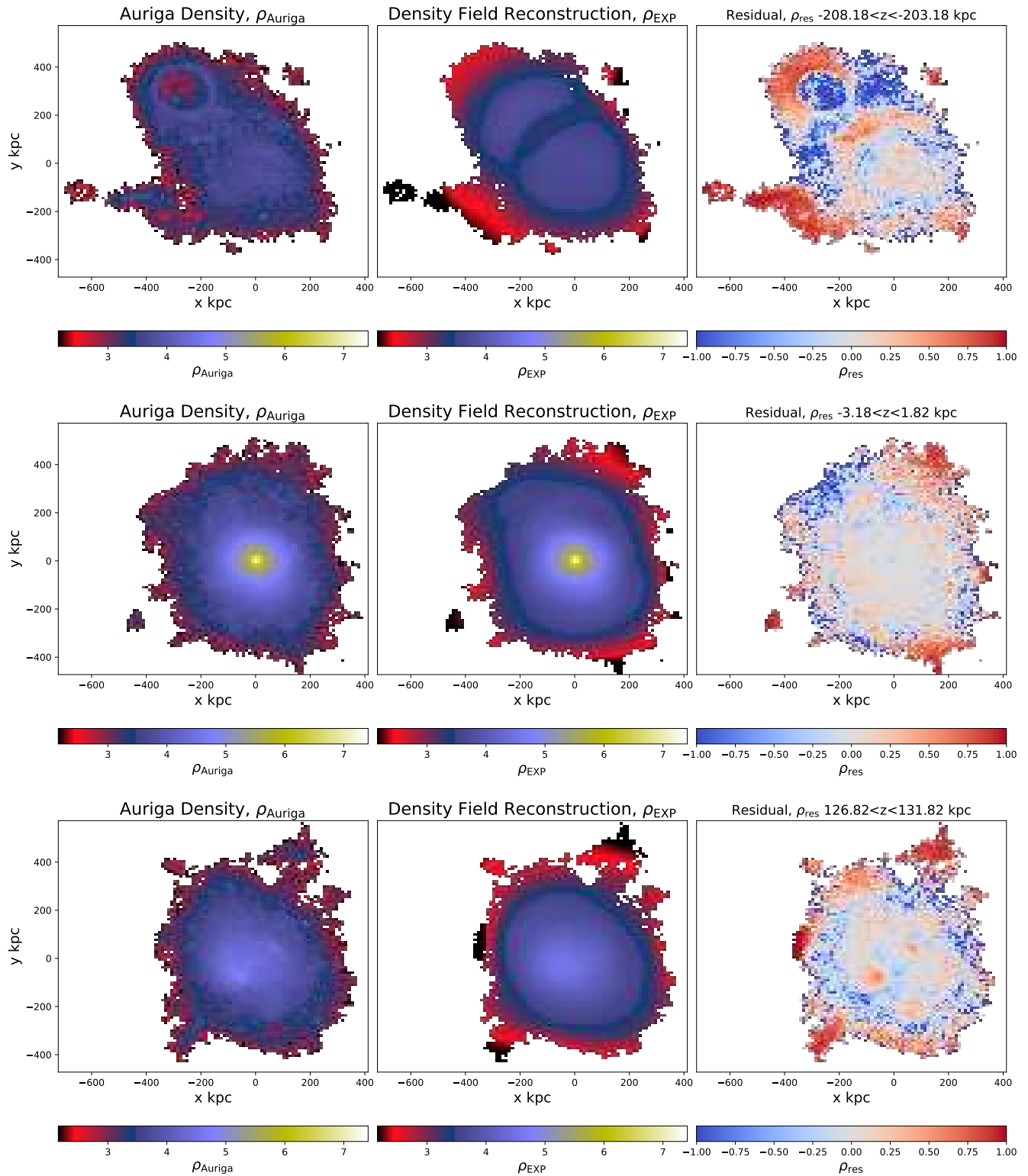


Figure 5.4.2: Reconstruction of the density field of the halo at  $z = 0$ . Each row corresponds to the slice height of the Au 21 DM halo:  $-208.2 < z < -203.2$  kpc (top panels),  $-3.2 < z < 1.8$  kpc (middle panels), and  $126.8 < z < 131.8$  kpc (bottom panels). The left panels correspond to the surface density map of the slice using Auriga DM particles. The middle panels show the median density map reconstructed by EXP. The right panels show the residuals between the Auriga surface density map and the EXP estimation. The residuals show low error values in the center of the halo, the error increasing at the outskirts and in the presence of substructures.

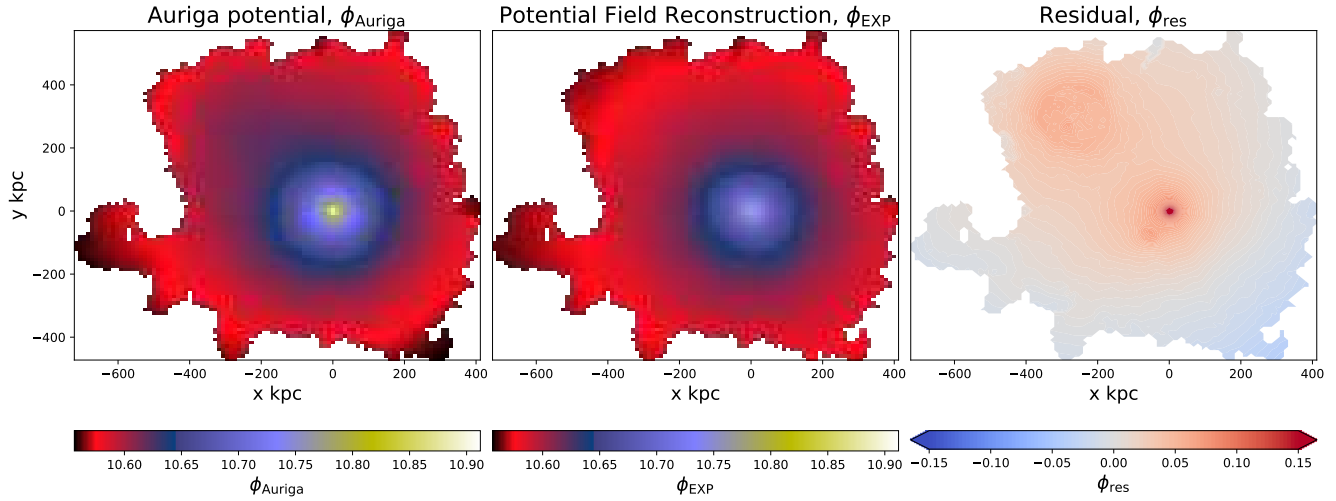


Figure 5.4.3: Reconstruction of the potential field of the halo at  $z = 0$ . The left panel corresponds to the median potential map using the potential values extracted from the Auriga catalog. The middle panel shows the median potential map reconstructed by EXP. The right panel shows the residuals between the Auriga potential map and the EXP estimation. The residuals are less than 18 percent and correspond to the satellites interacting with the central subhalo and the baryonic component in the center of the halo, the rest are less than the 5 percent difference.

#### 5.4.4 Potential field reconstruction

We also explore how well the basis function can reconstruct the potential field of the Au21 dark matter halo, we use EXP to compute the coefficients (as described in Equation 5.2.6). We use the all positions of the DM particles from the Auriga simulation at  $z=0$ . The potential field is reconstructed from EXP considering the equation 5.2.3. In Fig. 5.4.3 we present a comparison between both potential field maps. The left panel shows the median potential map obtained directly from the Auriga simulations. The middle panel shows the reconstructed median potential map obtained from the EXP code. In both plots, we constructed the potential maps using a 2D histogram. The right panel shows the residual between these two potential fields, defined as:

$$\phi_{\text{res}} = \frac{\phi_{\text{Auriga}} - \phi_{\text{EXP}}}{\phi_{\text{Auriga}}} \quad (5.4.2)$$

Interestingly, we observe that the residual does not exceed 18 percent error. The largest differences are found in the northwest region, where the most massive satellite in the halo is located. In addition, the central region has large residuals for two reasons. First, due to the presence of a smaller satellite in the southwest region and, second, due to the contribution to the potential from the baryonic component of the the host galaxy. This is included in the potential extracted from the numerical model but not in the EXP reconstruction. Nonetheless, we can see from the regions where the potential is dominated by the DM distribution, the BFE reconstruction provide a good representation of the DM halo potential field.

### 5.4.5 Stability of the basis reconstruction over time

Similar to previous sections, we compute coefficients for the density field from the EXP code. For this analysis, we construct basis functions of the DM halo density field at three different redshift,  $z = 0, 0.35, 0.95$ . We then use each of these basis to reconstruct the density field of the halo at the three  $z$ . As an example, a  $z = 0$  we derive a reconstruction of the corresponding DM density field using the basis functions obtained at  $z = 0, 0.35, 0.95$ . Our goal is to characterize whether a set basis function, obtained at a given time, can be used to reconstruct the halo at different times. This allows us to check the stability of the sets of basis functions in time, so we can capture and interpret the time evolution of the halos through of coefficients. Conversely, if the set of basis functions changes in time, the interpretation of the coefficients becomes non-trivial. Similar to section 5.4.3, we obtain the density fields through the equation 5.2.3 from EXP code. Figures 5.4.4, 5.4.5, 5.4.6 show a slice of the DM density field crossing through the halo center. The values shown here are the normalized by the monopole term, allowing to highlight asymmetries in the distribution:

$$\Delta\rho = \frac{\rho}{\rho_{000}} - 1. \quad (5.4.3)$$

Here  $\rho$  represents the overall reconstructed density field, for all  $m, l, n$ , and  $\rho_{000}$  is the lower-order monopole density ( $l = n = 0$ ). With  $\Delta\rho$  we can visualize, for example, the overdensity that is produced in the DM halo when a satellite passes through it, as well as the triaxiality of the halo, among others features. Figure 5.4.4 shows the results obtained when considering the distribution of DM particles at  $z = 0$ . The top panels shows the results of reconstructing the density field with the three different basis; i.e.  $\Delta\rho_{z=0}^{z_{\text{basis}}=0}$ ,  $\Delta\rho_{z=0}^{z_{\text{basis}}=0.35}$ ,  $\Delta\rho_{z=0}^{z_{\text{basis}}=0.95}$ . The lower left panel of these figures is the density map of the halo, while the middle and lower right panels highlights the differences between the three  $\Delta\rho$ . For simplicity, the notation of these maps is the difference of the overdensity field from the set of basis functions at  $z$  with those reconstructed from other  $z$ ,  $R_{z_{\text{basis}}_{\text{halo}}}^{z_{\text{basis}}} = \Delta\rho_{z_{\text{halo}}}^{z_{\text{basis}}_{\text{halo}}} - \Delta\rho_{z_{\text{halo}}}^{z_{\text{basis}}}$ . For example, the bottom middle and right panels of Fig. 5.4.4 the difference between the overdensity fields are  $R_0^{0.35} = \Delta\rho_{z=0}^{z_{\text{basis}}=0} - \Delta\rho_{z=0}^{z_{\text{basis}}=0.35}$  and  $R_0^{0.95} = \Delta\rho_{z=0}^{z_{\text{basis}}=0} - \Delta\rho_{z=0}^{z_{\text{basis}}=0.95}$ , respectively.

At  $z = 0$  (Fig. 5.4.4) we note that the set of basis functions computed at  $z = 0$  and  $z = 0.35$  can reconstruct the overdensity field more correctly than what is achieved with the basis at  $z = 0.95$ . This can be seen from the bottom middle and right panels. Note that  $\Delta\rho_{z=0}^{z_{\text{basis}}=0.35}$  shows very small residual, except for the very outer region of the DM halo, where a wake can be seen in  $\Delta\rho_{z=0}^{z_{\text{basis}}=0}$ . At  $z = 0.35$  the halo is less extended than at  $z = 0$ . As a result, the higher  $z$  basis fail to accurately reconstruct the outer regions  $z = 0$  density distribution. The residuals are even larger for  $\Delta\rho_{z=0}^{z_{\text{basis}}=0.95}$ . As previously discussed, the extension of the halo at  $z = 0.95$  is even shorter and, as result, the basis function fail to reconstruct the outer regions. Note in the top right panel of Fig. 5.4.4 that the density reconstruction of the  $z = 0$  density distribution, reconstructed with the  $z = 0.95$  basis, is basically consistent with the monopolar distribution, completely failing to capture the existing asymmetries and perturbations. For the intermediate snapshot of Au21 at  $z = 0.35$  (Fig. 5.4.5) we see similar results to the previous figure, with  $\Delta\rho_{z=0.35}^{z_{\text{basis}}=0.95}$  not recovering the density field correctly. Note however that  $z=0$  basis can reconstruct the overall  $z = 0.35$  density field, albeit a series of high frequency residuals. These residuals are the result of imposing a common maximum number of radial orders when computing the two basis. As a result, the  $z = 0$  basis, associated with a more extended halo, contains more extended radial orders. Finally, the halo at  $z = 0.95$  (Fig. 5.4.6)

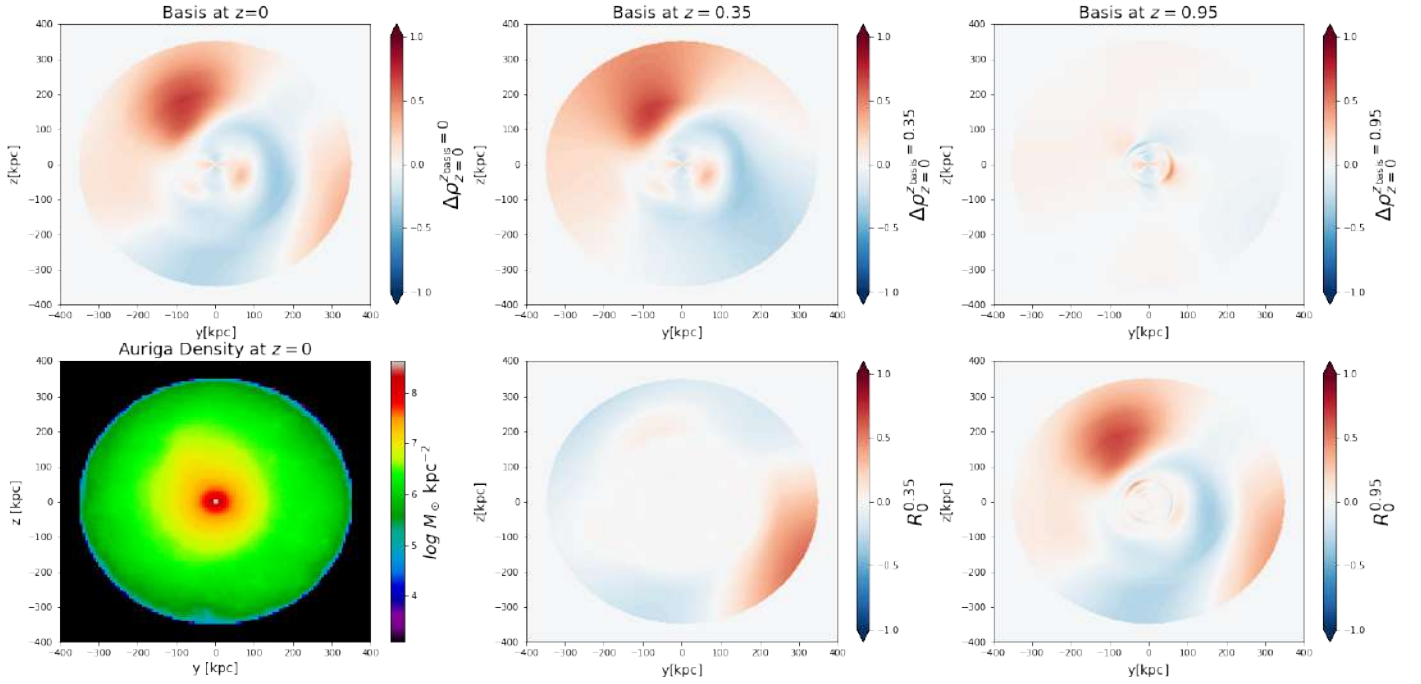


Figure 5.4.4: Reconstruction of the overdensity field,  $\Delta\rho$ , of the halo at  $z = 0$  using three different set of basis functions (top panels). The color code corresponds to the value of  $\Delta\rho_{z=0}^{z=basis}$ , with the sub-index indicating the epoch of the halo and the super-index is the set of basis functions that was used. Additionally, the color range is fixed between -1 and 1. In the bottom left panel, we display the surface density distribution using the Auriga particles at  $z = 0$ , while the bottom middle and right panels show the differences between  $\Delta\rho_{z=0}^{z=basis=0}$  and the other homologous parameters.

is the less extended, when compared to the other two distributions at lower redshifts. We note that  $\Delta\rho$  can be reconstructed by the three sets of basis functions in this  $z$ . Notice that the color code remains fixed between  $|\Delta\rho_{\text{redshift}}| < 0.8$ , but the contours often exceed this range.

From 5.4.4, 5.4.5, and 5.4.6 we can conclude that the basis functions at  $z = 0$  can reconstruct the overdensity field better than the other set of basis functions at the three considered times. The main reason for this is that the configuration used to build the basis functions at  $z = 0$  covers a larger radial range (up to  $R_{200}$ ) than the others. However, the reconstruction of the overdensity field using the  $z=0$  cannot effectively resolve the small scale structure of the halo. In all set of basis functions,  $n_{\text{max}} = 15$  is used, but with different radial ranges (0 to  $R_{200}$  of the corresponding  $z$ ). This leads to different distributions of radial nodes for each basis function set. To correct this issue, it is convenient to increase the value of  $n_{\text{max}}$  for higher  $z$  snapshots. In a future analysis, we will explore how the basis functions rebuild the halo using a fixed truncation radius and particles belonging to the FoF halo for any time. Considering these results, we can use the coefficients at  $z = 0$  to capture the time evolution of the halo.

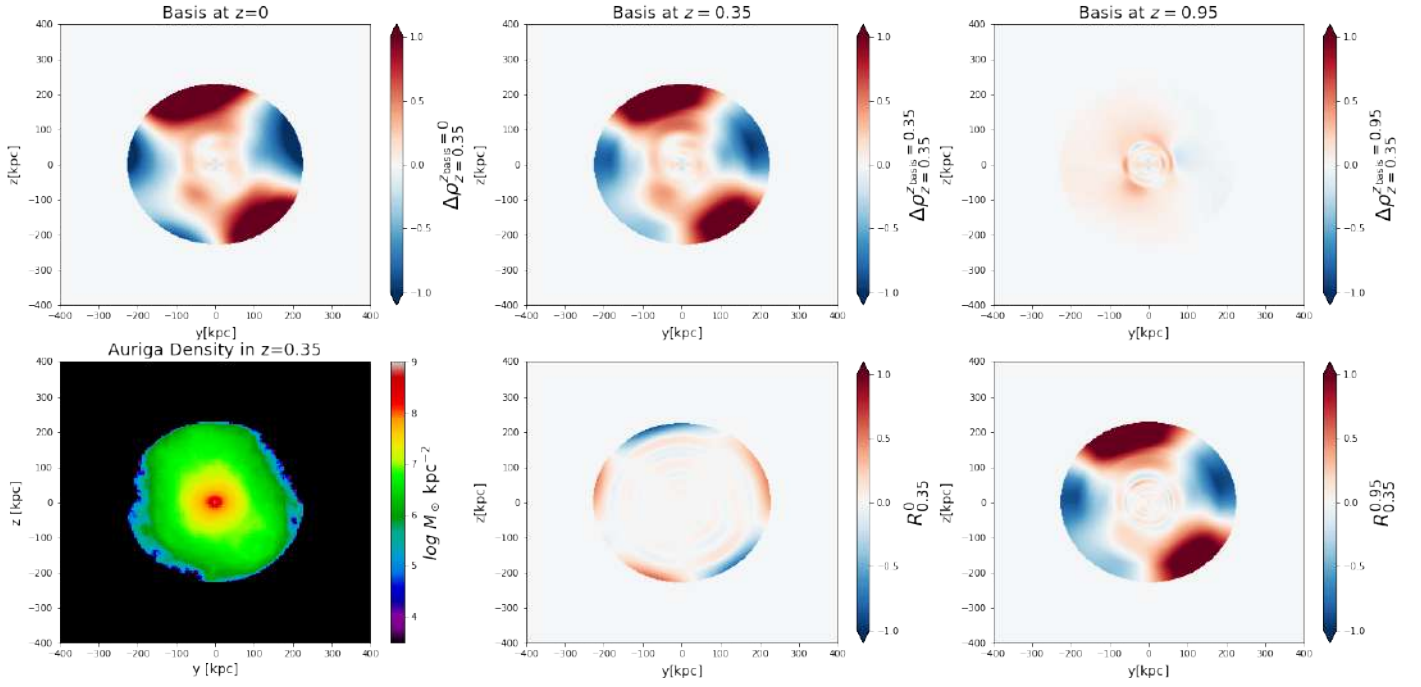


Figure 5.4.5: Reconstruction of the overdensity field of the halo at  $z = 0.35$ , the description is the same that Fig. 5.4.4, but we compare  $\Delta \rho_{z=0.35}^{z_{\text{basis}}=0.35}$  with the other sets of basis functions.

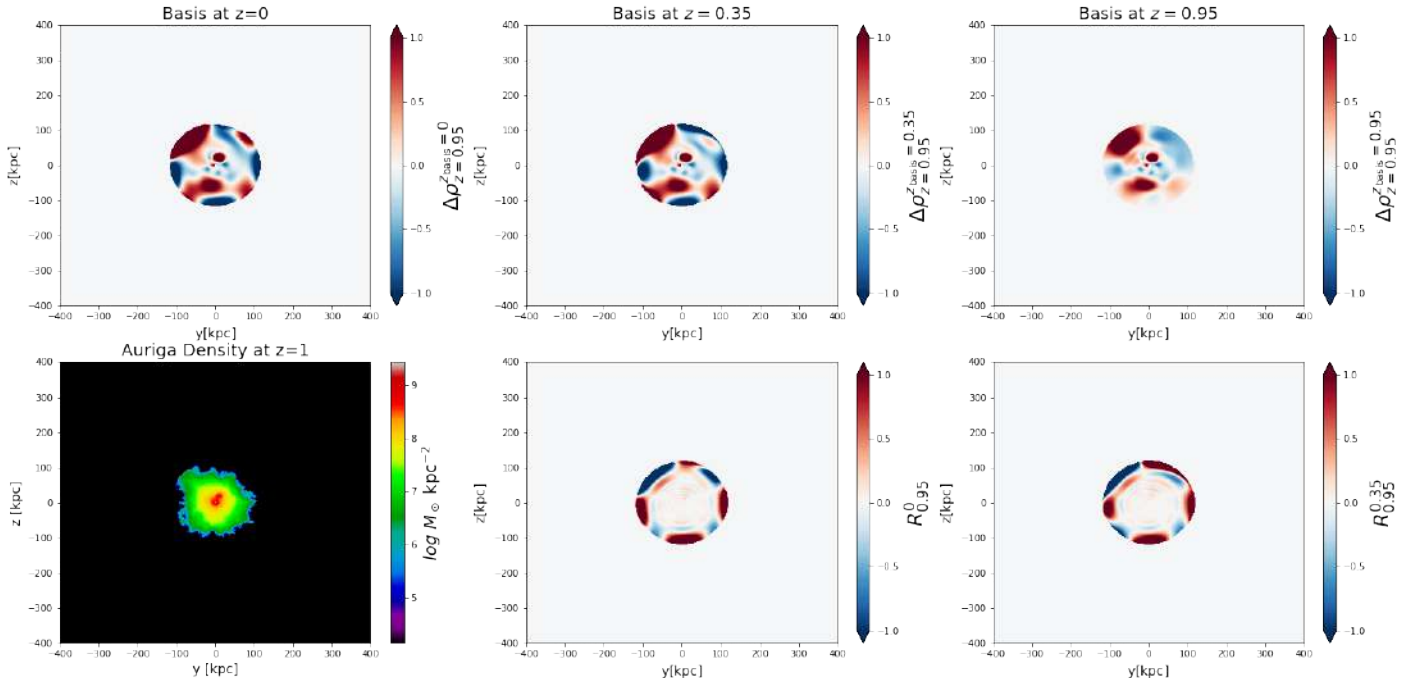


Figure 5.4.6: Reconstruction of the overdensity field of the halo at  $z = 0.95$ , the description is the same that Fig. 5.4.4, but we compare  $\Delta \rho_{z=0.95}^{z_{\text{basis}}=0.95}$  with the other sets of basis functions.

## 5.5 Discussion and Future work

In this chapter, we present the preliminary results of a comprehensive study of the distribution of DM halos and their response when interacting with massive satellite galaxies. The main goal of this study is to identify overdensity wakes in DM halos using basis function expansion analysis, which allows us to expand the potential and density fields of an ensemble of particles. This method allows us to characterize the harmonic orders that contribute significantly to the perturbation. As shown in Chapter 4, morphological asymmetries, such as lopsidedness, are associated with less cohesive gravitational forces and asymmetric DM halos. Interestingly, vertical patterns, such as corrugations and warps, may be associated with a torque exerted on the embedded disk by the wake overdensity (Weinberg, 1998; Gómez et al., 2016, 2017). This suggests a satellite-halo-disk interaction (Vesperini & Weinberg, 2000), where the passage of the satellite’s pericenter can lead to significant quadrupolar distortions.

These findings have motivated us to study in more detail how the DM overdensity wakes induced by the passage of a satellite, can exert a torque on the baryonic disk. Our goal is to study the effects of these torques on the galactic disk and whether these perturbations in the DM halo are associated with morphological asymmetries such as lopsidedness and warps. To this end, we used state-of-the-art cosmological hydrodynamical simulations of six MW-like halos from the Auriga project at level 3. These are high-resolution zoom-in cosmological simulations that allow us to study the disk and DM halo perturbations in great detail. The halos have virial masses in the range of 1 to  $2 \times 10^{12} M_{\odot}$ .

To decompose the potential and density fields of the DM halo, we used EXP, a powerful tool that uses the BFE method. As described in Section 5.2, the BFE method is a technique that computes the potential and density fields by projecting particles onto a set of biorthogonal basis functions (Eq. 5.2.1) that satisfy the Poisson equation (Eq. 5.2.2). In particular, in EXP the biorthogonal functions are described by the solutions derived from spherical harmonics for angular coordinates and by the solutions of the Sturm-Liouville equation for radial coordinates when spherical coordinates are considered. Consequently, the basis functions are determined by constructing the lower-order monopole function as input, which corresponds to the radial mass distribution of the DM halo. In this way, EXP constructs the basis functions and estimates the coefficients for an ensemble of particles, allowing us to obtain the potential and density fields decomposed into several radial and angular terms.

In this chapter, we presented preliminary work, where we computed set of basis functions at three different times, for the Au21 halo:  $z = 0, 0.35$  and  $0.95$ . These sets of basis functions were derived from spherical density models truncated at their respective  $R_{200}$  values. We reconstructed the density fields relative to the density monopole,  $\Delta\rho$ , to identify DM overdensities using these three sets of basis functions and compared between them. We repeated this analysis at the three redshifts mentioned above. Our results show that the set of basis function derived at  $z = 0.95$  does not correctly reconstruct the DM overdensity fields for later redshifts ( $z = 0.35$  and  $0.95$ ), but it performs well at its corresponding redshift. On the other hand, in comparison with the other sets of basis functions, the set of basis functions obtained at  $z = 0$  correctly reconstructs the DM overdensity field for all redshifts. However, their overdensity values are high at  $z = 0.35$  and  $0.95$ , suggesting to explore other values of  $n_{max}$ ,  $l_{max}$  and other parameters of the basis configuration. For example, we observe that the truncated radial order at  $n_{max} = 15$  is not enough to reconstruct small scale structures in the inner regions of the halo. This suggests increasing  $n_{max}$  for higher  $z$  distributions would be required. Overall, these comparisons show that the BFE reconstruction by EXP provides a good representation of the DM halo density and potential field.

As mentioned above, the main goals of this project are to identify overdensity wakes in the dark matter halo and to understand how the torque induced by these wakes is linked to asymmetric features in the baryonic component. To achieve this, it is necessary to aisle the overdensity wakes through time and estimate the torque they exert on the embeded disc. Our results will significantly contribute to the understanding of the halo-disk connection in the evolution and history of MW-like disk galaxies.

# Chapter 6

## Summary

The study of galaxy formation and evolution can be traced back to around 1920, during a significant event known as the Great Debate, involving two astronomers, Harlow Shapley and Heber Curtis. This debate was about the nature of our own Galaxy and the size of the Universe. Significant progress with regards to those question was made years later thanks to the pioneering work of Edwin Hubble and Henrietta Swan Leavitt, who measured distances using variable stars and their period-luminosity relationship. This provided the fundamentals behind the definition of a galaxy as a bounded system of stars and gas, far away from our "island universe" (now the Milky Way galaxy, MW), an "isolated micro-universe".

Galaxies in the Universe exhibit a wide range of shapes, sizes, and colors, and they are arranged hierarchically. When we examine many of these galaxies, taking into account their velocity (using the Doppler effect) and their distance, we observe a fundamental pattern: galaxies that are farther away are receding from us at a faster rate than those that are closer. This observation not only indicates that the entire Universe is expanding, at a rate of about  $67.8 \text{ km s}^{-1} \text{ Mpc}^{-1}$  (Planck Collaboration et al., 2020), but it also implies that if we were to rewind time, we could infer that the distance between galaxies would be closer, indicating a previous state of higher cosmic density. This phenomenon leads us to consider the idea that at some point the universe experienced a state of greater compactness, initiated with what we know now as the Big Bang. During this primordial era, the universe was extremely hot and dense, but as it expanded, it also cooled (more details are discussed in Chapter 1). One of the most iconic moments corresponds to the first recombination era, when the Universe had cooled enough for photons to move freely, filling the Universe isotropically and homogeneously. This is now referred to as the Cosmic Microwave Background (CMB) radiation (Penzias & Wilson, 1965). The CMB plays an important role in astronomical observations because it provides information about the history and evolution of the Universe. It is a valuable window into the composition of the early Universe, providing insight into the initial conditions of the universe. This information is crucial for understanding the formation and subsequent evolution of galaxies, and therefore, it constitutes one of the fundamental hypotheses upon which this thesis is built.

Throughout the 20th century, astronomers studied the structure, evolution, and properties of galaxies in great detail, leading to the development of extragalactic astrophysics as a field in its own right. However, as in all areas of astronomy, this would not have been possible without observational data. In recent years, the amount of astronomical data available has increased exponentially. Remarkable galaxy surveys have not only put theories and models to the test, but have also set the stage for further growth in the wealth of information. In the coming years, we expect to explore the observable universe with unprecedented

precision. This exploration will span a wide range of wavelengths and include deeper observations, driven by the advent of groundbreaking galaxy surveys such as the Legacy Survey of Space and Time (LSST; LSST Science Collaboration et al. (2009)) and the Sloan Digital Sky Survey (SDSS; York et al. (2000)), which have pushed the limits of our empirical understanding of galaxy formation and evolution. These surveys allow us to study the morphology of galaxies and the origin of their perturbations, a topic closely related to the objective of this Thesis. The distribution of stars and their content is highly relevant for understanding various physical processes and their interaction history. Surveys such as MANGA (Bundy et al., 2014) and CALIFA (Sánchez et al., 2012) allow us to explore chemical abundances, stellar ages, kinematic properties, among others. This has allowed the community to characterize stellar density profiles of external galaxies, and study their relation with the chemical and age distributions (e.g., Ruiz-Lara et al., 2016, 2017b) incorporating diverse evolutionary histories of galaxies. Current and near future observational studies of the kinematics and structure of the stellar halo, such as Gaia<sup>1</sup> Gaia Collaboration et al. (2016, 2023), LAMOST (Cui et al., 2012; Zhao et al., 2012), DESI (DESI Collaboration et al., 2023), H3 (Conroy et al., 2019), among others, reveal the structure and kinematic state of the stellar halo of the MW galaxy. The halo of the MW store relevant information about their merger history, the interaction with other galaxies in the past and currently. The mentioned surveys offer us invaluable information, allowing us to detect the kinematic signatures which could be induced by the response of our dark matter halo (e.g. Garavito-Camargo et al., 2019) to the recent interaction with the Large Magellanic Cloud. This drove the analysis presented in this Thesis with regards to perturbation in the DM distribution and their gravitational perturbations.

At the same time, the development of galaxy formation models has progressed significantly over the last few decades. Hydrodynamical simulations have evolved to the point where they can simulate substantial cosmic volumes while self-consistently incorporating intricate algorithms for modeling complex baryonic physical processes. New simulations such as EAGLE (Schaye et al., 2015), Illustris-TNG (Nelson et al., 2018, 2019b), and Auriga (Grand et al., 2017) have revolutionized the study of galaxy formation and evolution. These simulations provide an extensive numerical database for studying the birth and evolution of galaxies in a wide range of environments, from isolated galaxies to massive galaxy clusters.

With all these technological advances, astronomy has advanced by giant leaps in many areas. It is constantly trying to answer the fascinating questions we ask about the Universe and its components. As one question is answered, another question arises. Much remains to be explored in the field of galaxy formation and evolution, in particular the role of dark matter in the evolution and formation of galaxies, or the role of the environment and how it affects galaxies. To understand the formation and evolution of galaxies, it is therefore necessary to have access to both, high resolution observational and numerical data. Such data can allow us not only to characterize in detail important overall properties of galaxies, such as morphology, density and metallicity profiles, but also perturbations within them. For instance, as discussed in this Thesis, lopsidedness, a form of morphological asymmetry where the disk display a distribution of stars and gas more elongated on one side than the other. To study this asymmetry through numerical models it is necessary to have well resolved galaxies, with a sufficient number of particles allowing us to explore their outskirts. Lopsidedness is relevant to explore because it is one of the most common morphological asymmetries in late-type disk galaxies, with about 30 percent of them displaying this perturbation. Indeed, observational results suggest that the Milky Way displays lopsidedness (Kalberla & Dedes, 2008). Furthermore, the study of stellar populations in a disk galaxy, including stel-

---

<sup>1</sup><https://gea.esac.esa.int/archive/documentation/GDR3/index.html>

lar mass profiles, metallicity and age gradients, and others, provides valuable information to understand the interaction history of galaxies with their environment. In this context, morphological perturbations such as lopsidedness, warps, or vertical corrugations may result from interactions with other galaxies, such as mergers, flybys by massive satellites, gas accretion, even the disk’s response to a density wake formed in the host dark matter halo. Thus, both the content of the stellar populations and their morphology may be related to the formation history of their galaxy. In this thesis, we address these research questions using high-resolution cosmological simulations and contrast them with observational results. With the goal of understanding the origin of the different stellar distribution on disk galaxies, in Chapter 3 (based in Varela-Lavin et al. (2022)) we studied the surface density profiles ( $\Sigma$ ) of disk-dominated galaxies selected from the largest volume simulation of the EAGLE project. Our goal was to explore if different density profiles,  $\Sigma(r)$ , can be associated with different evolutionary histories and present global properties. To do this, we classified the sample of simulated galaxies into three different types (TI, TII, and TIII) based on their  $\Sigma(r)$ . We correlate these different density profiles with their morphology, stellar age profiles, star formation rate (SFR) surface densities, mono-age stellar distributions, and the variation in their vertical height and dispersion. The study showed that EAGLE disks have the expected  $\Sigma(r)$  distributions, with TIII and TI being the more common types. It was found that there is a correlation between morphology (quantified by  $D/T$ ) and disk types, with TII disks being more common in late-type spirals, while TI and TIII disks are commonly found in early-type spirals, in agreement with observational findings. The analysis also revealed a correlation between the inner disk scale lengths and the stellar spin parameter ( $\lambda$ ) for all three disk types, with TII discs having the largest inner disk scale lengths. We also identified four types of age profiles in the discs: negative, U-shaped, positive, and  $\lambda$ -shaped age profiles. The U-shape age profiles were characterized by a significant increase in star formation activity in the inner regions of the disc, along with a higher contribution of intermediate age populations in the outer regions. In TI discs, dominated by U-shape and negative age profiles, the mono-age stellar populations showed an inside-out formation scenario, with  $\Sigma_{\text{SFR}}$  profiles decreasing systematically with increasing galactocentric distance. Star formation in the inner regions was attributed to interactions with nearby galaxies and radial migration. TII discs showed mainly negative or U-shaped age profiles, with the change in the slope of the age distributions resulting from a lower contribution of young stars. TIII discs showed an up-bending of their profiles, accompanied by a sharp decrease in the fraction of old stars within the  $R_{\text{br}}$ . These discs appeared to be more stable to perturbations driving gas inflows into the inner regions, possibly due to accreted material from interactions or minor mergers in the outer regions. As just discussed, the study of galaxy morphology provides another way of analysing the physical mechanism that redistribute the stellar and gas material within them. A fundamental question in this context is: “What is the importance of the morphological perturbations in the galaxy history, and what distinguishes galaxies that exhibit perturbations from those that do not?” With this in mind, in Chapter 4 (based in (Varela-Lavin et al., 2023)), our main goal was to explore lopsided perturbations in disk galaxies, i.e. galaxies that exhibit a global  $m = 1$  non-axisymmetric perturbation in their stellar mass distribution. We focused our analysis on a sample of 240 disc-dominated Milky Way-like mass central subhalos obtained from the fully cosmological hydrodynamical simulation, TNG50, of the IllustrisTNG project. This sample contains stellar masses between  $10^{9.5}$  and  $10^{11.2} M_{\odot}$ . Similar to the observational studies, there is an increase in their lopsided amplitude with radius in the outer disk regions ( $r \gtrsim 0.5R_{26.5}$ ). In addition, lopsided galaxies showed a nearly constant or slightly varying radial distribution of phase angles, indicating a slow winding of the phase angle in the outskirts. Contrasting symmetric and asymmetric/lopsided

galaxies, we analysed their structural parameters such as stellar half-mass radius ( $R_{50}^*$ ), total stellar mass ( $M_*$ ), central surface density ( $\mu_*$ ), and stellar concentration ( $C_*$ ). We found that lopsided galaxies tend to have more extended central regions. We demonstrated that lopsided discs systematically show lower  $\mu_*$  values than their symmetric counterparts. This trend is also being seen at different redshifts. These results are consistent with previous observations based on SDSS data (R08), and suggest that lower central densities renders galaxies more susceptible to lopsided perturbations. We have further explored the gravitational cohesiveness of the halos in which the sampled galaxies reside. For this purpose, we consider their baryonic and dark matter components. We find that lopsided galaxies tend to have weaker gravitationally cohesive halos compared to their symmetric counterparts. Interestingly, we also note that the halos of lopsided galaxies tend to be asymmetric and have higher spin. The latter suggests that lower  $\mu_*$  and larger extended galaxies are more likely to reside in less gravitationally cohesive halos. In this way, compact or strongly cohesive disks are likely to be associated with low spin in the halo. There are several mechanism that can give rise to extended discs. As discussed in Grand et al. (2017), large disks could be formed by quiescent mergers, bringing high angular momentum material into the pre-existing disk. In addition, it has also been shown that halos with larger spin are likely to host more extended discs. On the other hand, strong mergers and strong AGN feedback can significantly reduce the final disk size by either destroying the pre-existing disk or by inhibiting gas accretion to the outskirts. These results suggest that weakly gravitationally cohesive galaxies are more likely to develop lopsidedness in their galactic discs. Galaxies with these characteristics are susceptible to gravitational perturbations from various cosmological events, such as minor mergers, fly-bys with other galaxies, among others. The study presented in Chapter 4 suggest a intricate connection between the disk and halo.

Disk galaxies can present a variety of morphological asymmetries, such as warps or corrugations. Some studies suggest that these types of vertical distortions may be related to gravitational interactions between a satellite and its host. These same interactions can yield resonances that affect the distribution of its dark matter halo, causing overdensity wakes. In Chapter 5 of this Thesis we studied the DM distribution and their response to satellite passages near central galaxies. The study aims to identify DM overdensity wakes using basis function expansion of the DM potential-density pair to shed light on the harmonic orders that contribute significantly to perturbations in the embedded galactic discs. More precisely, this analysis also seeks to quantify the effects of the torques arising from these perturbations, and whether they are associated with asymmetries, such as lopsidedness, warps, and others. The study uses state-of-the-art cosmological hydrodynamical simulations of Milky Way-like halos from the Auriga project. These simulations provide high-resolution data for halos in the mass range of  $1$  to  $2 \times 10^{12} M_\odot$ . To decompose the potential and density fields of the DM halo, our study uses the EXP tool, which employs the Basis Function Expansion (BFE) method. This method projects particles onto a set of biorthogonal basis functions to compute potential and density fields, dissecting them in several terms with different power. The preliminary results of this study indicate that the set of basis functions obtained by EXP at  $z = 0$  can reconstruct the density and potential fields of the dark matter halo better than other sets of basis functions generated at earlier time. This is because at earlier times halos are less extended. Thus, those basis constructed fail to accurately reconstruct the outer region of the more extended halos at later times. The results presented in these Thesis open several new paths to develop in the future. The preliminary analysis presented in Chapter 5 has shown that BFE reconstruction of DM halos represent a powerful tools to characterize the onset of density perturbations and their impact on galactic discs. As a result it could allow us to understand the link between the torque induced by the wakes with morphological

---

perturbation in the disk, such as lopsidedness, warps, vertical corrugations, among others. The BFE method could also be applied to potential density pair associated with the host galactic disc. This would allow us to explore the distribution of the barionic component in different terms or sets of basis functions. As we discussed previously, highly gravitational cohesive galaxies could be correlated with strong AGN activity, in contrast to less cohesive galaxies, which are associated with lopsidedness. It will be interesting to study the correlation of AGN activity and galaxy morphology perturbations such as lopsidedness. As presented in this thesis, we have explored the different behaviors of stellar density profiles and lopsidedness as a morphological perturbation in the stellar component. The physical processes driving these galactic characteristics, as well as their connection with their environment, are likely to be similar. Therefore, it is important for future work to perform an analysis that connects both behaviors of the stellar component in order to unravel the different evolutionary histories of these galaxies.

## Acknowledgments

### 6.0.1 Financial acknowledgments

I acknowledge the financial support from the Vicerrectoria de Investigación de la Universidad de La Serena through the "Beca Doctoral", from the financial support from ANID/"Beca de Doctorado Nacional"/21221776, from the Max Planck Society through a Partner Group grant, and from the Basal project FB210003 of the Center for Astrophysics and Related Technologies (CATA).

### 6.0.2 Personal acknowledgments

In this section, I would like to express my sincere gratitude to all the people who have accompanied and supported me during this journey. Your advice, patience, encouragement and affection have been fundamental to achieving this milestone.

I am deeply grateful to my supervisor, Facundo A. Gómez, for his invaluable support and guidance throughout this process. His human quality, patience and advice allowed me to grow not only as an astronomer, but also as a person. I immensely value the time and effort he dedicated to my training, from the beginning to the end of my PhD, and even afterwards. His trust in me allowed me to collaborate on projects with other colleagues and gave me the opportunity to learn and develop even further. I feel fortunate to have had him as a supervisor and friend, and I hope that we can continue working together for a long time. I also thank Patricia Tissera for believing in me during my undergraduate studies. Thanks to her, I became interested in working with hydrodynamic simulations. Since I showed her my interest, she has provided me with her support and patience, allowing me to learn valuable skills that prepared me for my PhD. I hope to continue learning from her experience in a new project. I thank Nicolás Garavito-Camargo for his support during my internship at the CCA (Flatiron Institute) and among other events. His advice and availability have been invaluable to my professional growth. You are a great person in many ways and I hope that we can continue working together in the future.

To my PhD professors, Julia Arias, Alexandre Roman, Antonela Monachesi and Rodolfo Angeloni, I thank them for their dedication to teaching and for transmitting their passion for Astronomy to me. Thanks to them, I was able to acquire a deep knowledge in various areas of this fascinating discipline. I would also like to thank the Thesis Advancement Committee, composed of Hector Cuevas, Ricardo Amorín, Patricia Tissera and Facundo Gómez, for their advice and for the time they dedicated to listening to my progress during this period. I also thank the members of my thesis evaluation committee, Rory Smith, Maria Celeste Artale and Nicolas Garavito, for their time and valuable suggestions for improving this manuscript.

To my PhD colleagues, with whom I shared pleasant moments in the office, discussions about our progress and problems, and also moments of coffee, mates, barbecues and beers. I especially thank my generation colleagues, Camila, Dania and Mario, for their support during this PhD process. To my undergraduate friends, Kata Montenegro, Cata Flowers, Jorge, Javier, Carla and Homero, I thank them for the great moments we shared, for their unconditional support and for keeping in touch despite the fact that each one has followed their own path. You are great!

To my wife, Ayleen, for her unconditional moral support all these years. Thank you for understanding me, for being my grounding cable, and for encouraging me in difficult times. Despite the joys and difficulties,

we have shared a great life experience together. I love you very much, my little squirrel (:.  
To my parents, Silvio and Genoveva, for their constant support and encouragement since I was a child. Thank you for teaching me the love of learning and for motivating me to follow my dreams. You are great people and I admire you so much. I love you (:.  
To my sister Giannina, for our deep conversations about life and the universe. You are a very capable person and I admire you for your achievements. All these thanks are proof that I have not been alone on this path. Your support, love, and trust have motivated me to keep going, to not give up in the face of difficulties, and to achieve my goals. Although this achievement is personal, I recognize that I could not have achieved it without the support of all the people who have accompanied me.

# Bibliography

- Alfaro E. J., Pérez E., González Delgado R. M., Martos M. A., Franco J., 2001, *ApJ*, 550, 253
- Ann H. B., Park J. C., 2006, *NewA*, 11, 293
- Antoja T., et al., 2018, *Nature*, 561, 360
- Antoja T., Ramos P., López-Guitart F., Anders F., Bernet M., Laporte C. F. P., 2022, *A&A*, 668, A61
- Athanassoula E., 2005, *MNRAS*, 358, 1477
- Aumer M., White S. D. M., 2013, *MNRAS*, 428, 1055
- Bahé Y. M., et al., 2016, *MNRAS*, 456, 1115
- Bakos J., Trujillo I., Pohlen M., 2008, *ApJL*, 683, L103
- Baldry I. K., et al., 2012, *MNRAS*, 421, 621
- Baldwin J. E., Lynden-Bell D., Sancisi R., 1980, *MNRAS*, 193, 313
- Barnes J. E., Hernquist L., 1996, *ApJ*, 471, 115
- Barrow J. D., 1983, *QJRAS*, 24, 24
- Bauer A. E., et al., 2013, *MNRAS*, 434, 209
- Bellhouse C., et al., 2021, *MNRAS*, 500, 1285
- Belokurov V., Kravtsov A., 2022, *MNRAS*, 514, 689
- Belokurov V., et al., 2006, *ApJL*, 642, L137
- Benitez-Llambay A., 2015, *py-sphviewer: Py-SPHViewer v1.0.0*, doi:10.5281/zenodo.21703, <http://dx.doi.org/10.5281/zenodo.21703>
- Besla G., Peter A. H. G., Garavito-Camargo N., 2019, , 2019, 013
- Bigiel F., Leroy A., Walter F., Brinks E., de Blok W. J. G., Madore B., Thornley M. D., 2008, *The Astronomical Journal*, 136, 2846
- Binney J., 1992, *ARA&A*, 30, 51

- Binney J., Tremaine S., 1987, *Galactic dynamics*
- Binney J., Tremaine S., 2008, *Galactic Dynamics: Second Edition*
- Bland-Hawthorn J., Tepper-García T., 2021, *MNRAS*, 504, 3168
- Boggess N. W., et al., 1992, *ApJ*, 397, 420
- Bondi H., 1952, *MNRAS*, 112, 195
- Bondi H., Hoyle F., 1944, *MNRAS*, 104, 273
- Booth C. M., Schaye J., 2009, *MNRAS*, 398, 53
- Bosma A., 1981, *AJ*, 86, 1791
- Bournaud F., Combes F., Jog C. J., Puerari I., 2005, *A&A*, 438, 507
- Brooks A., Christensen C., 2016, in Laurikainen E., Peletier R., Gadotti D., eds, *Astrophysics and Space Science Library Vol. 418, Galactic Bulges*. p. 317 (arXiv:1511.04095), doi:10.1007/978-3-319-19378-6\_12
- Brooks A., Governato F., Brook C., Quinn T., 2007, in *American Astronomical Society Meeting Abstracts*. p. 111.02
- Bruzual G., Charlot S., 2003, *MNRAS*, 344, 1000
- Bullock J. S., Johnston K. V., 2005, *ApJ*, 635, 931
- Bundy K., et al., 2014, *The Astrophysical Journal*, 798, 7
- Cataldi P., Pedrosa S. E., Tissera P. B., Artale M. C., 2021, *MNRAS*, 501, 5679
- Chabrier G., 2003, *Publications of the Astronomical Society of the Pacific*, 115, 763
- Chandrasekhar S., 1943, *ApJ*, 97, 255
- Choi J.-H., Weinberg M. D., Katz N., 2009, *MNRAS*, 400, 1247
- Clutton-Brock M., 1972, *Ap&SS*, 16, 101
- Clutton-Brock M., 1973, *Ap&SS*, 23, 55
- Coc A., Vangioni E., 2017, *International Journal of Modern Physics E*, 26, 1741002
- Cole S., Lacey C., 1996, *MNRAS*, 281, 716
- Conroy C., et al., 2019, *ApJ*, 883, 107
- Conroy C., Naidu R. P., Garavito-Camargo N., Besla G., Zaritsky D., Bonaca A., Johnson B. D., 2021, *Nature*, 592, 534

- Conselice C. J., Bershadsky M. A., Jangren A., 2000, *ApJ*, 529, 886
- Conselice C. J., Bershadsky M. A., Dickinson M., Papovich C., 2003, *AJ*, 126, 1183
- Cooper A. P., et al., 2010, *MNRAS*, 406, 744
- Courant R., Hilbert D., 1989, *Methods of mathematical physics*
- Crain R. A., et al., 2015, *MNRAS*, 450, 1937
- Crain R. A., et al., 2017, *MNRAS*, 464, 4204
- Cui X.-Q., et al., 2012, *Research in Astronomy and Astrophysics*, 12, 1197
- Cullen L., Dehnen W., 2010, *MNRAS*, 408, 669
- Cunningham E. C., et al., 2020, *ApJ*, 898, 4
- DESI Collaboration et al., 2023, arXiv e-prints, p. arXiv:2306.06308
- D'Souza R., Bell E. F., 2018, *Nature Astronomy*, 2, 737
- Dalcanton J. J., Spergel D. N., Summers F. J., 1997, *ApJ*, 482, 659
- Dalla Vecchia C., Schaye J., 2012, *MNRAS*, 426, 140
- Davis M., Efstathiou G., Frenk C. S., White S. D. M., 1985, *ApJ*, 292, 371
- De Lucia G., Helmi A., 2008, *MNRAS*, 391, 14
- Debattista V. P., Sellwood J. A., 1999, *The Astrophysical Journal*, 513, L107
- Debattista V. P., Sellwood J. A., 2000, *ApJ*, 543, 704
- Debattista V. P., Mayer L., Carollo C. M., Moore B., Wadsley J., Quinn T., 2006, *ApJ*, 645, 209
- Debattista V. P., Roškar R., Loebman S. R., 2017, *The Impact of Stellar Migration on Disk Outskirts*. p. 77, doi:10.1007/978-3-319-56570-5\_3
- Dehnen W., Aly H., 2012, *Monthly Notices of the Royal Astronomical Society*, 425, 1068
- Dib S., et al., 2021, *A&A*, 655, A101
- Dolag K., Borgani S., Murante G., Springel V., 2009, *MNRAS*, 399, 497
- Dolfi A., Gomez F. A., Monachesi A., Varela-Lavin S., Tissera P. B., Sifon C., Galaz G., 2023, arXiv e-prints, p. arXiv:2306.04639
- Durier F., Dalla Vecchia C., 2012, *MNRAS*, 419, 465
- Earn D. J. D., 1996, *ApJ*, 465, 91

- Elagali A., Lagos C. D. P., Wong O. I., Staveley-Smith L., Trayford J. W., Schaller M., Yuan T., Abadi M. G., 2018, MNRAS, 481, 2951
- Elmegreen B. G., Hunter D. A., 2006, ApJ, 636, 712
- Erwin P., Pohlen M., Beckman J. E., 2008, AJ, 135, 20
- Eskridge P. B., et al., 2002, ApJS, 143, 73
- Fairall A. P., 1995, Ap&SS, 230, 225
- Fall S. M., Efstathiou G., 1980, MNRAS, 193, 189
- Faucher-Giguère C.-A., Lidz A., Zaldarriaga M., Hernquist L., 2009, ApJ, 703, 1416
- Fellhauer M., et al., 2006, ApJ, 651, 167
- Few J. M. A., Madore B. F., 1986, MNRAS, 222, 673
- Fisher D. B., Drory N., 2008, AJ, 136, 773
- Fontanelli P., 1984, A&A, 138, 85
- Fragkoudi F., et al., 2020, MNRAS, 494, 5936
- Freeman K. C., 1970, ApJ, 160, 811
- Frenk C. S., White S. D. M., Davis M., Efstathiou G., 1988, ApJ, 327, 507
- Fridman A. M., Poliachenko V. L., 1984, Physics of gravitating systems. II - Nonlinear collective processes: Nonlinear waves, solitons, collisionless shocks, turbulence. Astrophysical applications
- Fridman A. M., et al., 1998, Astronomy Letters, 24, 764
- Fujii M. S., Baba J., Saitoh T. R., Makino J., Kokubo E., Wada K., 2011, The Astrophysical Journal, 730, 109
- Furlong M., et al., 2015, MNRAS, 450, 4486
- Gaia Collaboration et al., 2016, A&A, 595, A2
- Gaia Collaboration et al., 2018, A&A, 616, A11
- Gaia Collaboration et al., 2023, A&A, 674, A1
- Gao L., White S. D. M., 2006, MNRAS, 373, 65
- Garavito-Camargo N., Besla G., Laporte C. F. P., Johnston K. V., Gómez F. A., Watkins L. L., 2019, ApJ, 884, 51

- Garavito-Camargo N., Besla G., Laporte C. F. P., Price-Whelan A. M., Cunningham E. C., Johnston K. V., Weinberg M., Gómez F. A., 2021, *ApJ*, 919, 109
- García-Ruiz I., Sancisi R., Kuijken K., 2002, *A&A*, 394, 769
- García de la Cruz J., Martig M., Minchev I., James P., 2021, *MNRAS*, 501, 5105
- Gargiulo I. D., et al., 2019, *MNRAS*, 489, 5742
- Genel S., et al., 2014, *MNRAS*, 445, 175
- Genel S., Fall S. M., Hernquist L., Vogelsberger M., Snyder G. F., Rodriguez-Gomez V., Sijacki D., Springel V., 2015, *ApJL*, 804, L40
- Ghosh S., Saha K., Jog C. J., Combes F., Di Matteo P., 2022, *MNRAS*, 511, 5878
- Gibson B. K., Pilkington K., Brook C. B., Stinson G. S., Bailin J., 2013, *A&A*, 554, A47
- Giocoli C., Tormen G., Sheth R. K., van den Bosch F. C., 2010, *MNRAS*, 404, 502
- Gómez F. A., Helmi A., Brown A. G. A., Li Y.-S., 2010, *MNRAS*, 408, 935
- Gómez F. A., Coleman-Smith C. E., O’Shea B. W., Tumlinson J., Wolpert R. L., 2012, *ApJ*, 760, 112
- Gómez F. A., Helmi A., Cooper A. P., Frenk C. S., Navarro J. F., White S. D. M., 2013, *MNRAS*, 436, 3602
- Gómez F. A., Besla G., Carpintero D. D., Villalobos Á., O’Shea B. W., Bell E. F., 2015, *ApJ*, 802, 128
- Gómez F. A., White S. D. M., Marinacci F., Slater C. T., Grand R. J. J., Springel V., Pakmor R., 2016, *MNRAS*, 456, 2779
- Gómez F. A., White S. D. M., Grand R. J. J., Marinacci F., Springel V., Pakmor R., 2017, *MNRAS*, 465, 3446
- Gómez F. A., et al., 2021, *ApJ*, 908, 27
- Gozman K., et al., 2023, *ApJ*, 947, 21
- Grand R. J. J., Springel V., Gómez F. A., Marinacci F., Pakmor R., Campbell D. J. R., Jenkins A., 2016, *MNRAS*, 459, 199
- Grand R. J. J., et al., 2017, *MNRAS*, 467, 179
- Grand R. J. J., Pakmor R., Fragkoudi F., Gómez F. A., Trick W., Simpson C. M., van de Voort F., Bieri R., 2022, *arXiv e-prints*, p. arXiv:2211.08437
- Guth A. H., 1981, *PhRvD*, 23, 347
- Gutiérrez L., Erwin P., Aladro R., Beckman J. E., 2011, *AJ*, 142, 145

- Harmsen B., Monachesi A., Bell E. F., de Jong R. S., Bailin J., Radburn-Smith D. J., Holwerda B. W., 2017, *MNRAS*, 466, 1491
- Haynes M. P., Hogg D. E., Maddalena R. J., Roberts M. S., van Zee L., 1998, *AJ*, 115, 62
- Helmi A., White S. D. M., 1999, *MNRAS*, 307, 495
- Hernquist L., 1990, *ApJ*, 356, 359
- Hernquist L., Ostriker J. P., 1992, *ApJ*, 386, 375
- Hernquist L., Weinberg M. D., 1992, *ApJ*, 400, 80
- Herpich J., et al., 2015, *MNRAS*, 448, L99
- Herpich J., Stinson G. S., Rix H. W., Martig M., Dutton A. A., 2017, *MNRAS*, 470, 4941
- Hirschmann M., De Lucia G., Wilman D., Weinmann S., Iovino A., Cucciati O., Zibetti S., Villalobos Á., 2014, *MNRAS*, 444, 2938
- Hodge P., 1986, *Publications of the Astronomical Society of the Pacific*, 98, 1095
- Holwerda B. W., Pirzkal N., de Blok W. J. G., Bouchard A., Blyth S. L., van der Heyden K. J., Elson E. C., 2011, *MNRAS*, 416, 2415
- Hopkins P. F., 2013, *MNRAS*, 428, 2840
- Hubble E., 1926, *Contributions from the Mount Wilson Observatory / Carnegie Institution of Washington*, 324, 1
- Hunt J. A. S., Stelea I. A., Johnston K. V., Gandhi S. S., Laporte C. F. P., Bédorf J., 2021, *MNRAS*, 508, 1459
- Ixaru L., De Meyer H., Vanden Berghe G., 1999, *Computer Physics Communications*, 118, 259
- Jacyszyn-Dobrzyniecka A. M., et al., 2016, , 66, 149
- Jenkins A., 2010, *MNRAS*, 403, 1859
- Jenkins A., 2013, *MNRAS*, 434, 2094
- Jiang I.-G., Binney J., 1999, *MNRAS*, 303, L7
- Jing Y. P., 2000, *ApJ*, 535, 30
- Jog C. J., 1997, *ApJ*, 488, 642
- Jog C. J., 1999, *ApJ*, 522, 661
- Jog C. J., 2000, *ApJ*, 542, 216

- Jog C. J., Combes F., 2009, *PhR*, 471, 75
- Johnson A. C., Petersen M. S., Johnston K. V., Weinberg M. D., 2023, *MNRAS*, 521, 1757
- Johnston K. V., Hernquist L., Bolte M., 1996, *ApJ*, 465, 278
- Kalberla P. M. W., Dedes L., 2008, *A&A*, 487, 951
- Kalnajns A. J., 1976, *ApJ*, 205, 745
- Kennicutt Robert C. J., 1989, *ApJ*, 344, 685
- Kennicutt Robert C. J., 1998, *ApJ*, 498, 541
- Kereš D., Katz N., Weinberg D. H., Davé R., 2005, *MNRAS*, 363, 2
- Khademi M., Yang Y., Hammer F., Nasiri S., 2021, *A&A*, 654, A7
- Khoperskov S., et al., 2023, *A&A*, 677, A91
- Kornreich D. A., Lovelace R. V. E., Haynes M. P., 2002, *ApJ*, 580, 705
- LSST Science Collaboration et al., 2009, arXiv e-prints, p. arXiv:0912.0201
- Lacey C., Cole S., 1994, *MNRAS*, 271, 676
- Lagos C. d. P., et al., 2015, *MNRAS*, 452, 3815
- Lagos C. d. P., Theuns T., Stevens A. R. H., Cortese L., Padilla N. D., Davis T. A., Contreras S., Croton D., 2017, *MNRAS*, 464, 3850
- Lagos C. d. P., Schaye J., Bahé Y., Van de Sande J., Kay S. T., Barnes D., Davis T. A., Dalla Vecchia C., 2018, *MNRAS*, 476, 4327
- Lagos C. d. P., Emsellem E., van de Sande J., Harborne K. E., Cortese L., Davison T., Foster C., Wright R. J., 2020, arXiv e-prints, p. arXiv:2012.08060
- Laine J., et al., 2014, *MNRAS*, 441, 1992
- Laporte C. F. P., Gómez F. A., Besla G., Johnston K. V., Garavito-Camargo N., 2018a, *MNRAS*, 473, 1218
- Laporte C. F. P., Johnston K. V., Gómez F. A., Garavito-Camargo N., Besla G., 2018b, *MNRAS*, 481, 286
- Lequeux J., Peimbert M., Rayo J. F., Serrano A., Torres-Peimbert S., 1979, *A&A*, 80, 155
- Levine S. E., Sparke L. S., 1998, *ApJL*, 496, L13
- Levine E. S., Blitz L., Heiles C., 2006, *ApJ*, 643, 881

- Li Z.-Y., Ho L. C., Barth A. J., Peng C. Y., 2011, *ApJS*, 197, 22
- Lilleengen S., et al., 2023, *MNRAS*, 518, 774
- Lintott C., et al., 2011, *MNRAS*, 410, 166
- Łokas E. L., 2021, *A&A*, 655, A97
- Łokas E. L., 2022, *A&A*, 662, A53
- Louis T., et al., 2017, , 2017, 031
- Lowing B., Jenkins A., Eke V., Frenk C., 2011, *MNRAS*, 416, 2697
- Ludlow A. D., Fall S. M., Schaye J., Obreschkow D., 2021, *MNRAS*, 508, 5114
- MacArthur L. A., González J. J., Courteau S., 2009, *MNRAS*, 395, 28
- Marinacci F., Pakmor R., Springel V., 2014, *MNRAS*, 437, 1750
- Marinacci F., Grand R. J. J., Pakmor R., Springel V., Gómez F. A., Frenk C. S., White S. D. M., 2017, *MNRAS*, 466, 3859
- Marinacci F., et al., 2018, *MNRAS*, 480, 5113
- Martínez-Serrano F. J., Serna A., Doménech-Moral M., Domínguez-Tenreiro R., 2009, *ApJL*, 705, L133
- Massey R., Kitching T., Richard J., 2010, *Reports on Progress in Physics*, 73, 086901
- McAlpine S., et al., 2016, *Astronomy and Computing*, 15, 72
- Minchev I., Famaey B., 2010, *ApJ*, 722, 112
- Minchev I., Famaey B., Quillen A. C., Di Matteo P., Combes F., Vlajić M., Erwin P., Bland-Hawthorn J., 2012a, *A&A*, 548, A126
- Minchev I., Famaey B., Quillen A. C., Dehnen W., Martig M., Siebert A., 2012b, *A&A*, 548, A127
- Minchev I., Martig M., Streich D., Scannapieco C., de Jong R. S., Steinmetz M., 2015, *ApJL*, 804, L9
- Mo H. J., Mao S., White S. D. M., 1998, *MNRAS*, 295, 319
- Monachesi A., et al., 2013, *ApJ*, 766, 106
- Monachesi A., Bell E. F., Radburn-Smith D. J., Bailin J., de Jong R. S., Holwerda B., Streich D., Silverstein G., 2016, *MNRAS*, 457, 1419
- Monachesi A., et al., 2019, *MNRAS*, 485, 2589
- Muñoz-Mateos J. C., et al., 2013, *ApJ*, 771, 59

- Naiman J. P., et al., 2018, *MNRAS*, 477, 1206
- Navarro J. F., Frenk C. S., White S. D. M., 1995, *MNRAS*, 275, 720
- Navarro J. F., Frenk C. S., White S. D. M., 1996, *ApJ*, 462, 563
- Nelson D., et al., 2015, *Astronomy and Computing*, 13, 12
- Nelson D., et al., 2018, *MNRAS*, 475, 624
- Nelson D., et al., 2019a, *Computational Astrophysics and Cosmology*, 6, 2
- Nelson D., et al., 2019b, *MNRAS*, 490, 3234
- Noordermeer E., Sparke L. S., Levine S. E., 2001, *MNRAS*, 328, 1064
- Noordermeer E., van der Hulst J. M., Sancisi R., Swaters R. A., van Albada T. S., 2005, *A&A*, 442, 137
- Nulsen P. E. J., Fabian A. C., 2000, *MNRAS*, 311, 346
- Pakmor R., Springel V., Bauer A., Mocz P., Munoz D. J., Ohlmann S. T., Schaal K., Zhu C., 2016, *MNRAS*, 455, 1134
- Pakmor R., et al., 2017, *MNRAS*, 469, 3185
- Pakmor R., Guillet T., Pfrommer C., Gómez F. A., Grand R. J. J., Marinacci F., Simpson C. M., Springel V., 2018, *MNRAS*, 481, 4410
- Patel E., et al., 2020, *ApJ*, 893, 121
- Patterson F. S., 1940, *Harvard College Observatory Bulletin*, 914, 9
- Pedrosa S. E., Tissera P. B., 2015, *A&A*, 584, A43
- Peebles P. J., 1966, *PhRvL*, 16, 410
- Peebles P. J. E., 1980, *The large-scale structure of the universe*
- Penzias A. A., Wilson R. W., 1965, *ApJ*, 142, 419
- Perez J., Michel-Dansac L., Tissera P. B., 2011, *MNRAS*, 417, 580
- Petersen M. S., Weinberg M. D., Katz N., 2021, *MNRAS*, 500, 838
- Petersen M. S., Weinberg M. D., Katz N., 2022, *MNRAS*, 510, 6201
- Phookun B., Mundy L. G., 1995, *ApJ*, 453, 154
- Pillepich A., et al., 2018, *MNRAS*, 473, 4077
- Pillepich A., et al., 2019, *MNRAS*, 490, 3196

- Planck Collaboration et al., 2014, *A&A*, 571, A16
- Planck Collaboration et al., 2016, *A&A*, 594, A13
- Planck Collaboration et al., 2020, *A&A*, 641, A6
- Pohlen M., Trujillo I., 2006, *A&A*, 454, 759
- Price D. J., 2008, *Journal of Computational Physics*, 227, 10040
- Quillen A. C., Dougherty J., Bagley M. B., Minchev I., Comparetta J., 2011, *MNRAS*, 417, 762
- Reichard T. A., Heckman T. M., Rudnick G., Brinchmann J., Kauffmann G., 2008, *ApJ*, 677, 186
- Reshetnikov V., Combes F., 1998, *A&A*, 337, 9
- Reshetnikov V. P., Mosenkov A. V., Moiseev A. V., Kotov S. S., Savchenko S. S., 2016, *MNRAS*, 461, 4233
- Richter O. G., Sancisi R., 1994, *A&A*, 290, L9
- Rix H.-W., Zaritsky D., 1995, *ApJ*, 447, 82
- Rodriguez-Gomez V., et al., 2015, *MNRAS*, 449, 49
- Roediger J. C., Courteau S., MacArthur L. A., McDonald M., 2011, *MNRAS*, 416, 1996
- Roediger J. C., Courteau S., Sánchez-Blázquez P., McDonald M., 2012, *The Astrophysical Journal*, 758, 41
- Romero-Gómez M., Mateu C., Aguilar L., Figueras F., Castro-Ginard A., 2019, *A&A*, 627, A150
- Rosas-Guevara Y. M., et al., 2015, *MNRAS*, 454, 1038
- Rosito M. S., Tissera P. B., Pedrosa S. E., Lagos C. D. P., 2019a, *A&A*, 629, L3
- Rosito M. S., Tissera P. B., Pedrosa S. E., Rosas-Guevara Y., 2019b, *A&A*, 629, A37
- Roškar R., Debattista V. P., Stinson G. S., Quinn T. R., Kaufmann T., Wadsley J., 2008a, *ApJL*, 675, L65
- Roškar R., Debattista V. P., Quinn T. R., Stinson G. S., Wadsley J., 2008b, *ApJL*, 684, L79
- Roškar R., Debattista V. P., Brooks A. M., Quinn T. R., Brook C. B., Governato F., Dalcanton J. J., Wadsley J., 2010, *MNRAS*, 408, 783
- Roškar R., Debattista V. P., Loebman S. R., 2013, *MNRAS*, 433, 976
- Rudnick G., Rix H.-W., 1998, *AJ*, 116, 1163
- Ruiz-Lara T., et al., 2016, *MNRAS*, 456, L35

- Ruiz-Lara T., et al., 2017a, *A&A*, 604, A4
- Ruiz-Lara T., Few C. G., Florido E., Gibson B. K., Pérez I., Sánchez-Blázquez P., 2017b, *A&A*, 608, A126
- Saha K., Combes F., Jog C. J., 2007, *MNRAS*, 382, 419
- Sáiz A., Domínguez-Tenreiro R., Tissera P. B., Courteau S., 2001, *MNRAS*, 325, 119
- Sánchez-Blázquez P., Courty S., Gibson B. K., Brook C. B., 2009, *MNRAS*, 398, 591
- Sánchez-Blázquez P., Ocvirk P., Gibson B. K., Pérez I., Peletier R. F., 2011, *MNRAS*, 415, 709
- Sánchez-Blázquez P., et al., 2014, *A&A*, 570, A6
- Sánchez-Gil M. C., Alfaro E. J., Pérez E., 2015, *MNRAS*, 454, 3376
- Sánchez-Saavedra M. L., Battaner E., Florido E., 1990, *MNRAS*, 246, 458
- Sánchez S. F., et al., 2012, *A&A*, 538, A8
- Sánchez S. F., Galbany L., Walcher C. J., García-Benito R., Barrera-Ballesteros J. K., 2023, *MNRAS*,
- Schaller M., Dalla Vecchia C., Schaye J., Bower R. G., Theuns T., Crain R. A., Furlong M., McCarthy I. G., 2015, *MNRAS*, 454, 2277
- Schaye J., 2004, *ApJ*, 609, 667
- Schaye J., Dalla Vecchia C., 2008, *MNRAS*, 383, 1210
- Schaye J., et al., 2015, *MNRAS*, 446, 521
- Schoenmakers R. H. M., Franx M., de Zeeuw P. T., 1997, *MNRAS*, 292, 349
- Sellwood J. A., 2013a, in Oswalt T. D., Gilmore G., eds, , Vol. 5, *Planets, Stars and Stellar Systems. Volume 5: Galactic Structure and Stellar Populations*. p. 923, doi:10.1007/978-94-007-5612-0\_18
- Sellwood J. A., 2013b, *The Astrophysical Journal Letters*, 769, L24
- Sellwood J. A., Binney J. J., 2002, *MNRAS*, 336, 785
- Sérsic J. L., 1963, *Boletín de la Asociación Argentina de Astronomía La Plata Argentina*, 6, 41
- Sersic J. L., 1968, *Atlas de Galaxias Australes*
- Shen S., Mo H. J., White S. D. M., Blanton M. R., Kauffmann G., Voges W., Brinkmann J., Csabai I., 2003, *MNRAS*, 343, 978
- Solar M., Tissera P. B., Hernandez-Jimenez J. A., 2020, *MNRAS*, 491, 4894
- Springel V., 2005, *MNRAS*, 364, 1105

- Springel V., 2010, MNRAS, 401, 791
- Springel V., Hernquist L., 2003, MNRAS, 339, 289
- Springel V., White S. D. M., Tormen G., Kauffmann G., 2001, MNRAS, 328, 726
- Springel V., et al., 2005, Nature, 435, 629
- Springel V., et al., 2018, MNRAS, 475, 676
- Swaters R. A., Schoenmakers R. H. M., Sancisi R., van Albada T. S., 1999, MNRAS, 304, 330
- Takeuchi T. T., Tomita A., Nakanishi K., Ishii T. T., Iwata I., Saitō M., 1999, ApJS, 121, 445
- Tawfeek A. A., et al., 2021, NewA, 87, 101603
- Teklu A. F., Remus R.-S., Dolag K., Beck A. M., Burkert A., Schmidt A. S., Schulze F., Steinborn L. K., 2015, ApJ, 812, 29
- Tissera P. B., Lambas D. G., Abadi M. G., 1997, MNRAS, 286, 384
- Tissera P. B., White S. D. M., Scannapieco C., 2012, MNRAS, 420, 255
- Tissera P. B., Scannapieco C., Beers T. C., Carollo D., 2013, MNRAS, 432, 3391
- Tissera P. B., Beers T. C., Carollo D., Scannapieco C., 2014, MNRAS, 439, 3128
- Tissera P. B., Pedrosa S. E., Sillero E., Vilchez J. M., 2016, MNRAS, 456, 2982
- Tissera P. B., Rosas-Guevara Y., Bower R. G., Crain R. A., del P Lagos C., Schaller M., Schaye J., Theuns T., 2019, MNRAS, 482, 2208
- Tissera P. B., Rosas-Guevara Y., Sillero E., Pedrosa S. E., Theuns T., Bignone L., 2022, MNRAS, 511, 1667
- Torrey P., Vogelsberger M., Sijacki D., Springel V., Hernquist L., 2012, MNRAS, 427, 2224
- Trayford J. W., Schaye J., 2019, MNRAS, 485, 5715
- Tremaine S., Weinberg M. D., 1984, MNRAS, 209, 729
- Tully R. B., Fisher J. R., 1977, A&A, 54, 661
- Urrejola-Mora C., Gómez F. A., Torres-Flores S., Amram P., Epinat B., Monachesi A., Marinacci F., de Oliveira C. M., 2022, ApJ, 935, 20
- Varela-Lavin S., Tissera P. B., Gómez F. A., Bignone L. A., Lagos C. d. P., 2022, MNRAS, 514, 5340
- Varela-Lavin S., Gómez F. A., Tissera P. B., Besla G., Garavito-Camargo N., Marinacci F., Laporte C. F. P., 2023, MNRAS, 523, 5853

- Vasiliev E., Belokurov V., Erkal D., 2021, MNRAS, 501, 2279
- Vegetti S., Lagattuta D. J., McKean J. P., Auger M. W., Fassnacht C. D., Koopmans L. V. E., 2012, Nature, 481, 341
- Vera-Casanova A., et al., 2022, MNRAS, 514, 4898
- Vesperini E., Weinberg M. D., 2000, ApJ, 534, 598
- Vogelsberger M., Genel S., Sijacki D., Torrey P., Springel V., Hernquist L., 2013, MNRAS, 436, 3031
- Vogelsberger M., et al., 2014a, MNRAS, 444, 1518
- Vogelsberger M., et al., 2014b, Nature, 509, 177
- Vollmer B., Nehlig F., Ibata R., 2016, A&A, 586, A98
- Vulcani B., Poggianti B. M., Smith R., Moretti A., Jaffé Y. L., Gullieuszik M., Fritz J., Bellhouse C., 2022, ApJ, 927, 91
- Wagoner R. V., 1973, ApJ, 179, 343
- Walcher C. J., et al., 2014, A&A, 569, A1
- Walker I. R., Mihos J. C., Hernquist L., 1996, ApJ, 460, 121
- Wang J., et al., 2018, MNRAS, 479, 4292
- Weinberg M. D., 1989, MNRAS, 239, 549
- Weinberg M. D., 1994, ApJ, 421, 481
- Weinberg M. D., 1995, ApJL, 455, L31
- Weinberg M. D., 1998, MNRAS, 299, 499
- Weinberg M. D., 1999, The Astronomical Journal, 117, 629
- Weinberg M. D., Katz N., 2007, MNRAS, 375, 425
- Weinberg M. D., Petersen M. S., 2021, MNRAS, 501, 5408
- Weinberger R., et al., 2017, MNRAS, 465, 3291
- Wendland H., 1995, Advances in Computational Mathematics, 4, 389
- White S. D. M., 1983, ApJ, 274, 53
- Widrow L. M., Bonner G., 2015, MNRAS, 450, 266
- Widrow L. M., Gardner S., Yanny B., Dodelson S., Chen H.-Y., 2012, The Astrophysical Journal Letters, 750, L41

- Wiersma R. P. C., Schaye J., Smith B. D., 2009a, MNRAS, 393, 99
- Wiersma R. P. C., Schaye J., Theuns T., Dalla Vecchia C., Tornatore L., 2009b, MNRAS, 399, 574
- Willett K. W., et al., 2013, MNRAS, 435, 2835
- Xu Y., Newberg H. J., Carlin J. L., Liu C., Deng L., Li J., Schönrich R., Yanny B., 2015, ApJ, 801, 105
- Yoachim P., Roškar R., Debattista V. P., 2012, ApJ, 752, 97
- York D. G., et al., 2000, AJ, 120, 1579
- Younger J. D., Cox T. J., Seth A. C., Hernquist L., 2007, ApJ, 670, 269
- Zaritsky D., Rix H.-W., 1997, The Astrophysical Journal, 477, 118
- Zaritsky D., Kennicutt Robert C. J., Huchra J. P., 1994, ApJ, 420, 87
- Zaritsky D., et al., 2013, ApJ, 772, 135
- Zel'dovich Y. B., 1970, A&A, 5, 84
- Zhao G., Zhao Y., Chu Y., Jing Y., Deng L., 2012, arXiv e-prints, p. arXiv:1206.3569
- Zhu L., et al., 2018, Nature Astronomy, 2, 233
- Zibetti S., White S. D. M., Brinkmann J., 2004, MNRAS, 347, 556
- de Blok W. J. G., Walter F., Brinks E., Trachternach C., Oh S.-H., Kennicutt R. C., 2008, The Astronomical Journal, 136, 2648
- de Vaucouleurs G., 1959, Handbuch der Physik, 53, 275
- van Eymeren J., Jütte E., Jog C. J., Stein Y., Dettmar R. J., 2011, A&A, 530, A30
- van der Kruit P. C., 1979, A&AS, 38, 15
- van der Marel R. P., 2001, AJ, 122, 1827